Technical University of Denmark

DTU

Nanostructuring of Solar Cell Surfaces

Davidsen, Rasmus Schmidt; Hansen, Ole; Boisen, Anja; Schmidt, Michael Stenbæk

[Link back to DTU Orbit](#)

DTU Library
Technical Information Center of Denmark

DTU

Nanostructuring of Solar Cell Surfaces

Rasmus Schmidt Davidsen
PhD Thesis March 2016

Supervisors:
Professor Ole Hansen
Professor Anja Boisen
Senior Researcher Michael Stenbæk Schmidt

DTU Nanotech
Department of Micro- and Nanotechnology

Cover Image: Scanning Electron Microscope image of a Ni/Cu front contact cross-section surrounded by nanostructures on a laser-doped selective emitter, black Si solar cell. The nanostructures were made by maskless reactive ion etching and the contact cross-section was defined by a focused ion beam. The metal contact was formed by light-induced plating subsequent to laser-doping. This type of cell reached the highest efficiency for black Si solar cells in this work.

Preface

This thesis has been submitted to the Department of Micro- and Nanotechnology at the Technical University of Denmark (DTU) in partial fulfillment of the requirements for acquiring the PhD degree. The research providing the foundation for the thesis has been conducted over a period of 2 years and 11 months from November 1st 2012 to October 1st 2015. The work has been carried out at the Department of Micro- and Nanotechnology at the Technical University of Denmark and has been supervised by Professor Ole Hansen, Professor Anja Boisen and Senior Researcher Michael Stenbæk Schmidt. The initial hypothesis of the thesis was to directly replace conventional texturing methods in the solar industry with black Si made by maskless reactive ion etching (RIE). A general restriction of the work in this thesis has been the focus on scalable and industrially relevant processes and materials only. Thus, the first experimental investigation was the fabrication and characterization of RIE- and conventionally textured 'industrial' 156x156 mm^2 Si solar cells in collaboration with the Institute for Energy Technology (IFE) in Norway. Since the result of this investigation showed the need for further cell improvement, especially related to the surface passivation and emitter of the cell, the remainder of the research work was focused on the development of a second batch of improved black Si solar cells and analysis of the surface passivation and emitter formation on black Si. The second batch of laser-doped black Si cells was realized at the School of Photovoltaic and Renewable Energy Engineering, University of New South Wales (UNSW) in Sydney, Australia, where I was privileged to spend 4 months (August-December 2014) at my external research stay under the supervision of Professor Allen Barnett and Professor Stuart Wenham.

Throughout the project I have had the pleasure of supervising 6 engineering students in their B.Sc.-projects and additionally 7 engineering students in smaller student projects. Their work has contributed to the outcome of this thesis and the discussions with these students along the way has certainly improved my own understanding and overview of the project. Furthermore I have participated in fruitful discussions with fellow researchers at the EU PVSEC conferences in Frankfurt (2012), Paris (2013) and Hamburg (2015) and MNE conferences in London (2013) and Haag (2015). The project has been funded by DTU Nanotech.

<div align="right">

Rasmus Schmidt Davidsen
Copenhagen, March 2016

</div>

"Vast Power of the Sun is Tapped by Battery Using Sand Ingredient." [1]

Front page headline of the New York Times, April 26, 1954

---

[1] Attributed to Professor Martin A. Green (UNSW) who used this quote in his lecture "Evolution of Silicon Solar Cells" at UNSW in April, 2013.

Abstract

Solar energy is by far the most abundant renewable energy source available, but the levelized cost of solar energy is still not competitive with that of fossil fuels. Therefore there is a need to improve the power conversion efficiency of solar cells without adding to the production cost.

The main objective of this PhD thesis is to develop nanostructured silicon (Si) solar cells with higher power conversion efficiency using only scalable and cost-efficient production methods. The nanostructures, known as 'black silicon', are fabricated by single-step, maskless reactive ion etching and used as front texturing of different Si solar cells. Theoretically the nanostructure topology may be described as a graded refractive index in a mean-field approximation between air and Si. The optical properties of the developed black Si were simulated and experimentally measured. Total AM1.5G-weighted average reflectance well below 1% was measured for different crystalline grades of Si. Furthermore, the reflectance of RIE-textured Si remains below that of KOH-textured Si at all incident angles below 70°. RIE- and conventionally textured, screen-printed Si solar cells were fabricated on 156x156 mm^2 CZ Si wafers and characterized for comparison. Power conversion efficiency of 16.5% was obtained for this batch of RIE-textured Si solar cells. The efficiency of the KOH-textured reference cell was 17.8%. Quantum Efficiency measurements and carrier loss analysis show that the lower efficiency of the RIE-textured cells is primarily due to increased emitter and surface recombination. The large-area screen-printed solar cells were furthermore characterized at varying incident angles. The angle-dependent analysis shows that RIE-textured cells have a higher normalized power output averaged over the range of incident angles between 0 and 90°. This result indicates the potential of improved cell performance and higher output power at diffuse light conditions and during daily and yearly operation. A second batch of RIE-textured solar cells with laser-doped selective emitters (LDSE) was fabricated. A power conversion efficiency of 18.1% and a fill factor of 80.1% were obtained by laser doping and subsequent Ni/Cu plating in combination with RIE-texturing. This result shows the potential of improved efficiency of RIE-textured compared to conventionally textured cells, especially when laser doping on black Si is combined with improved surface passivation schemes such as atomic layer deposition (ALD) of Al_2O_3. ALD Al_2O_3 passivation on black Si yields surface recombination velocity (SRV) below 80 cm/s and implied open-circuit voltage (iV$_{OC}$) of 680 mV. Surface recombination velocity of 20 cm/s and implied open-circuit voltage of 695 mV is obtained for black Si passivated by doped poly-Si and a tunnel oxide.

Dansk Resumé

Solenergi er den energikilde med den største tilgængelige mængde energi, men den normaliserede omkostning for solenergi er stadig ikke konkurrencedygtig med fossile brændsler. Derfor er der behov for at forbedre solcellers effektivitet uden at forøge produktionsomkostningen.

Hovedformålet med denne PhD afhandling er at udvikle nanostrukturerede silicium (Si) solceller med højere effektivitet kun ved hjælp af skalérbare og omkostningseffektive produktionsmetoder. Nanostrukturerne, også kaldet 'sort silicium', produceres med en et-trins, maskeløs reaktiv ion æts (RIE) og bliver brugt som forside teksturering af forskellige Si solceller. Teoretisk kan nanostruktur topologien beskrives som et gradueret brydnings-indeks i en gennemsnits-felt approksimation mellem luft og Si. De optiske egenskaber af det udviklede sorte Si blev simuleret og målt eksperimentelt. Den totale AM1.5G-vægtede gennemsnitlige reflektans blev målt til markant under 1% for forskellige typer krystallinsk Si. Ydermere er reflektansen af RIE-tekstureret Si lavere end for KOH-tekstureret Si for alle indfaldsvinkler under 70°. RIE- og konventionelt teksturerede, screen-printede Si solceller blev fabrikeret på 156x156 mm^2 CZ Si skiver og karakteriseret til sammenligning. En effektivitet på 16.5% blev opnået for denne batch RIE-teksturerede Si solceller. Effektiviteten af de KOH-teksturerede reference-celler var til sammenligning 17.8%. Kvante-effektivitets målinger og analyse af ladningsbærer-tab viser at den lavere effektivitet for de RIE-teksturerede celler primært skyldes forøget overflade- og emitter-rekombination. De store screen-printede solceller blev desuden karakteriseret ved varierende indfaldsvinkel. Den vinkel-afhængige analyse viser at RIE-teksturerede celler har en højere normaliseret udgangs-effekt i gennemsnit over indfaldsvinkler i intervallet 0-90°. Dette resultat indikerer et potentiale for forbedret ydeevne og højere udgangs-effekt ved diffust lysindfald og i løbet af daglig og årlig operation. En anden batch RIE-teksturerede solceller med laser-doteret selektiv emitter (LDSE) blev fabrikeret. En effektivitet på 18.1% og en fill factor på 80.1% blev opnået via laser-dotering og efterfølgende Ni/Cu-plettering i kombination med RIE-teksturering. Dette resultat viser potentialet for endnu højere effektivitet for RIE-teksturerede solceller, især hvis laser-dotering på sort Si kombineres med forbedret overflade passivering som fx atom-lags-deponering (ALD) af Al$_2$O$_3$. ALD Al$_2$O$_3$ passivering på sort Si resulterer i overflade rekombinations hastighed (SRV) under 80 cm/s og antaget tomgangs-spænding (iV$_{OC}$) på 680 mV. Overflade rekombinations hastighed på 20 cm/s og antaget tomgangs-spænding på 695 mV er opnået for sort Si passiveret med doteret poly-Si og tunnel oxid.

Acknowledgements

Contents

List of Figures

List of Tables

Abbreviations

ALD	Atomic Layer Deposition
AM	Air Mass
AR	Anti Reflective
BS	Black Silicon
BSF	Back Surface Field
CZ	Czochralski
DTU	Danmarks Tekniske Universitet (Technical University of Denmark)
ECV	Electrochemical Capacitance-Voltage
EQE	External Quantum Efficiency
FF	Fill Factor
FIB	Focused Ion Beam
FZ	Float-Zone
HF	HydroFluoric acid
HIT	Heterojunction with Intrinsic Thin layer
IBC	Interdigitated Back Contact
ICP	Inductively Coupled Plasma
IPA	Iso-Propyl Alcohol
IQE	Internal Quantum Efficiency
I$_{SC}$	Short-Circuit Current
IV	Current-Voltage
iV$_{OC}$	Implied open-circuit Voltage
KOH	Potassium Hydroxide
LDSE	Laser Doped Selective Emitter
LED	Light Emitting Diode
LPCVD	Low-Pressure Chemical Vapour Deposition

MACE	Metal-Assisted Chemical Etching
MPP	Maximum Power Point
NP	Non-Polished
μ-PCD	micro-PhotoConductance Decay
PECVD	Plasma Enhanced Chemical Vapour Deposition
PE	Path-length Enhancement
PERC	Passivated Emitter and Rear Cell
PERL	Passivated Emitter, Rear Locally diffused
PERT	Passivated Emitter, Rear Totally diffused
pFF	Pseudo Fill Factor
PL	PhotoLuminescence
POCl$_3$	Phosphorus Oxy-tri-Chloride
PSG	Phosphor-Silicate Glass
QSSPC	Quasi-Steady-State PhotoConductance decay
RF	Radio Frequency
RIE	Reactive Ion Etching
RTP	Rapid Thermal Processing
SDR	Saw Damage Removal
SEM	Scanning Electron Microscope
SERS	Surface-Enhanced Raman Spectroscopy
SF$_6$	Sulphur Hexafluoride
SIMS	Secondary Ion Mass Spectroscopy
SiN$_x$:H	Hydrogenated Silicon Nitride
SRH	Shockley-Read-Hall
SRV	Surface Recombination Velocity
SSP	Single-Side Polished
TE	Transverse Electric
TM	Transverse Magnetic
TMA	Tetra Methyl Aluminium
UNSW	University of New South Wales

Physical Constants

Avogradro's constant	N_{A}	$=$	$6.022\ 140\ 857\ 74 \times 10^{23}\ \mathrm{mol}^{-1}$
Boltzmann constant	k	$=$	$1.380\ 648\ 52 \times 10^{-23}\ \mathrm{m}^2 \cdot \mathrm{kg} \cdot \mathrm{s}^{-2} \cdot \mathrm{K}^{-1}$
Dirac constant (Planck's reduced)	$\hbar$	$=$	$1.054\ 571\ 80 \times 10^{-34}\ \mathrm{J} \cdot \mathrm{s}$
Electronic Charge	q	$=$	$1.602\ 176\ 62 \times 10^{-19}\ \mathrm{C}$
Planck's constant	h	$=$	$6.626\ 070\ 04 \times 10^{-34}\ \mathrm{J} \cdot \mathrm{s}$
Speed of Light	c	$=$	$2.997\ 924\ 58 \times 10^{8}\ \mathrm{m} \cdot \mathrm{s}^{-1}$

Symbols

A	absorptance	%
A_c	cell area	m^2
B	radiative recombination coefficient	cm^3 s^{-1}
$\mathbf{B}$	magnetic flux density	V·s·m^{-2} or T
C	dose	cm^{-2}
C_n0	electron Auger coefficient	cm^3 s^{-1}
C_p0	hole Auger coefficient	cm^3 s^{-1}
d	thickness of anti-reflective coating	nm
D_n	electron diffusivity	cm^2/s
D_p	hole diffusivity	cm^2/s
$\mathbf{E}$	electric field	V/m
E_ph	photon energy	W
f	metal coverage	%
f_p	photon frequency	Hz
f_i	fraction of silicon to air in the i'th layer	-
G	generation rate	cm^{-3} s^{-1}
$\mathbf{H}$	magnetic field	A/m
h	sheet thickness	m
I	current	A
I_L	photo-current	A
I_PL	photoluminescence intensity	-
I_0	thermal recombination current	A
J_d	total diffusion current density through pn-junction	mA/cm^2
J_gen	generation current density	mA/cm^2
J_n	electron current density	mA/cm^2

J_p	hole current density	mA/cm^2
J_total	total current density through pn-junction	mA/cm^2
J_0	thermal recombination current density	mA/cm^2
J_SC	short-circuit current density	mA/cm^2
k_0	wavenumber in vacuum	m^{-1}
L_n	diffusion length of electrons	m
L_p	diffusion length of holes	m
M_W	molar mass	g/mol
N_A	acceptor concentration	cm^{-3}
N_D	donor concentration	cm^{-3}
N_ph	spectral photon flux density	-
n	electron density	cm^{-3}
$n_\mathrm{i,eff}$	refractive index of effective medium	-
n_air	refractive index of air	-
n_i	intrinsic carrier density	cm^{-3}
n_id	ideality factor	-
n_r	refractive index	-
$n_{i=1,2,..}$	refractive index of layers $i = 1, 2..$	-
n_int	refractive index of intermediate layer	-
n_Si	refractive index of silicon	-
N_S	sheet carrier density	cm^{-2}
p	hole density	cm^{-3}
p_c	contact pitch	μm
P_in	incident power density	W/m^2
P	incident optical power	W
P_0	optical power at normal incidence	W
P_el	electrical output power	W
R	reflectance	%
R_S	series resistance	Ω
R_SH	shunt resistance	Ω
R_s	reflectance of s-polarized light	%
R_p	reflectance of s-polarized light	%
R_H	Hall coefficient	-

r_{sp}	rate of spontaneous emission	$\mathrm{cm}^{-3}\mathrm{s}^{-1}$
r_{H}	Hall scattering factor	-
$\mathbf{S}$	Poynting's vector	$\mathrm{W/m}^2$
$S_{\mathrm{rear,eff}}$	effective rear surface recombination velocity	cm/s
S_{cont}	contact surface recombination velocity	cm/s
S_{pass}	passivated surface recombination velocity	cm/s
T	absolute temperature	K
T_{r}	transmittance	%
U	recombination rate	$\mathrm{cm}^{-3}\ \mathrm{s}^{-1}$
U_{A}	Auger recombination rate	$\mathrm{cm}^{-3}\ \mathrm{s}^{-1}$
U_{R}	radiative recombination rate	$\mathrm{cm}^{-3}\ \mathrm{s}^{-1}$
V	voltage	V
V_{j}	junction voltage	V
V_{OC}	open-circuit voltage	V
W	wafer thickness	$\mu\mathrm{m}$
W_{e}	edge length of cell	m
α	absorption coefficient	cm^{-1}
α_{BB}	black-body absorptivity	%
$\Delta\eta$	separation of quasi Fermi levels	eV
η	power conversion efficiency	%
η_{int}	internal efficiency	%
η_{app}	apparent efficiency	%
θ	incident angle	degrees
λ	wavelength	nm
μ_{H}	Hall mobility	$\mathrm{cm}^2\ \mathrm{V}^{-1}\ \mathrm{s}^{-1}$
ρ	resistivity	$\Omega\mathrm{cm}$
ρ_{b}	density	$\mathrm{g/cm}^3$
τ_{eff}	effective minority carrier lifetime	s
τ_{bulk}	bulk minority carrier lifetime	s
τ_{surface}	surface minority carrier lifetime	s
τ_{rad}	radiative minority carrier lifetime	s
τ_{Auger}	Auger minority carrier lifetime	s

τ_{SRH}	Shockley-Read-Hall minority carrier lifetime	s
τ_{p}	minority carrier lifetime of holes	s
τ_{n}	minority carrier lifetime of electrons	s
Φ_0	optical intensity	$\mathrm{W/m^2}$
ϕ	rotation angle around θ-tilted cell plane	degrees
Ψ_{av}	average normalized electrical power output	%
ω	angular frequency	$\mathrm{s^{-1}}$

Chapter 1

Introduction

Climate change and global warming [1, 2] caused by burning of fossil fuels and the resulting increase in CO_2 emissions [3] has led to an urgent need for abundant and cost-efficient renewable energy sources. This need becomes even more urgent considering the projected increase in the global population by 2 to 4 billion people, which is expected by 2050 [4]. Solar energy is by far the most abundant renewable energy source available [5]: The surface of the Earth receives in the range of 89 [6] to 120 PW [7][1] from the Sun. In comparison, the global power consumption in 2012 was 17.7 TW [8][2]. In other words, we constantly receive much more energy from the Sun than we consume and only have to use a small fraction of the available solar energy to cover our total energy consumption. However, the cost of transforming the energy in sunlight into usable electrical energy must be comparable to the cost of energy from fossil fuels such as gas and coal in order for solar energy to be truly cost-competitive.

A cost-efficient source of electrical energy must have a levelized cost of electricity[3] lower than the average cost of power in the grid. This level is also referred to as 'grid parity'. The average levelized cost of electricity for photovoltaics is still higher than the cost of electricity generated from fossil fuels such as coal and gas [9]. Figure 1.1 shows the levelized cost of electricity from different power sources for comparison. The cost of solar cell electricity or power, typically given in terms of $/W_{\mathrm{p}}$,[4] may only be lowered by decreasing the production cost, increasing the power output or preferably both simultaneously. In order to decrease cost and increase power output simultaneously novel processes must be introduced in the conventional production of solar cells. These processes must result in an increased power conversion efficiency of the solar cells, while making the fabrication process itself cheaper. At the same time only sufficiently cheap and abundant materials may be used in the cell production in order to be able to scale the production to the order of magnitude of the global power consumption, that is the TW range.

This thesis investigates the use of nanostructures on the surface of silicon (Si) solar cells. The nanostructure topology - also referred to as black silicon - changes the interface between air and Si, such that reflection from the solar cell surface may be suppressed

---

[1]One PW is 10^{15} Watt

[2]One TW is 10^{12} Watt

[3]The levelized cost of energy or electricity is defined as the average total cost of an energy or electricity source per kWh over its lifetime.

[4]US $ per Watt peak output power equivalent
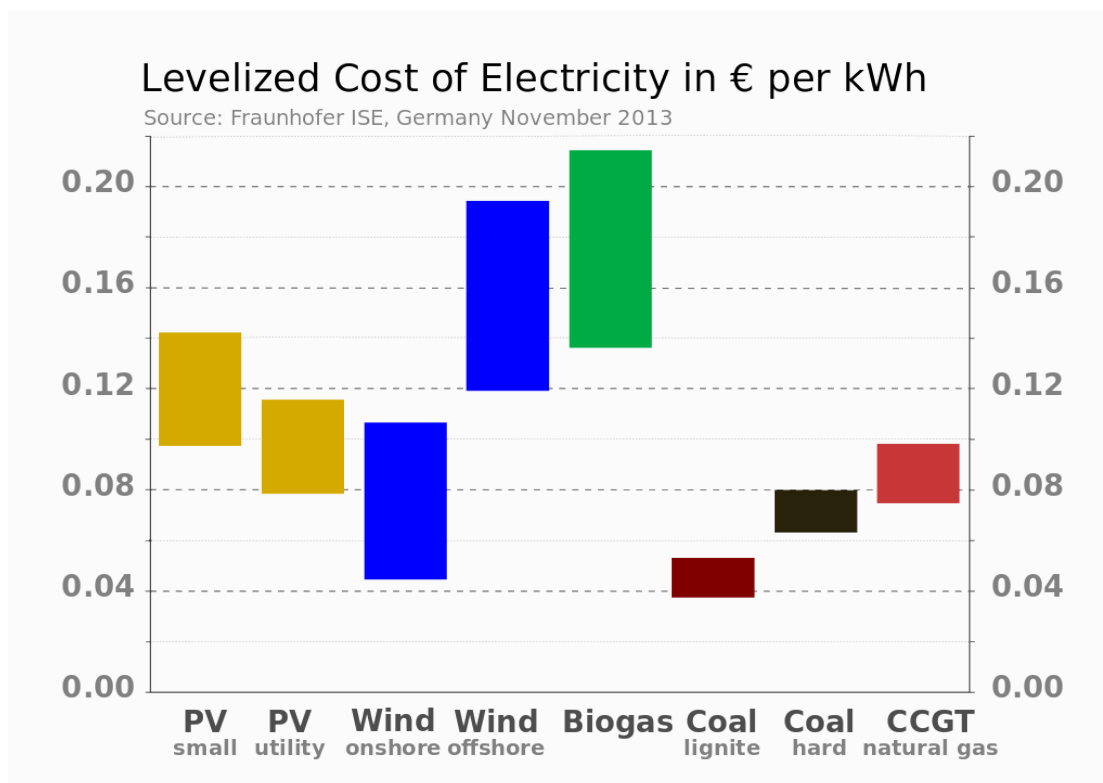
FIGURE 1.1: Levelized cost of electricity from different power sources for comparison. The average levelized cost of electricity from photovoltaics (PV) is still higher than that of coal and gas. [9]

completely. This leads to a reduced optical loss for the solar cell, which may lead to increased power conversion efficiency, if the additionally absorbed photons generate additional power output.

Nanoscale texturing of Si surfaces has been shown [10–16] to reduce the total weighted average optical reflectance to well below 1% over a broad range of wavelengths and incident angles. Compared to the typical front surface reflectance of ~ 2 and $\sim 8\%$, from conventionally textured mono- [17] and multi-crystalline [18] Si solar cells, respectively, nanoscale texturing such as described in [19–23] offers a potential for improved power conversion efficiency of Si solar cells due to reduced reflectance loss. Glunz [24] quantified the optical losses in terms of current density for different types of Si solar cells. The result is shown in Figure 1.2.

Figure 1.2 shows that the current density of Si solar cells may be increased by several mA/cm^2 by reducing the optical losses. Optical losses may not be avoided completely, but the analysis indicates the potential for improved cell performance by reducing optical losses, such as reflectance loss. Therefore the proposed nanostructure process may replace texturing in conventional Si solar cell production. Since the proposed black Si process is a dry, single step, maskless and scalable texturing process, it may also lead to a reduction of the overall production cost of Si solar cells by replacing conventional texturing and/or anti-reflective (AR) coating. Thus, the technology has the potential of improving the levelized cost of electricity for Si photovoltaics and thereby making solar cells a more cost-competitive energy source and potentially the dominant, abundant renewable energy source of the future.
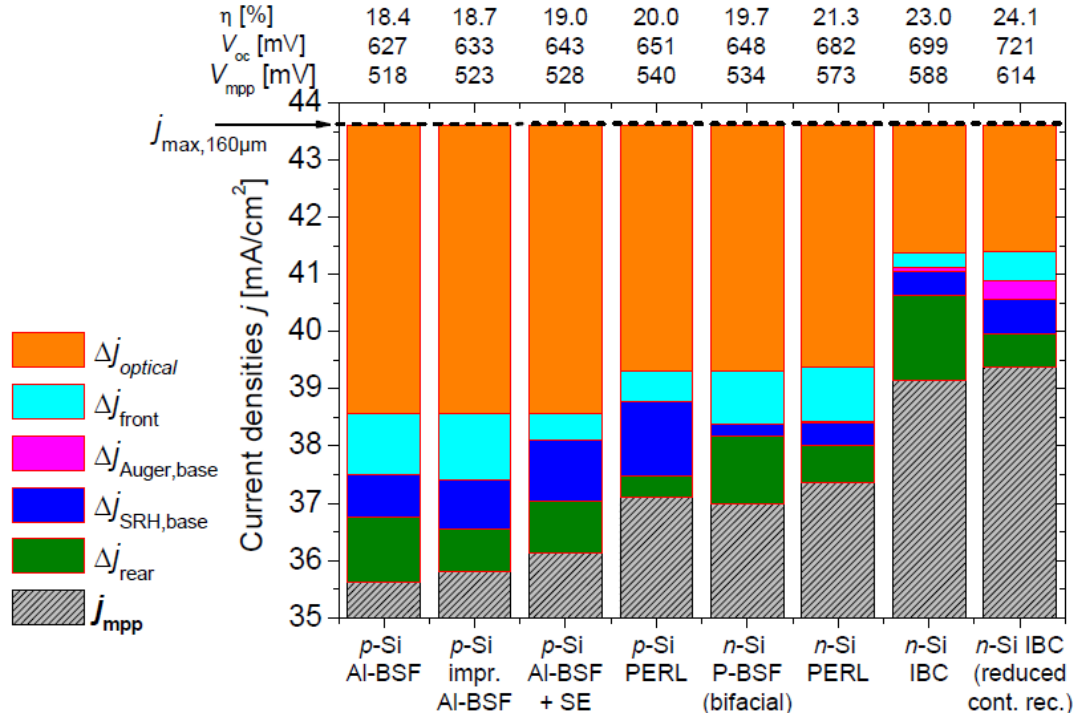
FIGURE 1.2: Optical loss analysis given in terms of current densities for different types of Si solar cells [24]

However, this requires a confirmed improvement of the power conversion efficiency of nanostructured Si solar cells and a successful transfer of the nanostructure texturing process to industrial Si solar cells. This thesis aims to achieve both of these milestones.

1.1 Sunlight

The Sun emits electromagnetic radiation in the wavelength range $\sim 250 - 2500$ nm. The flux density of this radiation varies with wavelength as seen in Figure 1.3 [25]. The integral of the spectral density curve gives the wavelength weighted value of irradiance just outside the Earth's atmosphere - known as the Solar Constant - and is 1.361 kW/m^2 [26]. Due to absorption and scattering of the light through the atmosphere the irradiance is lower at the surface of the Earth. On a clear day, at sea level, the irradiance at the surface of the Earth is ~ 1000 W/m^2. The actual irradiance at the surface of the Earth depends on the path length of the light travelling through the atmosphere and this path length further depends on the incident angle of the light. Thus, a representative parameter called air-mass (AM) has been defined as:

$$AM = \frac{1}{\cos(\theta)}, \qquad (1.1)$$

where θ is the angle of the light compared to zenith, which is defined as perpendicular to the surface of the Earth. A standard spectrum has been defined to an air-mass of 1.5 including diffuse and direct radiation globally. This spectrum is called AM1.5G and may also be referred to as '1-sun' when measurements are performed using this spectrum. The spectrum just outside the atmosphere is referred to as 'AM0'.
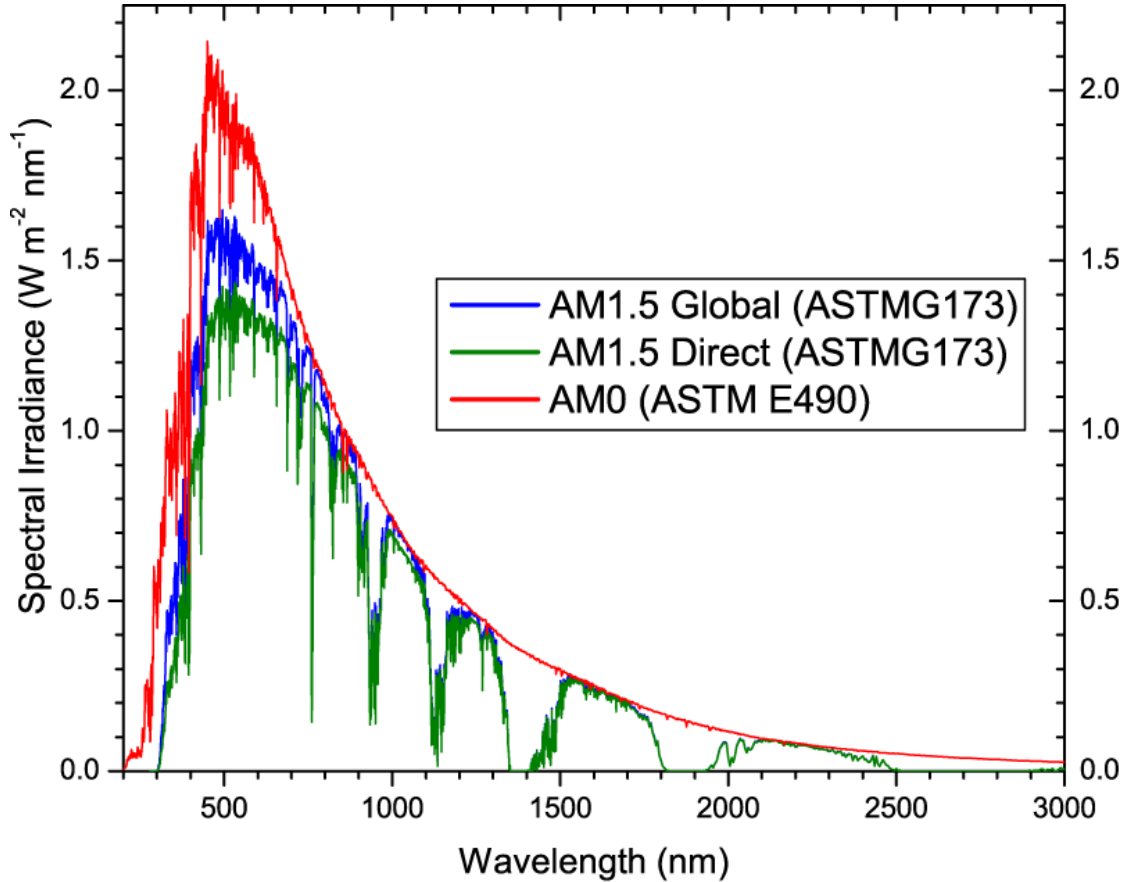
FIGURE 1.3: Standard solar spectrum, AM1.5G, shown as spectral irradiance as function of wavelength. The AM0 spectrum and the direct part of the AM1.5G spectrum are also shown. [25]

1.2   Photovoltaic Effect

The French physicist Alexandre-Edmond Becquerel was the first to discover the photovoltaic effect in 1839 [27] (at the age of 19) by immersing platinum electrodes into an acidic solution and illuminating the solution, which resulted in measurable current and voltage and thereby the first photovoltaic cell. Later work by Adams and Day [28], Fritts [29] and Grondahl [30] introduced solid solar cell devices using materials like Cu and Se, until Russell Ohl in 1941 [31] produced the first Si pn-junction solar cell. This lead to the first 'modern' Si solar cell with a significant power conversion efficiency around 4% developed by Chapin, Fuller and Pearson at Bell Labs in 1954 [32]. This cell was the starting point for the development of modern Si solar cells. In the following, the photovoltaic effect will be briefly explained.

When a photon with energy, E_{ph}, is incident on a piece of semiconductor material it may be reflected away from, transmitted through or absorbed in the material. The photon energy is given by:

$$E_{\mathrm{ph}} = \frac{hc}{\lambda}, \tag{1.2}$$

where h is Planck's constant, c is the speed of light and λ is the photon wavelength.

A photon is absorbed in semiconductor material by delivering its energy to an electron, which is then excited to a higher energy state. In semiconductors the range of energy states in which electrons cannot exist is called the bandgap, defined as the energy difference between the top of the valence band and the bottom of the conduction band. Figure 1.4 shows a schematic drawing of the bandgap. Only photons with energy
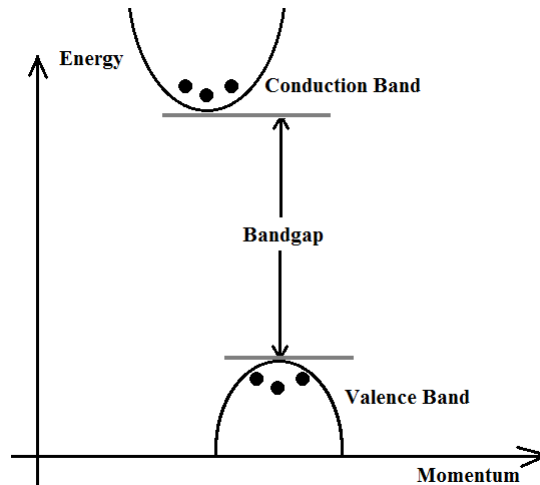
FIGURE 1.4: Schematic drawing of the bandgap in semiconductors.

higher than the bandgap of the semiconductor may excite electrons from the valence band to the conduction band. If N_{ph} is the spectral photon flux density, the maximum generation current density, J_{gen}, of the solar cell may be calculated according to

$$J_{\mathrm{gen}} = q \int_{E_{\mathrm{g}}}^{\infty} N_{\mathrm{ph}} d\mathrm{E}, \tag{1.3}$$

where q is the electronic charge and E_{g} is the bandgap energy. The maximum generation current density of a Si solar cell is 46 mA/cm^2. Si has a bandgap of ~ 1.12 eV corresponding to photons with a wavelength of ~ 1.11 μm. According to equation 1.2 photon energy is inversely proportional to the wavelength, meaning that only photons with a wavelength below ~ 1.11 μm contribute to the excitement of electrons. Since Si is an indirect bandgap semiconductor even photons with energy higher than the bandgap may require additional momentum from phonons in order to excite electrons to the conduction band. This explains the weaker absorption of photons in Si compared to direct bandgap materials such as gallium arsenide (GaAs) and cadmium telluride (CdTe), also applied as photovoltaic materials by several groups [33–38].

When an electron is excited to the conduction band it leaves behind a covalent bond able to move freely in the crystal lattice. This absence of an electron is denoted a 'hole' and is treated as a positive charge similar to but with opposite charge as the electron. Thus, an electron-hole pair has been generated. These charge carriers diffuse and in presence of a pn-junction - two adjacent regions of the semiconductor with an excess of holes and electrons, respectively - the electron and hole will be separated by the built-in electric field due to their opposite charge. The charge separation creates a voltage difference and a photocurrent between the two sides of the pn-junction. This current and voltage can be collected by external terminals connected to the p- and n-side of the junction, respectively. An electron on the p-side of the junction will be a minority carrier until it crosses the junction and becomes a majority carrier on the n-side. There is a risk

that the electron recombines with one of the holes on the p-side. Thus, it is crucial that the minority carriers are swept across the junction before they recombine in order to be successfully collected at the terminals and contribute to the generated photo-current and -voltage. The collection probability of the charge carriers is a function of the diffusion length, the distance from the depletion region, where the collection probability is unity, and the surface passivation [39, 40].

1.3   Silicon Solar Cells

More than 90% [41] of commercial solar cells are made from a Si substrate. Even though other materials, typically III-V semiconductors, theoretically have more ideal band gaps for photovoltaic power conversion, as seen in Figure 1.5, Si remains the dominant material in the solar industry. The reasons for this include the abundance of Si raw material[5], the stability of Si over time, the fully developed large-scale production of Si wafers and cells, relatively high power conversion efficiency and as a result the competitive $/W_p$ cost of Si solar cells compared to other types of solar cells. The competitive $/W_p$ cost is attributed to a combination of inexpensive raw materials, economies of scale and relatively high power conversion efficiency. The record efficiency for mono-crystalline Si solar cells is 25.6% [42] and 20.8% for multi-crystalline Si solar cells [33], while the theoretical maximum efficiency, known as the Shockley-Queisser limit [43], is $\sim 33\%$ for single-junction Si solar cells under AM1.5G illumination at a temperature of 300 K. Including free carrier absorption and Auger recombination, which is arguably more realistic, the maximum efficiency for Si cells is 29.8% [44].

The industrial Si solar cell production consists of $\sim 62\%$ multi and $\sim 38\%$ mono crystalline Si [41]. Due to increased recombination at the grain boundaries and the lack of effective texturing multi crystalline Si cells have lower power conversion efficiency than mono crystalline Si [33]. However, since multi-crystalline Si wafers are cast directly into the square shape matching the desired shape of the final cells, multi crystalline Si is cheaper to manufacture compared to mono crystalline Si, which is grown in cylindrical ingots using the Czochralski method. Recently a third type of Si has gained interest in the solar industry and research; quasi-mono (or cast mono) crystalline Si [45–48]. Quasi-mono crystalline Si is cast like multi crystalline, but the crucible contains a mono crystalline seed, which results in a high degree of mono-crystallinity. This technique potentially offers efficiencies comparable to that of mono and cost comparable to that of multi crystalline Si, making it a very promising candidate material for future Si wafer and cell production. Figure 1.6 shows photographs of mono, multi and two different quasi-mono crystalline Si wafers. As mentioned multi crystalline Si cells are not as effectively textured as mono crystalline Si, since conventional alkaline texturing takes advantage of the difference in etch rates for different crystal planes in mono crystalline Si. Since crystal planes are randomly oriented in multi crystalline Si, alkaline texturing is not effective and isotropic acidic texturing is used instead. For the same reason, a suitable texturing process for quasi-mono crystalline Si has not yet been developed, due to the multi-crystalline nature of that material. Interestingly, the maskless RIE-texturing investigated in this work enables texturing of all three types of Si material with no or minimal changes of the texturing process.

---

[5]Si is the second must abundant element in the Earth crust after oxygen. Si makes up $\sim 28\%$ of the Earth crust.
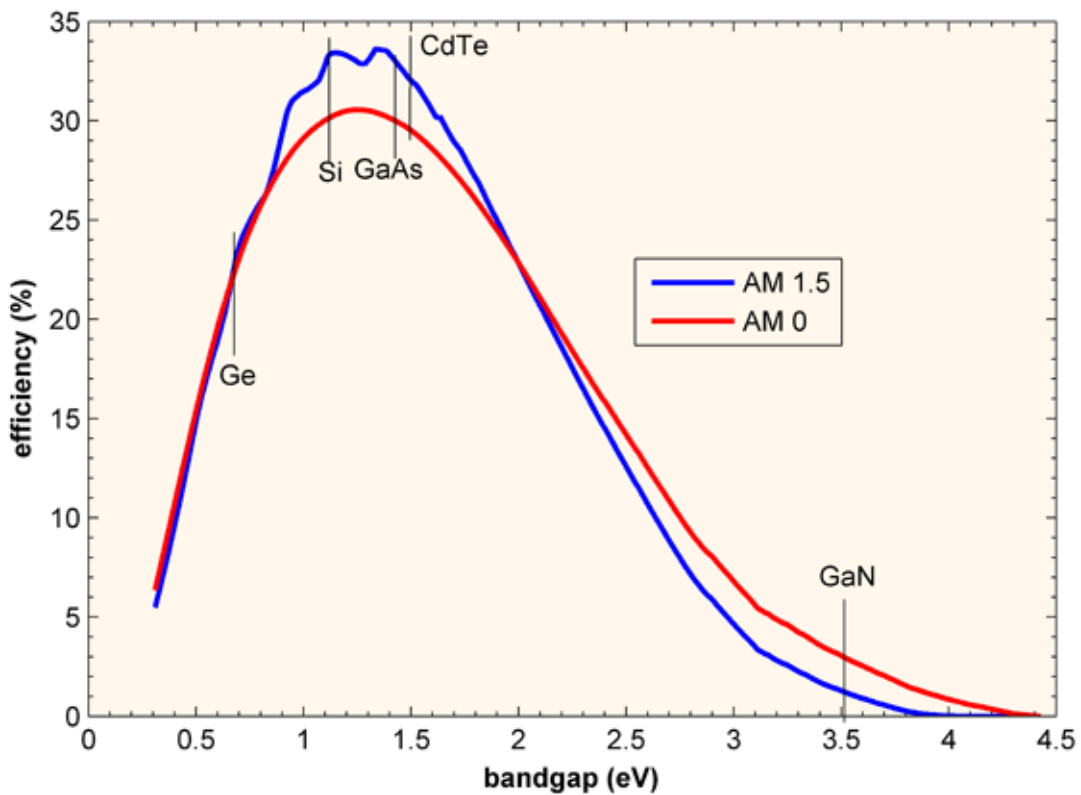
FIGURE 1.5: Maximum theoretical power conversion efficiency of solar cells as function of band gap energy at 300 K. The efficiency is shown for AM0 and AM1.5 spectral intensity, respectively. Selected materials are indicated at their respective band gap energies. Courtesy www.pveducation.org.
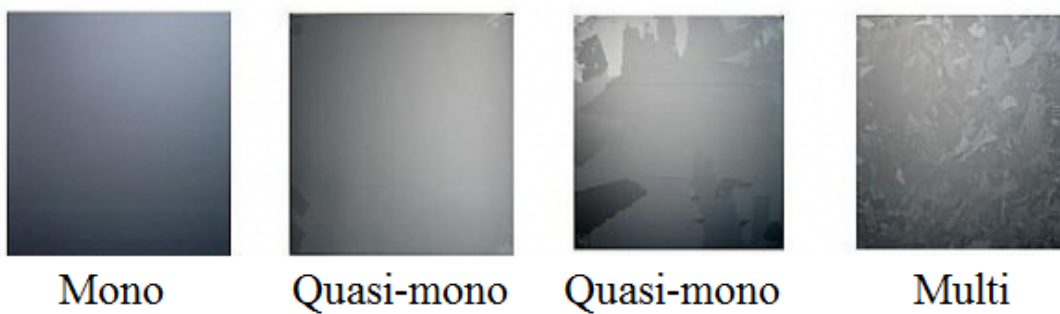
FIGURE 1.6: Photographs of (left) mono, (right) multi and (middle) two different quasi-mono crystalline Si wafers with different mono-crystallinity. Courtesy of JA Solar.

Conventional Si solar cells are typically produced on 156x156 mm^2, ~ 200 μm thin Si substrates by the following process steps:

- Saw Damage Removal (SDR)

- Front Surface Texturing

- Emitter Diffusion

- Deposition of Anti-Reflective (AR) Coating

- Screen-printing of front (Ag) and rear (Al) contacts

- Co-Firing of Front and Rear Contacts

- Edge Isolation

Conventional Si cells are made from p-type Si with a phosphorus-doped n-type emitter on the front. Saw damage removal and texturing are typically done in the same bath: For mono-crystalline Si the bath is alkaline typically consisting of potassium hydroxide (KOH) or sodium hydroxide (NaOH) [49–51, 84] with the addition of iso-propyl alcohol (IPA) or similar [52] in the case of texturing. For multi-crystalline Si the bath is acidic typically consisting of hydrofluoric (HF) and nitric acid (HNO_3) [53, 54]. Emitter diffusion is typically done in a tube furnace at temperatures in the range 800-900 °C using liquid $POCl_3$ as dopant source. The AR-coating, which also serves as front passivation, typically consists of $\sim$ 60-75 nm hydrogenated silicon nitride, SiN_x:H, deposited by plasma enhanced chemical vapour deposition (PECVD) [55–57]. Typical process parameters will be provided in more detail in later chapters.

1.3.1 Advanced Si Cell Types

The most dominant advanced Si cell types focus on optimization of the rear of the cell, which for conventional cells simply consists of fully-metallized Si with a doped back-surface field (BSF) on the entire rear, resulting from Al-doping when the screen-printed rear Al is fired [58]. Such rear design is not ideal, since Si-metal interfaces are recombination centers. Thus, the metal to Si ratio on the rear should be minimized, while maintaining sufficiently low series resistance of the rear contact. This requires a passivated rear with local contact openings. If local openings in the rear dielectric are made without any additional doping, the cell is called Passivated Emitter and Rear Cell (PERC) [59]. If the rear is highly doped at the local openings, the cell structure is called Passivated Emitter, Rear Locally diffused (PERL) [60]. If the rear contains selective doping, such that the back-surface field is highly doped at the local contacts, but more lightly doped on the remaining rear surface, the structure is called Passivated Emitter Rear Totally diffused cell (PERT)[60]. The doping level must be minimized in order to minimize Auger recombination, but a highly doped area is needed at the metal-Si contacts in order to shield minority carriers and ensure good ohmic contacts between metal and Si. Therefore, the PERL structure is in principle ideal, if the rear contact spacing allows for sufficient lateral conduction of charge carriers leading to high fill factors. However, the PERC structure might be more suitable for industrial solar cells, since the cell processing is typically more simple. Figure 1.7 shows a sketch of PERT, PERC and PERL cell structures, respectively. While the PER_x structures optimize the rear of the cell, certain advanced cell structures optimize the front of the cell: Due to a similar balance between minimized Auger recombination, good ohmic contact between metal and Si and shielding of minority carriers, the optimal front structure of the cell is a selective emitter, which consists of a lightly doped emitter with local, highly doped areas underneath the front contacts. The main challenge when forming a selective emitter is the need of scalable, low-cost processes that open dielectrics and diffuse dopants locally. For PERL cells and similar high-efficiency laboratory concepts this is typically done by means of photolithography and additional thermal diffusion steps. However, such processes are too expensive and not scalable enough for the solar industry.
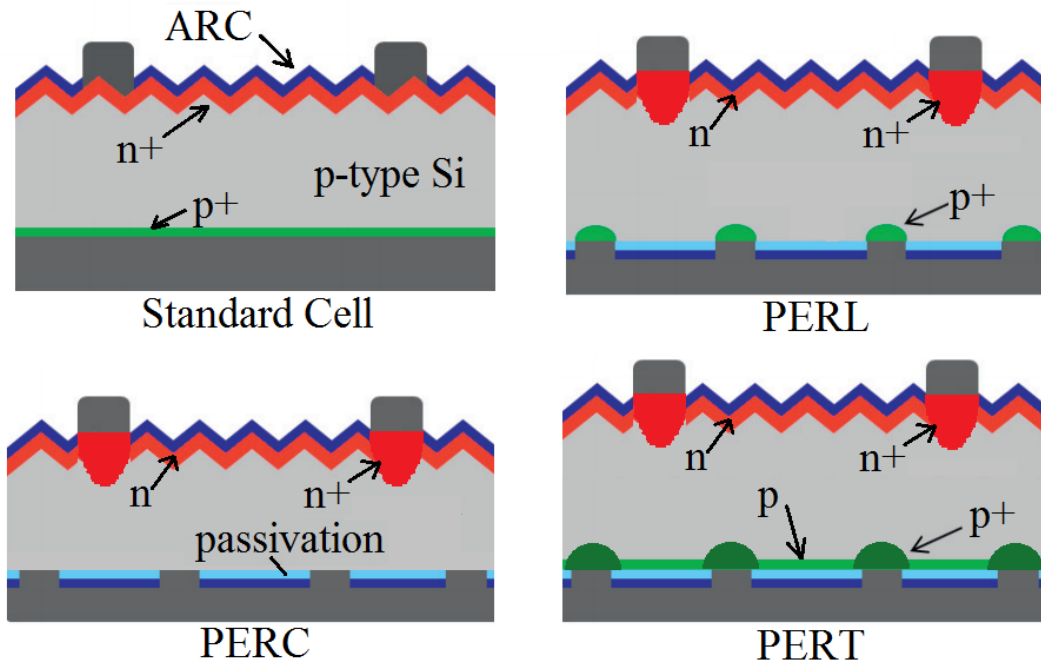
FIGURE 1.7: Sketches of standard (top, left), PERC (bottom, left), PERL (top, right) and PERT (bottom, right) type Si solar cells, respectively.

1.3.2 Laser Doping

A promising solution to this problem is the use of laser doping in order to form a laser doped selective emitter (LDSE) solar cell [61]. Laser doping was first described by Fairfield in 1968 [62]. In LDSE cells a laser beam is used to locally melt Si in the pattern of the front contacts. The melting point of Si is 1414 °C and when Si is heated and melted the resulting thermal mismatch between Si and the dielectric passivation layer induces a stress in the thin dielectric film, which removes the dielectric layer. If dopant atoms are placed in the vicinity of the molten Si region, liquid phase diffusion of these dopants into Si ensures high doping levels in these locally defined regions. Dopant atoms are typically spun on top of the dielectric layer in a liquid solution (such as phosphoric acid in case of phosphorus doping) prior to the laser process, but could also be incorporated into the dielectric film, such as aluminium, which is a p-type dopant to Si, in Al_2O_3. Since the liquid phase diffusion rate is much higher than solid state diffusion, high doping levels can be achieved in less than a second. After the laser beam is removed, the molten Si recrystallizes and the dopant atoms are incorporated into the Si crystal, leaving the Si highly-doped in these local areas defined by the laser. Figure 1.8 shows a sketch of the mechanism behind laser doping. Since the dielectric layer has been removed exactly in the desired pattern of the front contacts, laser doping allows for subsequent electroplating of metals such as Ni and Cu. Since the surface is only electrically conducting in the laser-doped regions, the metal ions will only plate in the locally defined openings, making the contact formation selective. Furthermore, since the diffusion process itself happens in a fraction of a second, laser doping can be a very fast and scalable process. In principle only the hardware of the laser system, such as the speed of moving the laser beam across wafer surfaces, limit the throughput of the process.
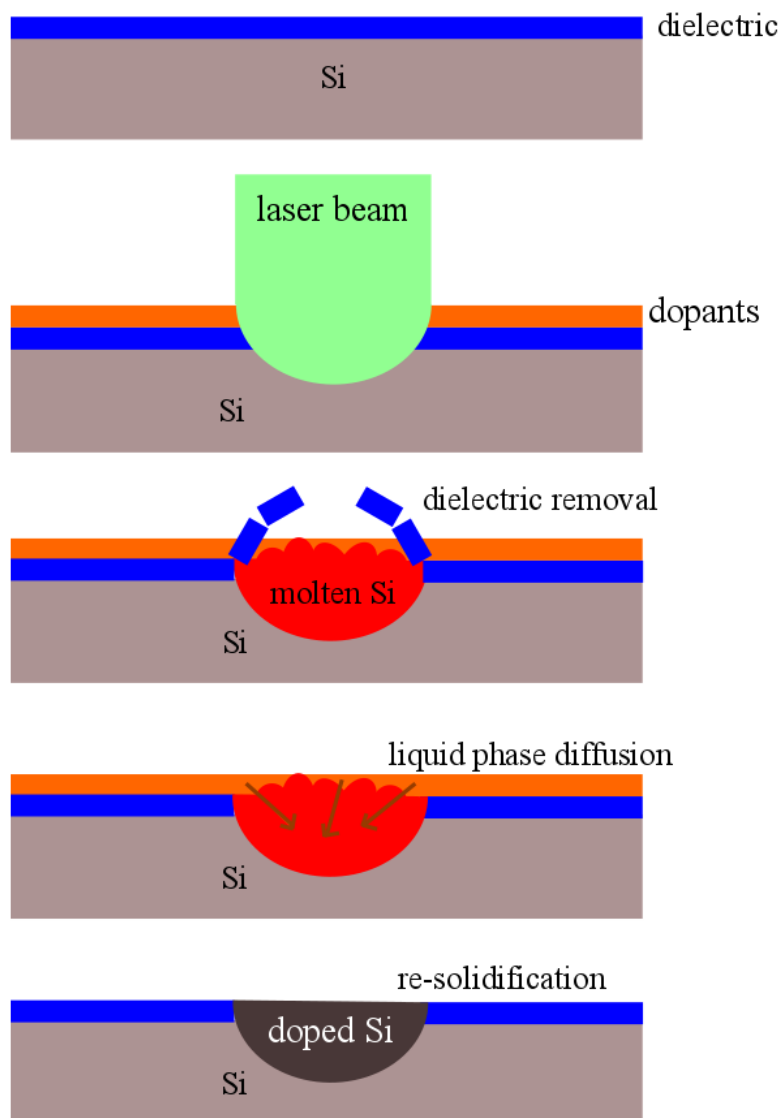
FIGURE 1.8: Sketch of the mechanism behind laser doping. The laser beam heats Si
to above its melting point. The expansion caused by the molten Si results in removal
of the overlying dielectric. If doping atoms are present in the vicinity of the molten Si,
the dopants diffuse into the liquid phase Si and finally re-solidification of Si
incorporates the dopants in the Si lattice, when the laser is removed.

The primary reason for the relatively low efficiencies reported for black Si solar
cells so far is the significant emitter and surface recombination [20, 63] resulting from
increased surface area, defects from the texturing process and increased emitter doping
through the nanostructured surface yielding increased Auger recombination. These ef-
fects usually lead to reduced short-circuit current and open-circuit voltage. Therefore
this thesis focuses on the optimization of nanostructured Si solar cells by combining
nanoscale texturing with complementary processes and cell designs such as laser doped
selective emitters.

1.4 Thesis Outline

The objective of this work is to demonstrate and optimize the use of nanostructures as a texturing method for Si solar cells and to improve the power conversion efficiency of nanostructured solar cells, while applying only processes and materials that are scalable to the throughput of the solar industry. The objectives are to understand, analyze, design, fabricate and characterize nanostructured Si solar cells. The contents of each chapter of the thesis are outlined below.

Chapter 2

Chapter 2 describes the theory of solar radiation, pn-junction diodes, solar cell operation and the theory behind the formation and optical properties of black Si.

Chapter 3

Chapter 3 presents and discusses the experimentally measured optical properties of black Si including reflectance, absorption and light trapping properties.

Chapter 4

Chapter 4 presents the design, fabrication, results and discussion of industrial-sized screen-printed black Si solar cells. Furthermore, a detailed angle-resolved characterization of the solar cells is presented.

Chapter 5

Chapter 5 presents the design, fabrication, results and discussion of laser-doped selective emitter (LDSE) black Si solar cells.

Chapter 6

Chapter 6 discusses different passivation schemes and emitter formation on nanostructured Si.

Chapter 7

Chapter 7 presents an outlook for the nanostructured Si solar cells and their potential industrial application. The outlook includes suggestions for further improved cell designs to be tested in research, but also the potential for application of nanostructured solar cells in the solar industry.

Chapter 8

Chapter 8 concludes the thesis by summarizing the obtained results and observations.

Chapter 2

Theory

2.1 PN-junction Diode

The physical basis for a solar cell is a pn-junction. A pn-junction is formed, when semi-conductor material with an excess of holes (p-type) is put in contact with semiconductor material with an excess of electrons (n-type). Due to the gradient in electron and hole concentration at the interface, charge carriers diffuse from regions of high concentration to regions of low concentration, according to Fick's first law. However, since electrons and holes are charged, they leave behind oppositely charged ions on each side of the junction. The region containing these charged ions is called the depletion region, because each side of the junction in this region is depleted for charge carriers. The oppositely charged ions lead to a built-in potential due to the electric field formed between the oppositely charged ion cores fixed in the crystal lattice. This built-in potential counteracts the diffusion of charge carriers across the junction, since the direction of the electric field - by nature - is opposite to the diffusive flow of charge carriers. Thus in thermal equilibrium there are two currents, drift and diffusion current, with equal magnitude and opposite sign, resulting in zero net current of the device.

When an external input, such as applied voltage or illumination, affects the pn-junction device, the built-in potential either increases or decreases: In forward bias, when a positive voltage is applied to the p-side and negative voltage to the n-side, the net electric field is decreased since the applied electric field has opposite polarity to the built-in electric field. This increases the diffusion current across the junction. The diffusion current consists of majority carriers that become minority carriers when injected on the opposite side of the junction. Minority carriers will diffuse away from the junction until they eventually recombine with majority carriers. Thus, the diffusion current is actually a recombination current and a direct measure of the recombination in the device. This will be used extensively when referring to the 'saturation current', I_0, or 'saturation current density', J_0. Since the recombination allows for further diffusion current flow across the junction, the recombination or saturation current is constant under steady-state conditions.

In reverse bias, when a negative voltage is applied to the p-side and positive voltage to the n-side, the built-in potential is increased, which consequently decreases the diffusion current. Since solar cells are operated under forward bias, this work primarily focuses on forward bias.

A solar cell is essentially a pn-junction diode in forward bias under illumination. When the pn-junction diode is illuminated, electron-hole pairs are generated as described in Chapter 1. Electrons on the p-side and holes on the n-side of the junction are then swept across the junction due to the built-in electric field, unless they recombine before they diffuse to the vicinity of the junction, where they are affected by the built-in potential. Thus, from a current perspective the illumination generates an additional current, the photocurrent, in the opposite direction than the diode current.

The basic equations for pn-junction diodes are the transport equation 2.1 and the continuity equation 2.2, both shown here for electrons, but hold similarly for holes if n is replaced with p and proper sign changes are made:

$$\mathbf{J}_{\mathrm{n}} = q\mu_{\mathrm{n}} n \mathbf{E} + q D_{\mathrm{n}} \nabla n \tag{2.1}$$

$$\frac{\partial n}{\partial t} = \frac{1}{q} \nabla \cdot \mathbf{J}_{\mathrm{n}} + (G - U) = 0, \tag{2.2}$$

where μ is the mobility, q is the electronic charge, D is the diffusivity, $\mathbf{E}$ is the electric field, p and n are the carrier densities on each side of the junction and U and G are the recombination and generation rate, respectively. Equations 2.1 and 2.2 are given in three dimensions, but will be treated in one dimension only in the following. This is sufficient in the case of a pn-junction diode solar cell. The transport equation 2.1 basically describes that the current density consists of a drift and diffusion term as described previously. Figure 2.1 shows a schematic drawing of a pn-junction.

2.1.1 Carrier Lifetime and Surface Recombination

An actual solar cell can be considered a slab of semiconductor material with finite thickness, W, and bulk minority carrier lifetime [64, 65], τ_{b}, defined as the time it takes before excited minority carriers recombine in the bulk. We consider a situation with a generation rate of excess charge carriers, G, and surface recombination velocity at the front and rear, S_{f} and S_{r}, respectively. The situation is sketched in Figure 2.2. The charge carrier variation may then be described by combining the transport and continuity equations 2.1 and 2.2, such that

$$\frac{\partial \Delta n}{\partial t} = \frac{1}{q} \frac{\partial J_{\mathrm{n}}}{\partial x} + G - \frac{\Delta n}{\tau} \simeq D_{\mathrm{n}} \frac{\partial^2 \Delta n}{\partial x^2} + G - \frac{\Delta n}{\tau_{\mathrm{b}}}, \tag{2.3}$$

where Δn is the excess electron density, D_{n} is the electron diffusivity and the electric field is assumed zero.

We may integrate equation 2.3 with respect to x from $x = 0$ to $x = W$ in order to evaluate the mean excess electron density as function of time, $\langle \Delta n(t) \rangle$, such that

$$\langle \frac{\partial \Delta n}{\partial t} \rangle = \frac{1}{W} \int_{x=0}^{x=W} \frac{\partial \Delta n}{\partial t} \, dx = \frac{1}{W} \int_{x=0}^{x=W} D_{\mathrm{n}} \frac{\partial^2 \Delta n}{\partial x^2} + G - \frac{\Delta n}{\tau_{\mathrm{b}}} \, dx, \tag{2.4}$$

which yields

$$W \langle \frac{\partial \Delta n}{\partial t} \rangle = D_{\mathrm{n}} \frac{\partial \Delta n}{\partial x} \bigg|_{\mathrm{x=W}} - D_{\mathrm{n}} \frac{\partial \Delta n}{\partial x} \bigg|_{\mathrm{x=0}} + \langle G \rangle W - \frac{\langle \Delta n \rangle}{\tau_{\mathrm{b}}} W, \tag{2.5}$$
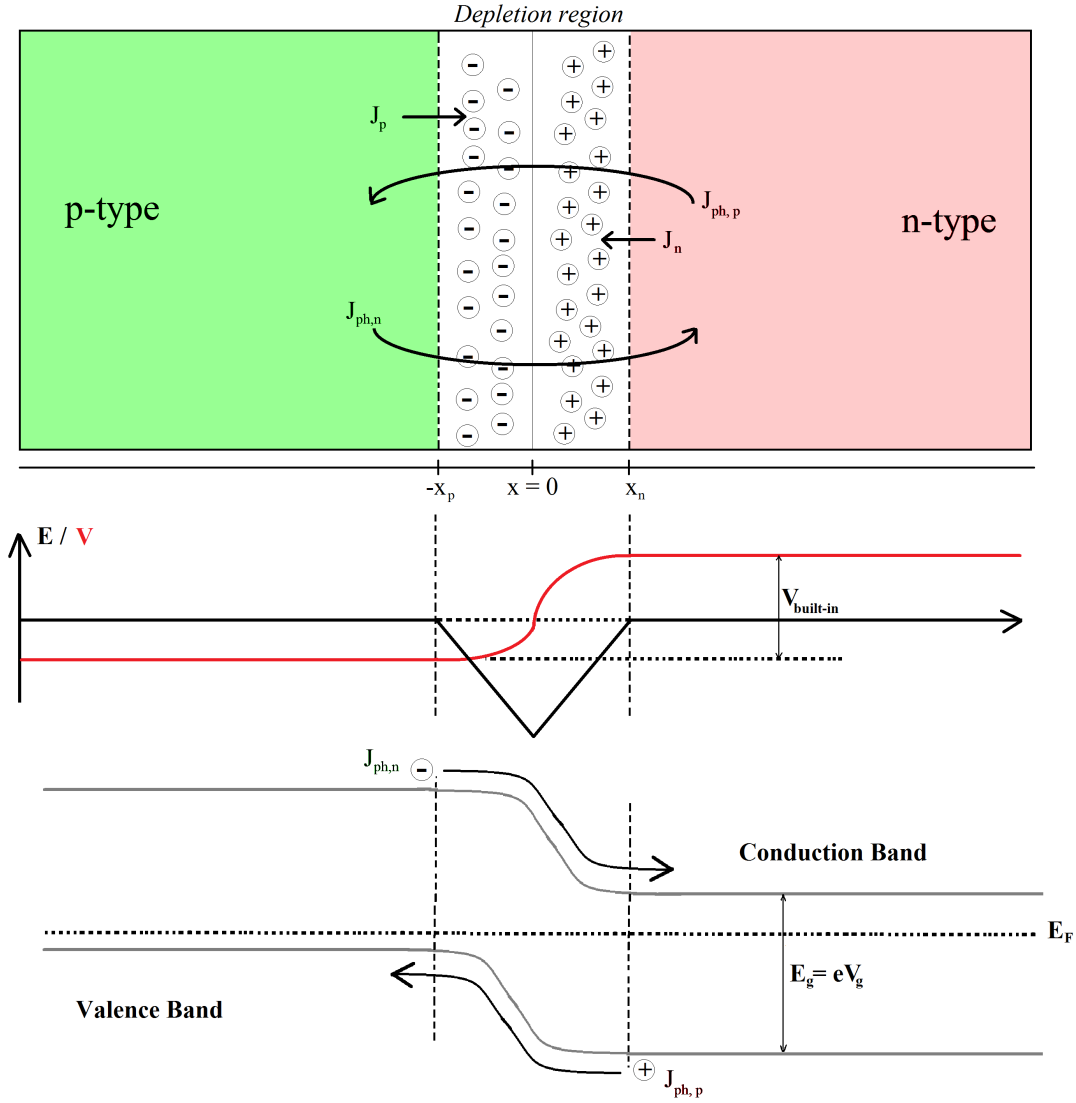
FIGURE 2.1: Schematic drawing of a pn-junction. $J_{n,p}$ are the electron and hole diffusion current densities and $J_{ph,n}$ and $J_{ph,p}$ are the electron and hole photo-current densities, respectively. **E** is the electric field and V is the built-in voltage of the junction. The bottom part of the image shows the band diagram of the junction, the direction of the photo currents and the band gap.

where $\langle u \rangle$ is the average value of u. The boundary conditions due to the surface recombination velocities are

$$-D_n \frac{dn}{dx}\bigg|_{x=W} = S_f \Delta n_{x=W} \tag{2.6}$$

and

$$D_n \frac{dn}{dx}\bigg|_{x=0} = S_r \Delta n_{x=0}. \tag{2.7}$$

Using the boundary conditions in equation 2.6 and 2.7 yields

$$W \langle \frac{\partial \Delta n}{\partial t} \rangle = (-S_f \Delta n_{x=W} - S_r \Delta n_{x=0}) \Delta n + \langle G \rangle W - \frac{\langle \Delta n \rangle}{\tau_b} W, \tag{2.8}$$
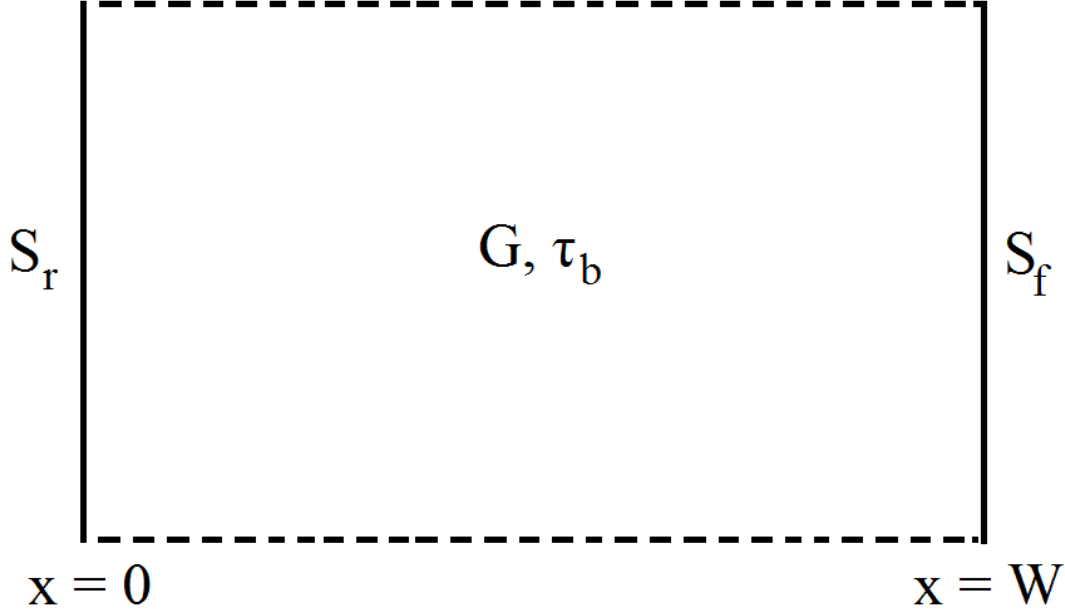
FIGURE 2.2: Sketch of generation and recombination in semiconductors

which may be rewritten by dividing with $\langle \Delta n \rangle$ and W

$$\frac{1}{\langle \Delta n \rangle} \langle \frac{d\Delta n}{dt} \rangle = \frac{\langle G \rangle}{\langle \Delta n \rangle} - \frac{1}{\tau_{\mathrm{b}}} - \left(\frac{1}{W} \frac{-S_{\mathrm{f}} \Delta n_{x=W} - S_{\mathrm{r}} \Delta n_{x=0}}{\langle \Delta n \rangle} \right) = \frac{\langle G \rangle}{\langle \Delta n \rangle} - \frac{1}{\tau_{\mathrm{eff}}} \qquad (2.9)$$

where we have introduced the effective recombination lifetime given by

$$\frac{1}{\tau_{\mathrm{eff}}} = \frac{1}{\tau_{\mathrm{b}}} + \left(\frac{1}{W} \frac{S_{\mathrm{f}} \Delta n_{x=W} + S_{\mathrm{r}} \Delta n_{x=0}}{\langle \Delta n \rangle} \right) \qquad (2.10)$$

If the change in excess carrier density does not vary much through the sample, such that $\Delta n_{x=W} \simeq \Delta n_{x=0} \simeq \langle \Delta n \rangle$, which is the case for thin samples, equation 2.10 simplifies to

$$\frac{1}{\tau_{\mathrm{eff}}} = \frac{1}{\tau_{\mathrm{b}}} + \left(\frac{S_{\mathrm{f}} + S_{\mathrm{r}}}{W} \right) \qquad (2.11)$$

Charge carrier recombination at the surface is typically the dominant recombination mechanism, since surfaces represent an abrupt termination of the semiconductor crystal lattice. This termination allows for energy states within the bandgap, at which charge carriers may recombine.

The average distance charge carriers diffuse before recombining - either at a surface or in the bulk - is an important measure called the diffusion length, L, defined as

$$L = \sqrt{D\tau_{\mathrm{b}}}, \qquad (2.12)$$

where D is the diffusivity and τ_{b} is the bulk minority carrier lifetime, which is the

time it takes for the charge carrier to recombine. For a slab of semiconductor material with width, W, surface recombination dominates for $W \ll L$, but can be neglected for $W \gg L$. This will be used when calculating the ideal diode equation in the next section.

The effective minority carrier lifetime is generally characterized by the change in carrier density, when excess charge carriers are generated for instance by illumination such as in solar cells. The effective lifetime may be defined from the continuity and transport equations 2.1 and 2.2, where the recombination rate, U, is given by the change in carrier density divided by the effective lifetime according to

$$U = \frac{n(t) - n_0}{\tau_{\text{eff}}}.$$ (2.13)

Since the recombination rate may be expressed as the difference between the generation rate, $G(t)$, and the change in minority carriers with time, $\frac{dn(t)}{dt}$, we may write the effective lifetime as

$$\tau_{\text{eff}} = \frac{n(t) - n_0}{G(t) - \dfrac{dn(t)}{dt}}.$$ (2.14)

If the change in carrier density is zero or negligible and the generation term, G(t), is known, equation 2.14 simplifies and the effective lifetime may be measured directly as a function of time, by measuring the carrier density via photoconductance. This method is called Quasi-Steady-State Photoconductance Decay (QSSPC). Quasi-steady state conditions are typically obtained by applying a flash of light with a decay, which is longer than the carrier lifetime of the sample. Since the light intensity decays over time as seen in Figure 2.3, the measured lifetime will be a function of carrier density, which enables injection-dependent characterization of the carrier lifetime. Since the lifetime is
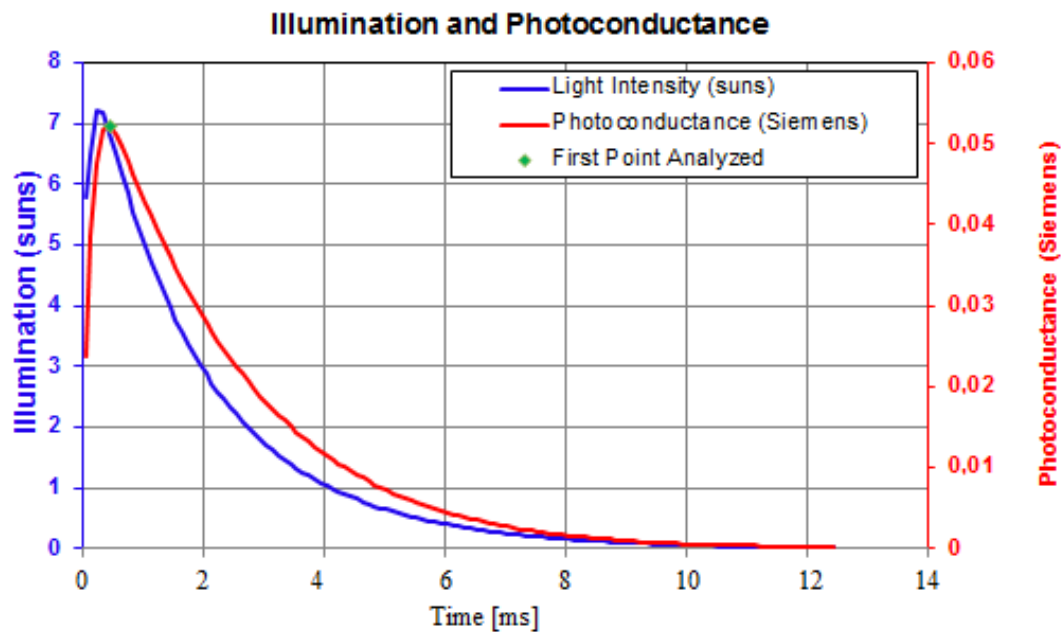
FIGURE 2.3: Example of photoconductance decay measurement such as in quasi-steady-state photoconductance decay (QSSPC) measurements of minority carrier lifetime.

a direct measure of recombination in the material, the bulk lifetime may be described as a combination of the three different recombination mechanisms in semiconductor material according to

$$\frac{1}{\tau_{\text{bulk}}} = \frac{1}{\tau_{\text{rad}}} + \frac{1}{\tau_{\text{Auger}}} + \frac{1}{\tau_{\text{SRH}}}, \tag{2.15}$$

where τ_{rad} refers to the radiative, τ_{Auger} to the Auger and τ_{SRH} to the Shockley-Read-Hall recombination, respectively. These terms depend differently on the doping density of the material. For instance Auger recombination scales with the square of the carrier density according to equation 2.22, which means that the Auger term in equation 2.15 dominates for highly doped material.

Charge carriers may recombine in the bulk or at the surface of the material. The effective lifetime, defined in equation 2.11 takes into account both bulk and surface recombination according to

$$\frac{1}{\tau_{\text{eff}}} = \frac{1}{\tau_{\text{bulk}}} + \frac{1}{\tau_{\text{surface}}} \tag{2.16}$$

SRH-recombination is a result of defects in the material. Since a surface is essentially a completely defected crystal lattice, recombination at the surface is typically very important and dominates the effective lifetime. From equation 2.12 it appears that the lifetime depends on the thickness of the wafer with respect to the diffusion length, since charge carriers in thicker wafers on average have a longer way to the defected surface. For this reason a surface-recombination velocity (SRV) [66–68] or effective surface recombination velocity, S_{eff}, is conveniently defined directly from equation 2.11, as a measure of surface recombination, which is comparable for wafers with different thicknesses according to

$$S_{\text{eff}} = \left(\frac{1}{\tau_{\text{eff}}} - \frac{1}{\tau_{\text{bulk}}} \right) \frac{W}{2}, \tag{2.17}$$

where W is the thickness of the wafer (i.e. assuming equal recombination velocities at both surfaces).

2.2 Recombination

As described previously it is crucial that the excited charge carriers are collected before they recombine in Si solar cells. An excited charge carrier, for instance an electron in the conduction band, exists in a meta-stable state, which means that it will move to a lower, stable energy state after a certain time. In case of an electron in the conduction band it will eventually move back to the valence band and occupy an empty state. This effectively means that a free hole in the valence band is simultaneously removed. This process is called recombination and results in loss of free electron-hole pairs. In general, there are three different types of recombination mechanisms in Si. These will be briefly covered in the following.

2.2.1 Radiative Recombination

In radiative recombination the electron directly combines with a hole in the valence band. Therefore radiative recombination is a band-to-band recombination mechanism. The excess energy from the recombination event must correspond to the band gap of the

semiconductor and is released as a photon. This also implies that the emitted photon has an energy equal to or very close to the band gap and therefore has a very small absorption coefficient in the material. This means that the photon most likely escapes and the energy does not contribute to the electron-hole pair generation in the solar cell. However, it should be mentioned that re-absorption of emitted photons does occur and the positive effect of this re-absorption is enhanced by effective light trapping schemes.

Radiative recombination is essentially a result of the detailed balance for solar cells [43], which dictates that all processes must be balanced by their reverse processes at thermal equilibrium. This means that the optical generation rate of electron-hole pairs is exactly balanced by the radiative recombination rate. The radiative recombination may be described as the blackbody radiation of the semiconductor material. Kirchhoff's law dictates that all bodies at a temperature, T, radiates electromagnetic energy and that the emission only depends on the wavelength, λ, (or photon frequency, f_p) and temperature, T. Planck's law [69] quantifies the emitted spectral radiance, $b(f_p, T)$, of a body in thermal equilibrium at a temperature, T, given by

$$b(f_p, T) = \frac{2hf_p^3}{c^2} \frac{1}{e^{\frac{hf_p}{kT}} - 1}, \tag{2.18}$$

where f_p is the photon frequency.

The Sun is an example of a body emitting black body radiation at a temperature of ~ 6000 K. A solar cell may also be described as a black body emitting electromagnetic energy. In this case the solar cell may be described by the emission it would have as a black body, its external quantum efficiency, Q_{ext}, and exponentially enhanced by the cell voltage, V, as explained in [70] such that

$$\Phi_L = Q_{ext}\Phi_{BB}e^{qV/kT}, \tag{2.19}$$

where Φ_L is the luminescence emission of the cell and Φ_{BB} is the emission of the cell if it were a perfect black body. Interestingly, it follows from equation 2.19 that a good radiative emitter must also be a good solar cell. This explains why a photoluminescence (PL) measurement is a useful indication of the solar cell performance [71].

If the system is not in thermal equilibrium the radiative recombination rate is given by

$$U_R = B(np - n_i^2) \tag{2.20}$$

where B is the radiative recombination coefficient, n and p are the electron and hole concentrations, respectively, and n_i is the intrinsic electron concentration. The radiative recombination coefficient, B, is related to the total recombination rate per unit volume, $U_{R,t}$, given by the Shockley-van-Roosbroeck equation [40, 72]:

$$U_{R,t} = n_i^2 B = 8\pi c(kT/hc)^3 \int_0^\infty [(\alpha n_r^2 u^2)/(e^u - 1)]du \tag{2.21}$$

where α is the absorption coefficient, n_r is the refractive index and $u = hf_p/kT$. Equation 2.21 may be derived from Planck's law seen in equation 2.18.

It appears from equation 2.20 and 2.21 that the radiative recombination rate only depends on temperature and constant material parameters of the semiconductor such as absorption coefficient, refractive index and intrinsic carrier concentration. This means

that at a given temperature and photon frequency, radiative recombination per unit volume will be constant and independent of any solar cell design changes. However, the total radiative recombination of the cell may be reduced via re-absorption of emitted photons by improving light trapping in the cell. The practical implication is that most efforts of improving solar cell structures aim at reducing all non-radiative recombination mechanisms, since radiative recombination can not be avoided. On the other hand, measuring radiative relative to non-radiative recombination events, such as in PL, directly indicates the optical generation rate due to the detailed balance of reverse processes, as described.

Since radiative recombination is a direct band-to-band recombination mechanism, it is dominant for direct band gap materials. For indirect band gap materials, such as Si, a phonon is needed to complete the recombination process. This reduces the effect of radiative recombination in Si. Radiative recombination is mostly known from light-emitting diodes (LED) typically made from direct band gap semiconductors, in which the photon emission from radiative recombination is more effective due to the direct band gap.

2.2.2   Auger Recombination

Auger recombination is also a band-to-band recombination mechanism, but differs from radiative recombination in that the excess energy released from the recombination event is transferred to a third charge carrier instead of an emitted photon. The third charge carrier may be an electron in the conduction band or a hole in the valence band. In both cases the third charge carrier is excited to a higher energy state within its respective band and subsequently relaxes by phonon emission thus releasing heat.

It follows that the Auger recombination becomes more important when the concentration of charge carriers is high. This is the case in two scenarios, namely (a) highly doped material and (b) high injection. The Auger recombination rate is given by

$$U_A = (pC_{p0} + nC_{n0})(np - n_i^2), \tag{2.22}$$

where $C_{n0,p0}$ are the electron and hole Auger coefficients, respectively. It is seen from equation 2.22 that the Auger recombination rate scales quadratically with carrier concentration, with the first term in the first parenthesis in equation 2.22 dominating for highly doped p-type material and the second term dominating for highly doped n-type material. Thus, in order to minimize Auger recombination doping level must be minimized. Obviously, other constraints on doping levels for the bulk and emitter of the solar cell means that certain doping levels are needed and a compromise between minimized Auger recombination and other effects must be found.

2.2.3   Shockley-Read-Hall Recombination

Shockley-Read-Hall (SRH) recombination occurs through energy states within the band gap. These energy levels arise from impurities or defects in the lattice. Any semiconductor surface will by definition contain a large number of defects, since the lattice is abruptly changed. Thus, SRH recombination is the dominant recombination mechanism at the surface. The SRH recombination process is a two-step process, in which (1) a

charge carrier is trapped at the energy state within the band gap, (2) a charge carrier from the opposite band moves to the same energy level, where the two charge carriers recombine before the first charge carrier is thermally re-emitted to its original band. Since recombination only happens if the first charge carrier is not re-emitted before the second charge carrier moves to the same energy level, the distance from the intermediate energy state to the band edge is important, since it changes the probability of re-emission before recombination takes place. Thus, defect levels close to the conduction or the valence band are the least critical, while mid-gap defect levels are the most critical. An example of a mid-gap defect, which is relevant for Si solar cells, is the contamination with heavy metals such as iron, copper or gold.

As mentioned SRH recombination is dominant at the surface, but especially for nanostructured surfaces SRH recombination plays a dominant role: First of all the effective surface area is significantly enhanced due to the nanostructures. This simply results in a higher number of defect states compared to a flat surface. Furthermore, additional defects and impurities may be introduced in the plasma texturing process. This will be the case for all texturing methods to some degree, but may be larger for some texturing methods e.g. RIE-texturing, if ion bombardment results in a more defected surface and impurities are incorporated during texturing. However, impurity incorporation is also an issue for alkaline texturing, in which potassium ions are critical due to the risk of increased SRH recombination.

2.3 Derivation of the ideal diode equation

If we consider the semiconductor slab in Figure 2.2 and assume only radiative and Auger recombination, an ideal solar cell may be described. The one dimensional continuity equation 2.2 in steady state is given by

$$\frac{\partial n}{\partial t} = \frac{1}{q}\frac{\partial J_\mathrm{n}}{\partial x} + G - b(pn - p_0 n_0) = 0 \qquad (2.23)$$

for electrons and

$$\frac{\partial p}{\partial t} = -\frac{1}{q}\frac{\partial J_\mathrm{p}}{\partial x} + G - b(pn - p_0 n_0) = 0 \qquad (2.24)$$

for holes, where b represents Auger and radiative recombination. If we let J_L be the current density through the solar cell and assume that the solar cell has carrier selective contacts, such that electrons exit the cell at one end (at $x = 0$) and holes at the opposite end (at $x = W$), integration of the continuity equation gives

$$J_\mathrm{n}(W) - J_\mathrm{n}(0) = -q \int_0^W G \ dx + q \int_0^W b(pn - p_0 n_0) \ dx = -J_\mathrm{L} \qquad (2.25)$$

for electrons and

$$J_\mathrm{p}(W) - J_\mathrm{p}(0) = q \int_0^W G \ dx - q \int_0^W b(pn - p_0 n_0) \ dx = J_\mathrm{L} \qquad (2.26)$$

for holes, since $J_\mathrm{n}(W) = 0$ and $J_\mathrm{p}(0) = 0$ due to the assumed carrier selective contacts.

Since the integral $\int_0^W G\,dx$ is the total number of absorbed photons per unit area, the first term in equation 2.25 and 2.26 is the photocurrent density

$$J_{\mathrm{ph}} = q \int_0^W G\,dx. \tag{2.27}$$

The last term in equation 2.25 and 2.26 is the total recombination current density, J_D:

$$J_D = q \int_0^W b(pn - p_0 n_0)\,dx, \tag{2.28}$$

since b was assumed to represent Auger and radiative recombination.

If electron and hole distributions are assumed thermalized such that quasi-Fermi levels, E_{Fn} and E_{Fp}, can be assigned and the Fermi-Dirac distribution may be approximated by a Maxwell-Boltzmann approximation, such that

$$n \simeq N_c \exp \frac{E_c - E_{Fn}}{kT} \tag{2.29}$$

for electrons and

$$p \simeq N_v \exp \frac{E_{Fp} - E_v}{kT} \tag{2.30}$$

for holes, where N_c and N_v are the effective density of states function for conduction and valence band, respectively.

Then the recombination current density may be described by quasi-Fermi levels

$$J_D = q \int_0^W b(pn - p_0 n_0)dx = qbp_0 n_0 \int_0^W \left(\exp \frac{E_{Fn} - E_{Fp}}{kT} - 1 \right) dx. \tag{2.31}$$

If the quasi-Fermi levels do not vary significantly across the slab, the recombination current term may be written as

$$J_D = qbp_0 n_0 W \left(\exp \frac{E_{Fn} - E_{Fp}}{kT} - 1 \right) = J_0 \left(\exp \frac{E_{Fn} - E_{Fp}}{kT} - 1 \right), \tag{2.32}$$

where J_0 is the saturation current density. Then the current through the solar cell, J_{L} may be written as

$$J_{\mathrm{L}} = J_{\mathrm{ph}} - J_D = J_{\mathrm{ph}} - J_0 \left(\exp \frac{E_{Fn} - E_{Fp}}{kT} - 1 \right) = J_{\mathrm{ph}} - J_0 \left(\exp \frac{qV}{kT} - 1 \right), \tag{2.33}$$

which is the well-known ideal Shockley diode equation.

2.3.1 Derivation of the pn-junction diode equation

In order to describe the solar cell quantitatively, the current through the pn-junction diode must be described. In the following derivation, current densities rather than currents will be considered. The current density through the pn-junction is the sum of the electron current density, J_{n}, at the edge of the depletion region on the p-side, $-x_{\mathrm{p}}$, and hole current density, J_{p}, at the edge of the depletion region on the n-side, x_{n}, of the junction assuming no recombination in the depletion region. This leads to the

expression

$$J_{\mathrm{d}} = J_{\mathrm{n}}(-x_{\mathrm{p}}) + J_{\mathrm{p}}(x_{\mathrm{n}}). \tag{2.34}$$

When diffusion dominates the transport of charge carriers, the current densities in the quasi-neutral p- and n-region of the junction, J_{p} and J_{n}, are described by Fick's first law according to equation 2.35 and 2.36. Quasi-neutral means that the electric field does not affect the charge carriers sufficiently far from the junction and therefore the drift term in the transport equation 2.1 is zero and the diffusion term dominates.

$$J_{\mathrm{n}} = qD_{\mathrm{n}}\frac{d\Delta n_{\mathrm{p}}(x)}{dx} \tag{2.35}$$

$$J_{\mathrm{p}} = -qD_{\mathrm{p}}\frac{d\Delta p_{\mathrm{n}}(x)}{dx} \tag{2.36}$$

In order to calculate the spatial variation in minority carrier density, $n(x)$ and $p(x)$, we differentiate the current density in equation 2.35 and 2.36 and insert into the continuity equation 2.2, which results in the second order differential equations

$$\frac{d^2 n(x)}{dx^2} = \frac{U(x) - G(x)}{D_{\mathrm{n}}} \tag{2.37}$$

$$\frac{d^2 p(x)}{dx^2} = \frac{U(x) - G(x)}{D_{\mathrm{p}}}. \tag{2.38}$$

It is noted that the second order derivatives of $n(x)$ and $p(x)$ equal the second order derivatives of the change in carrier concentration, $\Delta n(x)$ and $\Delta p(x)$, respectively, since $\Delta n(x) = n_{\mathrm{p}} - n_{\mathrm{p}0}$, where $n_{\mathrm{p}0}$ is assumed constant.

The general solution to the differential equations 2.37 and 2.38 obviously depend on the form of $U(x)$ and $G(x)$. The recombination term, $U(x)$, is given by

$$U = \frac{\Delta p}{\tau_{\mathrm{p}}}, \tag{2.39}$$

for holes in the n-type region, where τ_{p} is the bulk minority carrier lifetime of holes. In the case of constant generation and some bulk recombination according to equation 2.39 the general solution to equations 2.37-2.38 is given by equation 2.40, here shown for holes in the n-type region.

$$\Delta p(x) = C_1 \mathrm{e}^{-x/\sqrt{D_{\mathrm{p}}\tau_{\mathrm{p}}}} + C_2 \mathrm{e}^{x/\sqrt{D_{\mathrm{p}}\tau_{\mathrm{p}}}} + G\tau_{\mathrm{p}}, \tag{2.40}$$

where C_1 and C_2 are constants, τ_{p} is the hole lifetime and G is a constant generation term.

In order to solve the differential equations 2.37 and 2.38, boundary conditions are needed; in this case in terms of the change in minority carrier densities, $p(x_{\mathrm{n}})$ and $n(x_{\mathrm{p}})$, at the edges of the depletion region. These are each given by the equilibrium density multiplied by the Boltzmann factor, in which the energy is defined as the electronic charge, q, times the applied potential, V, as shown in equation 2.41 and 2.42.

$$\Delta n(x_{\mathrm{p}}) = \frac{n_{\mathrm{i}}^2}{N_{\mathrm{A}}}\left(\mathrm{e}^{\frac{qV}{kT}} - 1\right) \tag{2.41}$$

$$\Delta p(x_{\mathrm{n}}) = \frac{n_{\mathrm{i}}^2}{N_{\mathrm{D}}} \left(\mathrm{e}^{\frac{qV}{kT}} - 1 \right) \tag{2.42}$$

Furthermore, a second boundary condition must apply, since the minority carrier concentration must be finite, even as x goes to infinity. This means that C_2 in equation 2.40 must equal zero. Using this boundary condition and the expression for U(x), the general solution simplifies to

$$\Delta p(x) = C_1 \mathrm{e}^{-x/\sqrt{D_{\mathrm{p}}\tau_{\mathrm{p}}}} + G\tau_{\mathrm{p}}, \tag{2.43}$$

where $\sqrt{D_{\mathrm{p}}\tau_{\mathrm{p}}}$ is the diffusion length of holes, L_{p}. Using the first boundary condition to evaluate C_1 yields the solution

$$\Delta p(x) = \left(\frac{n_{\mathrm{i}}^2}{N_{\mathrm{D}}} \left(\mathrm{e}^{\frac{qV}{kT}} - 1 \right) - G\tau_{\mathrm{p}} \right) \mathrm{e}^{-x/L_{\mathrm{p}}} + G\tau_{\mathrm{p}}. \tag{2.44}$$

Now the current density can be evaluated by inserting equation 2.44 into equation 2.36 and differentiate with respect to x, which yields

$$J_{\mathrm{p}}(x) = \frac{qD_{\mathrm{p}}}{L_{\mathrm{p}}} \left[\frac{n_{\mathrm{i}}^2}{N_{\mathrm{D}}} \left(\mathrm{e}^{\frac{qV}{kT}} - 1 \right) - G\tau_{\mathrm{p}} \right] \mathrm{e}^{-x/L_{\mathrm{p}}}. \tag{2.45}$$

Finally, the total current density through the junction is the sum of the electron and hole current densities at the edges of the depletion region (x=0), which yields the expression for the total current

$$J_{total} = \left(\frac{qD_{\mathrm{p}}}{L_{\mathrm{p}}} \frac{n_{\mathrm{i}}^2}{N_{\mathrm{D}}} + \frac{qD_{\mathrm{n}}}{L_{\mathrm{n}}} \frac{n_{\mathrm{i}}^2}{N_{\mathrm{A}}} \right) \left(\mathrm{e}^{\frac{qV}{kT}} - 1 \right) - qG \left[L_{\mathrm{p}} + L_{\mathrm{n}} \right], \tag{2.46}$$

where the factor, $\left(\frac{qD_{\mathrm{p}}}{L_{\mathrm{p}}} \frac{n_{\mathrm{i}}^2}{N_{\mathrm{D}}} + \frac{qD_{\mathrm{n}}}{L_{\mathrm{n}}} \frac{n_{\mathrm{i}}^2}{N_{\mathrm{A}}} \right)$, is the saturation current density, J_0, and the generation term is the short-circuit current density, J_{SC}, which gives the ideal diode equation in the usual form

$$J = J_0 \left(\mathrm{e}^{\frac{qV}{kT}} - 1 \right) - J_{\mathrm{SC}}. \tag{2.47}$$

In [73] Cuevas *et al.* suggest to refer to J_0 as the *thermal recombination current density* or simply *recombination parameter*, since J_0 actually varies with illumination and from reverse to forward bias. Equation 2.46 shows that the injection dependence of J_0 is related to the diffusion length, which depends on the injection-dependent carrier lifetime. Therefore J_0 does not represent a saturation of the output current as such, but is rather a cumulative representation of the different recombination currents in the device.

2.3.2 Finite width solution to Diode Equation

Equation 2.46 was derived for a pn-junction in which both p- and n-regions were assumed infinitely wide. This was used in the second boundary condition, which led to the requirement $C_2 = 0$ in equation 2.40. A more realistic scenario for solar cells, is a pn-junction with the two regions being much smaller than the diffusion length, such that $W_{\mathrm{n}} << L_{\mathrm{p}}$ in the case of holes in the n-type region. In this case, the diffusion equation

2.38 simplifies because the recombination rate, $U(x)$, is assumed to be zero, such that

$$\frac{d^2 p(x)}{dx^2} = \frac{-G(x)}{D_{\mathrm{p}}}.$$ (2.48)

The general solution to equation 2.48 now takes the form

$$\Delta p(x) = \frac{-G(x)}{2D_{\mathrm{p}}} x^2 + Ax + B$$ (2.49)

The device now has a surface at which charge carriers recombine and we may assume infinite surface recombination velocity, S. From equation 2.6-2.7 this implies zero excess minority carrier concentration at the surface, $\Delta p_{\mathrm{n,s}}$, which means that

$$p_{\mathrm{n,s}} = p_{\mathrm{n,0}}$$ (2.50)

for holes in the n-type region and similarly for electrons in the p-type region.

Using this boundary condition and the first boundary condition in equation 2.42, which is still valid, leads to the solution for the excess hole concentration, $\Delta p(x)$, in a device with a finite (n-type) emitter width, $W_{\mathrm{n}} << L_{\mathrm{p}}$:

$$\Delta p(x) = \frac{G(x)}{2D_{\mathrm{p}}} x^2 + \left(\frac{G(x)}{2D_{\mathrm{p}}} W_{\mathrm{n}} - \frac{n_{\mathrm{i}}^2}{N_{\mathrm{D}} W_{\mathrm{n}}} \left(\mathrm{e}^{\frac{qV}{kT}} - 1 \right) \right) x + \frac{n_{\mathrm{i}}^2}{N_{\mathrm{D}}} \left(\mathrm{e}^{\frac{qV}{kT}} - 1 \right)$$ (2.51)

Again the current density is found by differentiating with respect to x according to equation 2.36, which then gives the solution

$$J_{\mathrm{p}} = qD_{\mathrm{p}} \frac{d\Delta p(x)}{dx} = qD_{\mathrm{p}} \left(\frac{G(x)}{D_{\mathrm{p}}} x + \frac{G(x)}{2D_{\mathrm{p}}} W_{\mathrm{n}} - \frac{n_{\mathrm{i}}^2}{N_{\mathrm{D}} W_{\mathrm{n}}} \left(\mathrm{e}^{\frac{qV}{kT}} - 1 \right) \right)$$ (2.52)

A similar expression can be derived for the electron current density in the p-region by replacing the emitter width, W_{n}, with the p-type base width, W_{p}, in this case. The total current density is then the sum of electron and hole current densities at the edges of the depletion region

$$J_{\mathrm{total}} = \left[qD_{\mathrm{p}} \frac{n_{\mathrm{i}}^2}{N_{\mathrm{D}} W_{\mathrm{n}}} + qD_{\mathrm{n}} \frac{n_{\mathrm{i}}^2}{N_{\mathrm{A}} W_{\mathrm{p}}} \right] \left(\mathrm{e}^{\frac{qV}{kT}} - 1 \right) - qG \left(\frac{W_{\mathrm{n}}}{2} + \frac{W_{\mathrm{p}}}{2} + W_{\mathrm{dep}} \right),$$ (2.53)

where W_{dep} is the width of the depletion region. The factor $\left[qD_{\mathrm{p}} \frac{n_{\mathrm{i}}^2}{N_{\mathrm{D}} W_{\mathrm{n}}} + qD_{\mathrm{n}} \frac{n_{\mathrm{i}}^2}{N_{\mathrm{A}} W_{\mathrm{p}}} \right]$ is then the recombination current density, J_0, and the generation term, $-qG \left(\frac{W_{\mathrm{n}}}{2} + \frac{W_{\mathrm{p}}}{2} + W_{\mathrm{dep}} \right)$ is the photocurrent.

2.4   Operation Principle of Solar Cells

An ideal silicon solar cell under illumination can be modelled as a pn-junction diode in parallel with a current source. The current source represents the photo-generated current, which has an opposite direction compared to the diode current. Furthermore, the equivalent electrical circuit contains a shunt resistor in parallel and a series resistor

in series with the diode. A schematic of the equivalent circuit is shown in Figure 2.4. If
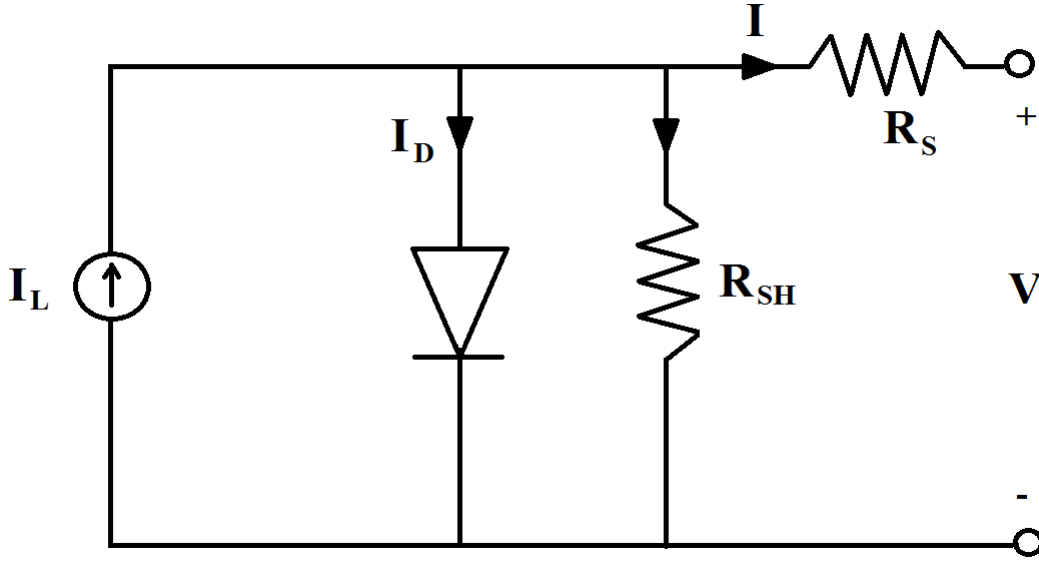
FIGURE 2.4: Equivalent electrical circuit of a solar cell. The circuit consists of a light source in parallel with a pn-junction diode and a shunt resistor, and in series with another resistor.

the diode is not ideal, the circuit may be modelled with a second diode in parallel with the pn-junction diode. This is referred to as the two-diode model. The non-ideality of the diode is typically accounted for by an ideality factor, n_{id}. The current through the pn-junction diode is described by the Shockley diode equation:

$$I_d = I_0 \left(\exp \left(\frac{qV_j}{n_{id}kT} \right) - 1 \right), \tag{2.54}$$

where I_d is the current through the diode, I_0 is the reverse saturation current, q is the elementary charge, V_j is the voltage across the diode and shunt resistor, n_{id} is the ideality factor, k is Boltzmann's constant and T is the absolute temperature. The Shockley diode equation in 2.54 may also be written in terms of current density rather than current by simply replacing I with J. When the diode is illuminated, a photocurrent is generated in the opposite direction as the diode current. This gives rise to the Shockley diode equation under illumination given in equation 2.55. This expression was derived for current density in the previous section and is analogous to equation 2.47.

$$I = I_L - I_0 \left(\exp \left(\frac{qV_j}{n_{id}kT} \right) - 1 \right), \tag{2.55}$$

where the total current, I, and the photocurrent, I_L, are defined with the same sign, which is opposite to the diode current, for convenience. Based on equation 2.55 and the equivalent circuit in Figure 2.4, the current of the solar cell is described by the characteristic equation, which includes series resistance, R_S, and shunt resistance, R_{SH}:

$$I = I_L - I_0 \left(\exp \left(\frac{q\left[V + R_S I\right]}{n_{id}kT} \right) - 1 \right) - \frac{V + R_S I}{R_{SH}}, \tag{2.56}$$

where V_j has been replaced by $V + R_S I$, because the current and series resistance contribute to the voltage across the diode in addition to the terminal voltage. Similarly, the current through the shunt resistor must be $I_{SH} = \frac{V_j}{R_{SH}}$ according to Ohm's law. This explains the last term in equation 2.56. It appears that equation 2.56 is a transcendental equation with no general analytical solution for I or V. However, the characteristic equation contains a lot of useful information about the solar cell operation.

In order to maximize the output power of the solar cell, the current and voltage between the terminals must be maximized. Thus, it can be concluded from the circuit in Figure 2.4 and equation 2.56 that

- Any currents in parallel with the photocurrent, such as I_0, must be minimized

- Series resistance must be minimized

- Shunt resistance must be maximized

Figure 2.5 shows an example of the current-voltage (IV) characteristic of a solar cell.
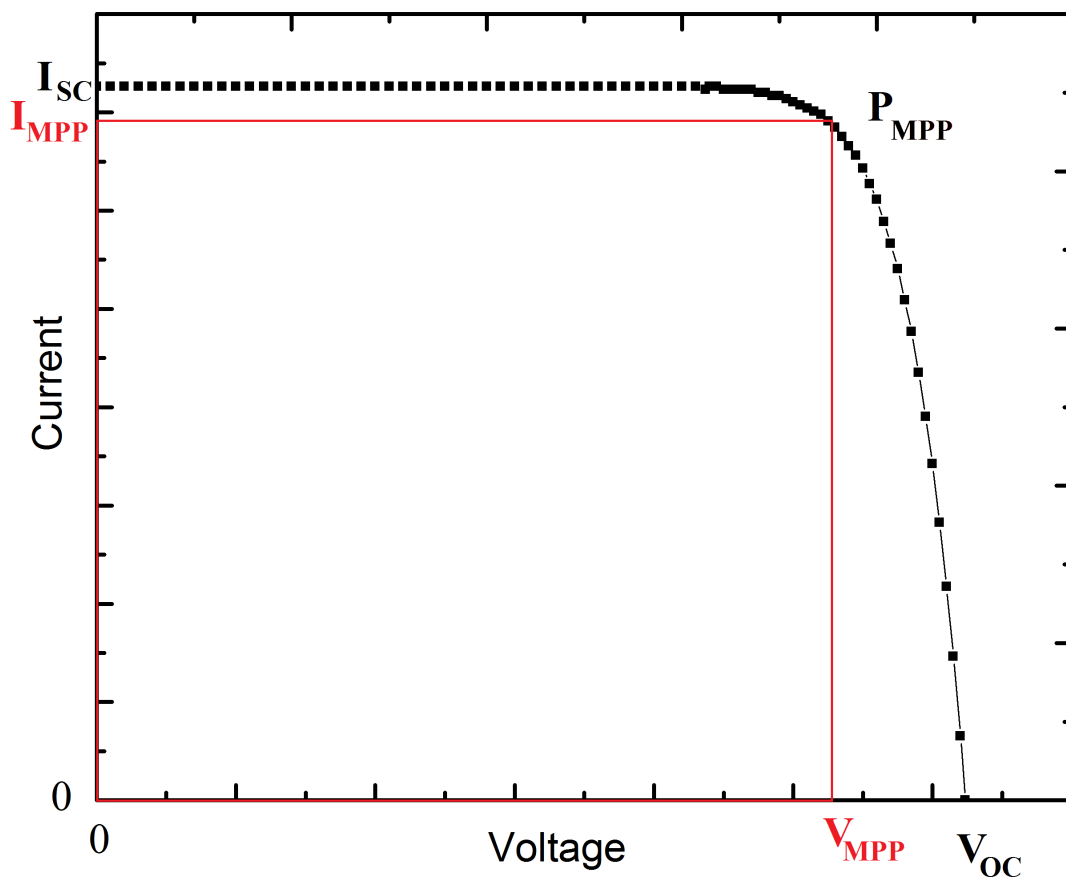
FIGURE 2.5: Schematic drawing of a current-voltage (IV)-characteristic of a solar cell. The short-circuit current, I_{SC}, is the current through the cell when the voltage is 0 and the open-circuit voltage, V_{OC}, is the voltage across the cell when the current is 0. The maximum power point, P_{MPP}, is defined as the largest product between current and voltage on the IV-curve.

The short-circuit current, I_{SC}, is the current through the cell when the voltage is 0. Similarly the open-circuit voltage, V_{OC}, is the voltage across the cell when the current is 0. The expressions for I_{SC} and V_{OC} may be directly deduced from equation 2.56. The power is the product between current and voltage and is therefore equal to zero at both open-circuit and short-circuit. The solar cell is ideally operated at the maximum power point, P_{MPP}, defined as the largest product of current and voltage on the IV-curve. The fill factor, FF, is given by:

$$\text{FF} = \frac{P_{MPP}}{I_{SC}V_{OC}} \tag{2.57}$$

The power conversion efficiency of the cell, η, is defined as:

$$\eta = \frac{P_{MPP}}{P_{in}A_{c}}, \tag{2.58}$$

where P_{in} is the incident power per area - typically 1000 W/m^2 at standard conditions - and A_c is the area of the cell.

2.5 Black Silicon

Black silicon is the term used for nanostructured Si, which appears visibly black, because the reflection of visible wavelengths is very low. The reflectance of the surface depends on the exact dimension and shape of the nanostructure topology. In general, the nanostructured surface may be described optically by a graded refractive index, because the nanostructured surface region is made up by some fraction of Si and air-filled voids surrounding the nanostructures, respectively. Therefore the effective refractive index within the nanostructured region must lie between the refractive index of Si and the refractive index of air and this leads to the explanation of the unique optical properties of black Si. The graded refractive index model for black Si will be described in the following.

2.5.1 Graded Refractive Index Model

The reflectance of light incident at an angle, θ, on an interface between two materials with different refractive indices, n_1 and n_2, can be described by the Fresnel equations 2.59-2.60 derived directly from Maxwell's equations:

$$R_{s} = \left| \frac{n_1 \cos(\theta) - n_2 \sqrt{1 - (\frac{n_1}{n_2}\sin(\theta))^2}}{n_1 \cos(\theta) + n_2 \sqrt{1 - (\frac{n_1}{n_2}\sin(\theta))^2}} \right|^2 \tag{2.59}$$

$$R_{p} = \left| \frac{n_1 \sqrt{1 - (\frac{n_1}{n_2}\sin(\theta))^2} - n_2 \cos(\theta)}{n_1 \sqrt{1 - (\frac{n_1}{n_2}\sin(\theta))^2} + n_2 \cos(\theta)} \right|^2, \tag{2.60}$$

where R_s and R_p denote reflectance of the s- and p-polarized light, respectively. If the electromagnetic radiation consists of equal amounts of s- and p-polarized waves, the total reflectance is:

$$R = \frac{R_s + R_p}{2} \tag{2.61}$$

which for normal incidence simplifies to

$$R = \left| \frac{n_1 - n_2}{n_1 + n_2} \right|^2 \tag{2.62}$$

From equation 2.62 it is clear that the reflectance is minimized when the difference between the refractive indices of the two media is minimized.

In the case of Si photovoltaics the material interface consists of air with refractive index $n_{air} = 1$ and Si with refractive index $n_{Si} \simeq 4$[1]. This abrupt change in refractive index at the Si-air interface results in a reflectance of 36% at normal incidence according to equation 2.62 assuming $n_{Si} = 4$. For a Si solar cell this would imply a 36% optical loss. In order to minimize the reflectance from this Si-air interface, it is advantageous to introduce intermediate layers with refractive indices between n_{air} and n_{Si}, since part of the waves propagating through multiple media will destructively interfere with reflected waves from the other interfaces. This is the mechanism behind anti-reflection coatings (ARC). If the reflection is zero, the intensity of the wave reflected from the Si-ARC interface must be equal to the intensity of the wave reflected from the ARC-air interface. At the same time the phase-shift, φ_p, between the two reflected waves must equal π times an integer in order to achieve destructive interference. The phase shift is given by two times the optical path length in the material with refractive index, n_{int}, in this case. This requirement leads to the quarter-wavelength restriction

$$\varphi_p = m\pi = 2d n_{int} k_0 = 2d \left(\frac{2\pi}{\lambda} \right) \Leftrightarrow d = \frac{\lambda}{4} m, \tag{2.63}$$

where d is the thickness of the AR-coating, k_0 is the wavenumber in vacuum, λ is the wavelength and m is an integer. In order to minimize parasitic absorption in the AR-coating itself, $m = 1$ yields the ideal solution, $d = \frac{\lambda}{4}$.

Equation 2.63 shows that reflectance can be minimized at a given wavelength by adjusting the thickness of the intermediate layer to exactly $\frac{1}{4}$ of the wavelength. Furthermore, the restriction that the intensity of the two reflected waves must be equal leads to equation 2.64, which is valid when the phase shift is an integer times π. In 2.64 n_1 corresponds to the refractive index of air, n_2 the refractive index of the AR-coating and n_3 the refractive index of Si.

$$R_1 = R_2 \Leftrightarrow \left| \frac{n_1 - n_2}{n_1 + n_2} \right|^2 = \left| \frac{n_2 - n_3}{n_2 + n_3} \right|^2 \tag{2.64}$$

Rearranging the expression in equation 2.64 yields the optimal refractive index of the intermediate layer or AR-coating according to

$$(n_1 - n_2)(n_2 + n_3) = (n_2 - n_3)(n_1 + n_2) \Leftrightarrow n_2 = n_{int} = \sqrt{n_1 n_3}. \tag{2.65}$$

Ideally, Fresnel reflectance is minimized over a broad range of wavelengths by applying an infinite number of thin layers with refractive indices gradually changing from n_{air} to n_{Si}. This is however not practical to realize if actual layers of different materials are to be deposited! Instead, texturing the Si surface with structures of appropriate dimensions and spacing may create a similar graded refractive index at the Si-air interface. Figure

---

[1]The refractive index of Si is wavelength dependent. The value given here is chosen as a representative average value for the relevant part of the solar spectrum, i.e. $\lambda = 300 - 1200$ nm.

2.6 shows a sketch of such graded refractive index. The nanostructured surface may be
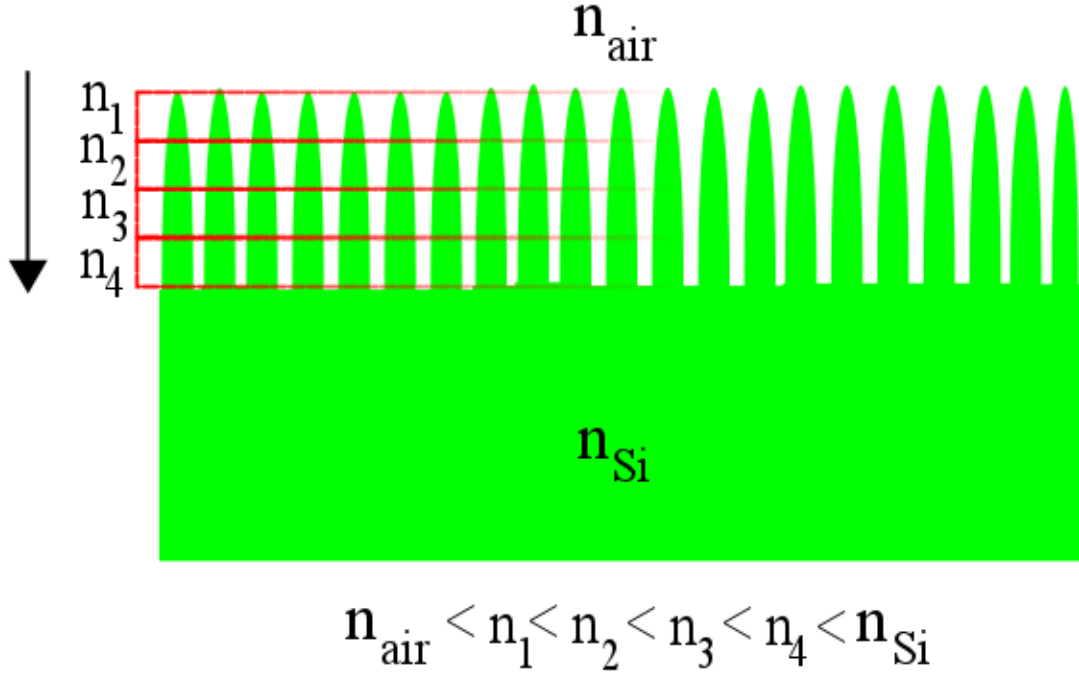
FIGURE 2.6: Sketch of the graded refractive index of black Si. The refractive index, n_r, changes gradually from that of air to that of silicon at the Si-air interface.

modelled as a layered structure in a mean-field approximation, in which the i'th layer has an effective refractive index, $n_{r,i,eff}$ weighted by the relative amount of Si and air, respectively, in the i'th layer, such that

$$n_{r,i,eff} = f_i n_{Si} + (1 - f_i) n_{air}, \tag{2.66}$$

where f_i is the fraction of Si in the i'th layer.

In order to suppress reflectance the spacing between nanostructures should be small enough to eliminate any abrupt change in refractive index on the entire surface. At the same time the structures should be large enough to ensure that all incident photons are subject to a gradually increasing refractive index. Thus, structures spaced too far apart and structures that are too small both result in a surface, which in part is optically flat i.e. part of the surface has an abrupt change in refractive index as opposed to a gradual change in refractive index. This poses requirements of the nanostructure topologies in order to realize minimal reflectance over a broad range of wavelengths.

From an optical perspective the broadband suppression of reflectance by a graded refractive index may be explained by the, in principle, infinite number of layers with different refractive index. This enables any phase difference according to equation 2.63 only restricted by the thickness of the graded refractive index. In other words, at any given wavelength there is a combination of two layers in a graded refractive index, which ensures destructive interference of the reflected beams. Thus, an interesting consequence of the quarter-wavelength criterion is that the depth of black Si has a required minimum value for a given wavelength range, say 300-1200 nm for Si solar cells, in order to ensure destructive interference for the longest wavelengths in the range. At a wavelength of

1200 nm the quarter-wavelength criterion dictates a black Si depth of 300 nm. This may explain why black Si structures in practice need a certain depth in order to minimize reflectance. However, it also indicates that structures much deeper than 300 nm are not necessary in order to suppress broadband reflectance of Si, if proper spacing and shape of nanostructures are realized. This is important, because surface recombination may scale with total surface area. This explains the focus on ~ 300 nm deep nanostructures in this work.

2.5.2 Black Silicon formation

The black Si nanostructures in this work are fabricated by means of reactive ion etching (RIE). In RIE the Si wafer is subject to a chemically reactive plasma at low pressure, typically between a few and a few hundred milliTorr [2]. The plasma is typically generated by a radio-frequency (RF) electromagnetic field with a frequency of 13.56 MHz. The frequency needs to be above a critical frequency, ~ 100 kHz, at which electrons oscillate, while ions are unaffected. Besides this, the requirement for the combination of frequency and power is that typical molecules used in RIE must be ioniozed due to the kinetic energy of electrons in the plasma. Typical ionization energies are on the order of 5-20 eV. Microwaves may also generate suitable plasma for some applications, including black Si for photovoltaics [74, 75]. The oscillations of the field ionize the gas molecules, thus forming a plasma. The RIE chamber consists of two parallel plate electrodes and the wafer is placed on the bottom electrode. Since the electric field is applied over these two electrodes the positive reactive ions in the plasma will be accelerated towards the bottom electrode and hit the wafer surface. Thus, the RIE process consists of an anisotropic physical sputtering and an isotropic chemically reactive etch of the wafer surface taking place simultaneously. The degree of chemical to physical etching may be tuned by adjusting the platen power and the relative concentrations of the different gas constituents. Figure 2.7 shows a sketch of a RIE chamber. In some cases the RIE chamber further comprises a coil surrounding the chamber and inductively generating the plasma. Such process is called inductively coupled plasma (ICP) RIE. This means that the platen power only serves to accelerate the reactive ions towards the wafer, while the coil generates and sustains the plasma. This makes certain ICP-RIE processes easier to control, since plasma generation and ion acceleration may be controlled separately. It was recently shown [76] that the combination of coil and platen power leads to improved minority carrier lifetime of black Si compared to RIE processes only using platen power.

In this work, seed gas to the RIE plasma consists of SF_6 and O_2. The ionization of SF_6 and dissociation of O_2 follows the reactions:

$$SF_6 + e^- \rightarrow SF_{6-x}^{y+} + xF^* + (y+1)e^- \tag{2.67}$$

$$O_2 + e^- \rightarrow 2O^* + e^-. \tag{2.68}$$
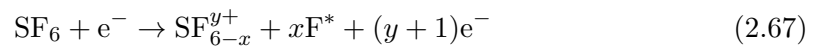
The fluorine radicals etch Si to form volatile gas such as SiF_4, while oxygen radicals react with these volatile products and passivate Si according to

$$xF^* + Si(s) \rightarrow SiF_x(g) \tag{2.69}$$

$$yO^* + SiF_x(g) \rightarrow SiO_yF_x(s). \tag{2.70}$$

---
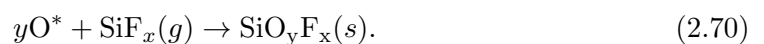
[2]Torr is a commonly used non-SI unit for pressure, defined as exactly $\frac{1}{760}$ of 1 standard atmosphere or 133.3 Pa.
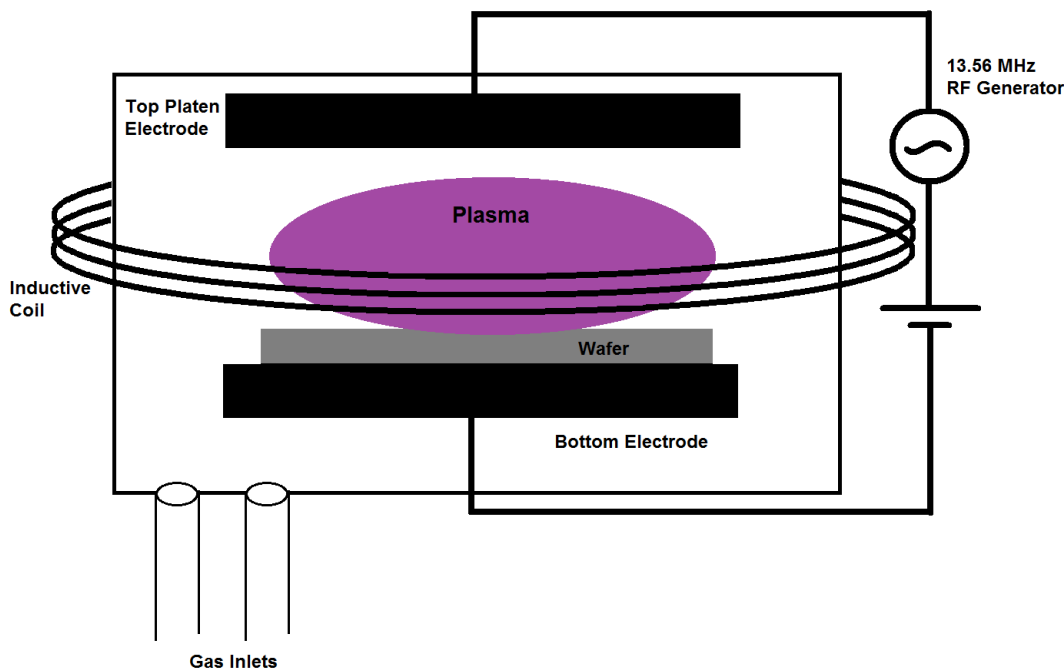
FIGURE 2.7: Schematic drawing of a reactive ion etching (RIE) chamber.

The radicals are responsible for the chemical etching, while the ions are responsible for the physical sputtering, which is anisotropic due to the direction of the electric field. Due to the anisotropic nature of the etch, any side walls of structures formed on the surface will be less exposed to the physical sputtering compared to the rest of the surface. This leads to a self-enhancing mechanism of forming structures on the surface leading to more vertical side walls and deeper trenches as the etch continues. The chemical reactions in equation 2.69 and 2.70 occur at every exposed Si area on the surface and this self-enhancing mechanism explains the formation of deeper and more vertical structures as soon as some topology on the surface is formed. However, the underlying explanation of why structures are formed at all and the seemingly random distribution of these, has not yet been fully explained in literature. In other words, some micro-masking needs to take place in order for the described etch to result in nanostructure formation. The explanation proposed here basically relies on two fundamental assumptions:

- Native oxide is present on the Si surface, when the etching starts

- The surface has a non-zero roughness.

If these two assumptions are valid, parts of the surface - but not the entire surface per definition - will be etched by the very first radicals to arrive at the surface. Statistically phrased, the time of arrival of the ions and radicals has a non-zero standard deviation averaged over a macroscopic surface area. The native oxide layer will be removed at these randomly placed spots slightly faster than on the rest of the surface. Once the oxide layer is removed the radicals will etch the underlying Si at these spots much faster than the ongoing removal of oxide on the rest of the surface. The etch rate ratio (or Si to SiO_2 selectivity) in 1:1 SF_6 and O_2 plasma is in the range of 10-40 [77, 78]. Thus, even if the deviation of oxide removal across the wafer is smaller than a fraction of a second, the difference in oxide and Si etch rate results in some structure formation

at these random spots. Figure 2.8 shows a sketch of the effect of surface roughness and native oxide. One may argue that the role of native oxide can be removed from
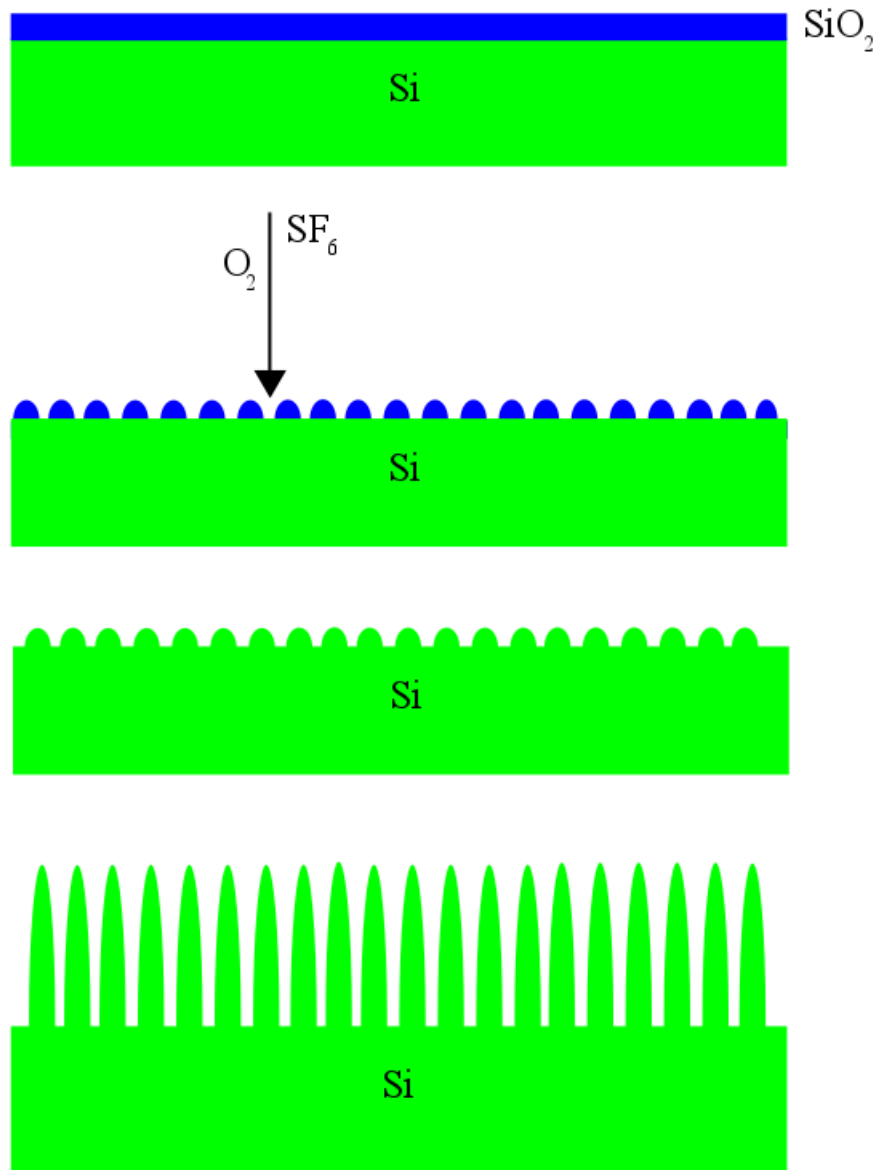
FIGURE 2.8: Sketch of the formation of black Si nanostructures due to surface roughness and native oxide on the Si surface.

the picture by performing a hydrofluoric (HF) acid pretreatment immediately prior to the RIE process. However, even the transfer of the wafer into the chamber and any stabilization time before processing will result in some oxidation of the Si surface. If the arguments here are valid, it follows that black Si formation is not possible on a perfectly flat surface with no surface roughness and no native oxide, assuming completely uniform plasma. This is extremely difficult to verify in practice. This also explains why multiple groups [11, 13, 20, 76, 89, 110] have been able to form black Si using different kinds of RIE and ICP-RIE equipment on many different kinds of Si substrates with different surface conditions e.g. with and without HF pretreatment. In other words, black Si nanostructure formation will occur on all practical Si surfaces at appropriate process conditions. Appropriate process conditions means that the gas flow ratio between SF_6

and O_2 has to be controlled precisely in order for the self-enhancing etching mechanism to occur in the first place. Too much SF_6 creates an almost isotropic etch known from isotropic dry etching of Si [79–81]. Too much O_2 increases the passivation layer thickness and at some point this eliminates the initial differences required to start the black Si formation. Thus, the gas flow ratio control is paramount for the black Si formation. The other controllable parameters in RIE, such as pressure, platen power and temperature, all affect the ionization and etching reactions and therefore these must also be carefully controlled to successfully form black Si on a given Si surface. Jansen *et al.* [83] explain this as a 'black Si regime' covering the combination of gas flow ratio, pressure and power resulting in black Si formation. It has been observed in practice that an ideal gas flow ratio for one particular RIE setup, including type of chamber and wafer, may not create black Si at all in a different RIE setup. Besides achieving black Si formation, it is obviously also important to adjust the specific nanostructure surface topology. This applies especially for photovoltaic applications, in which the nanostructures need to be sufficiently large and at a high area density for minimized reflectance, while minimizing the overall surface area for minimized surface recombination. The chamber pressure affects the topology, since higher pressure leads to more ion collisions and thus smaller effective flux of ions reaching the surface per unit area. This results in a lower density of structures, therefore a low pressure is typically ideal for solar cell applications. Increased etch time mainly increases the structure height and makes the side walls more vertical. Increased platen power increases the anisotropic part of the etch mechanism and may lead to deeper and more vertical structures similar to increasing the etch time. However changing the anisotropy of the etch, one way or the other, increases the risk of falling outside of the regime for black Si formation [83]. Adjusting the etch time may therefore be preferred if the gas flow ratio is on the limit of the regime. On the other hand, time should typically be minimized in an industrial production, thus all other parameters must be tuned to allow for this, while staying inside the black Si regime. Figure 2.9 shows SEM-images of different black Si surfaces fabricated by RIE.
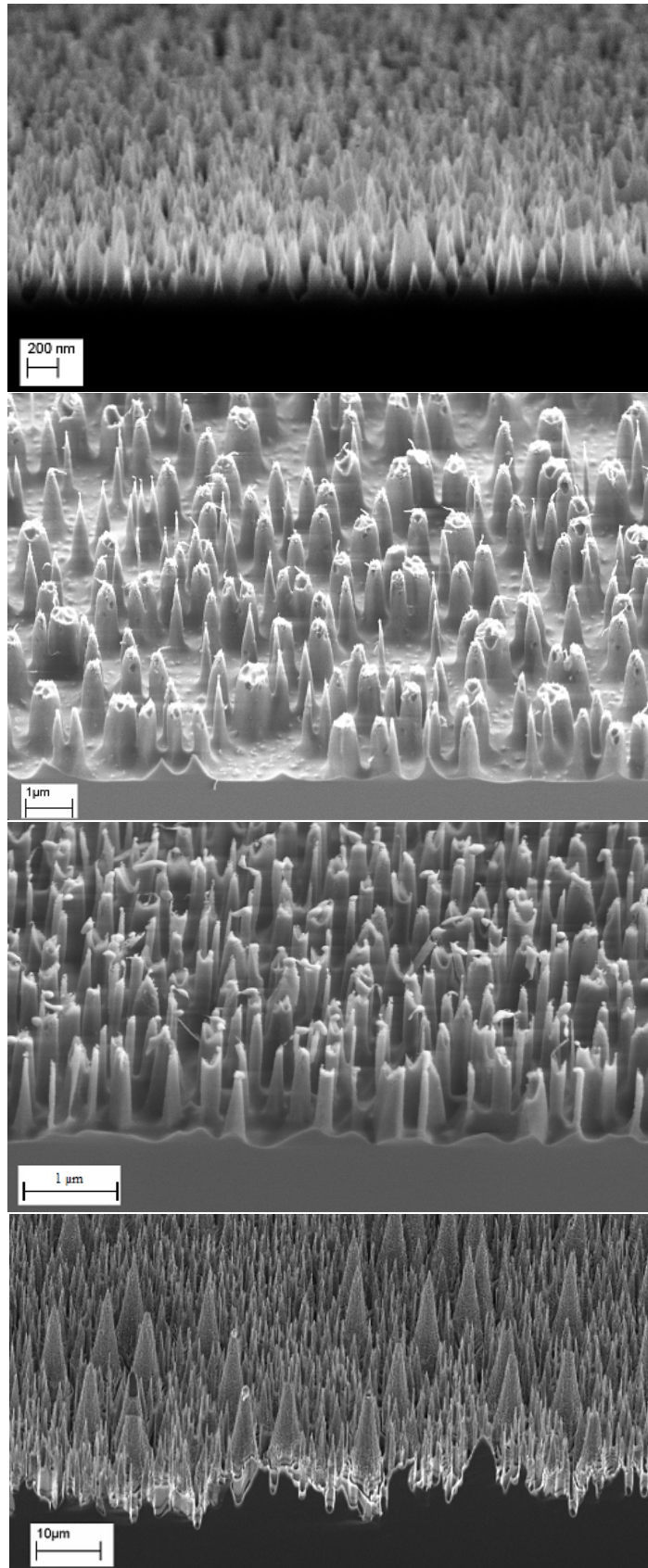
FIGURE 2.9: Scanning Electron Microscope (SEM) images of different black Si surfaces. The top image is an example of the topology typically used for solar cells in this work. The bottom image is an example of a topology with very low reflectance, but not necessarily ideal electrical properties for solar cells.

Chapter 3

Optical Properties of Black Si

3.1 Reflectance

As described in Chapter 2, the nanostructured Si surface suppresses the reflectance of light from the surface according to the graded refractive index model. In order to optimize the power conversion efficiency of solar cells, the optical absorption in the cell must be maximized. The absorbed light is by definition the amount of light, which is neither reflected nor transmitted through the material according to

$$A = 1 - T_{\mathrm{r}} - R, \tag{3.1}$$

where A is the absorptance, T_{r} is the transmittance and R is the reflectance.

For a solar cell light may be reflected from the Si surface (capped with AR-coating), the metal fingers and busbars or even reflected from the rear of the cell and escape all the way back through the front. The light may also be transmitted through the cell, which typically means it will be absorbed in the rear metal. Light may also be parasitically absorbed in the AR-coating itself. All these scenarios lead to optical losses that directly reduce the amount of charge carrier generation and thereby the efficiency and power output of the solar cell. Thus, it is critically important to minimize optical reflectance and transmittance. The primary advantage of black Si is the significant reduction of front surface reflectance, therefore reflectance measurements are in focus in this section.

Normal incidence reflectance measurements of the RIE-textured mono-, multi and quasi-mono Si surfaces were performed using a broadband lightsource (Mikropack DH-2000), an integrating sphere (Mikropack ISP-30-6-R), and a spectrometer (Ocean Optics QE65000, 280-1000 nm). The reference solar spectral irradiance for AM1.5G was used to calculate the weighted average reflectance in the wavelength range from 280-1000 nm.

Figure 3.1 shows the total (specular+diffuse) reflectance from a representative black Si surface and a KOH-textured Si surface with $\sim$ 60 nm PECVD SiN$_x$:H AR-coating as function of wavelength in the relevant wavelength range for Si solar cells, 300-1000 nm. The result in Figure 3.1 shows total reflectance below 1% of black Si for most wavelengths in the range 300-1000 nm. The reflectance of KOH-textured Si with AR-coating is higher for all wavelengths in the range, especially for wavelengths below 500 nm, where the difference in reflectance is very pronounced.
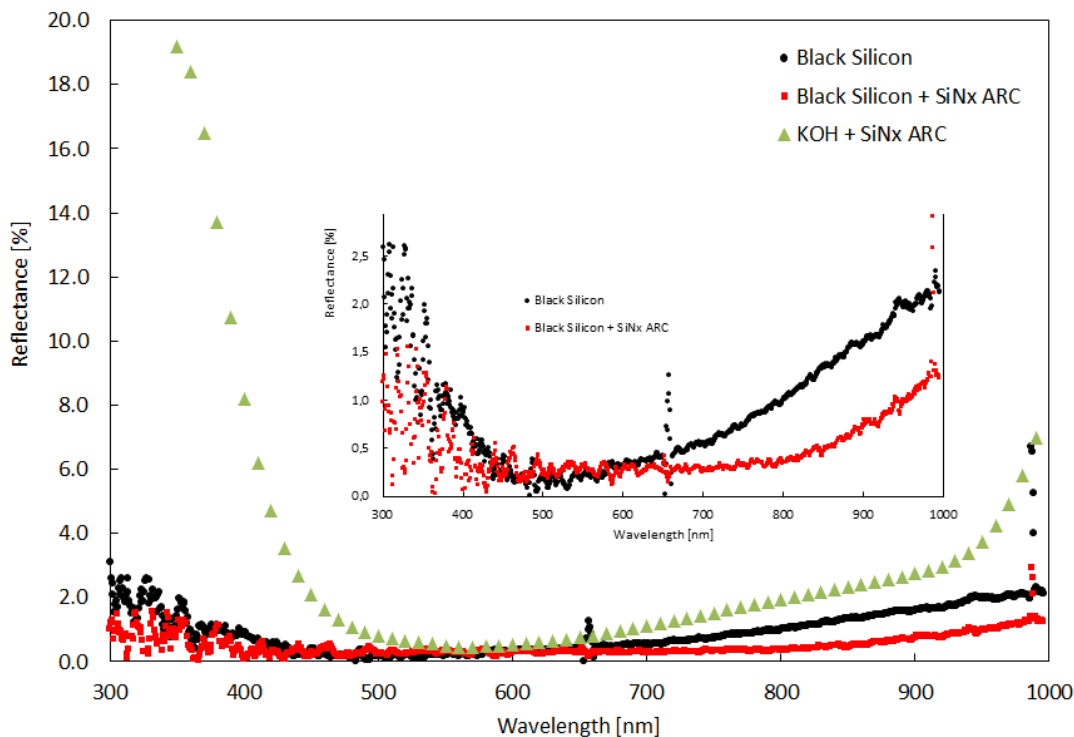
FIGURE 3.1: Total reflectance of RIE- and KOH-textured mono-crystalline Si, respectively, measured as function of wavelength. Both Si samples had ~ 60 nm PECVD SiN$_x$:H AR-coating and reflectance of the RIE-textured Si is shown with and without the AR-coating for comparison. The inset shows the same reflectance measurement focused on the reflectance range 0-2.5% for clarity.

The reflectance measurement in Figure 3.1 was measured on mono-crystalline black Si with and without any AR-coating. However, for practical solar cell applications the texturing method may be applied to mono-, multi- or quasi-mono-crystalline Si substrates and will typically be coated with AR-coating. Furthermore the solar cell needs an emitter (defined by the pn-junction), typically realized by thermal diffusion on the front, which may affect the reflectance due to oxidation of the Si surface. Therefore several reflectance measurements were performed on black Si made from mono-, multi- or quasi-mono-crystalline Si substrates with and without AR-coating and before and after emitter formation, respectively. The summary of these measurements is seen in Figure 3.2.

The result in Figure 3.2 shows total weighted average reflectance of RIE-textured Si below 1.1% for all three crystalline grades of Si, which is a clear improvement compared to KOH- and acidic-textured Si used in standard industrial Si solar cells. With AR-coating KOH-textured Si has a reflectance of 2% [17], while acidic-textured multi-crystalline Si with AR-coating has a reflectance of 8% [18]. The results furthermore show negligible increase in reflectance after emitter diffusion. The RIE-textured Si shows $\sim$ 0.1% minimum reflectance independent of crystalline grade. Figure 3.2 shows that the average reflectance is unaffected by the ~ 60 nm PECVD SiN$_x$:H AR-coating in this case.

However, since the graded refractive index of black Si is fundamentally different from that of conventionally textured or planar Si, it is not obvious, which thickness of SiN$_x$:H
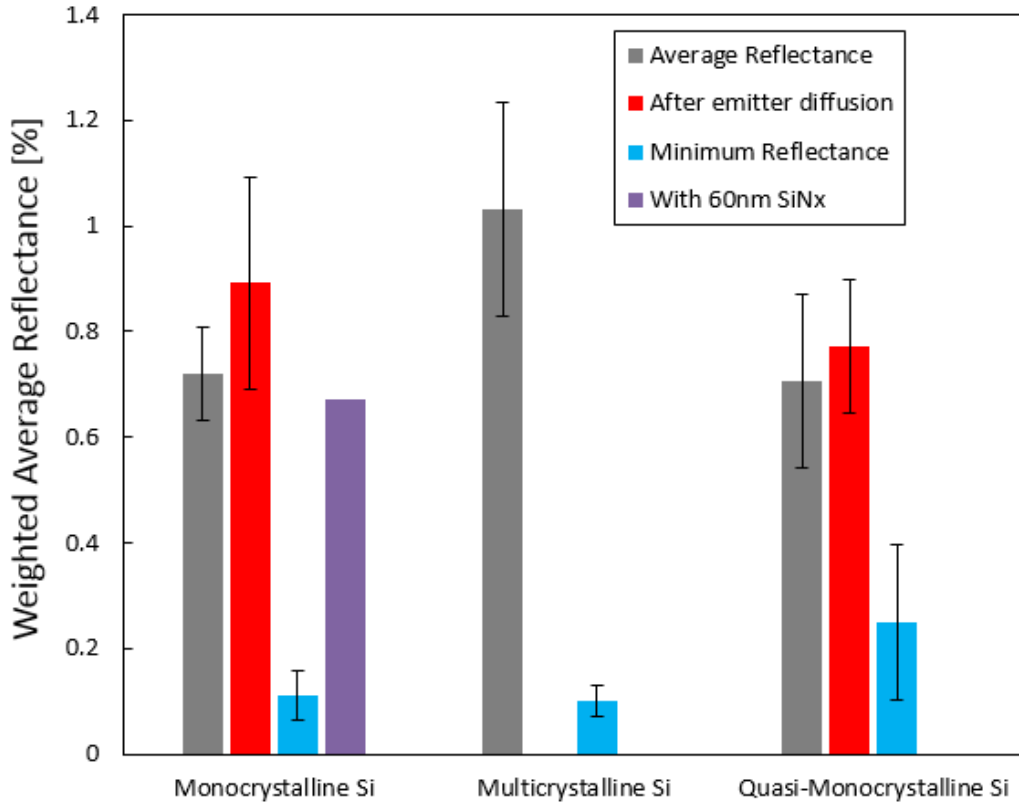
FIGURE 3.2: Total weighted (AM1.5) average reflectance before and after emitter diffusion as well as the minimum reflectance of mono-, multi- and quasi-mono Si surfaces, respectively. The average reflectance of RIE-textured mono-crystalline Si with ~ 60 nm PECVD SiN_x:H AR-coating is also shown. The error bars indicate the standard deviation based on several different samples per measurement [86].

AR-coating is optimal for black Si. In order to investigate this the deposition time of the PECVD SiN_x:H deposition was varied in steps of 2 minutes from the 'standard' time of 6 minutes and 30 seconds to 12 minutes and 30 seconds. The result is shown in Figure 3.3.

Figure 3.3 shows that a PECVD SiN_x:H deposition time of 6 minutes and 30 seconds yields the lowest reflectance of black Si. The deposition times are stated instead of the SiN_x:H thickness, because the thickness is not necessarily the same on black Si as on conventionally textured or planar Si, due to the increased surface area, which may change the deposition rate. Therefore the exact thickness on black Si is not fully known. On conventionally textured Si a 6 minutes and 30 seconds deposition yields a SiN_x:H thickness of ~ 60 nm.

In order to quantify the spatial uniformity of RIE-texturing, the reflectance was measured at different positions on a 156x156 mm^2 CZ wafer textured by maskless RIE. The total reflectance was measured in the wavelength range 300-1000 nm and the integrated average reflectance is plotted as function of distance from the wafer center in Figure 3.4.

The result in Figure 3.4 shows that the average reflectance is below 0.5% across the entire 156x156 mm^2 wafer. The average reflectance decreases towards the edge of
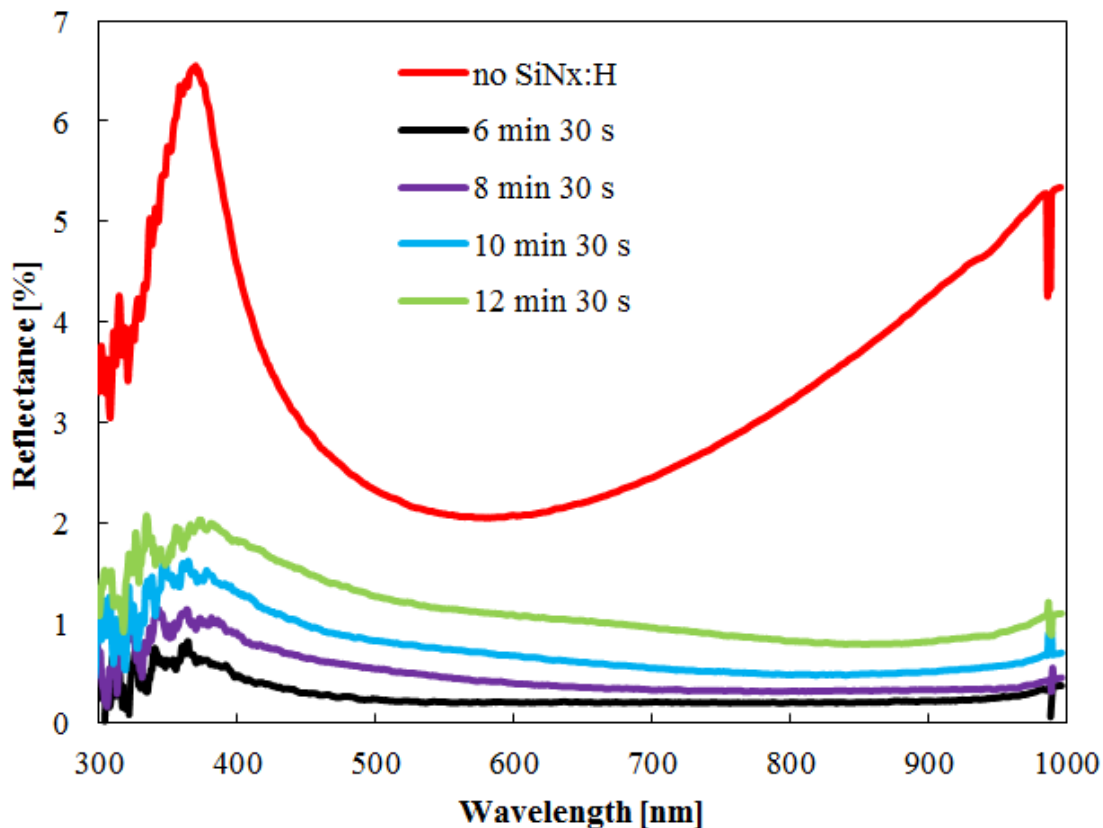
FIGURE 3.3: Total reflectance of black Si with SiN_x:H AR-coating as a function of wavelength in the range 300-1000 nm for four different PECVD SiN_x:H deposition times representing four different SiN_x:H thicknesses. The reflectance of black Si without AR-coating is shown for comparison.

the wafer, but even though the relative difference in reflectance from center to edge is significant, the absolute difference is on the order of 0.2%, which is smaller than typical absolute reflectance variations across KOH-textured mono-crystalline Si wafers [84].

The reflectance measurements shown in Figure 3.1-3.4 were all measured at normal incidence, meaning that the incident light beam is directed at an angle of 90° relative to the solar cell plane. However, under realistic operating conditions solar cells are subject to a broad range of different incident angles, representing daily, yearly and geographical variations of the incident angle and furthermore diffuse light conditions, such as during cloudy weather. For this reason, it is even more interesting to measure the total, weighted reflectance at different incident angles. This has been done for black Si and KOH-textured ('random pyramid') Si with ~ 75 nm SiN_x:H AR-coating and the result is shown in Figure 3.5. The angle-dependent optical reflectance was measured with monochromatic light from 350 nm to 1200 nm using an APEX monochromator illuminator with an Oriel Cornerstone 260 1/4m monochromator. A quartz crystal achromatic depolarizer from Thorlabs was used in the beam path to randomize the partly polarized light from the monochromator. The sample was inserted inside a 150 mm integrating sphere with a center mount configuration and rotated to any desired angle of incidence. The result in Figure 3.5 shows that the reflectance of RIE-textured Si is significantly below that of KOH-textured Si at all incident angles below 70°. Furthermore the reflectance of KOH-textured Si increases more with incident angle up to 50° than the reflectance of RIE-textured Si. For angles above 50° the reflectance of RIE-textured Si
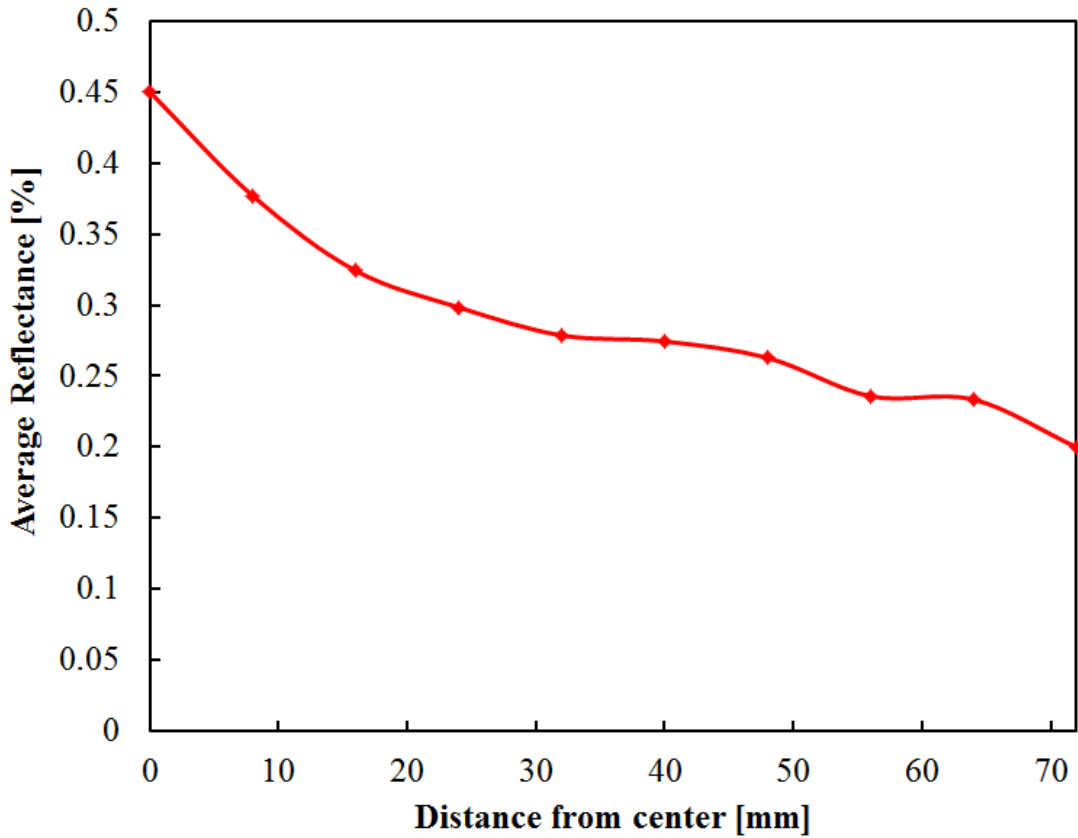
FIGURE 3.4: Total weighted (AM1.5) reflectance of RIE-textured Si averaged over the wavelength range 300-1000 nm as function of the distance from the center of a 156x156 mm^2 CZ wafer.

increases more with incident angle than that of KOH-textured Si. This result shows the potential for improved solar cell performance using RIE-texturing at non-ideal incident angles.

Besides investigating the angle-dependent total reflectance as seen in Figure 3.5, it is also interesting to investigate the specular and diffuse part of this total reflectance. Knowing the angle-dependent total reflectance, a relatively simple way of quantifying the diffuse and specular part of the reflectance, respectively, is to measure specular reflectance at different incident angles. This may for instance be done with an ellipsometer. Figure 3.6 shows the total and specular reflectance, measured with an integrating sphere and a Woollam VASE[1] Ellipsometer, respectively, as function of incident angle.

Figure 3.6 shows the measured specular and total reflectance as a function of the incident angle. Both the average reflectance in the wavelength range 300-1000 nm and the reflectance at 550 nm are shown. The reflectance is seen to be dominated by non-specular (diffuse) reflectance. The specular reflectance is seen to be very low, even at very high incident angles (i.e. below 0.1% at angles below 65°). This indicates some light scattering by the black Si nanostructures.

---

[1]Variable Angle Spectroscopic Ellipsometer
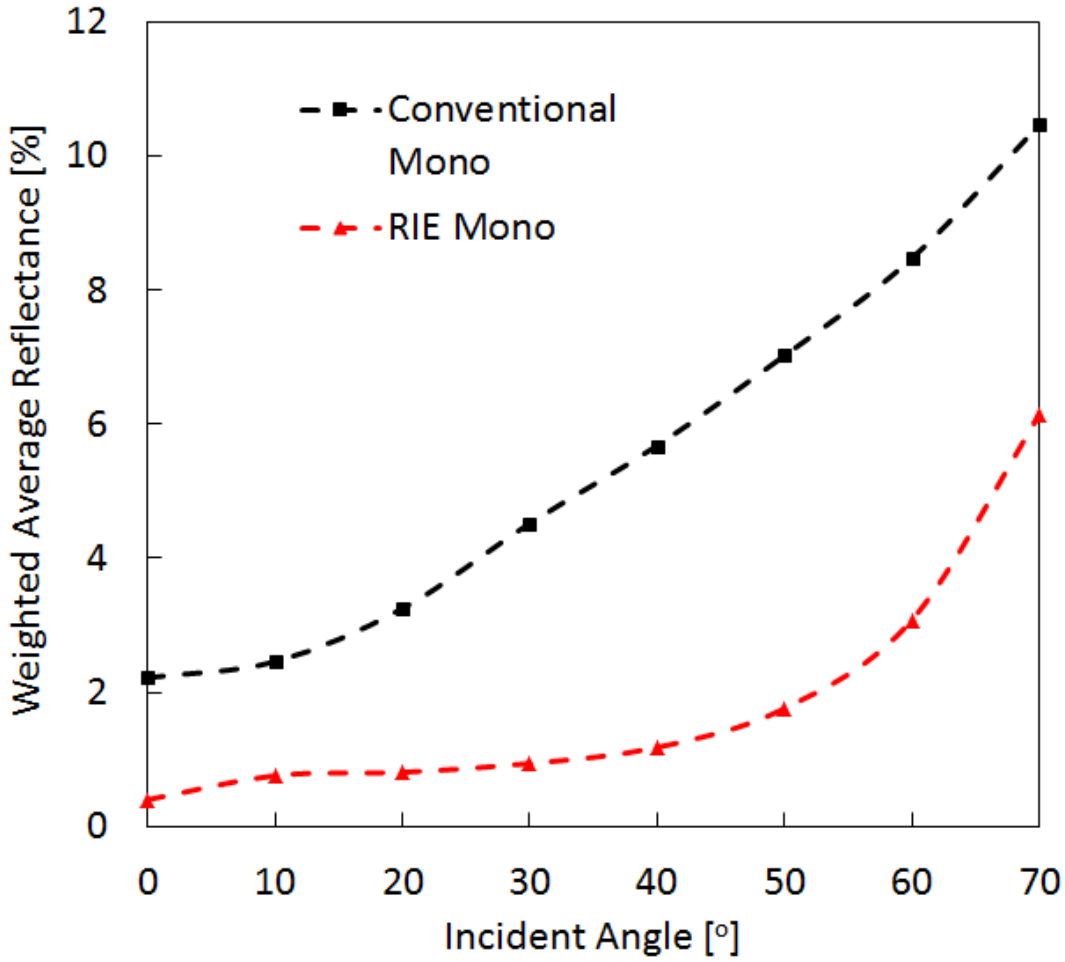
FIGURE 3.5: Incident angle dependent total weighted average reflectance of KOH-textured (squares) and RIE-textured (triangles) mono-crystalline Si substrates [86].

3.1.1 Simulation of Reflectance Properties

After measuring the angle-dependent reflectance shown in Figure 3.5 and 3.6 it is interesting to investigate whether the graded refractive index model may explain the observed angle-dependent reflectance behaviour of black Si. To simplify modelling of the reflectance of the black silicon nanostructure a mean field approach was used; here the refractive index, n_{r}, was varied gradually – either linearly or non-linearly – from that of silicon, n_{si}, to that of air, n_{air}, across a distance equal to the height, h, of the nanostructures according to

$$n_{\mathrm{r}}(z) = \begin{cases} n_{\mathrm{Si}} & \text{, for } z \leq 0 \\ n_{\mathrm{air}} & \text{, for } z \geq h \\ n_{\mathrm{air}} f(z, h, \Lambda) + n_{\mathrm{Si}} \left[1 - f(z, h, \Lambda) \right] & \text{, for } 0 < z < h \end{cases} \quad (3.2)$$

where Λ is a nonlinearity parameter. The index shape function was defined as $f(z, h, \Lambda) = \ln\left(1 + z/\Lambda\right) \big/ \ln\left(1 + h/\Lambda\right)$ in case of a non-linear index profile and $f(z, h, \Lambda) = z/h$ in case of a linear index profile; here the parameters $\Lambda = 10$ nm and $h = 300$ nm were used. With this index profile the time-harmonic Maxwell equations were solved in the form
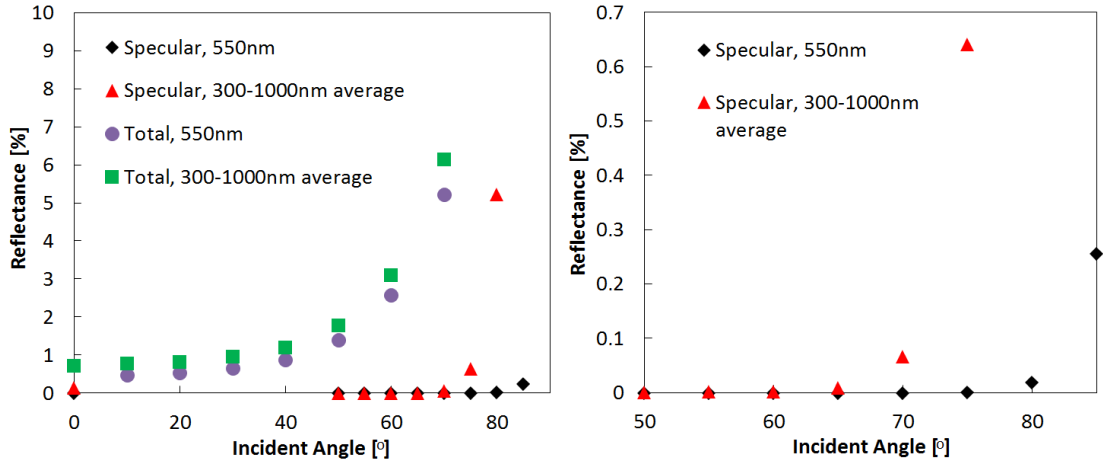
FIGURE 3.6: Measured specular and total reflectance as a function of incident angle. The average reflectance in the wavelength range 300-1000 nm and the value at a wavelength of 550 nm are shown to the left. The specular reflectance at incident angles from 50-85° is shown to the right.

of the Helmholtz equations (e.g. $\nabla^2\mathbf{E} = -k^2\mathbf{E}$, where k is the wave number) for the electric and magnetic fields $\mathbf{E}$ and $\mathbf{H}$, respectively. The calculation was done for the case of a plane optical wave of wavelength $\lambda = 550$ nm incident at an angle θ to the surface normal. The fields Poynting's vector $\mathbf{S} = \mathbf{E} \times \mathbf{H}$ and its time average z-components $\langle\mathbf{S}\rangle\cdot\mathbf{e}_z$ were calculated at the source and the detector, from which the reflectance R was calculated. The simulation was carried out using COMSOL software.

The results of the simulations are shown in Figure 3.7. In Figure 3.7 reflectances for
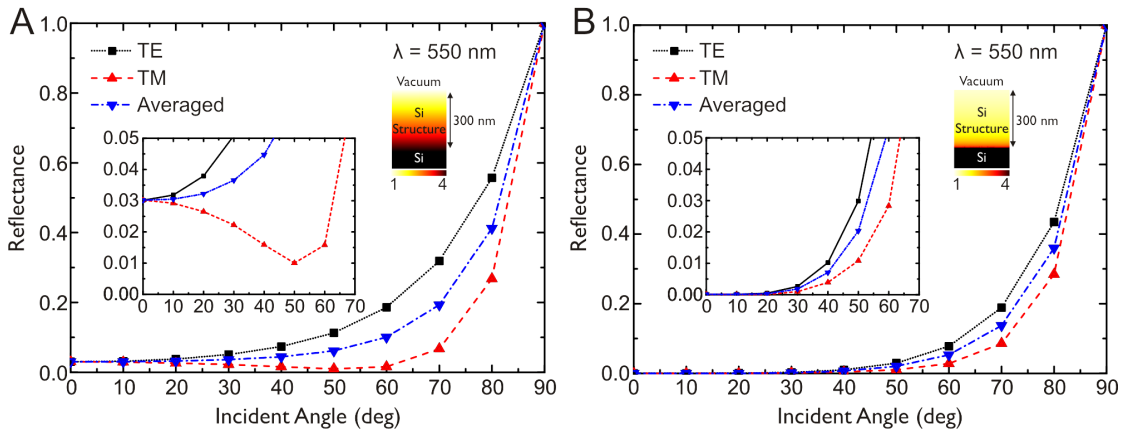
FIGURE 3.7: Simulated reflectance as function of incident angle at a wavelength of 550 nm for surfaces with nanostructures of 300 nm in height in case of (a) linearly graded refractive index, (b) non-linearly graded refractive index. The insets in (a) and (b) show the simulated reflectance at incident angles from 0-70°. [88]

transverse electric (TE) and transverse magnetic (TM) waves are shown along with the mean reflectance of a 50/50 mixture of TE and TM waves as a function of the incident angle. The calculated reflectances in Figure 3.7(a) are for a linearly graded index, while the reflectances for the nonlinear graded index are shown in Figure 3.7(b). As expected, the reflectance is higher for TE than for TM waves. In all cases the reflectance is very low (less than 1% for non-linear graded index and less than 5% for linearly graded index)

for incident angles below 45°. At larger incident angles the reflectance increases rather steeply. We observe that the reflectance resulting from the non-linear graded index is generally lower than the linear graded index and stays below 1% until the incident angle is increased above 45°. Thus, the trend of the simulated angle-resolved reflectance corresponds well with the experimentally measured angle-resolved reflectance. However, the experimentally measured specular reflectance is generally lower than the simulated reflectance. In addition the difference in reflectance between TE and TM waves is less pronounced for the non-linear graded index. We note, that the simple simulation model - by construction - is unable to model real diffuse reflection; this can be accomplished using a much more detailed model of the nanostructured surface, which is part of future work.

3.2   Absorption and Light Trapping

As described earlier, not only reflectance, but also transmittance of light through the cell is important for the solar cell efficiency. In this relation, texturing may also affect transmittance, since the angle, at which the light is scattered into the Si bulk affects the 'light trapping' in the cell. Light trapping essentially means that light, which is not reflected from the front surface, may be internally reflected on the rear and thereby the path length of the light travelling within the material is increased and as a result the probability for absorption within the solar cell is increased. In order for effective light trapping to occur the scattering angle of the light must be larger than the minimum angle required for total, internal reflection on the rear. This means that different texturing techniques, besides affecting the front surface reflectance, may affect the total light absorption due to changed light trapping properties.

Figure 3.8 shows the total light absorptance of RIE-textured Si without any further processing as function of wavelength. The absorptance was measured using a center-mount sample holder placed inside the integrating sphere. The incident angle of the light source deviated 8° from normal incidence due to the geometry of the measurement setup. Figure 3.8 shows that the absorptance of black Si is $\sim 99\%$ in most of the solar spectrum up to a wavelength of ~ 1000 nm, at which the light starts to transmit through the 200 μm thick Si wafer. The integrated average absorptance is 99.2% in the wavelength range 300-900 nm and the absorptance decreases to 91.7% at 1000 nm. The calculated absorptance of a 200 μm Si wafer without any texturing but with an assumed reflectance of 0% is plotted for comparison. Also, the simulated absorptance of a 200 μm Si wafer textured with upright random pyramids with 75 nm SiN_x:H AR-coating is shown for comparison. The simulated absorptance was done with a Monte-Carlo ray tracer. It is seen that RIE-texturing results in increased absorptance of wavelengths above 1000 nm compared to non-textured Si and similar absorptance of wavelengths above 1000 nm compared to conventionally textured mono-crystalline Si solar cells. This indicates some path-length enhancement (PE) of longer wavelengths within the RIE-textured wafer. Based on the absorption coefficient of Si [85] the path-length enhancement can be calculated according to

$$\text{PE}(\lambda) = \frac{A(\lambda)}{\alpha(\lambda)W},\tag{3.3}$$

where A is the measured absorptance, α is the absorption coefficient and W is the thickness of the wafer. The path-length enhancement, based on the measured absorptance in Figure 3.1, of RIE-textured Si is shown in Figure 3.9 in comparison with different
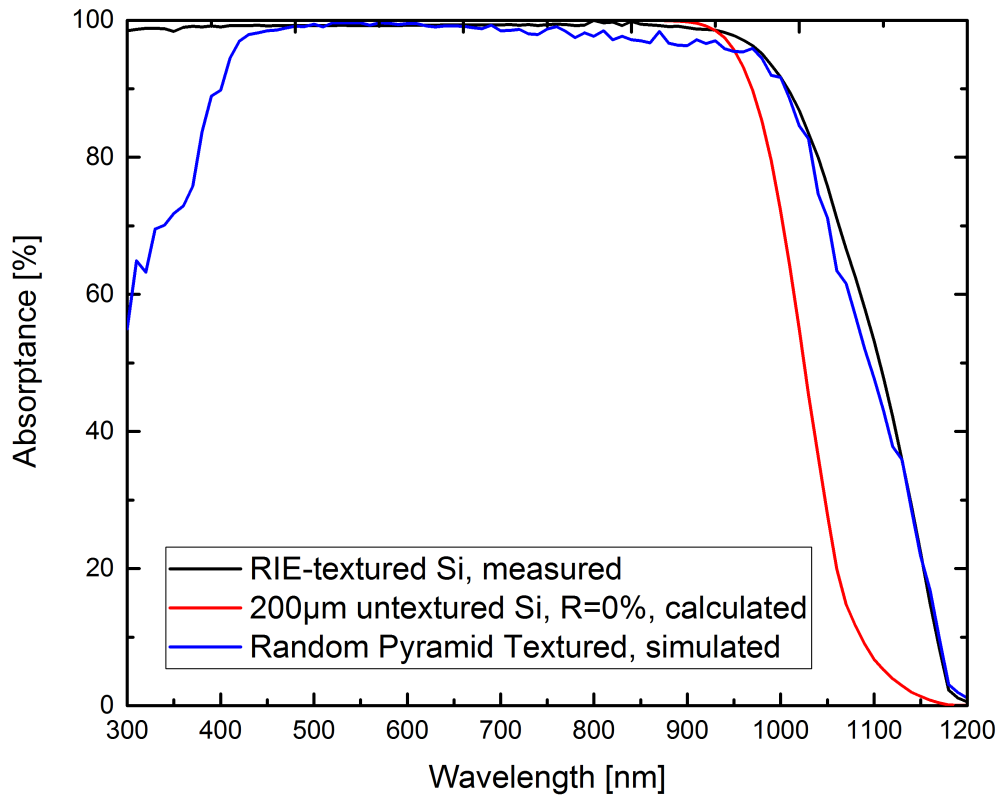
FIGURE 3.8: Light absorptance of the black Si surface before cell processing as function of the wavelength. The calculated absorptance of a 200 μm Si wafer with no texturing but with an assumed reflectance of 0% and the simulated absorptance of a 200 μm Si wafer textured with upright random pyramids with 75 nm SiN$_x$:H are plotted for comparison. The absorptance was measured with a center-mount inside an integrating sphere. The incident angle of the light source deviated 8° from normal incidence due to the geometry of the measurement setup [93].

conventional texturing and AR-coating combinations. Path-length enhancements of conventional texturing schemes were simulated using the Monte Carlo ray tracing calculator of PVLighthouse [2]. Figure 3.9 shows that RIE-textured Si yields path-length enhancement comparable to that of upright and inverted pyramid texturing. RIE-textured Si shows path-length enhancement up to 20 for a wavelength of $\sim$ 1160 nm.

It is noteworthy that the observed path-length enhancement and light trapping properties correspond well with the reflectance measurements in Figure 3.6 showing that the reflectance is dominated by diffuse reflectance. Both results indicate significant light scattering by the black Si nanostructures.

---

[2]https://www.pvlighthouse.com.au/calculators/
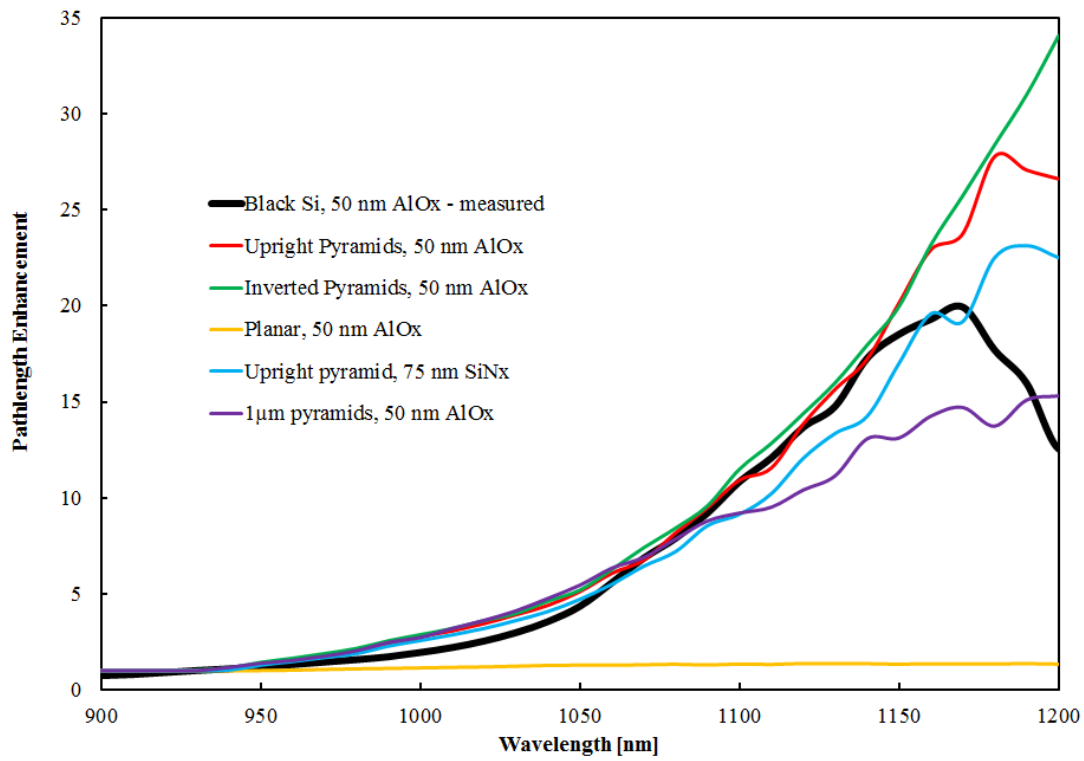
FIGURE 3.9: Path-length enhancement of Black Si calculated from the measured absorptance in comparison with path-length enhancement of upright and inverted pyramids with 30 nm Al_2O_3 and 75 nm SiN_x:H AR-coating, respectively. The path-length enhancements of all pyramid-textured schemes were calculated using a Monte Carlo ray tracer.

Chapter 4

Large-Area screen-printed black Si solar cells

This chapter contains results and discussion from the publication entitled "Angle-resolved characterization of nanostructured and conventionally textured silicon solar cells" [86] seen in Appendix D.

In order to test the maskless RIE-texturing on industrially relevant solar cells and compare with conventional texturing, a batch of 156x156 mm^2 p-type, CZ mono-, multi- and quasi-mono-crystalline Si cells was fabricated. The objective of this cell fabrication was primariy to compare maskless RIE with conventional texturing methods in terms of solar cell performance, but also to verify that black Si may be applied to full-size, industrial Si solar cells.

4.1 Fabrication Approach

The maskless RIE process presented in this work is applied as the texturing step in the following solar cell fabrication process:

- Saw damage removal by etching in 30% KOH at 75 °C for 2 minutes and subsequent cleaning in 20% HCl at room temperature for 5 minutes and rinsing in deionized water.

- Texturing using maskless RIE at room temperature in a O$_2$ and SF$_6$ plasma with a gas flow ratio of O$_2$:SF$_6$ $\sim$ 1:1, chamber pressure of 28 mTorr, 13.56 MHz radio-frequency platen power of 30 W using a STS RIE system.

- Emitter formation using a tube furnace from Tempress Systems with liquid POCl$_3$ as dopant source and N$_2$ as carrier gas at a temperature of 840 °C and atmospheric pressure for 50 min in O$_2$ ambient, followed by removal of phosphor-silicate glass (PSG) in 5% hydrofluoric acid (HF).

- Plasma enhanced chemical vapour deposition (PECVD) of 60 nm hydrogenated amorphous silicon nitride (SiN$_x$:H) anti-reflective coating at 400 °C using a PlasmaLab System133 from Oxford Instruments.

- Screen-printing of Ag front and Al rear contacts with standard Ag and Al pastes using an Ekra X5-STS screen printer, followed by co-firing of the front and rear contacts at 800 °C using an RTC Model LA-309 belt furnace.

- Edge isolation by laser ablation using a J-1030-515-343 FS System from Oxford Lasers Ltd.

The starting substrates were 156x156 mm^2 p-type, CZ mono-, multi- and quasi-monocrystalline Si wafers with a thickness of 200 μm and a resistivity of 1-3 Ω cm.

4.2 Characterization

I-V curves and photovoltaic properties including short-circuit current, I_{SC}, open-circuit voltage, V_{OC}, fill factor, FF, and electrical output power, P_{el}, were measured on complete solar cells under 1 sun illumination (1000 W/m^2, AM1.5G) using a Newport Oriel 92190 large-area Xe light source and a Keithley 2651A high-power source meter.

A LEO 1550 Scanning Electron Microscope (SEM) was used to characterize the nanostructured surface topology.

4.3 Results

SEM-images of the nanostructured surfaces realized by maskless RIE in this work is seen in Figure 4.1.

The nanostructures seen in Figure 4.1 are conical-like hillocks randomly distributed across the entire solar cell surface. The nanostructures have an average height of 300-400 nm with an area density of ∼100 μm^{-2}. The topology is shown with and without ∼60nm PECVD SiN$_x$:H in Figure 4.1. It is seen from Figure 4.1(a) that the SiN$_x$:H AR-coating does not change the RIE-textured topology significantly, but makes the nanostructure edges slightly more round and smooth. The AR-coating may be seen in Figure 4.1(a) as a thin layer, slightly lighter in colour, on top of the hillocks.

Current density-voltage (J-V) characteristics were measured on RIE- and conventionally textured mono, multi and quasi-mono crystalline Si cells, respectively. Figure 4.2 shows the (J-V)-curves of the RIE- and conventionally textured mono crystalline cells for comparison. Figure 4.2 shows that both short-circuit current density and open-circuit voltage of the KOH-textured mono crystalline Si cell are higher than the RIE-textured black Si cell. The short-circuit current density, J_{SC}, open-circuit voltage, V_{OC}, fill factor, FF and power conversion efficiency at normal incidence of the fabricated screen-printed solar cells are summarized in Table 4.1.

Table 4.1 shows that the RIE-textured cells have lower power conversion efficiency than the conventionally textured cells primarily due to lower short-circuit current density, but also reduced open-circuit voltage. Figure 4.3 shows the external (EQE) and internal (IQE) quantum efficiency of the RIE- and KOH-textured mono-crystalline Si cells, respectively. Figure 4.3 shows that the IQE at wavelengths below 700 nm is significantly lower for the black Si cell compared to the conventionally textured Si cell. This
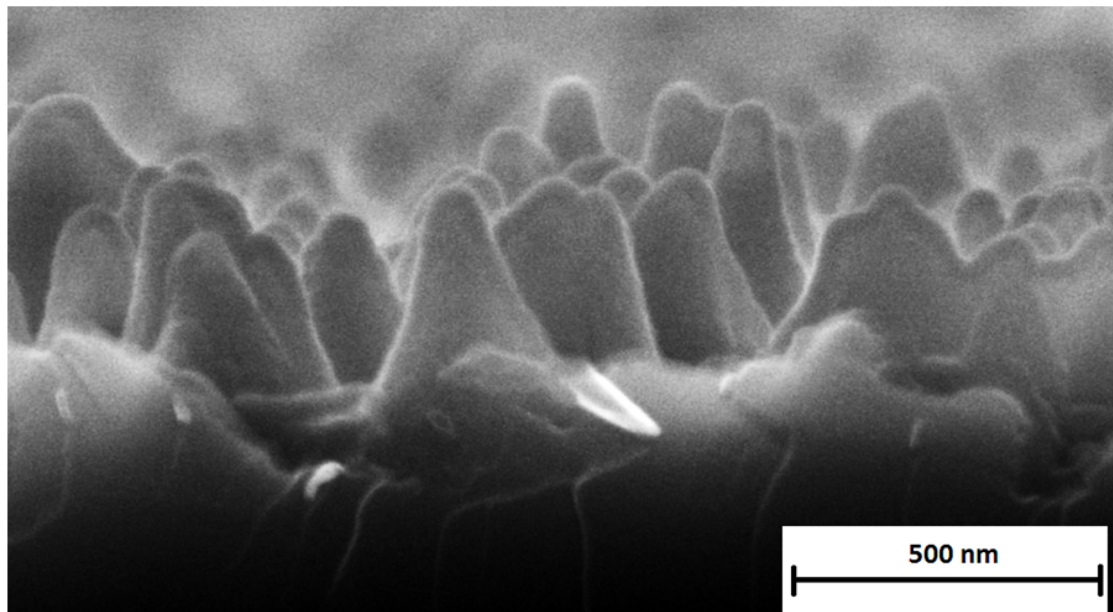
(a)
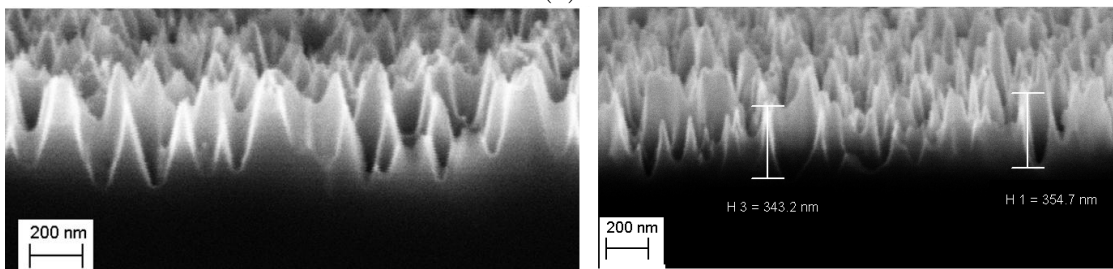
(b)
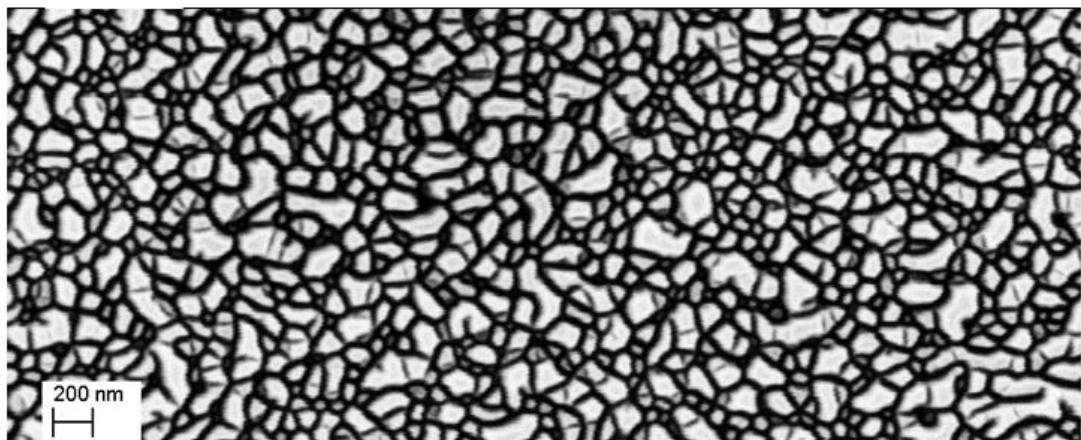
(c)

FIGURE 4.1: SEM-image at 45° (a,b) and 0° (c) tilt of the RIE-textured Si surface with (a) and without (b,c) ∼ 60nm PECVD SiN$_x$:H AR-coating, respectively.
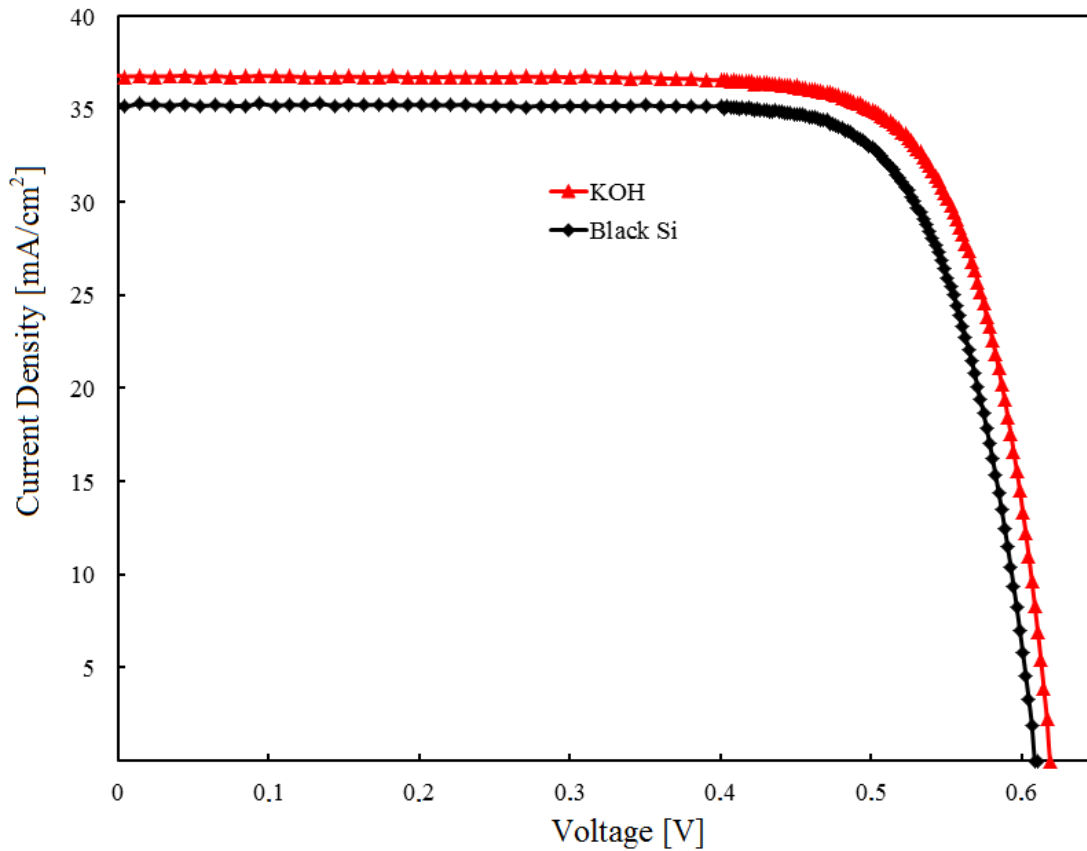
FIGURE 4.2: Measured current density as function of voltage ((J-V)-curve) of screen-printed RIE- and KOH-textured Si cells, respectively.

Normal Incidence				
Cell	Efficiency [%]	J_{SC} [mA/cm^2]	V_{OC} [mV]	FF
Conventional Mono	17.8	36.8	619	0.78
Conventional Multi	16.5	34.4	619	0.77
RIE Mono	16.5	35.2	609	0.78
RIE Multi	14.5	31.7	592	0.77
RIE Quasi-Mono	13.0	30.0	575	0.75

TABLE 4.1: Power conversion efficiency, short-circuit current density, open-circuit voltage and fill factor at normal incidence of conventionally and RIE-textured mono-, multi- and quasi-mono-crystalline Si cells, respectively.
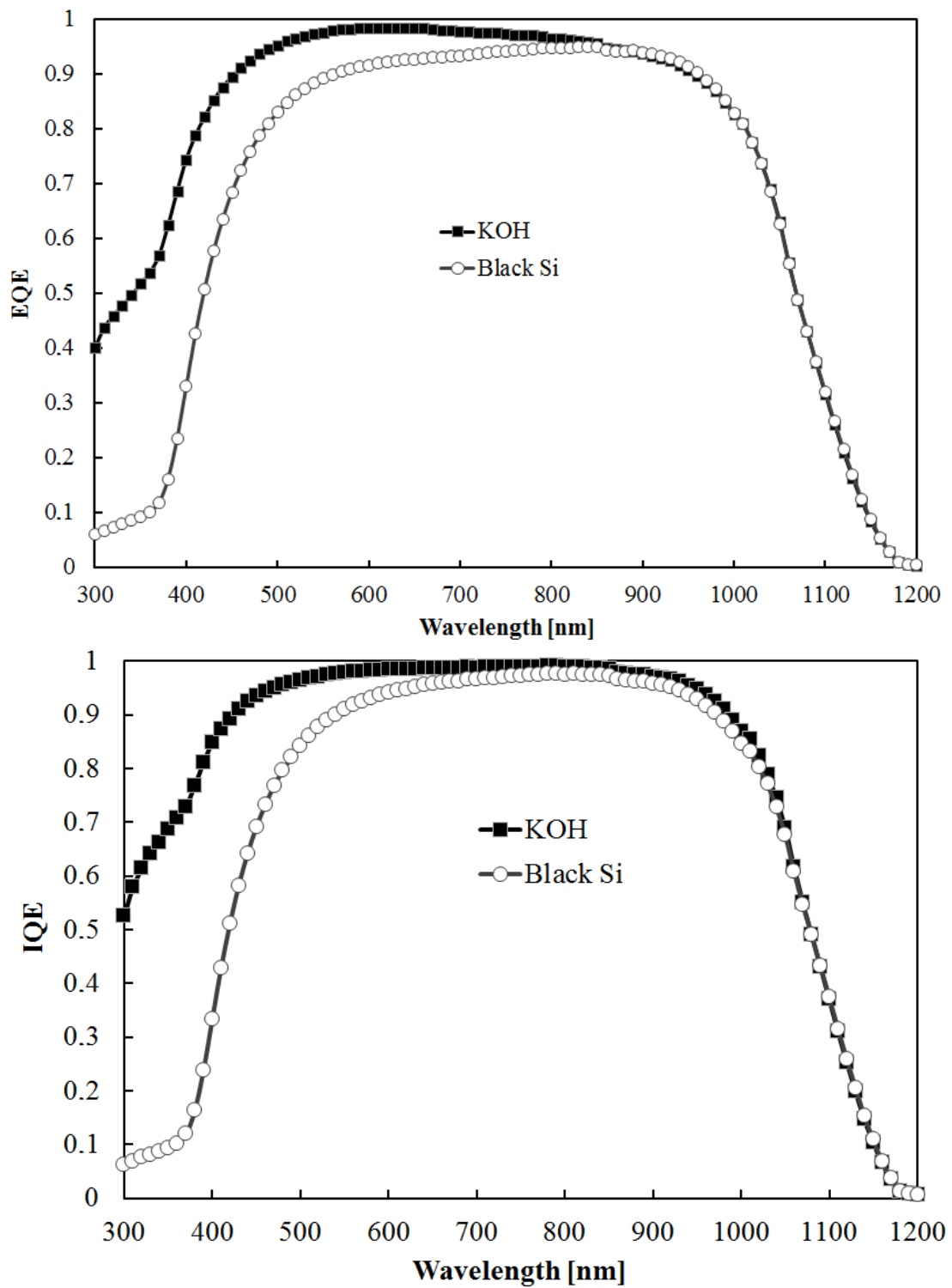
FIGURE 4.3: External (EQE) and internal (IQE) quantum efficiency as function of wavelength of the RIE- and KOH-textured mono-crystalline Si cells, respectively.

Surface	Total Carrier Loss $[\text{mA/cm}^2]$	Emitter $[\text{mA/cm}^2]$	Bulk $[\text{mA/cm}^2]$	Rear $[\text{mA/cm}^2]$
KOH	1.385	0.761	0.207	0.192
RIE	4.163	3.322	0.267	0.069

TABLE 4.2: 'Loss Analysis of Silicon Solar cells by IQE Evaluation' (LASSIE) quantifying the carrier losses in different parts of the RIE- and KOH-textured mono-crystalline Si solar cells, respectively. All values are in units of mA/cm^2.

indicates increased surface and emitter recombination, since the shorter wavelengths are absorbed close to the surface. The absorption length of 700 nm photons is ~ 4 μm, so the increased recombination seems to occur in the top ~ 4 μm part of the cell. Based on the IQE result, a 'Loss Analysis of Silicon Solar cells by IQE Evaluation' (LASSIE) was performed in order to quantify the carrier losses in the differently textured cells for comparison. The result of this analysis is shown in Table 4.2. Based on IQE-measurements and LASSIE analysis, the current and voltage losses may be explained by increased emitter and surface recombination [11]. For the screen-printed cells presented here, the texturing and thus reflectance was not fully optimized. Since the RIE-texturing has been further optimized after these cells were fabricated, with a resulting weighted average reflectance below 1% as shown in Chapter 3, the power conversion efficiency of screen-printed black Si solar cells may be improved in future work solely due to improved texturing. In addition, it was found that the RIE-chamber used for texturing these screen-printed cells may have been contaminated with heavy metals. This may partly explain the increased emitter and surface recombination of the black Si cells. Regardless of the underlying cause of the increased recombination, the result implies that improved surface passivation and emitter design is necessary in order to achieve comparable and preferably improved power conversion efficiency of black Si solar cells compared to conventionally textured solar cells.

4.4 Angle-Resolved Results

In order to characterize the solar cell performance at varying incident angles, I-V curves were measured on differently textured Si solar cells mounted and contacted on a stage, which prior to each I-V curve measurement was tilted to a position given by two angles, θ and ϕ, around two orthogonal axes: θ is the tilt of the cell plane with respect to the original, horizontal x-axis and ϕ is the tilt of the cell plane with respect to the tilted y-axis. The light source was fixed during all measurements. The measurement setup including the two angles θ and ϕ is sketched in Figure 4.4. The incidence angle was varied using two JVL QuickStep stepping motors connected to the solar cell stage. Each angle was randomly varied in steps of $10°$ in the range $0-90°$ unless otherwise specified. At each angle combination, (θ, ϕ), the I-V curve was measured under 1 sun and the result collected using LabView, such that a total of 100 I-V curves were measured for each cell. The measured I-V curves were then analyzed in order to determine I_{SC}, V_{OC}, FF and P_{el} at each angle combination, (θ, ϕ), using SciLab. Finally the angle-resolved photovoltaic properties were plotted and the average electrical power output normalized to the normal incidence power output was calculated in order to compare the angle-dependency of different cells.
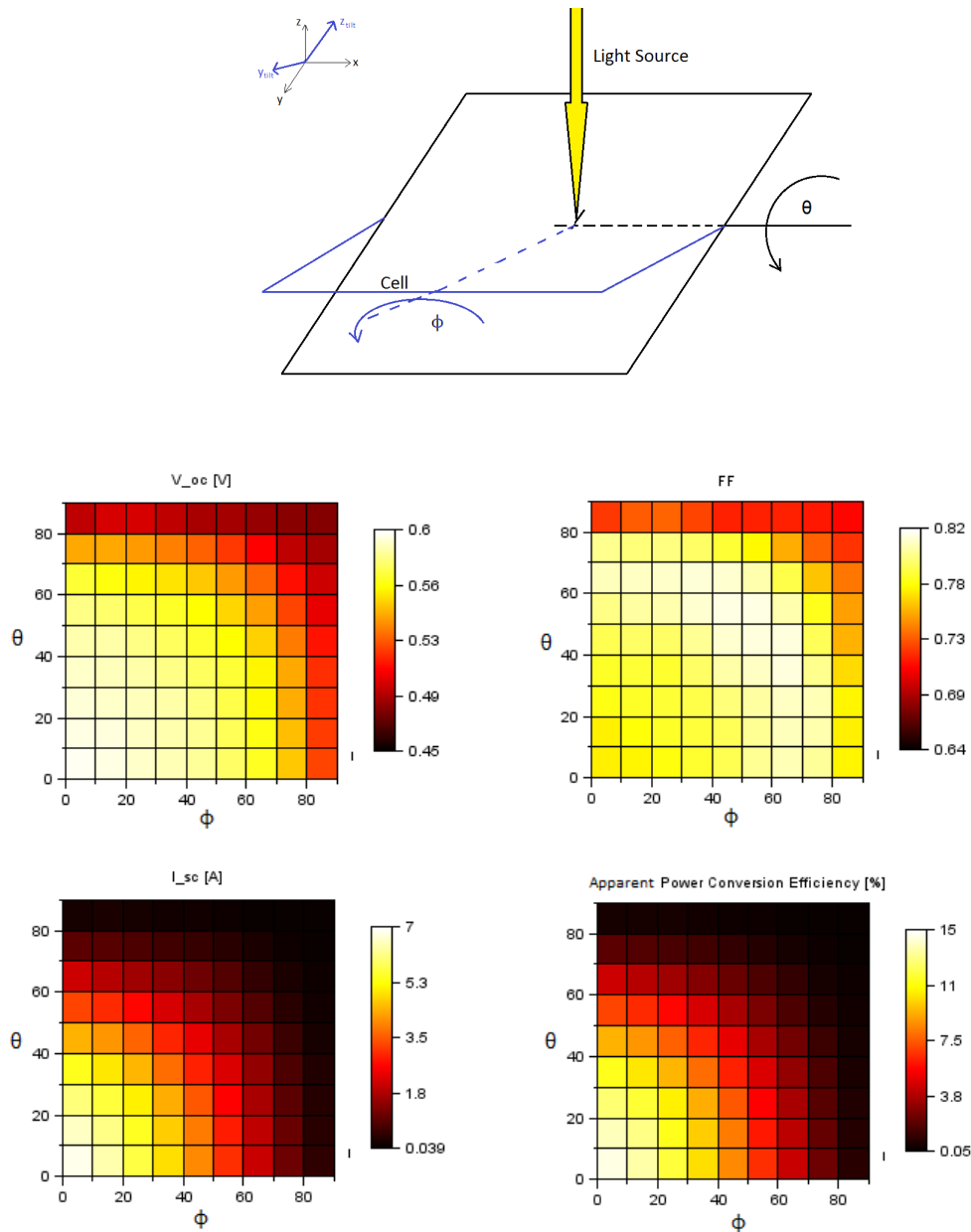
FIGURE 4.4: Angle-resolved measurement including short-circuit current, open-circuit voltage, fill factor and power conversion efficiency. The result is for a RIE-textured mono-crystalline Si solar cell. A sketch of the measurement and coordinate system is seen in the top of the figure. The angles, θ and ϕ are indicated.

Figure 3.5 in Chapter 3 shows that the reflectance of RIE-textured Si is significantly below that of KOH-textured Si at all incident angles below 70°. This result indicates the potential for improved solar cell performance using RIE-texturing at non-ideal incident angles. Figure 4.4 shows a sketch of the angle-resolved cell measurements and an example of the output angle-resolved cell results including short-circuit current, open-circuit voltage, fill factor and power conversion efficiency. There are two reasons for measuring parameters such as I_{SC}, V_{OC}, FF and power output as function of two different incident angles and plotting the result in a 2-D plot such as in Figure 4.4: First of all, the intention is to demonstrate a new and different method for characterization of solar cells in general. By measuring IV-data as function of two orthogonal incident

angles in combination, realistic angle-resolved scenarios such as diffuse light conditions can be investigated in more detail. Secondly, this method allows for a quantification of any asymmetric features of the solar cell with respect to incident angle of the light, whether on the surface or inside the cell. Examples of this are isotropic compared to anisotropic texturing methods and light trapping properties. We acknowledge that the asymmetric behaviour seen in Figure 4.4 is not significant considering the uncertainties of the measurement. Thus, the choice of a 2-D plot in this case is a demonstration of the method and its capabilities, rather than a thorough analysis of asymmetric angle-resolved behaviour.

Figure 4.4 shows that V_{OC} and FF do not change significantly for angles below $80°$. I_{SC} and consequently P_{el} decrease with increasing incident angle. This is expected since the optical input power, P, on the solar cell decreases with cosine to the incident angle, since the effective illuminated area decreases with cosine to the angle according to equation 4.1. In the experimental setup the optical power incident on the cell for angle variation θ is given by

$$P = P(\theta) = \Phi_0 W_e^2 \cos(\theta) = P_0 \ \cos(\theta) \tag{4.1}$$

under ideal conditions. Here W_e is the edge length of the cell, Φ_0 is the optical intensity and P_0 is the optical power incident on the cell at normal incidence. The efficiency of the cell, which may be angle dependent, is

$$\eta(\theta) = \frac{P_{el}(\theta)}{P(\theta)} \tag{4.2}$$

where P_{el} is the electrical output power at optimal load conditions. Part of any angular dependence in the efficiency is due to angular dependence of the reflection coefficient, $r(\theta)$, and this dependency is made explicit, if an internal efficiency η_{int} is defined such that

$$\eta(\theta) = \eta_{int}(\theta)[1 - r(\theta)] \tag{4.3}$$

The internal efficiency, $\eta_{int}(\theta)$, could be angle dependent due to increased photon path length within the silicon for increasing θ and consequently increasing collection probability.

These efficiencies are the physically relevant parameters for the cell. For convenient presentation of the raw measurement data, an artificial apparent efficiency, η_{app}, may be defined as

$$\eta_{app}(\theta) = \frac{P_{el}(\theta)}{P_0} = \eta(\theta) \cos(\theta) \tag{4.4}$$

and from the rightmost expression in equation 4.4, it is seen that if the cell has an efficiency without angular dependency, then the apparent efficiency has a cosine angular dependency. The measured apparent efficiency for the RIE-textured mono-crystalline Si cell is plotted in Figure 4.5; in the plot the expected apparent efficiency given in equation 4.4 assuming a constant η is also shown for comparison. For simplicity the results are only shown with angle variation in one axis. Figure 4.5 shows that the experimentally measured apparent efficiency is higher than expected for incident angles below $60°$. This may in part be explained by divergence of the light source, which changes the actual optical input power according to equation 4.5.

$$P(\theta) = \Phi_0 W_e^2 \frac{\cos(\theta)}{1 - (\frac{W_e}{2L} \sin(\theta))^2} \tag{4.5}$$
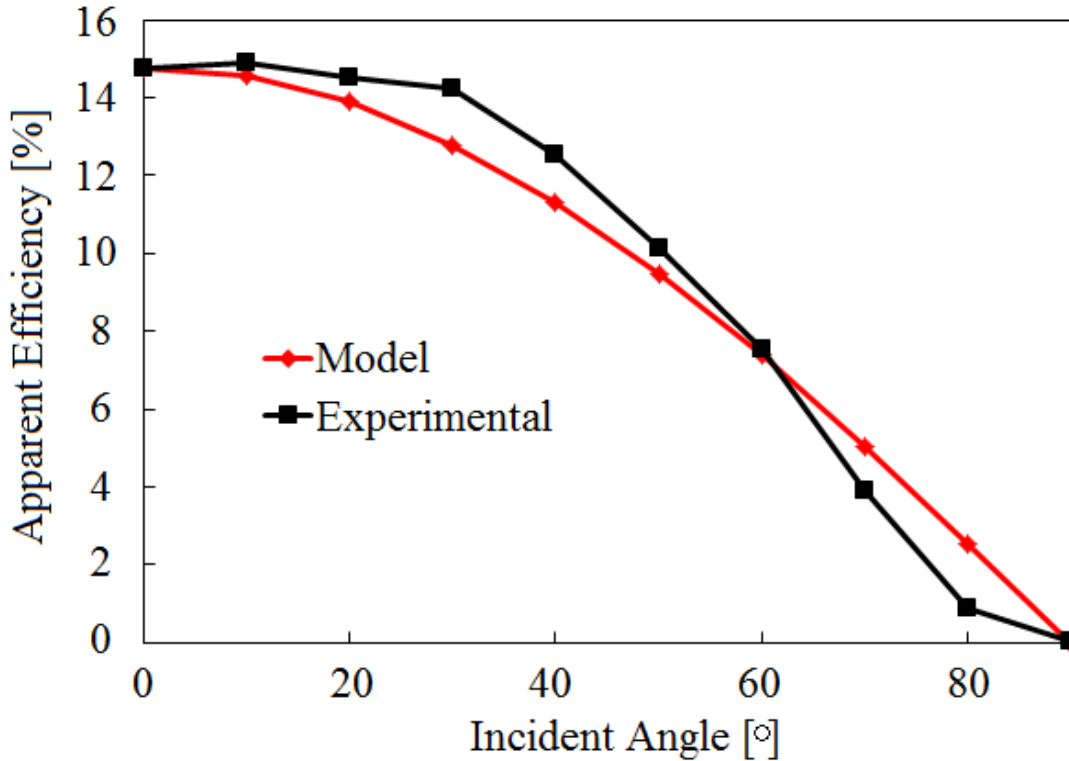
FIGURE 4.5: Angle-resolved apparent efficiency measurement as function of the incident angle in one axis in comparison with the expected apparent efficiency decreasing with cosine to the angle. Experimental data for the RIE-textured mono-crystalline Si solar cell are shown.

where L is a characteristic length parameter of the divergence. Note that the term $1 - (\frac{W_e}{2L} \sin(\theta))^2$ is a possible correction term related purely to the measurement setup. Equation 4.5 shows that divergence of the light source accounts for measured apparent efficiency values higher than expected. However, efficiency values lower than expected, as seen for incident angles higher than 60° in Figure 4.5, can not be explained by divergence of the light source and are most probably a result of increased reflectance at higher incident angles. P_{el} decreases according to equation 4.3 when the reflected part of the optical input power, $r(\theta)$, increases with incident angle as shown in Figure 3.5.

In order to evaluate the actual angle dependency of the differently textured solar cells, the measured electrical power output was normalized to the electrical power output at normal incidence, (0,0). Figure 4.6 shows the angle-dependent normalized power output for the RIE- and conventionally textured mono- and multi-crystalline Si cell, respectively, for comparison. Figure 4.6 shows that the RIE-textured mono- and multi-crystalline cells in general have slightly higher angle-resolved efficiency normalized to the efficiency at normal incidence compared to the conventionally textured cells. For certain incidence angles above 60° the conventionally textured mono-crystalline cell shows slightly higher normalized efficiency compared to the RIE-textured. Figure 4.6 also shows an asymmetric behaviour with respect to the two angles, θ and ϕ. The asymmetry occurs for both RIE- and conventionally textured cells, which indicates that the asymmetric behaviour is partly due to imperfections in the measurement setup. However, it is seen that the asymmetry is slightly larger for the conventional cells for most angles. This might be explained by the different rotational symmetries for the differently textured topologies: The black silicon cell - due to the random nature of the surface nanostructures – should
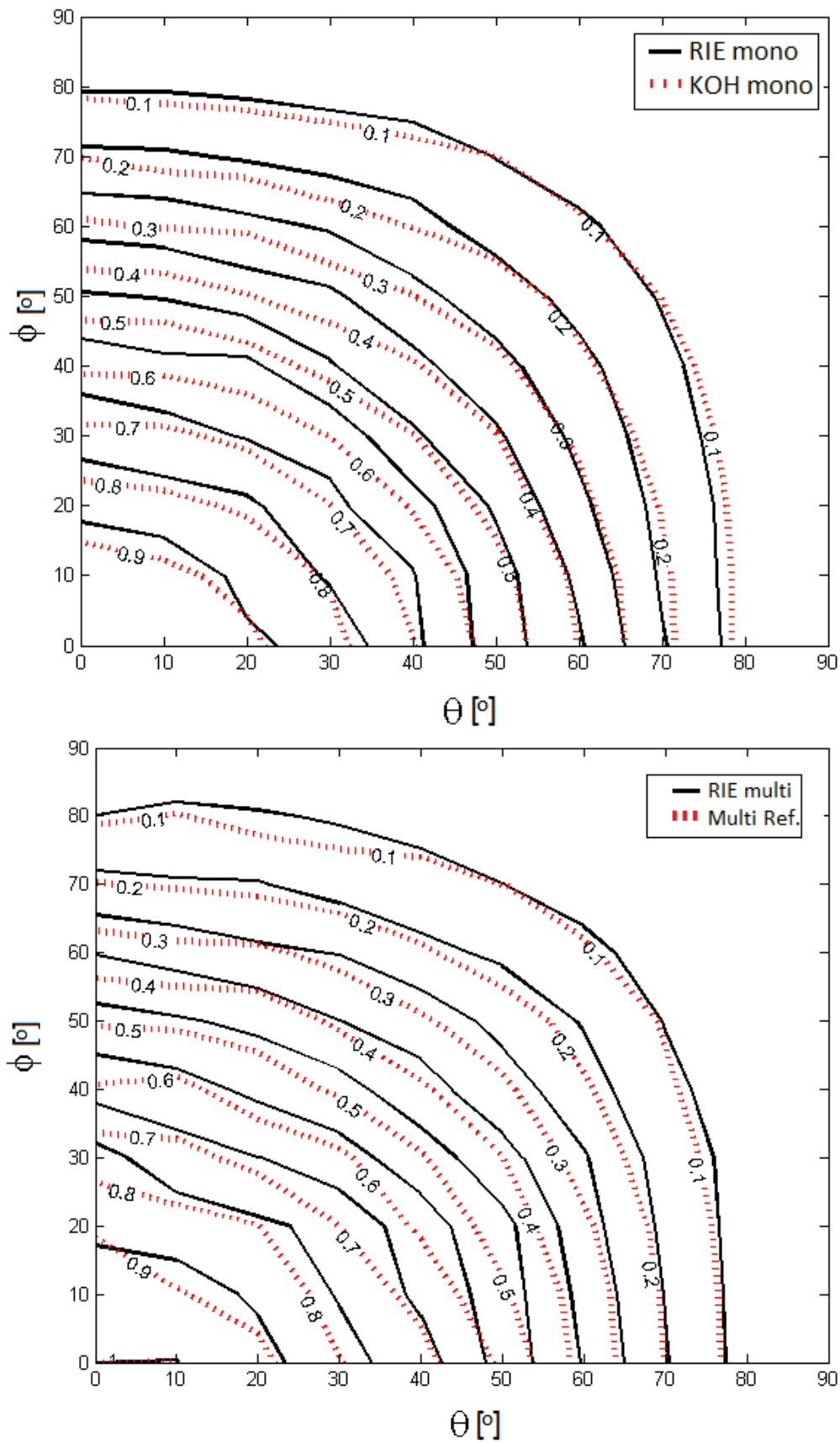
FIGURE 4.6: Angle-resolved electrical power output normalized to the power output at (0,0) for the RIE-textured and conventionally textured mono- (top) and multi-crystalline (bottom) Si cell, respectively.

Ψ_{av} [%], [$\theta;\phi$]	[0-90°;0-90°]	[0-40°;0-40°]
RIE Mono	30.44	75.15
RIE Multi	31.13	75.69
RIE Quasi-Mono	32.16	76.81
Conventional Mono	29.22	70.39
Conventional Multi	28.18	72.62

TABLE 4.3: Average normalized electrical power output relative to the power output at normal incidence, averaged over a range of incident angles from 0 to 90° and 0 to 40°, respectively, in two orthogonal axis for conventional and RIE-textured mono-, multi- and quasi-mono-crystalline Si solar cells, respectively.

only be affected by the polar angle of the incident light, whereas the azimuthal angle should not matter. The same may not be true for KOH textured cells, where the pyramids may be of random size, but they all share a fourfold symmetry in the azimuthal angle; it follows that some degree of variation with the azimuthal angle may be present for KOH cells.

The asymmetric behaviour may also be due to the front metallization, which reduces the symmetry to twofold or lower. Yet, the observed asymmetry is too small compared to the uncertainties of this measurement to conclude whether the asymmetry is actually due to topology differences or measurement inaccuracy.

Angle-resolved properties similar to the results in Figure 4.4 were measured for nanostructured mono-, multi- and quasi-mono-crystalline Si cells and conventionally textured mono- and multi-crystalline Si cells for comparison. Since texturing of quasi-mono-crystalline Si cells is not yet fully established or standardized, no quasi-mono-crystalline cell with conventional texturing was produced. Based on the measured angle-resolved electrical power output, the average normalized electrical power output, Ψ_{av}, relative to the power output at normal incidence can be compared for each of the differently textured cells. Ψ_{av} is given by the expression in equation 4.6 and the resulting values of average relative power output are shown in Table 2 and Figure 4.7.

$$\Psi_{\mathrm{av}} = \frac{1}{N} \sum_{\theta=0}^{90} \sum_{\phi=0}^{90} \frac{P_{\mathrm{el}}(\theta,\phi)}{P_{\mathrm{el}}(0,0)} \tag{4.6}$$

In equation 4.6 N denotes the total number of efficiency values which is being averaged over. In the case of averaging over incident angles in the range of 0-90° in steps of 10° in both axes, $N = 100$. P_{el} denotes the measured electrical power output of the cell. The results in Figure 4.7 and Table 4.3 show that the average normalized power output is also higher for the RIE-textured cells compared to the reference cells in the incident angle range of 0-40°. Furthermore the difference between the RIE-textured and the reference cells is even more significant in this smaller range of angles closer to normal incidence. This angular range is arguably more interesting than 0-90° due to e.g. higher sunlight intensity close to normal incidence and the effective restriction of incident angles of light reaching the solar cells due to refraction and reflection of light from the protective glass covering solar cells in practice. In order to account for these differences, it is needed to do a complete weighing of the different incident angles and angle ranges. Such analysis

FIGURE 4.7: Average normalized electrical power output in the range 0-90° and 0-40°, respectively, relative to the power output at normal incidence for conventionally and RIE-textured mono, multi and quasi-mono-crystalline Si cells, respectively.

is out of the scope of this work, but the results indicate the need for a more detailed analysis.

4.5   Discussion

The results in Table 4.1 show that the RIE-textured cells have lower power conversion efficiency at normal incidence due to increased surface recombination of the RIE-textured cells [11].
However, the average electrical power output normalized to the power output at normal incidence shown in Figure 4.7 is higher for the RIE-textured cells compared to the conventionally textured cells; both for mono- and multi-crystalline Si. This indicates a less angle-dependent power output of such nanostructured Si solar cells compared with conventionally textured Si solar cells in general. Less angle-dependent power output implies potentially higher power output over a broad range of incident angles representing e.g. angle variation during daily and yearly operation of solar cells and panels. Furthermore, and perhaps more importantly, such less angle-dependent behaviour as seen on Figure 4.7 represents improved performance under diffuse light conditions for nanostructured solar cells compared with conventionally textured solar cells. Since diffuse light is a realistic and important operating condition, which affects the performance of commercial solar cells and panels significantly, this result shows the potential of nanoscale texturing, such as maskless RIE-texturing, as a way of improving the overall performance of

Si solar cells by enhancing the diffuse and low light performance and thus create a more stable and angle-independent solar cell performance.

Chapter 5

LDSE black Si solar cells

This chapter contains results and discussion from the publication entitled "Black silicon laser-doped selective emitter solar cell with 18.1% efficiency" [93] seen in Appendix B.

This chapter presents the second batch of fabricated black Si cells. In order to improve the emitter properties of RIE-textured cells, a laser-doped selective emitter (LDSE) was combined with RIE-texturing. The work was mainly carried out at UNSW.

5.1   Laser Doping

Conventional doping of Si requires high temperatures and long processing times in order to obtain the required concentration of dopant atoms such as phosphorus and boron in the Si lattice. However, high temperatures and long processing times are not desired in the solar industry, which requires high throughput, low cost and low thermal budget. In the case of a selective emitter, local doping is needed. This means that a relatively accurate definition of the front contact pattern needs to be defined before or during the doping process itself. In the semiconductor industry, such local doping profiles could be achieved by photolithography followed a second thermal diffusion step. However, this is not suitable in solar cell production due to the low throughput and high cost of these process steps.

Laser doping is able to solve this problem, since highly doped areas can be defined locally in a single process step with a process time of a few seconds per solar cell. The mechanism behind laser doping is described in the following: The energy from the laser radiation heats up Si to its melting point of 1414 °C causing Si to be in its liquid phase for a short period of time, defined by the laser pulse length and the speed at which the beam moves across the surface. If dielectric layers are present on the Si surface, they will effectively be removed in the same process due to the thermal expansion of the underlying Si and the resulting induced stress in the, typically thin, dielectric layer. If dopant atoms such as phosphorus, boron or aluminium are present in the vicinity of the molten region, they diffuse into the molten Si. When the Si recrystallizes, the dopant atoms are incorporated into the lattice causing the Si to be doped. Figure 5.1 shows optical microscope images of a Si surface passivated by 30 nm Al_2O_3 and processed at different laser powers. At the lowest power, Si is melting underneath the dielectric layer. At higher powers the dielectric starts to crack and is partially removed. Finally the

dielectric coating is completely removed in a spot slightly smaller than the laser spot, causing doped, re-crystallized Si to be exposed. This process happens in the time it
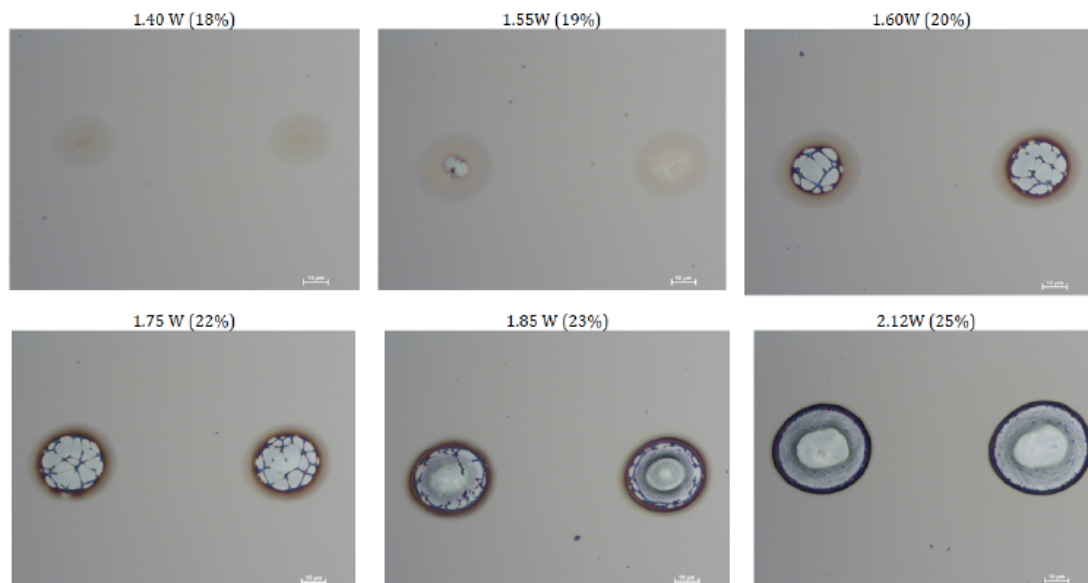
FIGURE 5.1: Microscope images of a Si surface passivated by 30 nm Al_2O_3 and processed at different laser powers, from 1.40 (top, left) to 2.12 W (bottom, right). Numbers in parenthesis are relative output powers compared to the maximum power. A laser tool from IPG Photonics producing 120 ns laser pulses with a wavelength of 1064 nm, writing speed of 0.73 m/s and a repetition rate of 10 kHz was used for this particular test. Courtesy Chantal Silvestre.

takes the laser beam to move across the surface and the molten Si to recrystallize and leaves a surface with local openings in the dielectric and highly doped areas exactly where the dielectric has been removed. This enables subsequent contact formation by electroplating, since metal ions (typically Ni and Cu) will selectively plate in the exposed highly doped Si areas. In practice the laser doping process only takes a few seconds for a standard solar cell area of 156 x 156 mm^2, depending on the laser writing speed, which is typically on the order of m/s. Furthermore very narrow front contacts may be formed, since the minimum feature size is defined by the laser beam and may be down to ~ 20 μm, which reduces the shadow loss compared to conventional, screen-printed front contacts with typical widths of ~ 100 μm. Thus, laser doping is a very fast and potentially scalable method of producing selective emitters and self-aligned front contacts.

In order to achieve a selective emitter without the use of multiple high-temperature process steps and photolithography, laser doping and subsequent self-aligned Ni/Cu-plating has been suggested by several groups [94, 96, 151]. The laser-doped selective emitter (LDSE) process offers excellent sheet resistance control, self-alignment of front metal contacts to the local highly doped areas and a fast, low-temperature process scalable to industrial throughput. Hallam *et al.* achieved 19.3% efficiency for a LDSE solar cell on large-area CZ Si substrates using an industrial turnkey production line with the addition of laser-doping and plating [97]. The LDSE process has also been successfully applied to bifacial silicon solar cells [98]. An important feature of the LDSE cell process is the replacement of screen-printed Ag front contacts with plated Ni/Cu-contacts. Due to the economic benefits of replacing Ag by Cu in the solar industry [46]

and the extensive studies of Ni/Cu-plating applied for Si solar cells [99–102] the self-aligned, high-performing Ni/Cu-plated front contacts is an important and promising feature of LDSE solar cells.

This chapter presents LDSE black Si solar cells fabricated on p-type CZ Si substrates textured by a single step, maskless RIE process. To our knowledge this combination has not been previously reported and the resulting cell is thus considered a first proof-of-concept. The emitter diffusion and surface passivation were not fully optimized, since the main goal of this study was the combination of LDSE and RIE-texturing. The primary objective of this work is to investigate how laser doping and plating processes are affected by the RIE-textured surface and vice versa. It is not obvious how a differently textured surface affects e.g. electrical properties of the laser doped regions and subsequent plating. The surface topology may alter the interaction between the laser beam and the material. Thus a different emitter profile may change the defect generation and risk of Schottky contact formation. Besides laser doping and plating, several process steps could be affected by changing from conventional to RIE-texturing: Emitter diffusion could change with effective surface area and deposition of anti-reflective coating may not yield the expected layer thickness and uniformity due to the nanostructured front surface. Such effects could then further affect the subsequent laser doping and plating processes. An example hereof is spurious plating on the surface in case of pinholes in the dielectric coating resulting from the altered surface topology.

Furthermore there are several aspects in which RIE-texturing potentially could improve the quality of the laser doping and plating processes:

- No or reduced beam coupling of the laser beam on the nanostructured Si surface. On conventional alkaline-textured surfaces, beam coupling is a well-known [103] issue, which leads to increased laser damage at the edge of the laser-doped area. Figure 5.2 from [103] shows a sketch of laser beam coupling on alkaline-textured surfaces. The hypothesis for black Si is that the structures are too small to couple the beam and that laser defects at the edge may therefore be avoided or minimized.

- Higher absorption of 532 nm photons in black Si compared to conventionally textured Si. This may lead to more effective doping, possibly realized at lower laser powers compared to conventional surfaces. Besides reducing the overall power budget of the cell production, reduced laser powers may also lead to reduced laser damage.

- A smaller volume of Si has to be melted per unit area illuminated by the laser in order to achieve a flat surface after re-solidification. A completely flat surface after laser doping may benefit the subsequent plating in order to achieve uniform and controlled plating.

For these reasons there is a need for an investigation of maskless RIE-textured LDSE solar cells.

5.2   Fabrication

The maskless RIE process presented in this work is applied as the texturing step in the following solar cell fabrication process:
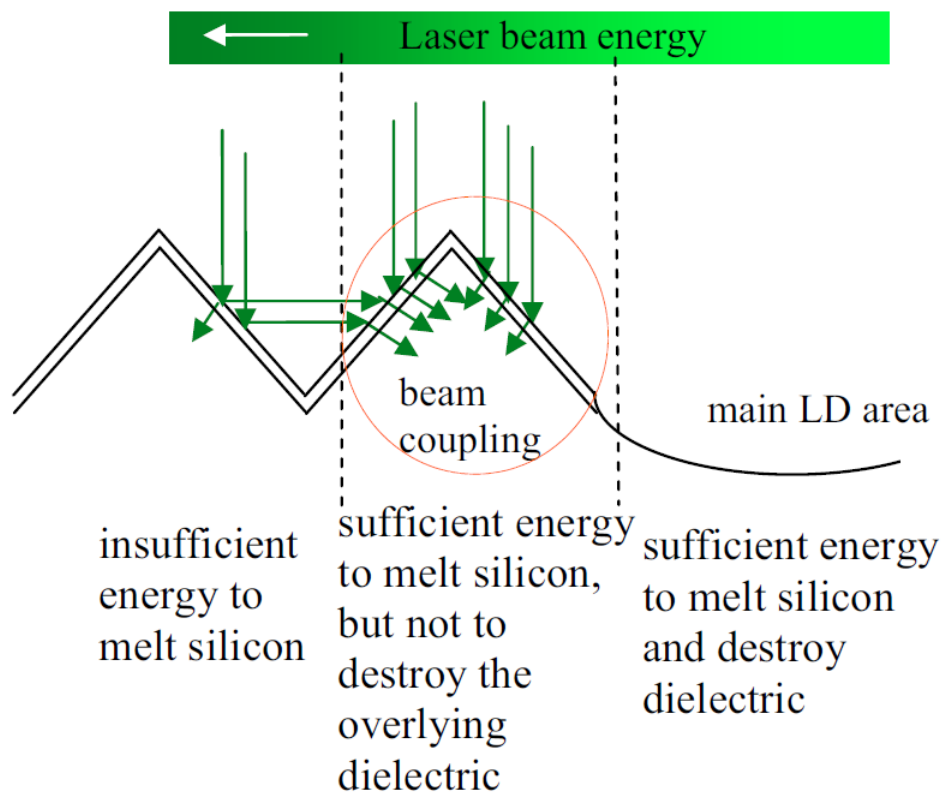
FIGURE 5.2: Sketch of laser beam coupling on conventionally textured Si surfaces taken from [103]. Beam coupling may cause laser defects such as pinholes or isolated Si balls at the edge of the laser-doped region.

- Saw damage removal by etching in 30% KOH at 75 °C for 2 minutes and subsequent cleaning in 20% HCl at room temperature for 5 minutes and rinsing in deionized water.

- Texturing using maskless RIE at room temperature in a O_2 and SF_6 plasma with a gas flow ratio of O_2:$SF_6 \sim$ 1:1, chamber pressure of 24 mTorr, 13.56 MHz radio-frequency platen power of 100 W using a SPTS RIE system.

- Emitter formation using a tube furnace from Tempress Systems with liquid $POCl_3$ as dopant source at a temperature of 770 °C and atmospheric pressure for 30 min in O_2 ambient, followed by post-oxidation at 850 °C for 40 min and removal of phosphor-silicate glass (PSG) in 5% hydrofluoric acid (HF).

- Plasma enhanced chemical vapour deposition (PECVD) of 75 nm hydrogenated amorphous silicon nitride (SiN_x:H) anti-reflective coating at 400 °C using a Roth & Rau MAiA tool.

- Screen-printing of Al rear contact with standard Al paste, which was fired using a Sierra Therm infra-red fast-firing furnace, with a peak temperature set point of 835 °C and a belt speed of 4500 mm/min.

- Laser doping of the front surface using spin-on of 85% phosphoric acid as doping source followed by laser doping using a continuous wave laser at a wavelength of 532 nm, 20 W laser power and 2-4 m/s laser scan speed.

- Light-induced plating of Ni acting as seed and barrier layer for the subsequent Cu plating

- Ni sintering using rapid thermal processing (RTP) in N_2 ambient at 350 °C for 2 minutes

- Light-induced plating of Cu onto the Ni seed layer

- Edge isolation by laser ablation using a 20 W Nd:YAG Lee laser tool.

The starting substrates were 25x25 mm^2 p-type, CZ mono-crystalline Si with a thickness of 200 μm and a resistivity of 1-3 Ω cm.

Figure 5.3 shows a schematic cross-section of the fabricated solar cell.
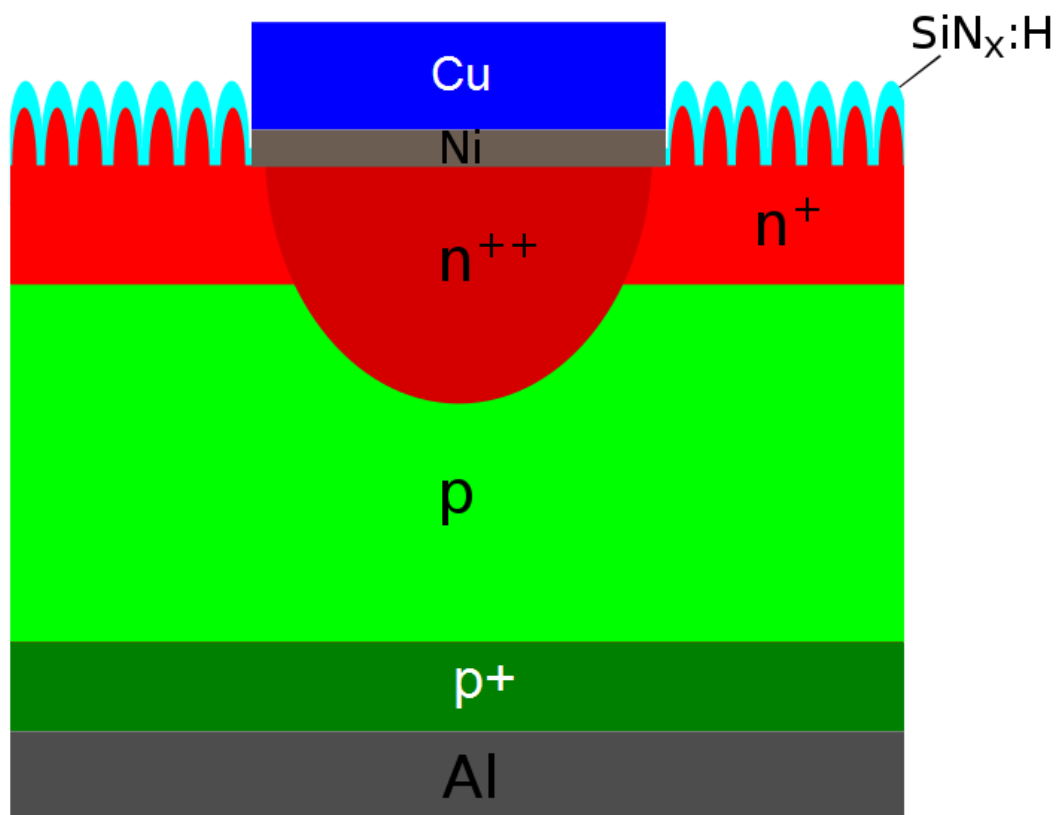
FIGURE 5.3: Sketch of the black Si LDSE solar cell structure. The cells are textured in a single-step, maskless RIE process. The highly doped regions of the selective emitter is formed by means of local laser doping using phosphoric acid dopant and a continuous wave laser. The rear contact is screen-printed and fired Al and the front contacts are plated Ni/Cu. The dimensions of the different layers are not to scale.

5.3 Characterization

J-V curves and photovoltaic performance including short-circuit current density, J_{SC}, open-circuit voltage, V_{OC}, fill factor, FF, and power conversion efficiency were measured on complete cells under 1 sun illumination (1000 W/m^2, AM1.5G) using a ELH halogen

light source, Advantest TR6143 DC Source Measurement Unit and Labview software for data collection. The illumination was calibrated using the known short-circuit current of a reference mono-crystalline Si screen-printed solar cell.

A LEO 1550 Scanning Electron Microscope (SEM) was used to characterize the nanostructured surface topology.

Suns-V_{OC} [113, 114] measurements were performed using a Sinton WCT-120 Lifetime tester. The J_{SC} value from the J-V measurement was used in the Suns-V_{OC} measurements.

Reflectance was measured using a Perkin Elmer integrating sphere and spectrometer. The absorptance was measured using a center mount sample holder inside the integrating sphere.

External Quantum Efficiency (EQE) was measured without bias light using a PV Measurement QE system and Internal Quantum Efficiency (IQE) was calculated based on the EQE and reflectance measurements.

Photoluminescence (PL) [116] was measured at open-circuit conditions using a BTi luminescence imaging tool.

Cross-sectional Focused Ion Beam (FIB)/SEM images of the plated Ni/Cu front contacts were taken using a Helios Nanolab 600 tool from FEI.

5.4   Results

Figure 5.4 shows a SEM image of the RIE-textured Si surface of the LDSE solar cell before any further processing.

Figure 5.4 shows a SEM image of the RIE-textured Si surface at $40°$ tilt before any further processing. The nanostructures have a height of $\sim$ 300-500 nm and a distance between the structures of $\sim$ 300-500 nm. The nanostructures are conical-like hillocks randomly distributed across the entire solar cell surface.

The fabricated RIE-textured LDSE solar cells were characterized under 1 sun illumination (1000 W/m^2, AM1.5G). Figure 5.5 shows the measured (J-V)-curve of the best black Si LDSE cell at 1 sun. The short-circuit current density, J_{SC}, is 36.3 mA/cm^2 and open-circuit voltage, V_{OC}, is 624 mV. The power conversion efficiency is 18.1% and the fill factor, FF, is 80.1%.

Figure 5.6 shows the pseudo light IV-curve and Suns-V_{OC} measurement of the best black Si LDSE cell.

The pseudo light J-V-curve and Suns-V_{OC} measurement seen in Figure 5.6 shows that the best black Si LDSE cell has a pseudo fill factor, pFF, of 82.3% and a pseudo power conversion efficiency, pEff, of 18.7% without the effect of series resistance. The high pFF indicates that shunting is low and the pseudo efficiency indicates that series resistance accounts for $\sim$ 0.6% point efficiency loss compared to the actual power conversion efficiency. The linearly increasing relationship between the illumination and V_{OC} seen in the bottom part of Figure 5.6 indicates that neither shunting nor Schottky contacts are significant for the best black Si LDSE cell. This is encouraging considering
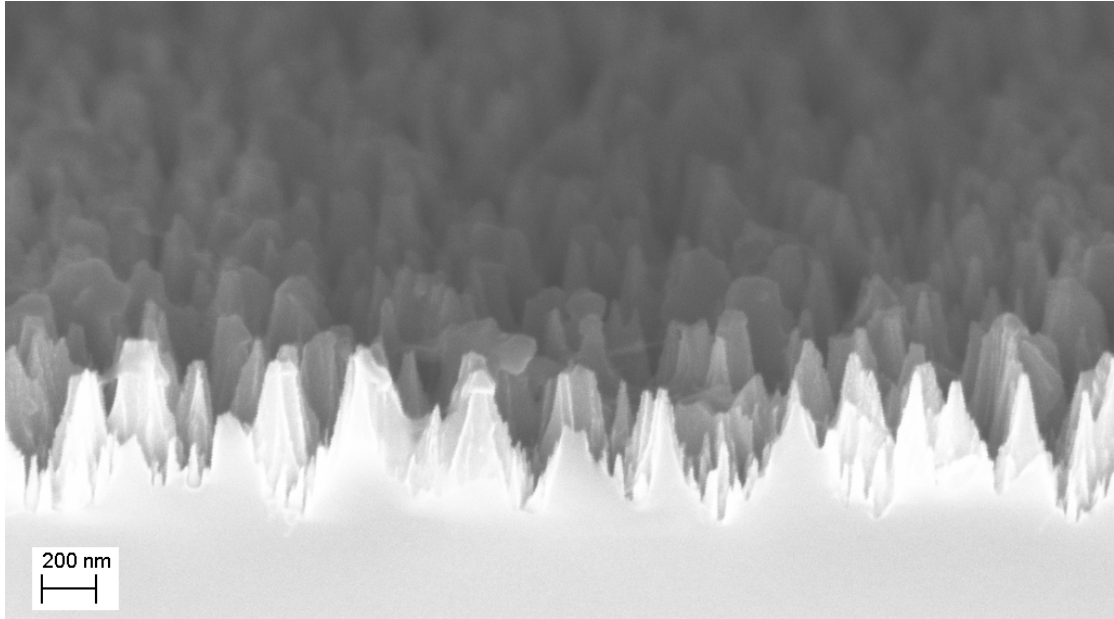
FIGURE 5.4: SEM-image at 40° tilt of the RIE-textured Si surface before any further processing. The nanostructures have a height of $\sim$ 300-500 nm and a distance between the structures of $\sim$ 300-500 nm. The nanostructures are conical-like hillocks randomly distributed across the entire solar cell surface.

the effect texturing may have on laser doping and plating processes, which could lead to increased defect generation. This does not seem to be the case from the Suns-V_{OC} measurement. The increase in V_{OC} for intensities of 6-7 suns compared to the double diode model may be due to saturation of the surface recombination, which dominates the cell performance at 1 sun.

Table 5.1 shows measured J_{SC}, V_{OC}, power conversion efficiency and FF for three different RIE-textured LDSE solar cells processed at three different laser speeds.

RIE-textured LDSE solar cells					
Laser Speed	Efficiency [%]	J_{SC} [mA/cm^2]	V_{OC} [V]	FF [%]	pFF [%]
2m/s	17.5	36.0	0.624	77.9	81.0
3m/s	18.1	36.3	0.624	80.1	82.3
4m/s	17.5	35.8	0.624	78.4	82.0

TABLE 5.1: Power conversion efficiency, short-circuit current density, open-circuit voltage and fill factor at 1 sun illumination (1000 W/m^2, AM1.5G) of conventionally and RIE-textured LDSE Si cells with laser speeds of 2, 3 and 4 m/s, respectively. Furthermore, the pseudo fill factor, pFF, determined by Suns-V_{OC} measurements is given.

The results in Table 5.1 show that the three RIE-textured LDSE solar cells have efficiencies in the range 17.5-18.1%. The differences are primarily due to differences in FF. The different fill factors may be explained by the different laser speeds according to the result in Figure 5.7, which shows Suns-V_{OC} at low injection for the three RIE-textured LDSE cells with different laser speeds.
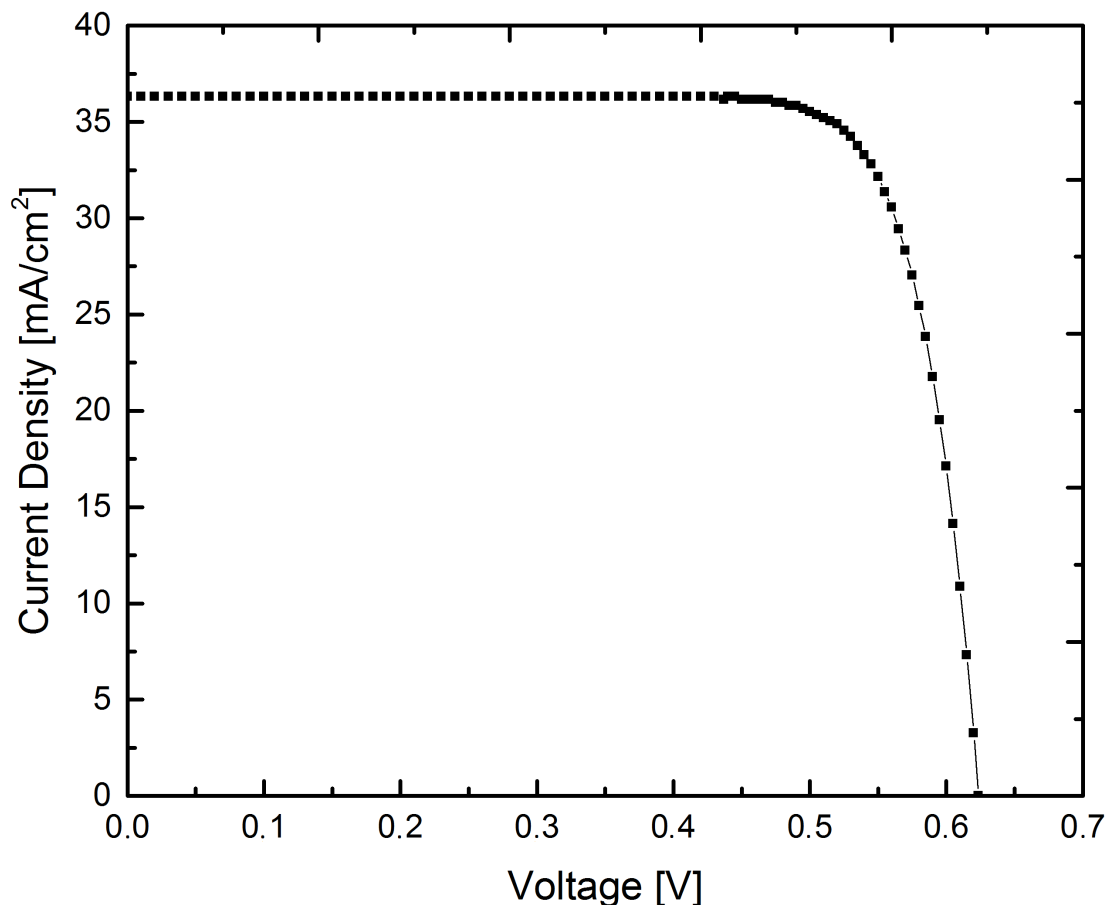
FIGURE 5.5: Current density-voltage characteristic of the best black Si LDSE solar cell under 1 sun illumination (1000 W/m^2, AM1.5G). The short-circuit current density, J_{SC}, is 36.3 mA/cm^2 and open-circuit voltage, V_{OC}, is 624 mV. The power conversion efficiency is 18.1% and the fill factor, FF, is 80.1%

Figure 5.7 shows that a laser speed of 3 m/s leads to the highest open circuit voltage at low injection and an almost linear relationship between V_{OC} and illumination intensity. The cell processed at a laser speed of 2 m/s has significantly lower V_{OC} at low injection and a less linear relationship between V_{OC} and intensity. This is also reflected in the lower pFF of this particular sample.

Figure 5.8 shows the dark-IV curves (semi-logarithmic plot) of the three RIE-textured LDSE cells with different laser speeds. Based on the dark-IV curves in Figure 5.8 the ideality factor of each cell was found: The inverse slope at the linear part of the curve, close to the maximum power point, is 306.2, 72.3 and 94.7 mV/decade for 2, 3 and 4 m/s, respectively. This corresponds to ideality factors of 5.1, 1.2 and 1.6, respectively. Thus, the cell processed at 3 m/s, which had the highest efficiency of the three, is also the closest to an ideal diode, whereas the cell processed at 2 m/s is very far from an ideal diode. The dark IV result confirms the trend of the Suns-V_{OC} measurement in Figure 5.7.

After Ni/Cu-plating it was clear that significant spurious plating had occurred and that the surface had local scratches and pinholes through the dielectric, in which Ni and Cu has plated unintentionally. The top part of Figure 5.9 shows photographs of the finished cells where the plating defects are visible. The bottom part of Figure 5.9
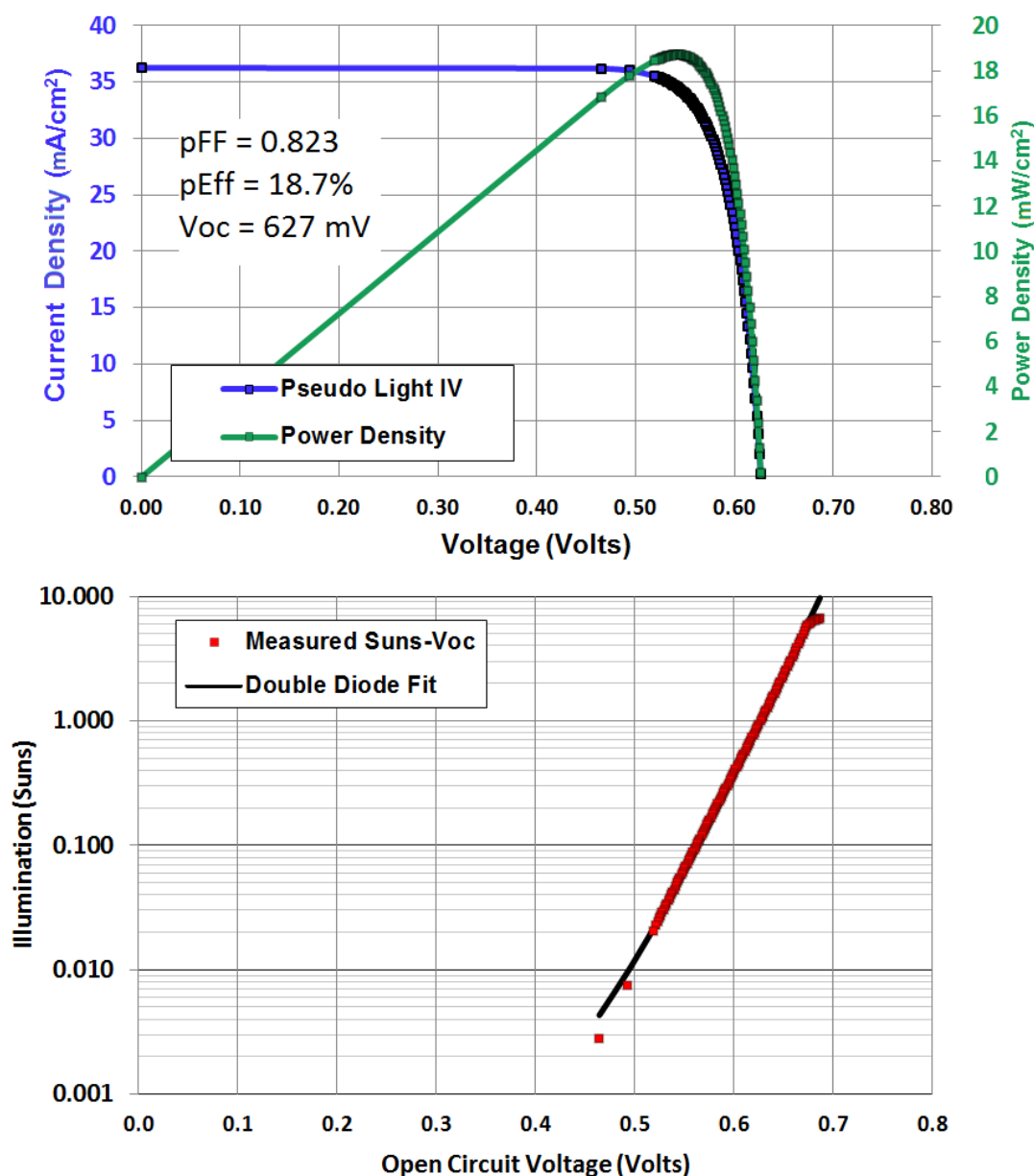
FIGURE 5.6: Result of the Pseudo Light J-V (top) and (bottom) Suns-V$_{OC}$ measurement of the best black Si LDSE cell processed at a laser speed of 3 m/s. The measurement shows a pseudo fill factor, pFF, of 82.3 % and a pseudo efficiency, pEff, of 18.7 % without the effect of series resistance.

shows a SEM-image of the RIE-textured surface of the final cells, where an example of the spuriously plated Ni/Cu is also visible. In order to investigate the lines defined by the laser, optical microscope images were taken. The top image in Figure 5.10 shows an optical microscope image of laser-doped lines on the RIE-textured Si surface. The images in Figure 5.10 were taken at the point where a metal finger intersects the busbar. The laser-scribed lines are approximately 20 μm wide with $\sim$ 5 μm laser damage on each side of the lines. Note that each busbar consists of 10 separate lines about 20 μm wide, spaced $\sim$ 80 μm apart and metallized in the same light-induced plating process as the
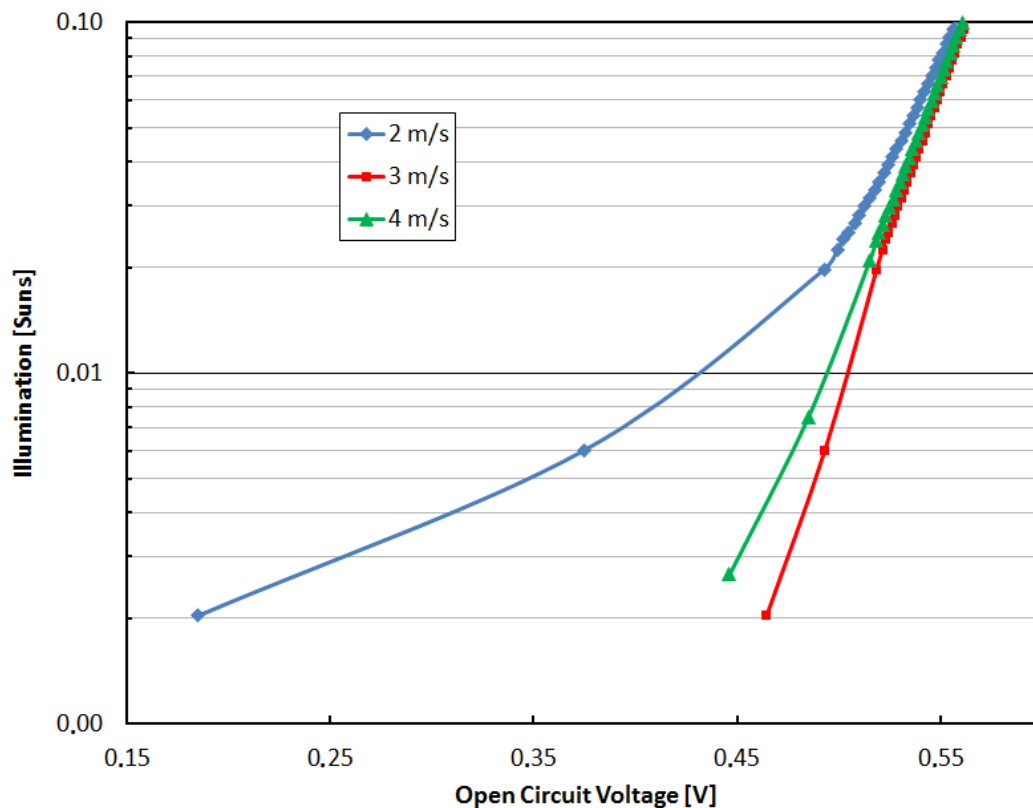
FIGURE 5.7: Suns-V_{OC} measurement at low injection of three black Si LDSE cells processed at laser speeds of 2, 3 and 4 m/s, respectively.

fingers. The middle image of Figure 5.10 shows an optical microscope image of the Ni/Cu-plated metal lines in this case from the busbar lines. It is seen that the plated contacts are between 18 and 28 μm wide. The total contact fraction is ~ 2.5 % of the total cell area assuming 23 μm wide fingers. The bottom image in Figure 5.10 shows a top-view SEM-image of a Ni/Cu-plated line. In the SEM-image an example of spurious metal plating is also seen.

Figure 5.11 shows a SEM-image of the cross-section of a laser-doped line plated with Ni/Cu. The cross-section was defined by a Focused Ion Beam (FIB). The plated metal line is ~ 30 μm wide and ~ 10 μm in height. The layer on top of the Ni/Cu-line is Pt used solely for sample protection during FIB cutting. Note that the black silicon nanostructures can be seen on the sides of the laser-doped line. The nanostructures are not seen in the laser-doped region in the center of the plated Si region, since the Si in this region has been melted and re-solidified during the laser doping process. Figures 5.12 and 5.13 show SEM-images of the interface between the nanostructured Si surface and the plated Ni/Cu at higher magnification.

Figure 5.14 shows EQE and IQE of the complete 18.1% cell and total reflectance of the RIE-textured Si with ~ 75 nm SiN$_x$:H anti-reflective (AR) coating, before any further processing. The IQE is calculated from the measured EQE and reflectance. The IQE plotted in Figure 5.14 might be underestimated, since the reflectance was measured on textured Si with AR-coating but without any metal, while the EQE was measured on the complete cell. The beam spot of the light source of the EQE-measurement was placed between two metal fingers, but any metal present within the beam spot of the
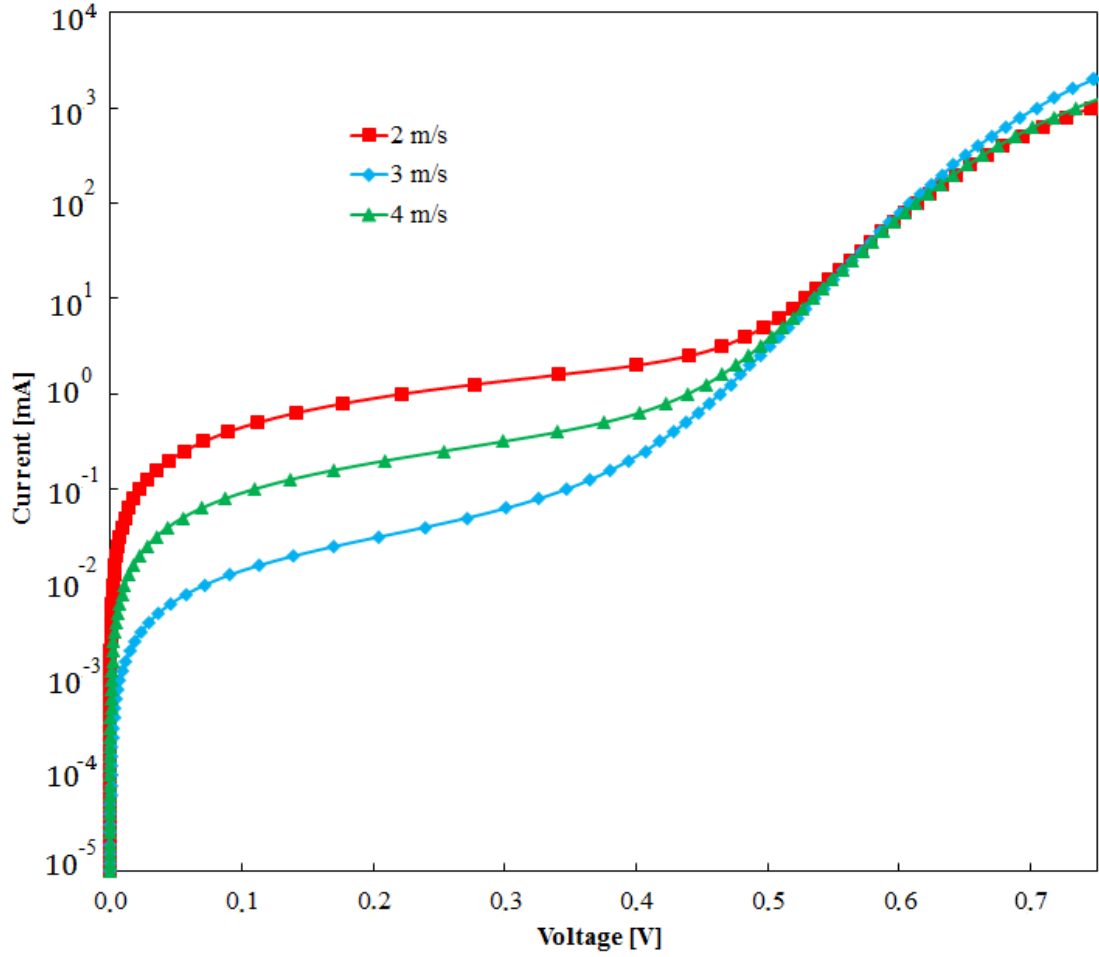
FIGURE 5.8: Dark IV-characteristic of three different black Si LDSE cells.

EQE-measurement, such as spuriously plated metal, will increase reflectance and thus decrease EQE and thereby the calculated IQE, since the reflectance on Figure 5.14 is measured without any metal on the surface. The low IQE for short wavelengths may be due to a too highly doped emitter resulting in increased Auger recombination and may also be due to increased surface recombination at the nanostructured Si surface.

The measured short-circuit current density can be compared to the expected value calculated from the EQE and the solar spectrum to verify consistency in the measurements. Let $E_\lambda(\lambda)$ be the solar spectral irradiance as a function of wavelength λ according to AM1.5G and $Q_{\text{ext}}(\lambda)$ the measured EQE. Then the spectral current density is $J_\lambda(\lambda) = q\lambda E_\lambda(\lambda)Q_{\text{ext}}(\lambda)/(hc)$ since hc/λ is the photon energy and q the unit charge, while h is Planck's constant and c the vacuum speed of light. It follows that the expected short-circuit current density is

$$J_{\text{SC}} = \int_{\lambda_{\min}}^{\lambda_{\max}} \frac{q\lambda}{hc} E_\lambda(\lambda)Q_{\text{ext}}(\lambda)\, \mathrm{d}\lambda. \tag{5.1}$$

A numerical integration using $\lambda_{\min} = 300$ nm and $\lambda_{\max} = 1200$ nm results in the expected short-circuit current density 36.5 mA/cm^2 which is in almost perfect agreement with the 36.3 mA/cm^2 that was measured.

Figure 5.15 shows the total reflectance of the RIE-textured surface with AR-coating
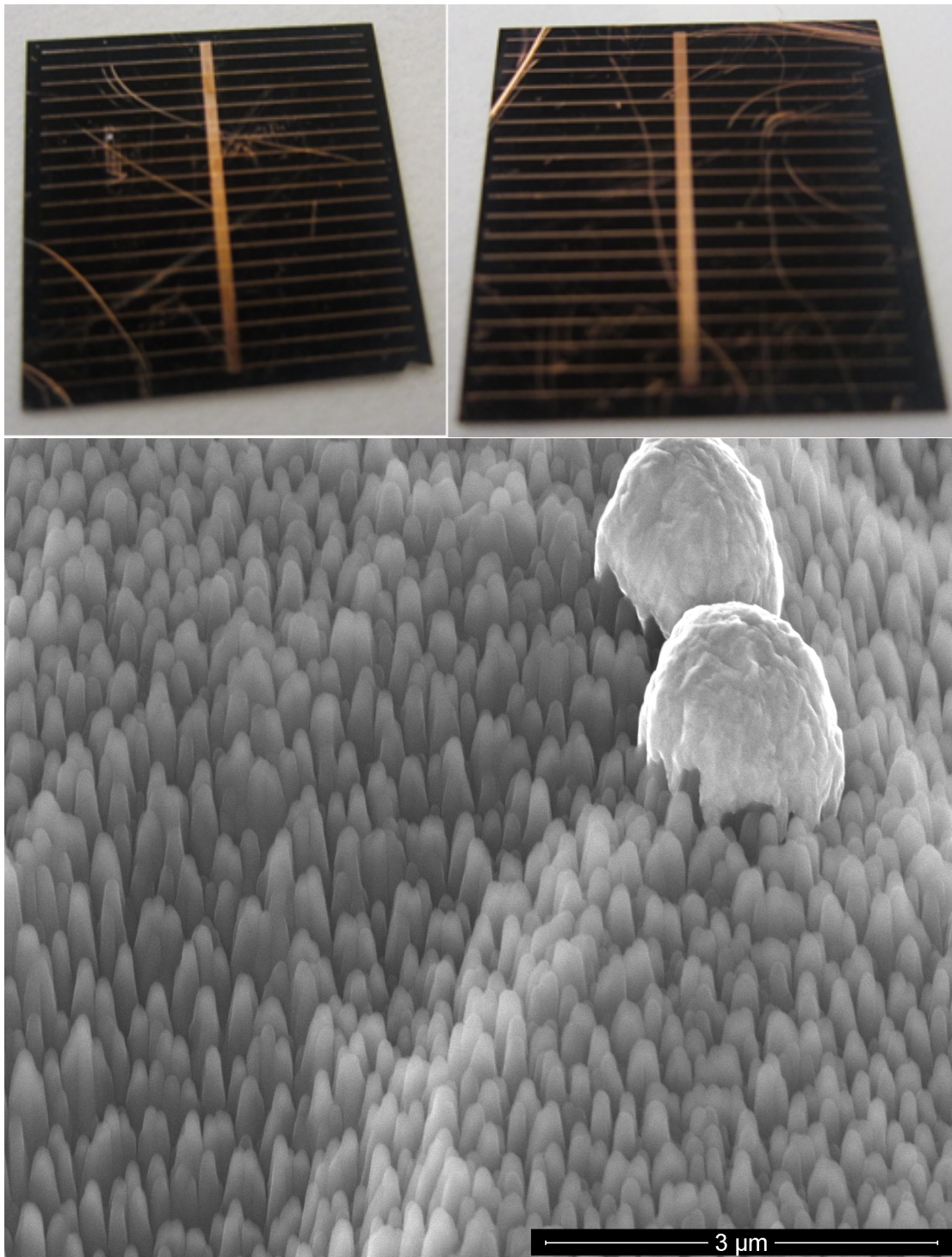
FIGURE 5.9: (Top) Photographs of two of the final black Si LDSE solar cells. The images show significant spurious plating of Ni/Cu and scratches in the front surface. (Bottom) SEM-image at 52° tilt of the RIE-textured surface of the final black Si LDSE solar cell surface. The SEM-image also shows examples of spuriously plated Ni/Cu.
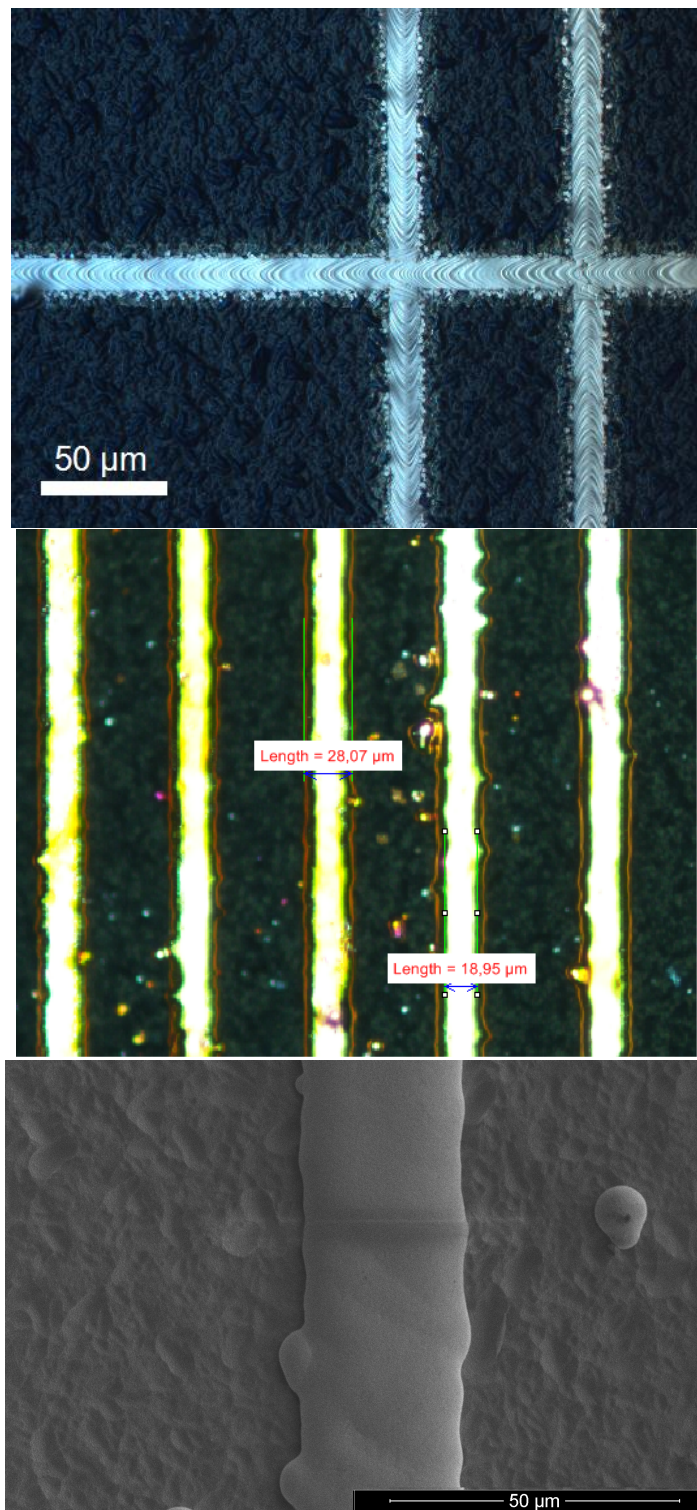
FIGURE 5.10: (Top) Optical microscope image of the laser-doped lines on the black Si front surface before Ni/Cu-plating. (Middle) Optical microscope image showing the width of the Ni/Cu-plated metal lines in this case from the busbar. (Bottom) Top-view SEM-image of a Ni/Cu-plated metal line.
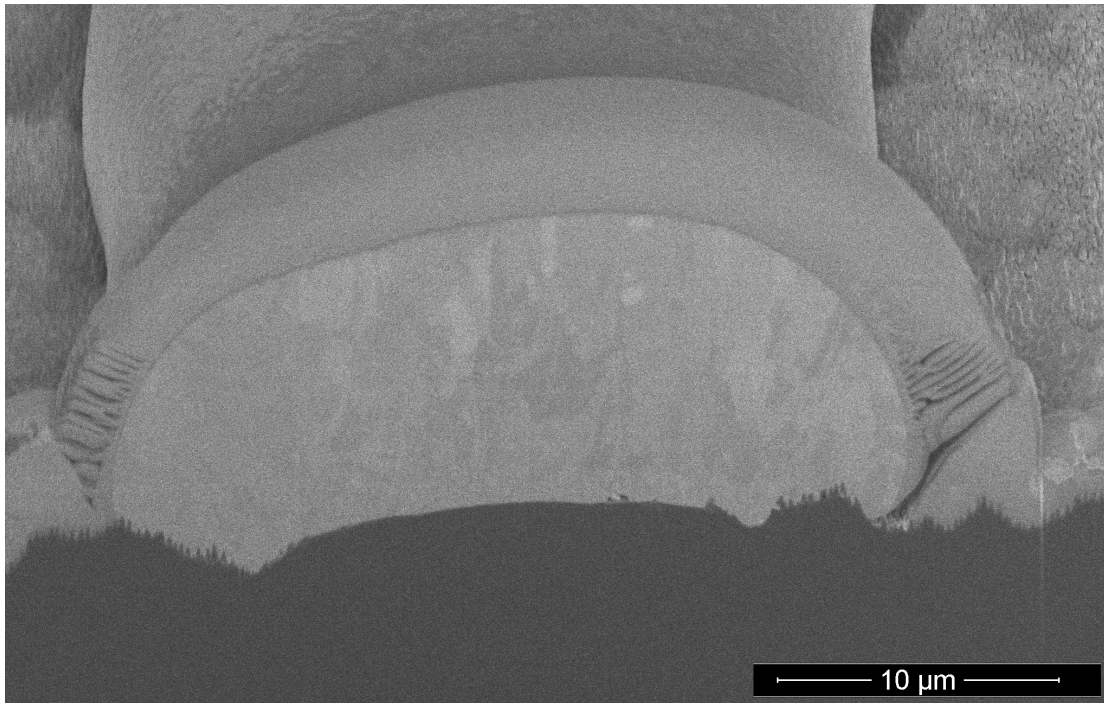
FIGURE 5.11: SEM-image at 52° tilt showing the cross-section of a Ni/Cu-plated metal line. The cross-section was defined by a Focused Ion Beam (FIB). The plated metal line is ~ 30 μm wide and ~ 10 μm in height. The layer seen on top of the Ni/Cu-line is Pt used solely for sample protection during FIB cutting. Note that the black silicon nanostructures are visible at the edges of the plated Ni/Cu line.

before and after Ni/Cu-plating, respectively, as function of wavelength. From Figure 5.15 it is clear that after metal plating the reflectance of the complete cell increases significantly. However, the increase is presumably partly due to the spurious plating seen in Figure 5.9. The beam spot size of the light source in the reflectance measurement was ~ 2 cm in diameter and covered the majority of the cell area including the busbar and metal fingers.

Figure 5.16 shows an open-circuit photoluminescence (PL) image of the 18.1% cell after Ni plating and sintering. The PL-image in Figure 5.16 shows increased recombination at the laser-doped, Ni-plated busbar and fingers, which is expected for Si-metal interfaces. Furthermore, circular points or agglomerations of lower PL-signal intensity can be seen all over the surface. This indicates that the firing temperature used after rear Al screen-printing was slightly too high for the particular samples, leading to a non-uniform back-surface field.

5.5   Discussion

The power conversion efficiency of 18.1% of the black Si LDSE cell fabricated in this work is comparable to the best efficiencies reported to date for front-contacted black Si solar cells [63, 89, 91]. Table 5.2 shows selected cell results reported for black Si solar cells [20]. From Table 5.2 it appears that the cell in this work has superior fill factor compared to existing black silicon cells, while J_{SC} and V_{OC} are on par or slightly reduced compared to [89] and [63]. The impressive efficiency result reported in [92]
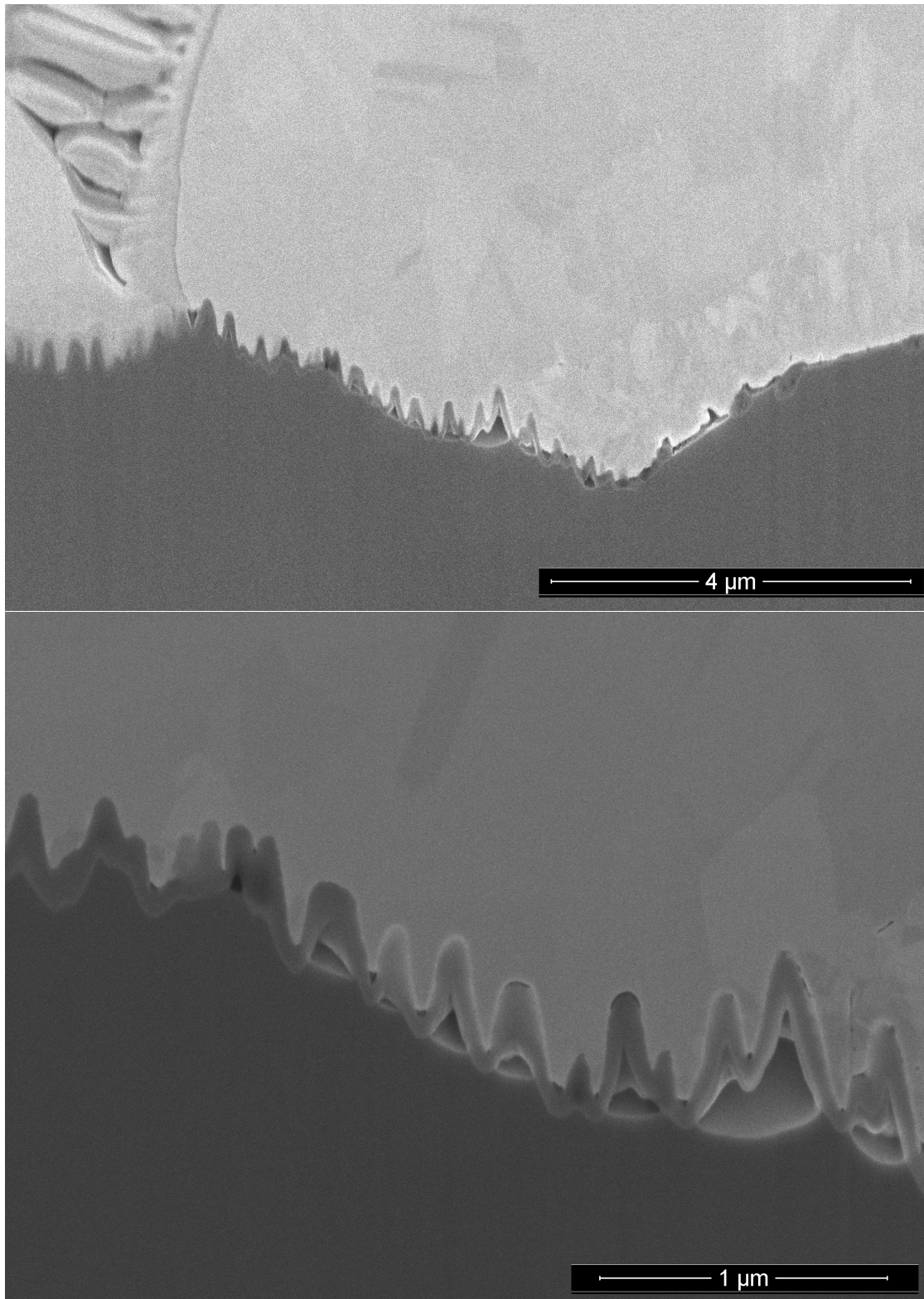
FIGURE 5.12: SEM-images at 52° tilt showing the cross-sectional interface between the RIE-textured Si surface and the plated Ni/Cu at two different magnifications.
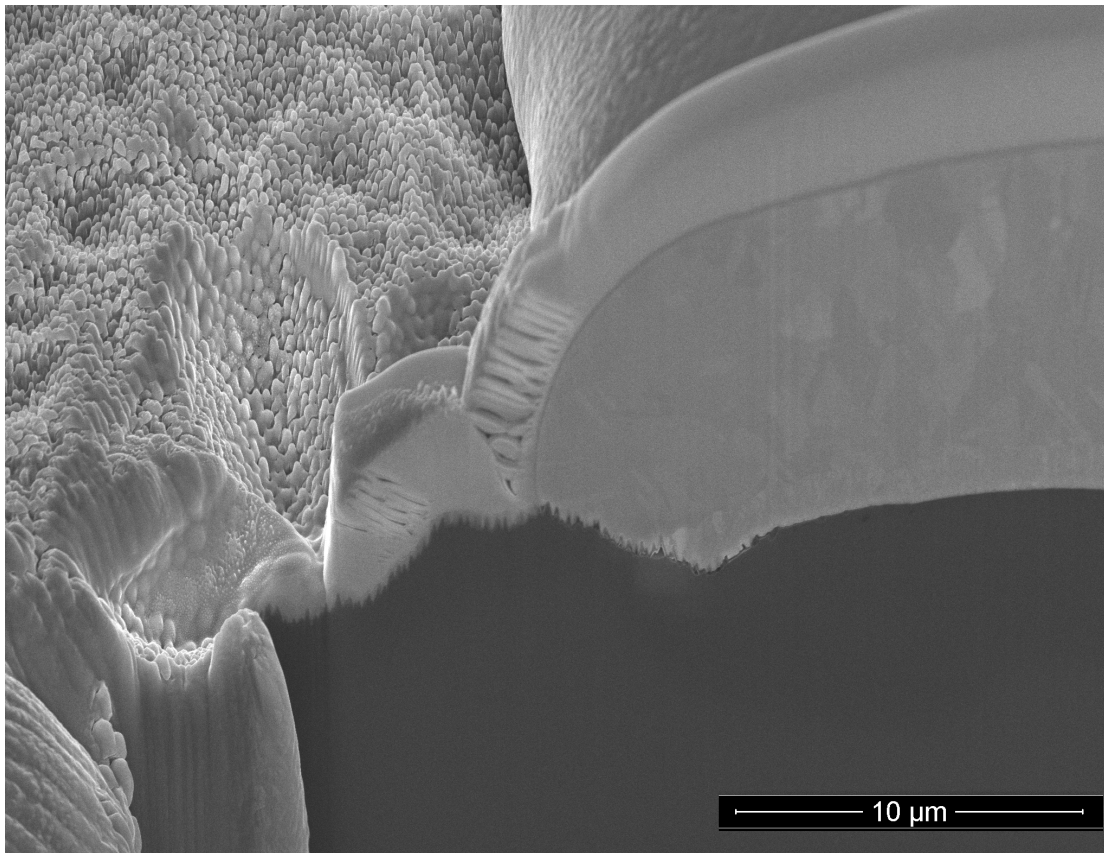
FIGURE 5.13: SEM-image at 52° tilt showing the cross-sectional interface between the RIE-textured Si surface and the plated Ni/Cu line. The nanostructures are seen adjacent to the Ni/Cu-plated line.

State-of-the-art Black Si cell results

Author	Texture	Eff. [%]	J_{SC} [mA/cm^2]	V_{OC} [V]	FF [%]	Cell Type Passivation, Cell Area
This work	RIE	18.1	36.3	0.624	80.1	CZ LDSE SiN$_x$, 6.25 cm^2
Repo *et al.* [89]	RIE	18.7	39.2	0.632	75.8	FZ PERL ALD Al$_2$O$_3$, 4 cm^2
Yoo *et al.* [90]	RIE	16.7	36.8	0.617	76.0	CZ Screen-printed SiN$_x$, 156.25 cm^2
Oh *et al.* [63]	MACE*	18.2	36.5	0.628	79.6	FZ, evaporated contacts Thermal SiO$_2$, 0.8081 cm^2
Wang *et al.* [91]	MACE*	18.2	41.3	0.598	75.1	CZ, evaporated contacts ALD Al$_2$O$_3$, 0.92 cm^2
Savin *et al.* [92]	RIE	22.1	42.2	0.665	78.7	FZ, IBC ALD Al$_2$O$_3$, 78.5 cm^2 (4")

TABLE 5.2: Selected black silicon solar cell results reported in literature. The table shows power conversion efficiency, J_{SC}, V_{OC}, fill factor, type of solar cell and Si substrate. For further details about the cell type we refer to the references.
Metal-Assisted Chemical Etching (MACE).
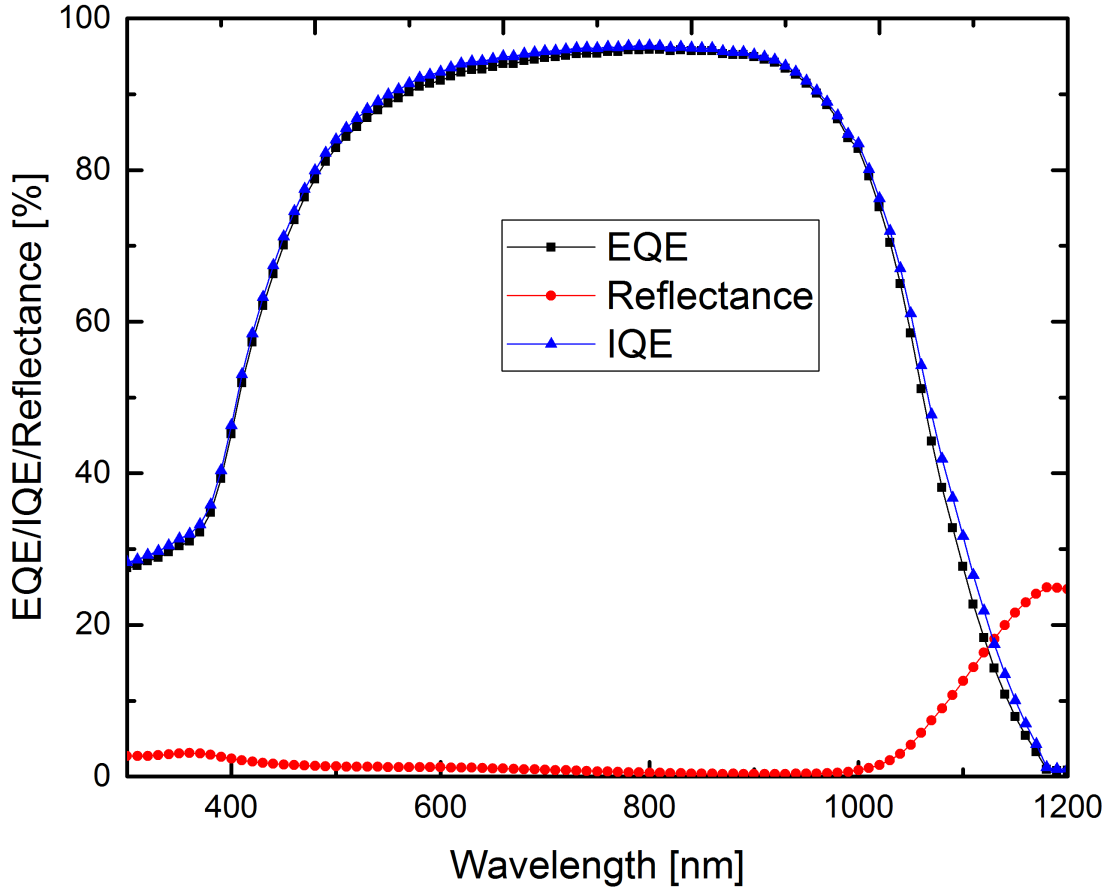
FIGURE 5.14: External and Internal Quantum Efficiency and total reflectance as function of wavelength of the 18.1% black Si LDSE solar cell. The reflectance data are for RIE-textured Si with AR-coating before any further processing. The IQE is calculated based on the measured EQE and reflectance of the surface measured before laser and plating processes. EQE was measured without any bias light.

may be partly explained by the interdigitated-back-contact (IBC) cell design typically resulting in higher J_{SC}. The higher efficiency and V_{OC} reported in [92] and [89] may be partly explained by the use of higher-quality FZ Si material.

The lack of improvement to J_{SC} and V_{OC} of the black Si LDSE cell in this work may be explained by the unintentionally too heavily doped emitter, inadequate surface passivation and the unintentional spurious plating; optimized processing is thus expected to improve both key parameters significantly. The very high fill factor on the other hand is due to a near optimum laser power and scan speed used during laser doping of the best device, resulting in very low contact resistance. We note that the optimum laser doping conditions are different from those on planar silicon probably due to stronger coupling of the laser power into the structure.

In general, this result is encouraging considering that industrial grade CZ Si wafers were used and that the complete cells in this work were not fully optimized: First of all the cells had significant spurious plating as shown in Figure 5.9. This induces a direct loss of current, since the reflectance of the complete cells is significantly higher than a similar cell without spurious plating. The reflectance difference is shown in Figure 5.15
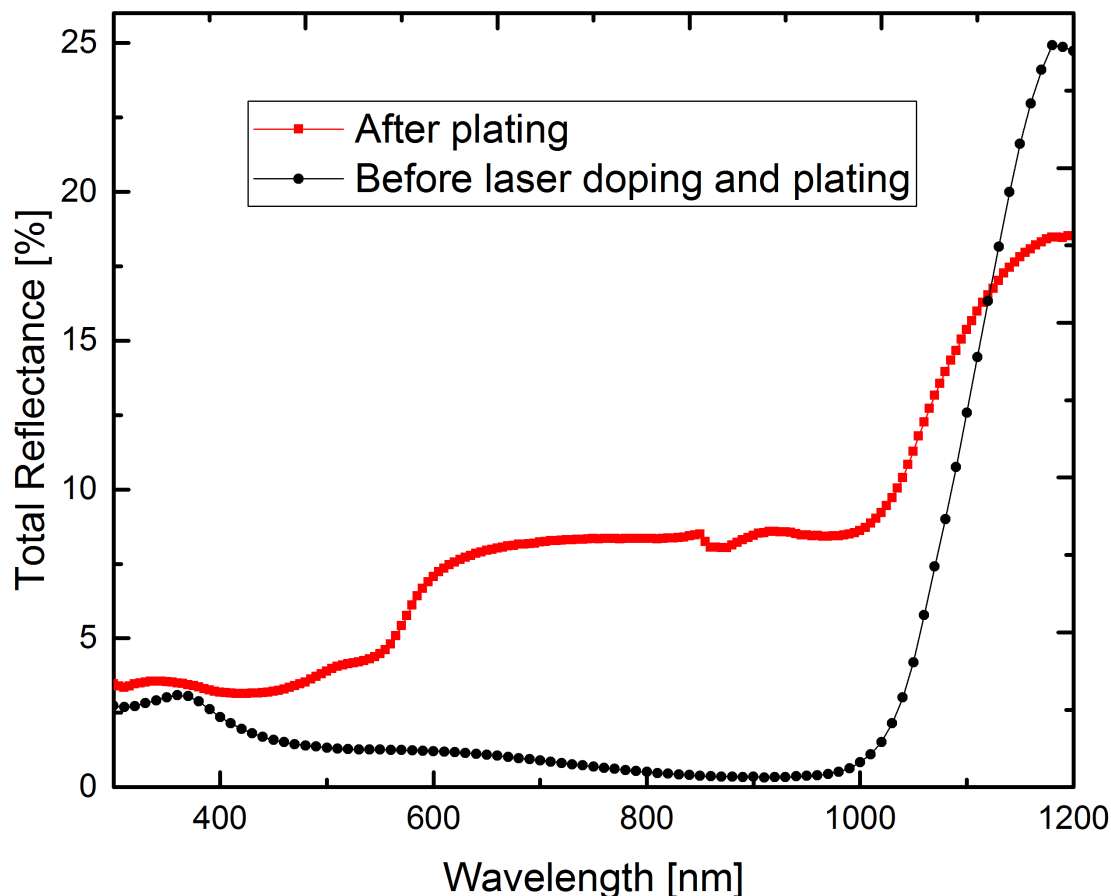
FIGURE 5.15: Total reflectance of the RIE-textured Si surface with AR-coating before and after laser doping and Ni/Cu-plating, respectively, as function of wavelength. The beam spot size of the light source was ~ 2 cm in diameter and covered the majority of the cell area including the busbar and metal fingers.

and the additional average reflectance in the range 300-1000 nm attributed only to spurious plating can be estimated by the following considerations: The average integrated reflectance in the range 300-1000 nm is 1.20% before plating and 6.38% after plating. The front contact grid only covers $\sim 2.5\%$ of the cell area assuming 23 μm wide fingers. Based on the metal grid coverage the grid itself only accounts for additional reflectance of $\sim 1.23\%$ assuming 50% reflectance of Cu in the wavelength range 300-1000 nm. The spurious plating must account for the difference between the additional reflectance after plating and reflectance from the grid. Thus the spurious plating accounts for $\sim 3.95\%$. This is a direct reflection loss, which can be at least partly avoided by minimizing spurious plating. Furthermore, spurious plating in scratches such as seen in Figure 5.9 is likely to cause increased surface recombination, since the plated metal contacts directly to a lightly doped emitter, which shields minority carriers less than a heavily doped emitter, thus causing enhanced recombination at the metal-Si interface. It is however encouraging that the Suns-V_{OC} measurement in Figure 5.6 does not indicate any increased defect generation or Schottky contact formation.

The Suns-V_{OC} result in Figure 5.7 indicates the relationship between laser speed and pseudo FF. From the result in Figure 5.7 it seems that 3 m/s leads to the most ideal performance, ultimately leading to a higher FF and power conversion efficiency than the cells processed at 2 and 4 m/s, respectively. The lower V_{OC} at low injection
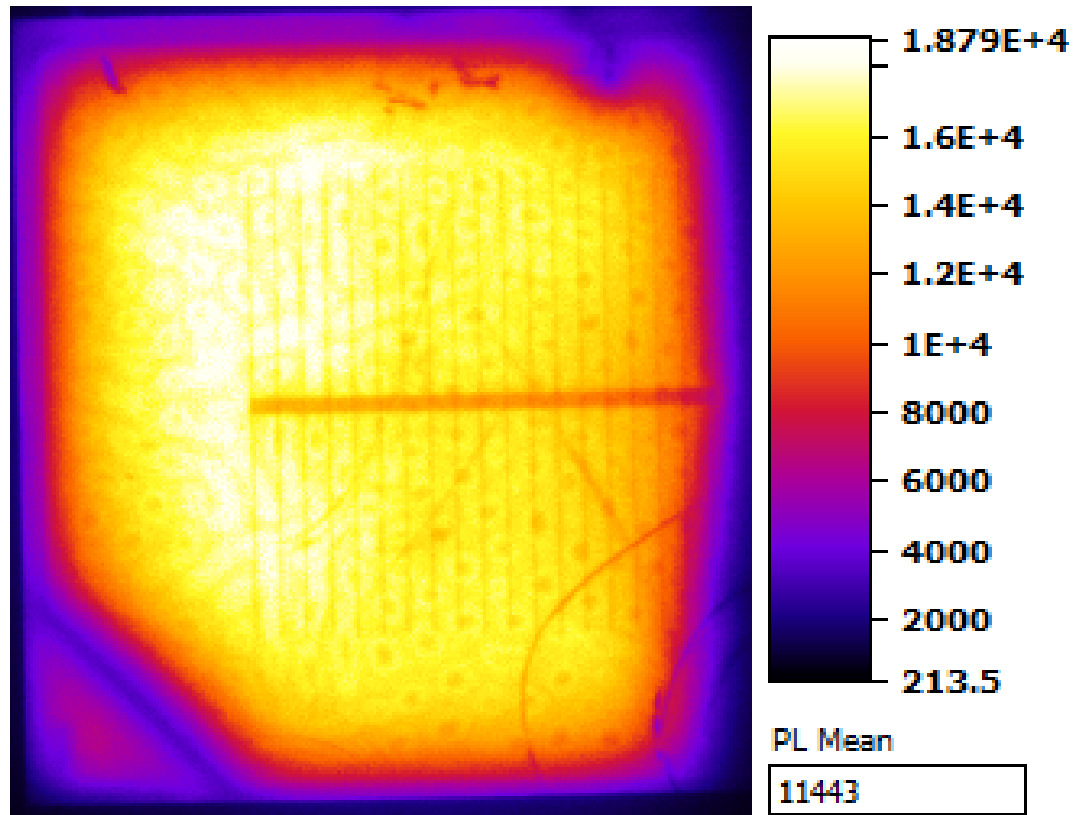
FIGURE 5.16: Open-circuit Photoluminescence (PL) image of the cell after Ni plating and sintering, but before Cu plating and edge isolation. The feature in the bottom left corner of the image is due to the shape of the screen-printed Al on the rear.

for the cell processed at 2 m/s may be due to increased laser damage at the slower scan speed leading to increased SRH recombination in the laser doped regions. The pseudo FF of the cell processed at 4 m/s is almost as high as for 3 m/s. However, the FF is still significantly lower, which indicates that the problem for this cell is rather series resistance. This may be due to a lighter doping caused by the faster scan speed. Thus, it seems that a laser speed of 3 m/s is close to the optimal compromise between minimized laser damage and minimized series resistance for RIE-textured laser-doped solar cells.

Assuming that the spurious plating is due to pinholes and other non-uniformities in the dielectric AR-coating, the problem could be minimized by increasing the thickness of the SiN_x:H layer. The layer may be even thinner than expected, because the deposition rate in the PECVD process may not be the same for RIE-textured Si compared to conventionally textured Si. Even a non-uniform layer would not induce spurious plating as long as the dielectric layer is completely covering the Si surface with sufficient thickness to completely isolate the surface from the plating electrolyte. It is assumed that the required pretreatment using hydrofluoric acid (HF) immediately prior to Ni plating further increases the risk of pinholes, since the SiN_x:H coating is etched by HF to some degree. A negative effect of increasing the SiN_x:H thickness could be increased reflectance and parasitic absorption in the AR-coating. However, the AR-properties of the SiN_x:H coating are less critical on RIE-textured Si, due to the very low reflectance from the black Si surface itself. The increased absorption in the AR-coating could be

minimized by adjusting the layer thickness and the HF process in order to minimize pinholes, while maintaining an acceptably low parasitic absorptance in the AR-coating.

The phosphorus emitter was too heavily doped resulting in a sheet resistance of 40 Ω measured with a 4-point probe after phosphorus diffusion. This was unintentional, since the full area sheet resistance of such selective emitter should ideally be on the order of 100 Ω, which was also measured on planar Si reference wafers from the same diffusion process. This suggests that the decreased sheet resistance is due to faster diffusion of dopant atoms through the nanostructured Si surface. By decreasing time and temperature of the diffusion process, we expect to improve the emitter in future studies. From the QE measurement seen in Figure 5.14 a significant decrease in EQE and IQE is seen for wavelengths below 600 nm. This indicates significant emitter and surface recombination, which is expected from black Si, if the surface is not well passivated. Since a standard SiN_x:H AR-coating was used as the only passivation layer on these cells, it is expected that the short wavelength response can be significantly improved in future studies by optimizing the SiN_x:H coating or by applying different dielectric coatings.

From the PL-image in Figure 5.16 small circular structures with slightly lower PL-signal can be seen. We suggest that this is due to a too high firing temperature used for rear Al screen-printing on these particular samples. We expect this to be improved in future studies.

By combining the potential improvements mentioned above significantly higher power conversion efficiency of this new kind of cell structure is expected. This will be investigated in future studies.

Chapter 6

Emitter and Passivation

6.1 Passivation by Atomic Layer Deposition

The primary drawback of black Si is the high surface recombination velocity resulting from the large surface area of the nanostructures and the plasma damage after texturing. In order to reduce the surface recombination velocity good passivation of the Si surface must be obtained. Based on the IQE and calculated current loss of black Si cells passivated with conventional SiN_x:H AR-coating as presented in Chapters 4 and 5, it appears that standard SiN_x:H passivation is not sufficient to fully solve the issue of increased surface recombination. Several groups have reported excellent passivation [104–108] and promising cell results [112] on Si and black Si [109, 110], respectively, using Al_2O_3 deposited by atomic layer deposition (ALD). Specifically, Otto *et al.* [109] reported 1.475 ms effective minority carrier lifetime at an injection level of 5×10^{15} cm^{-3} corresponding to a surface recombination velocity (SRV) of 13 cm/s for black Si passivated by ALD Al_2O_3. For comparison Otto *et al.* measured SRV of 12 cm/s for the planar Si reference, meaning that the normally increased surface recombination for black Si was successfully suppressed. Similarly, Savin *et al.* [110] reported SRV values between 9 and 22 cm/s for ALD-passivated black Si depending on resistivity and calculation methods. von Gastrow *et al.* [111] reported SRV values below 7 cm/s at an injection level of 1×10^{15} cm^{-3} for black Si surfaces passivated by ALD Al_2O_3. It should be noted that these values are strongly injection dependent and that minority carrier lifetime typically decreases with increasing injection.

In ALD the material deposition happens one atomic layer at a time, since the deposition method is completely surface-controlled. Thus, by first saturating the Si surface with one precursor (tetra-methyl-aluminium (TMA) in the case of Al_2O_3 deposition) and then introducing a second precursor (an oxidizer such as water or ozone), exactly one atomic layer of the reaction product (Al_2O_3 in the case of TMA and H_2O as precursors) is deposited. By purging the chamber and repeating this cycle a number of times, a given layer thickness can be deposited with a precision of ~ 1 Å. Figure 6.1 shows an ellipsometer measurement of the Al_2O_3 thickness distribution across a polished 4" Si wafer after 300 ALD cycles. Figure 6.2 shows a SEM-image of black Si passivated with Al_2O_3 deposited by ALD. Presumably there are two explanations behind the excellent passivation of black Si using ALD Al_2O_3:
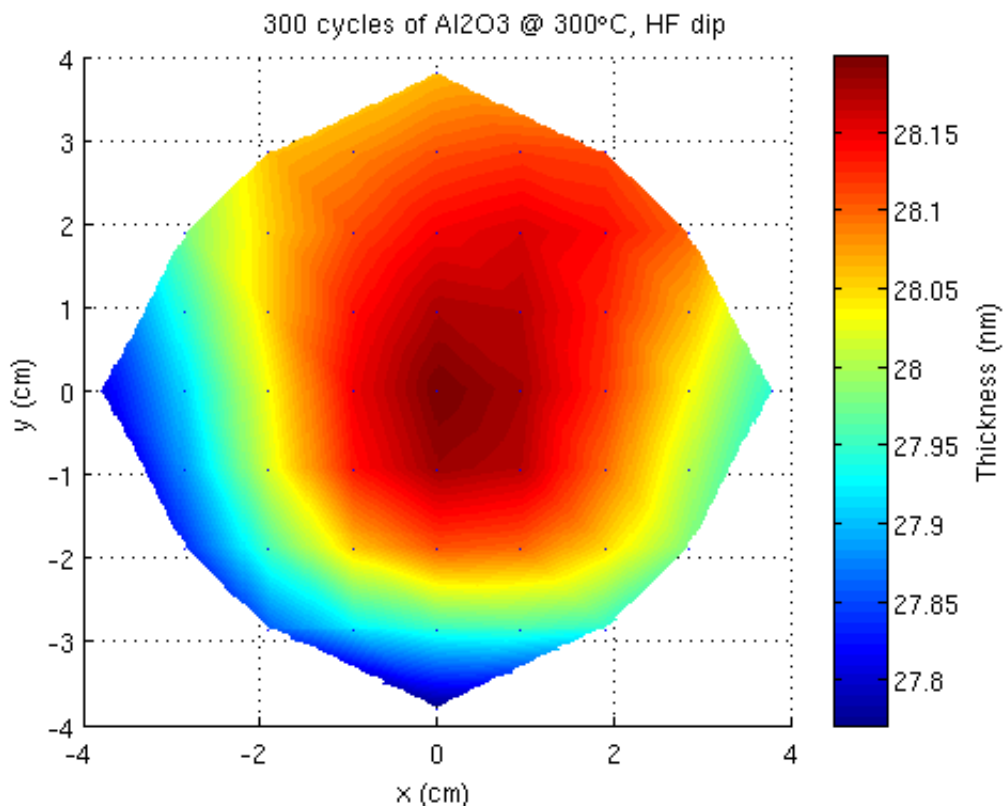
FIGURE 6.1: Ellipsometer measurement of the Al_2O_3 thickness distribution across a polished 4" Si wafer after 300 ALD cycles. The thickness varies 0.35 nm across the entire wafer and the deposition rate is 0.9 Å per cycle.

- Conformal coating of the nanostructured topology due to the deposition of a single atomic layer at a time.

- Passivation contributions from both chemical passivation and field-effect passivation due to the negative fixed charges in Al_2O_3.

In this project, a series of different ALD passivation tests were performed on black Si surfaces and planar Si surfaces for comparison. Different process parameters such as layer thickness, deposition temperature, oxidising precursor and post-annealing temperature were varied. Two different ALD systems were used; Picosun ALD R200 (DTU) and Cambridge Nanotech Savannah S100 (UNSW), and the resulting test structures were characterized by microwave photo-conductance decay (μ-PCD, Semilab WT-2000) at Aarhus University and quasi steady-state photo-conductance decay (QSSPC, WCT-120 Sinton Instruments) at UNSW, respectively. Figure 6.3 shows the typical output from μ-PCD lifetime measurements; a colour graph of the measured minority carrier lifetime across the wafer. The advantage of the μ-PCD measurement is the spatial resolution, which enables identification of localized defects or contamination that affect the measured average lifetime. The advantage of QSSPC is the ability to vary the carrier injection level and directly get calculated values for saturation current density, j_0, and implied open-circuit voltage, iV_{OC}, which the Sinton tool automatically outputs. iV_{OC} may be extracted directly from QSSPC-measurements, since the excess carrier
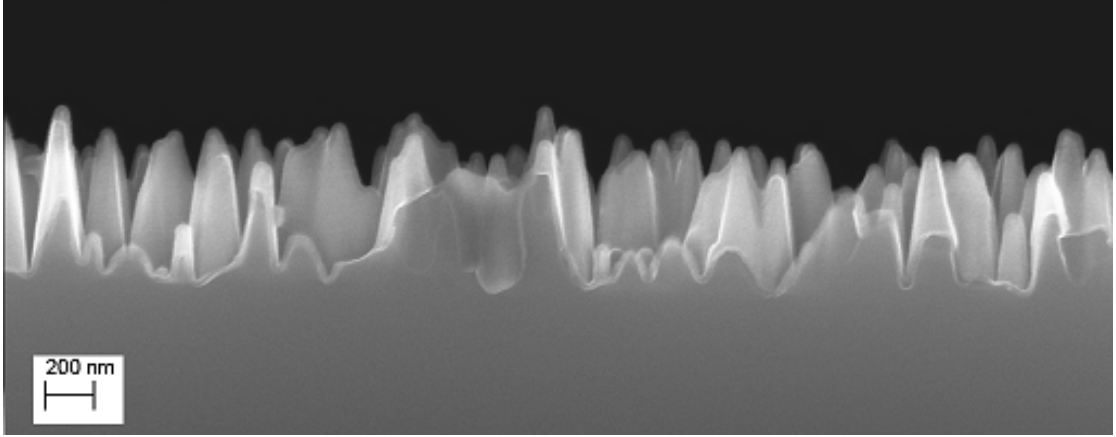
FIGURE 6.2: SEM-image showing a black Si surface passivated with Al_2O_3 deposited by ALD. The image illustrates the conformal covering of the nanostructures achieved by ALD. The Al_2O_3 can be seen as a slightly lighter colour on top of the nanostructures.

generation is given by [122]

$$\frac{(\Delta n + N_A)\, \Delta n}{n_i^2} = e^{q(iV_{OC})/kT},\tag{6.1}$$

which enables the determination of implied voltage at different excess carrier concentrations. In practice, iV_{OC} is extracted at 1 sun light intensity on a graph similar to the graph in Figure 6.4 (bottom, left). The saturation current density, j_0, similarly relates directly to the excess carrier density and the measured effective lifetime by re-arranging equation 2.11 [123] such that

$$\frac{1}{\tau_{eff}} = 2\frac{j_0}{qW}\left(\frac{N_A + \Delta n}{n_i^2}\right) + \frac{1}{\tau_b},\tag{6.2}$$

where W is the wafer thickness.

Injection level may also be varied in μ-PCD measurements, but in this project the two methods were used in a complementary way in order to investigate injection dependence with QSSPC and spatial variations with μ-PCD measurements. Figure 6.4 shows a typical output from a Sinton QSSPC lifetime measurement. When comparing measured lifetimes from μ-PCD and QSSPC, respectively, it is important to consider the injection level, since lifetime is strongly dependent on injection level as shown in Figure 6.4. In the case of QSSPC the average lifetime was extracted at a carrier injection level of 2×10^{16} cm^{-3}. This injection level was chosen, because the measured inverse lifetime curves gave the best linear fit as function of minority carrier density at this value for most samples. Such linear fit is needed in order to extrapolate the saturation current density, j_0, and implied open-circuit voltage, iV_{OC} [65, 113] according to equation 6.1 and 6.2. The average injection level for μ-PCD was 1.5-1.9 $\times$ 10^{16} cm^{-3}. The average lifetime from μ-PCD measurements is the spatial average over a full 4" wafer.

A third option for characterizing the lifetime is photoluminescence (PL) measurements that give the spatial resolution like μ-PCD. Figure 6.5 shows an example of a PL measurement on ALD-passivated black Si. The image in Figure 6.5 shows how
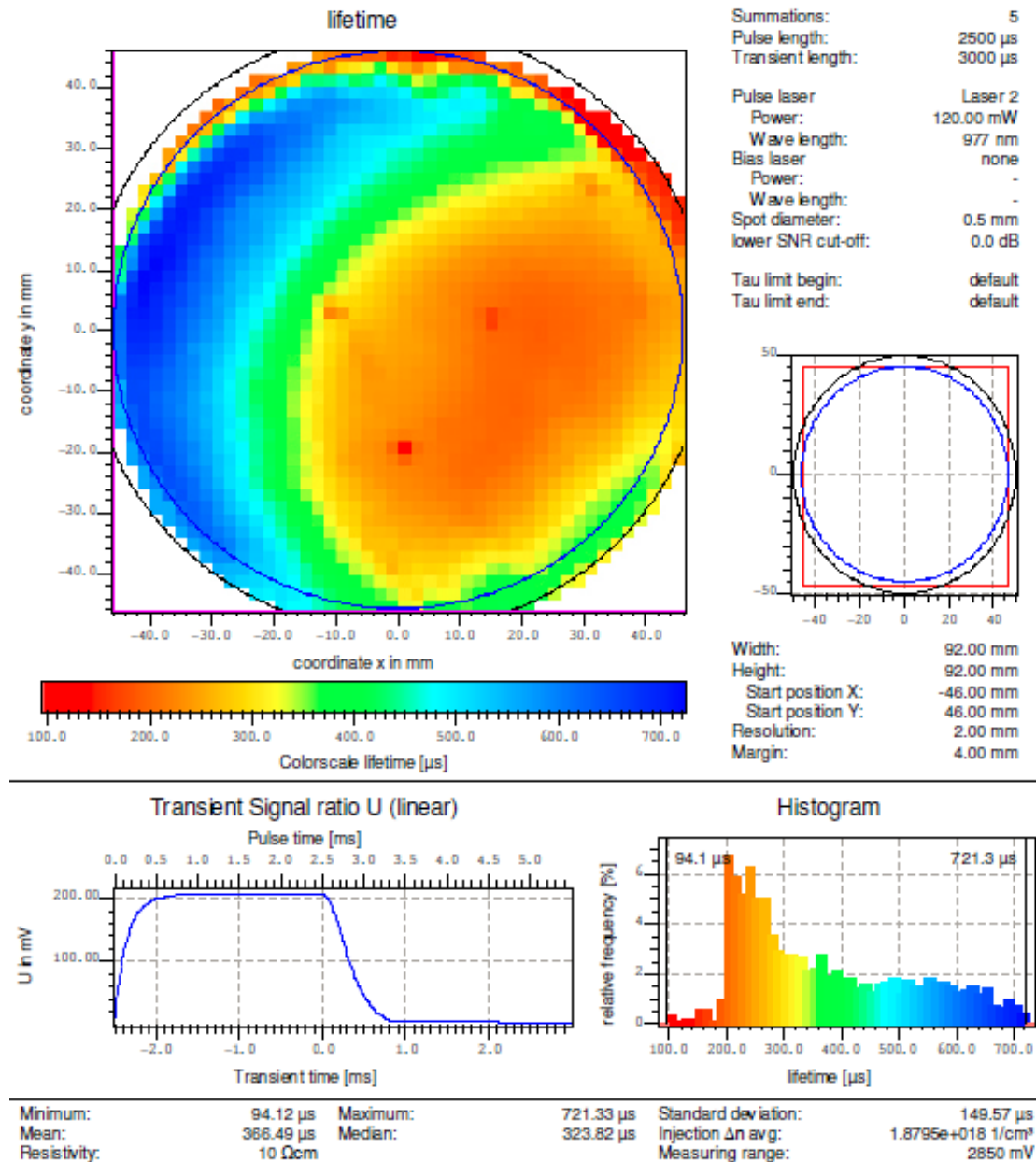
FIGURE 6.3: Example of the output from μ-photoconductance decay measurement of the minority carrier lifetime of an ALD-passivated black Si sample. The color graph in the upper left corner shows the spatial distribution of measured lifetimes across a 4" wafer. The smaller graphs in the bottom show the statistical distribution of measured lifetimes.

PL may be used to identify spatial variations in lifetime and overall solar cell performance. The PL signal scales with the effective lifetime and implied open-circuit voltage [65, 113, 114, 116], since the PL intensity, I_{PL}, is related to the separation of the quasi Fermi levels, $\Delta\eta$, according to [114, 115].

$$I_{\mathrm{PL}} \propto r_{\mathrm{sp}} = \frac{n_{\mathrm{r}}^2}{\pi^2 \hbar^3 c^2} \int_0^\infty (\hbar\omega)^2 \alpha_{BB}(\hbar\omega) \exp\left(\frac{-\hbar\omega}{kT}\right) \exp\left(\frac{\Delta\eta}{kT}\right) d(\hbar\omega), \qquad (6.3)$$

where r_{sp} is the rate of spontaneous emission, n_{r} is the refractive index, α_{BB} is the black-body absorptivity and ω is the angular frequency. Equation 6.3 is analogous to
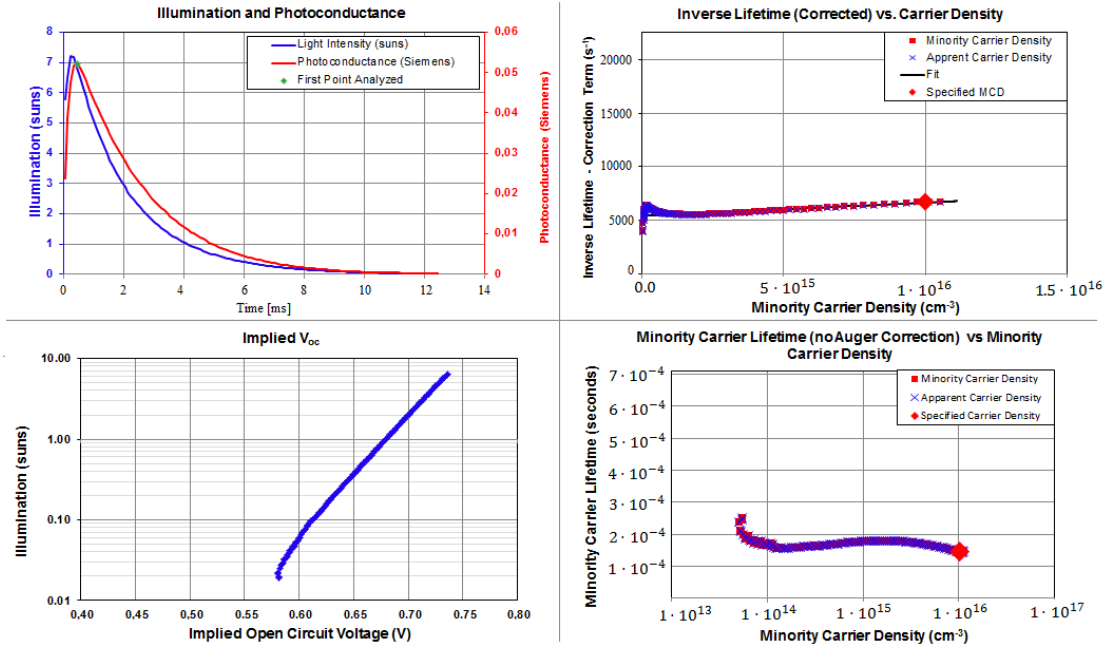
FIGURE 6.4: Example of the output from a quasi-steady state photoconductance (Sinton WCT-120) measurement of the minority carrier lifetime of an ALD-passivated black Si sample. The graph in the upper left corner shows the measured photoconductance as a function of time. The upper right graph shows the inverse carrier lifetime as function of the minority carrier density. The bottom left graph shows the calculated implied open-circuit voltage as function of illumination and the bottom right graph shows the minority carrier lifetime as function of carrier density (injection).

equation 2.19, which relates the EQE of the solar cell to its luminescence emission, but given here in terms of the separation of quasi Fermi levels, $\Delta\eta$, integrated over all angular frequencies representing the entire wavelength range, which is more applicable for semiconductor materials that are not necessarily complete solar cells.

In this case the ALD-passivated black Si wafer in Figure 6.5 clearly has a defect in the bulk or a scratch in the passivation layer, which affects the spatially averaged effective lifetime.

Throughout this project several batches of polished and black Si test wafers passivated with ALD Al_2O_3 have been fabricated and characterized. Since the objective of this work is to optimize the passivation of black Si, the focus in this chapter will be on the obtained carrier lifetimes and how these compare with results from the literature and other passivation techniques such as the 'standard' passivation of industrial Si solar cells; SiN_x:H deposited by PECVD. These results are based on a more detailed optimization of ALD-passivated black Si done primarily by Manuela Heiss [117], but only selected results will be presented here for clarity. However, a few key conclusions from this work are:

- A layer thickness of 30 nm Al_2O_3 is needed to passivate black Si. Thicker layers do not further reduce surface recombination.
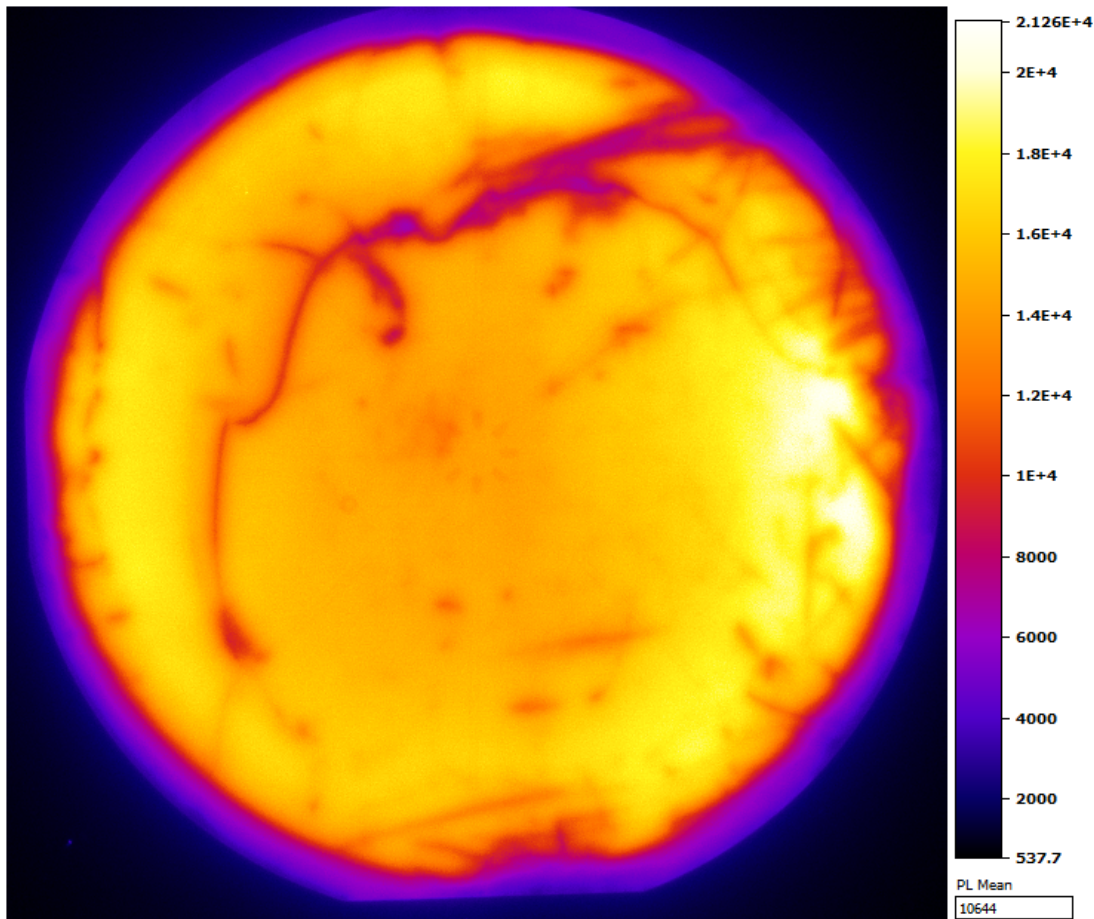
FIGURE 6.5: Example of the output from a photoluminescence (PL) measurement of an ALD-passivated black Si sample.

- Water seems to be a better choice compared to ozone as oxidizing precursor in the ALD process. This may be due to issues with the specific ALD system used in this work and may differ for other ALD systems.

- Using RCA1[1] as pre-cleaning immediately prior to the ALD process yields better passivation than a full RCA clean and better than no pre-cleaning at all.

- Removal of native oxide by buffered HF immediately prior to the ALD process increases surface recombination compared to samples without any HF pre-cleaning. It seems the native oxide plays a crucial role in the passivation quality.

- The optimal deposition temperature is 200 °C for p-type Si and 150 °C for n-type Si.

- Annealing for 15 min in N_2 atmosphere significantly improves the passivating effect. Annealing temperature of 350-375 °C is optimal. Later studies have indicated that 400-425 °C yields better results, so it seems the ideal annealing temperature depends on the annealing method and tool.

---

[1]RCA = Radio Corporation of America. A full RCA clean consists of RCA1 and RCA2, both performed at a temperature of 80 °C for 10 minutes, plus intermediate HF and water rinsing steps. RCA1 consists of NH_4OH, H_2O_2 and water, while RCA2 consists of HCl, H_2O_2 and water.

It should be stressed that these conclusions are solely based on the optimization done in this work using a specific ALD tool (Picosun R200 at DTU) and with a focus on optimized passivation of black Si. Thus the conclusions may not be generalized and used in other cases. The ALD systems used in this work are thermal ALD. Plasma ALD should also be investigated for comparison, but this was out of the scope of this work.

Table 6.1 lists the selected samples used in the passivation tests summarized in Table 6.2. All ALD samples were symmetric test samples passivated by Al_2O_3 on both sides; as deposited in the chamber. Table 6.2 presents an overview of the obtained results on average and maximum minority carrier lifetime results for selected black Si (bSi) samples passivated by ALD Al_2O_3 and PECVD SiN_x:H, respectively. The table further shows average and minimum surface recombination velocity (SRV), implied open-circuit voltage (iV_{OC}) and saturation current density (j_0)[2] calculated directly from the measured lifetimes.

Sample	ρ [Ω cm]	Type	W [μm]	Passivation	Deposition Tool
1	$5^{\dagger}$	CZ n ssp*	525	30 nm Al_2O_3	Picosun
2	$5^{\dagger}$	CZ n bSi ssp	525	30 nm Al_2O_3	Picosun
3	$5^{\dagger}$	CZ p bSi ssp	525	30 nm Al_2O_3	Picosun
4	$5^{\dagger}$	CZ n bSi ssp	525	30 nm Al_2O_3	Picosun
4'	$1.6^{\dagger}$	CZ n bSi ssp	525	30 nm Al_2O_3	Picosun
5	1.6	CZ p bSi np**	195	30 nm Al_2O_3	Cambridge
6	$5^{\dagger}$	CZ n bSi ssp	525	30 nm Al_2O_3	Picosun +
				+ 45 nm SiN_x:H	SPTS PECVD
7	$5^{\dagger}$	CZ p bSi ssp	525	60 nm SiN_x :H	SPTS PECVD
8	1.6	CZ p bSi np	195	50 nm Al_2O_3	Cambridge

TABLE 6.1: Overview of selected black Si samples passivated by different ALD and PECVD systems, respectively. The table shows the measured (or assumed) wafer resistivity, ρ, the Si wafer type and thickness, W, the passivation layer and the deposition tool. Note that sample 4' is sample 4 but with a different assumed resistivity for comparison.
*ssp = single-side polished
** np = non-polished
† assumed resistivity.

The results in Table 6.2 generally show significantly higher lifetimes of ALD Al_2O_3 on black Si compared to the conventional PECVD SiN_x:H (sample 7). However, the non-textured (polished), ALD-passivated sample 1 still has higher lifetime than the best of the ALD-passivated black Si samples. This is expected in any case, due to the larger and more defected surface, as discussed previously. Yet, minimum SRV values for some black Si samples are comparable to the average and minimum value of the polished reference sample. This indicates that spatial variations may account for part of the observed difference. Note that the absolute values of lifetime are strongly dependent on wafer thickness. Therefore SRV is a better and more comparable measure of the

---

[2]Implied open-circuit voltage and saturation current density was only calculated for the QSSPC measurements, since carrier injection was not varied in μ-PCD measurements.

Sample	Tool	τ_{av} [μs]	τ_{max} [μs]	SRV$_{av}$ [cm/s]	SRV$_{min}$ [cm/s]	iV_{OC} [mV]	j_0 [fA/cm^2]
1	μ-PCD	728	786	36	33	-	-
2	μ-PCD	298	330	88	80	-	-
3	μ-PCD	237	370	111	71	-	-
4	μ-PCD	336	721	78	36	-	-
4	QSSPC	160	420	164	63	649	97
4'	QSSPC	172	450	153	58	672	74
5	QSSPC	123	196	79	50	680	28
6	μ-PCD	355	687	74	38	-	-
7	μ-PCD	27	80	972*	122	-	-
8	QSSPC	146	180	67	54	679	30

TABLE 6.2: Average and maximum minority carrier lifetime results for selected black Si samples passivated by ALD Al$_2$O$_3$ and PECVD SiN$_x$:H, respectively. The table further shows average and minimum surface recombination velocity (SRV), implied open-circuit voltage (iV_{OC}) and saturation current density (j_0) calculated directly from the measured lifetime. In the case of QSSPC the average lifetime was extracted at a carrier injection level of 2×10^{16} cm^{-3}. The average injection level for μ-PCD was 1.5-1.9 $\times 10^{16}$ cm^{-3}.
*Since the SiN$_x$:H sample was not symmetrically passivated, the SRV may be half of this value.

passivation quality. The implied open-circuit voltage, iV_{OC}, is even more relevant considering potential cell performance. The highest iV_{OC} obtained with ALD-passivation in this work is 680 mV, which would enable improved cell efficiency in an actual black Si solar cell compared to the cell results obtained so far. However, the obtained surface recombination velocities in this work are not as low as the best results reported in literature by e.g. Otto *et al.* [109] and Savin *et al.* [110] for black Si. This may be due to differences in the black Si process, the ALD passivation process or a combination of the two. The slightly higher injection level used in this work compared to certain state-of-the-art results [109, 111] accounts for part of the difference in reported lifetimes and SRV values.

6.2 Tunnel oxide and doped poly-Si passivation

In 2014 the world-record power conversion efficiency for Si solar cells was obtained, when Panasonic achieved 25.6% efficiency [42] for a hetero-junction cell structure employing doped, hydrogenated amorphous Si (a-Si). This cell type is called hetero-junction with an intrinsic thin layer or HIT-cell in short. The record efficiency is first of all attributed to the excellent passivation quality of hydrogenated a-Si and the fully passivated emitter enabled by thin isolating layers allowing for tunnelling from the n- to the p-region. Based on this promising result and the issues with increased surface recombination for black Si, the combination of similar hetero-junction passivation on black Si seems like a

promising approach. In order to test this assumption, symmetric lifetime test samples were passivated in an approach similar to the HIT-cell; using doped poly-Si with an intermediate SiO_2 tunnel oxide to form a hetero-junction. This passivation stack was grown on black Si and planar Si for comparison and the lifetime was characterized with μ-PCD and QSSPC.

The tunnel oxide was grown wet-chemically in 68% HNO_3 at 95 °C for 10 minutes. This resulted in 1.2 nm SiO_2. Doped poly-Si was grown by low-pressure chemical vapour deposition (LPCVD) at a temperature of 580 °C using diborane (B_2H_6) and phosphine (PH_3) as dopant gasses for p- and n-type poly-Si, respectively, and silane (SiH_4) as Si gas source. The gas flows were 80, 7 and 7 sccm for SiH_4, B_2H_6 and PH_3, respectively. The grown Si layer is amorphous when grown at this temperature, but was subsequently annealed in N_2 atmosphere at 800 °C for 60 minutes in order to increase the crystal grain size and form poly-Si.

After fabrication the passivated planar and black Si samples were characterized by μ-PCD, QSSPC and PL, respectively. Figure 6.6 and 6.7 shows the μ-PCD and PL output, respectively, of the best black Si sample passivated with tunnel oxide and doped poly-Si. For comparison the data for a representative ALD-passivated black Si sample is shown.
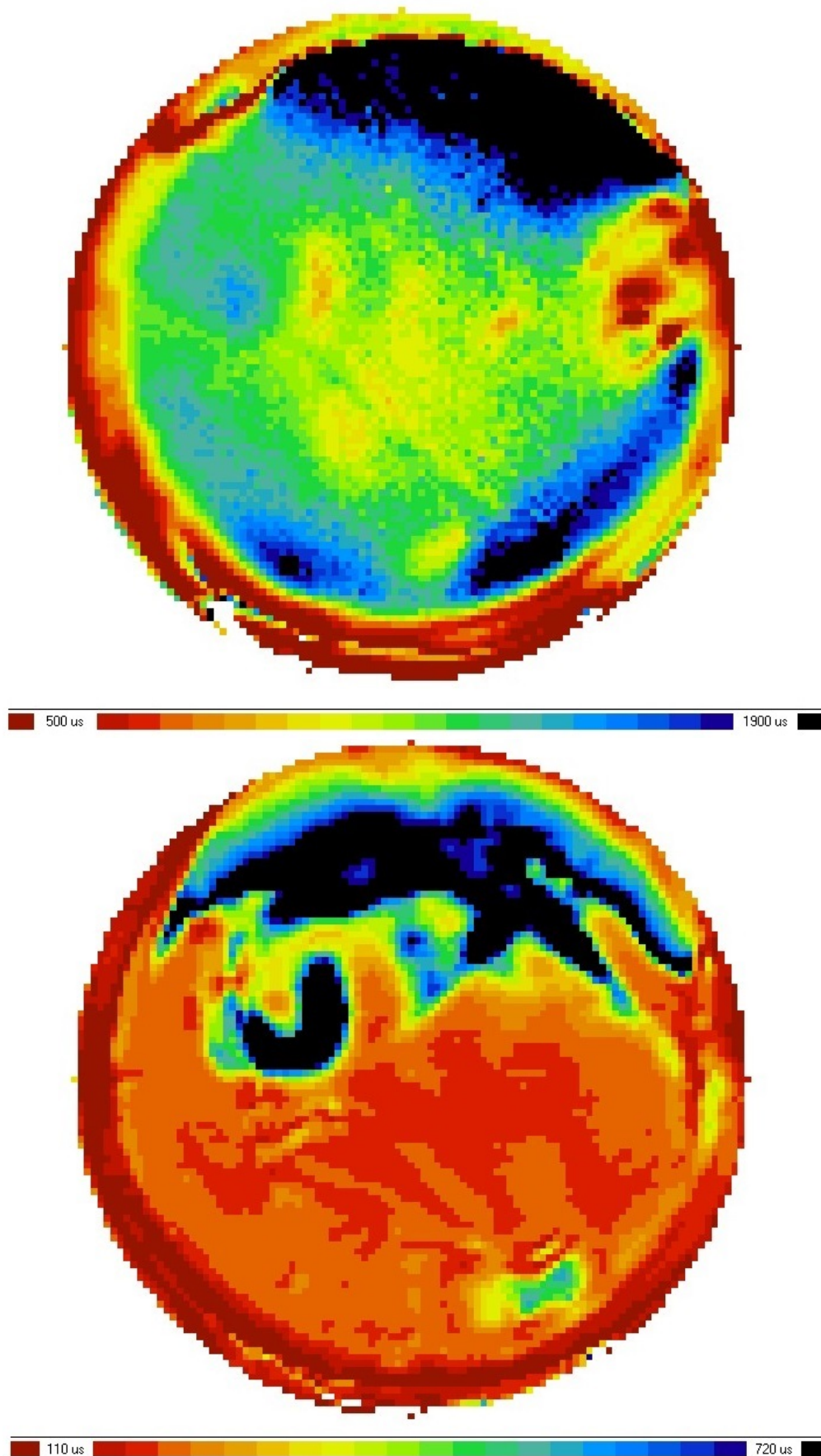
FIGURE 6.6: Example of the output from a μ-PCD lifetime measurement of a p-type black Si sample passivated by 1.2 nm tunnel oxide and n-type doped poly-Si (top) and a similar p-type black Si sample passivated by ALD Al_2O_3 (bottom) for comparison. Note the difference of the scale-bars from top to bottom image. The average lifetime of the sample passivated with doped poly is about 4 times larger than that of the ALD-passivated sample.
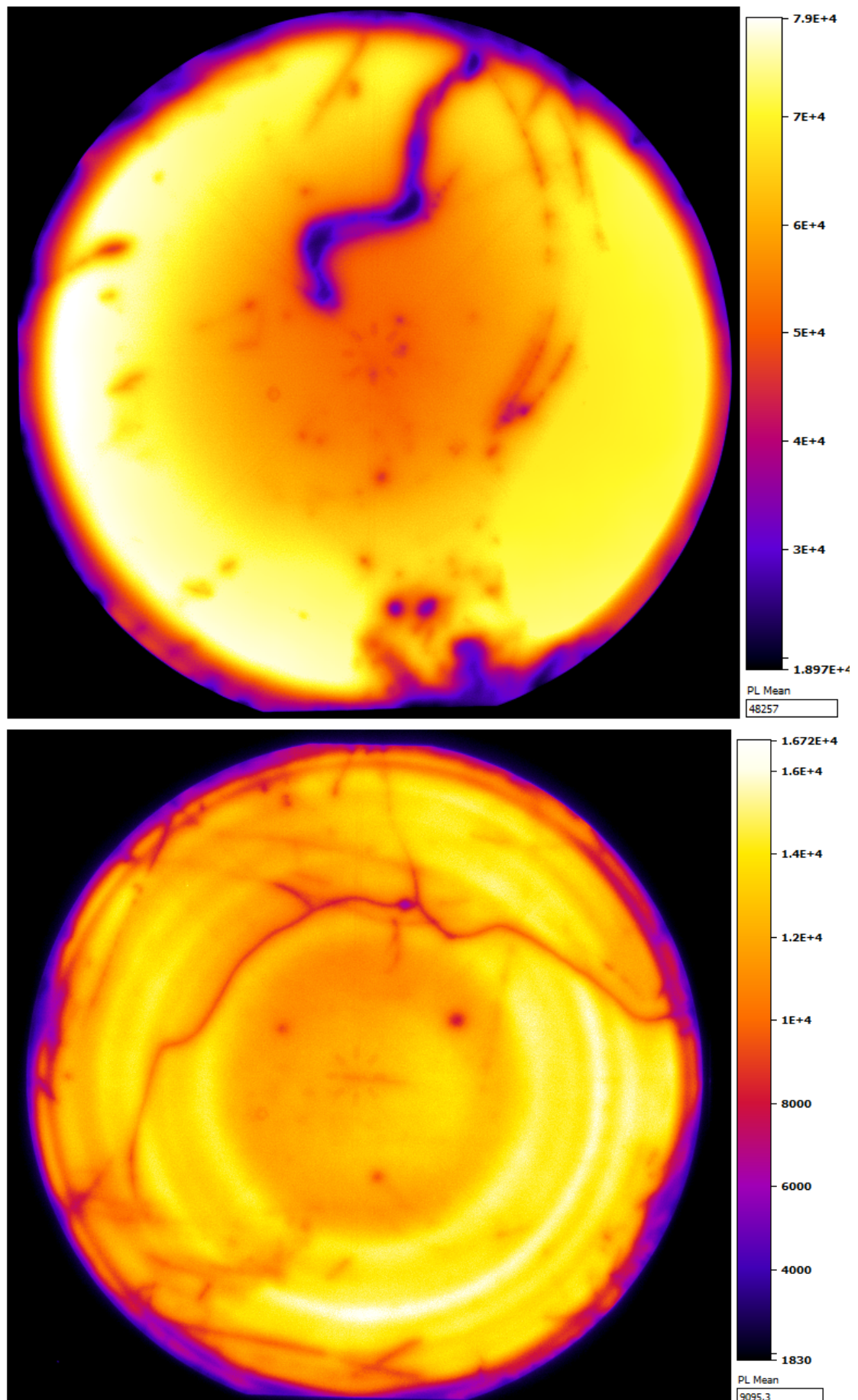
FIGURE 6.7: Example of the output from a photoluminescence (PL) measurement of a black Si sample passivated by doped poly-Si and tunnel oxide (top) and ALD Al_2O_3 (bottom) for comparison. Note the different scale-bars on the top and bottom PL-image, respectively. The difference in PL-signal is more than a factor of 4.

The results in Figure 6.6 and 6.7 show that the overall passivation quality of black Si passivated with doped poly-Si and tunnel oxide is significantly higher than that of ALD-passivated black Si. Note that the scale-bars are different on the top and bottom images in Figure 6.6 and 6.7. The difference in PL-signal is more than a factor of 4, which corresponds well with the lifetimes measured by μ-PCD seen in Figure 6.6.

Table 6.3 shows the summary of the measured lifetime of polished and black Si (bSi) passivated with tunnel oxide and doped poly-Si. Since the p-type poly-Si gave significantly worse results than the n-type poly-Si, most of the results for p-type have been omitted. The poor quality of the p-type poly-Si is probably due to an unoptimized gas flow of diborane in the p-type LPCVD process.

Sample	Meas.	τ_{av} [μs]	τ_{max} [μs]	SRV_{av} [cm/s]	SRV_{min} [cm/s]	iV_{OC} [mV]	j_0 [fA/cm^2]
p poly on n Si*	QSSPC	287	1320	91	20	674	199
p poly on p Si*	QSSPC	25	34	1050	772	561	2610
n poly on p bSi	μ-PCD	1247	5794	21	5	-	-
n poly on p bSi	QSSPC	294	2310	89	11	695	97
n poly on p Si	μ-PCD	2663	3700	10	7	-	-
n poly on p Si	QSSPC	445	2890	59	9	696	56
n poly on n Si	μ-PCD	1807	3300	15	8	-	-
n poly on n Si	QSSPC	491	4000	53	7	693	45

TABLE 6.3: Minority carrier lifetime results for selected polished and black Si (bSi) samples passivated by a 1.2 nm tunnel oxide and doped poly Si. The table shows surface recombination velocity (SRV), implied open-circuit voltage (iV_{OC}) and saturation current density (j_0) calculated directly from the measured lifetime. In the case of QSSPC the average lifetime was extracted at a carrier injection level of $2 \cdot 10^{16}$ cm^{-3}.
*Data from p-type poly-Si samples had to be extracted at lower injection levels due to lower lifetime.

The results in Table 6.3 show that tunnel oxide and n-type poly-Si is a very effective passivation layer both for polished and black Si. Since the extracted effective lifetime values are strongly injection dependent, as shown in Figure 6.8, the calculated iV_{OC} is probably a better indication of the passivation quality, than the lifetime.
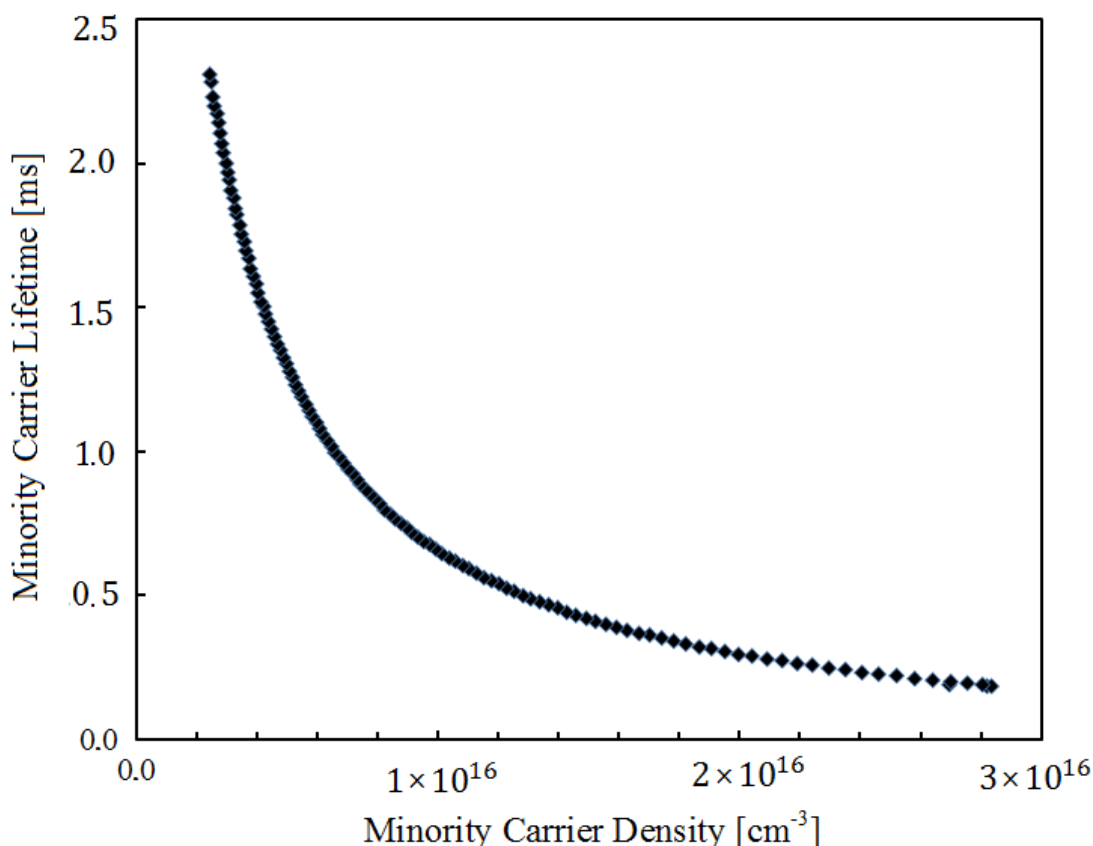
FIGURE 6.8: Minority carrier lifetime as function of the minority carrier density of the p-type black Si sample passivated by tunnel oxide and n-type doped poly-Si. The lifetime was measured with QSSPC (Sinton tool).

All parameters related to the passivation quality indicate excellent passivation by this combination of tunnel oxide and doped poly-Si on black Si: Lifetime well above 1 ms (depending on measurement technique and injection level), surface recombination velocity well below 100 cm/s, saturation current density below 100 fA/cm^2 and implied open-circuit voltage close to 700 mV are all indicators of a well-passivated surface, which is not trivial to obtain on black Si as explained previously.

If the implied V_{OC} of 695 mV could be realized in an actual cell, it would not only be the best black Si cell fabricated in this work, but the best voltage ever obtained with a black Si solar cell. Note that this was the first attempt to passivate black Si with tunnel oxide and doped poly-Si. Thus there is reason to believe that this result can be improved in future studies. Furthermore there was a clear scratch in the passivation layer of the best black Si sample, which must have a negative impact on the overall lifetime of the sample, as seen in Figure 6.7. This result confirms the promising properties of passivating black Si with a tunnel oxide and doped poly-Si and shows the ability to obtain implied voltages approaching 700 mV - even on black Si. It is also noteworthy, that the resistivity of these samples was unfortunately not measured prior to passivation. Therefore the resistivity used to calculate iV_{OC} was assumed to be 5 Ωcm, even though the resistivity range from the wafer supplier was 1-20 Ωcm. If the actual resistivity is 1 Ωcm, iV_{OC} may be up to 719 mV. It may also be lower, if the actual resistivity is higher than 5 Ωcm.

Another interesting result seen in Table 6.3 is the fact that n-type poly-Si yields very good passivation on both n- and p-type Si. This could be an advantage in certain cell structures such as n-type rear-junction or interdigitated back contact (IBC) cell types with the front passivated by n-type doped poly-Si or a front-contact cell with one polarity doped poly-Si on the front and the opposite on the rear. Chapter 7 discusses this further.

6.2.1 PC1D calculations

Based on the passivation results it seems possible to reach SRV $\sim$ 20 cm/s on black Si by using tunnel oxide and doped poly-Si. Such recombination velocities have also been reported for ALD-passivation on black Si by other groups [109, 110]. Therefore it is interesting to investigate which theoretical power conversion efficiency to expect, if such low SRV is combined with the low reflectance of black Si. For this purpose the PC1D software was used to simulate power conversion efficiency of different cells, in this case n-type substrates with a p-type emitter was assumed. Only SRV and front surface reflectance were varied and values of iV_{OC} and FF were assumed. J_{SC} was then calculated using PC1D with reflectance and SRV as input and based on this and the assumed iV_{OC} and FF the theoretical power conversion efficiency for different cells could be calculated. It was chosen to compare a well-passivated scenario (SRV = 20 cm/s) with a 'standard' scenario (SRV = 1000 cm/s) based on the measured SRV for black Si passivated by SiN$_x$:H. Furthermore it was chosen to compare weighted, average front reflectance of 2 and 0.5%, respectively. These reflectances represent KOH-textured mono-crystalline Si with standard SiN$_x$:H AR-coating and black Si, respectively. Furthermore, efficiencies were calculated based on experimentally determined corresponding values of reflectance and SRV for ALD-passivated black Si samples. Table 6.4 summarizes the calculations.

$R_{\text{w,av}}$ [%]	SRV [cm/s]	iV_{OC} [V]	J_{SC} [mA/cm^2]	η [%]
2	1000	650	**38.49**	**20.01**
2	20	695	**38.86**	**21.61**
0.5	1000	650	**39.14**	**20.35**
0.5	20	695	**39.59**	**22.01**
0.38	145	656		**21.4**
0.7	65	677		**21.6**
0.86	58	673		**21.6**

TABLE 6.4: PC1D calculation results of short-circuit current (J_{SC}) and power conversion efficiency (η) for cells with two different passivation schemes; assuming surface recombination velocities (SRV) of 20 and 1000 cm/s, and two different weighted, average front reflectances ($R_{\text{w,av}}$) of 0.5 and 2%, respectively. Implied open-circuit voltage (iV_{OC}) values were assumed according to the two different SRV values. Fill factor (FF) of 80%, emitter sheet resistance of 100 Ω/sq. and p-type emitter on n-type substrate were assumed in all cases. The three results in the bottom use experimental corresponding values of $R_{\text{w,av}}$, SRV and iV_{OC} for ALD-passivated black Si.

The results in Table 6.4 show that high-efficiency devices with efficiencies of 22% can be realized - without any advanced rear designs or selective emitters assumed - by combining the experimentally measured SRV and reflectance values of black Si passivated by ALD or tunnel-oxide/doped poly-Si. The results in Table 6.4 also show that power conversion efficiency may be improved by $\sim 0.4\%$ absolute by replacing conventional texturing with black Si. This would require similar SRV on black Si compared to conventionally textured Si.

6.3 Emitter Diffusion on Nanostructured Si

Based on the emitter diffusions performed on the fabricated solar cells in this project, it appeared that the resulting sheet resistance of the doped black Si surface differed significantly from the expected sheet resistance. This observation gave rise to an investigation of the diffusion properties on nanostructured Si compared to planar Si. The hypothesis was that the effective diffusion flux through the nanostructured Si surface could be larger than for planar Si due to the larger effective surface area of black Si. The question is how much the presumed difference in diffusion flux affects the resulting sheet resistance of an emitter in nanostructured Si.

6.3.1 Experimental Results

The initial observation was based on the conventional method for determining sheet resistance, four-point probe measurement. However, the interaction between the macroscopic four-point probe and the nanoscale surface structures is not clear. Therefore conventional four-point probe measurements may not give an accurate estimation of the actual sheet resistance of doped black Si. In order to determine the diffused profile, techniques such as secondary ion mass spectroscopy (SIMS) and electrochemical capacitance-voltage (ECV) measurements may be used. However, both of these techniques physically remove material from the surface, downward from the top of the surface. This induces a risk of over-estimating the doping concentration on the very top of the nanostructures, since those techniques do not adjust for the non-planar black Si surface. It was reported in [124] that ECV-profiles on KOH-textured surfaces need to be calibrated due to the increased surface area.

Table 6.5 and Figure 6.9 shows the initial four-point probe and ECV measurements, performed at UNSW, that gave rise to the investigation of dopant diffusion on nanostructured surfaces. The four-point probe and ECV measurements were performed on the nanostructured front and planar rear side of 156x156 mm^2 200 μm thick CZ p-type Si wafers with a resistivity of 1.6 Ωcm. The wafer was doped by phosphorus diffusion performed at 770 °C for 30 minutes using POCl$_3$ as dopant source and O$_2$ as carrier gas, with and without a post-oxidation, respectively, intended to reduce the phosphorus surface concentration.

Surface	Diffusion	$R_{\text{sheet,av}}$ [Ω/sq.]	Std.dev. [Ω/sq.]
black Si front	$POCl_3$	51.5	3
planar rear	$POCl_3$	82.3	2.8

TABLE 6.5: Average sheet resistance and standard deviation across a 4" wafer measured by a standard four point probe. The measurement was performed on the nanostructured front and planar rear, respectively, of a p-type CZ Si wafer with a phosphorus doped emitter obtained by $POCl_3$ thermal diffusion performed at 770 °C for 30 minutes.
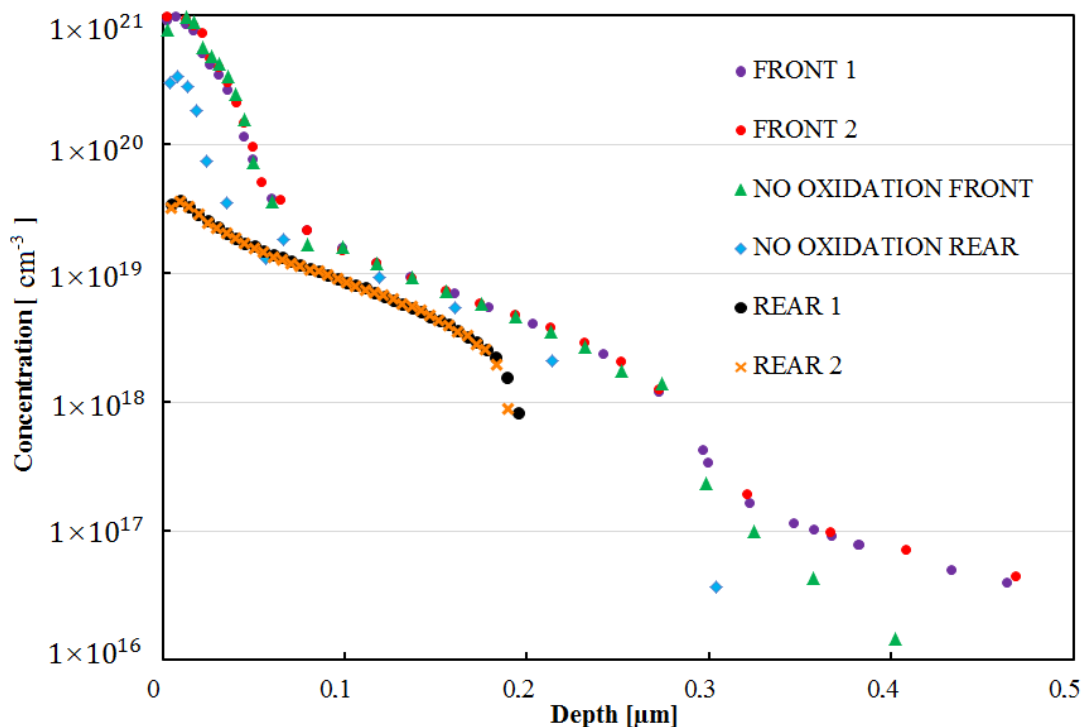
FIGURE 6.9: Electrochemical capacitance-voltage measurement of the doping profile of the nanostructured front and planar rear, respectively, of a phosphorus doped p-type Si wafer. The wafers were processed by $POCl_3$ thermal diffusion performed at 770 °C for 30 minutes.

The result in Figure 6.9 shows that the nanostructured front is more highly doped than the planar rear. Furthermore, the post-oxidation, intended to reduce surface concentration, does not reduce surface concentration on nanostructured Si.

In order to more accurately evaluate the resulting doping profiles on black Si compared with planar Si, ECV, micro-four point probe and Hall measurements were combined. Micro-four-point probe and Hall measurements were performed using a Capres microRSP-M200 micro-four point probe with a pitch between the four probes of 200 μm. The sheet resistance was measured with the micro-four-point probe by forcing a current through two of the four pins and measuring the resulting potential difference. The potential difference was measured at different lateral positions on the wafer surface starting 600 μm from the edge and approaching the edge of the sample in steps of varying length. The pin configuration was varied at each of these points according to the

method described in [125] and using the van der Pauw method to calculate the sheet resistance according to

$$e^{-\pi \bar{R}_\mathrm{A}/R_\mathrm{S}} + e^{-\pi \bar{R}_\mathrm{C}/R_\mathrm{S}} = 1 \tag{6.4}$$

where R_S is the actual sheet resistance to be determined and

$$\bar{R}_\mathrm{A} = \frac{R_{23,41} + R_{41,23} + R_{32,14} + R_{14,32}}{4} \tag{6.5}$$

$$\bar{R}_\mathrm{C} = \frac{R_{12,34} + R_{34,12} + R_{21,43} + R_{43,21}}{4} \tag{6.6}$$

In 6.5-6.6 $R_{ab,cd}$ denotes the resistance measured by forcing current from point a to b and measuring voltage between c and d. Thus the resistance indices $1-4$ correspond to the different possible configurations of the four-point measurement and the position of current and voltage probes, respectively. Figure 6.10 shows the result of micro-four-point probe measurements on 5 different black Si wafers; 4 p-type wafers with a phosphorus doped emitter and 1 n-type wafer with a boron doped emitter. The sheet resistance was measured on the nanostructured front and planar rear, respectively. The pitch between the four probes was 200 μm, the engagement depth was 30 μm and the distance from measurement point to wafer edge was varied from 0 to 600 μm.
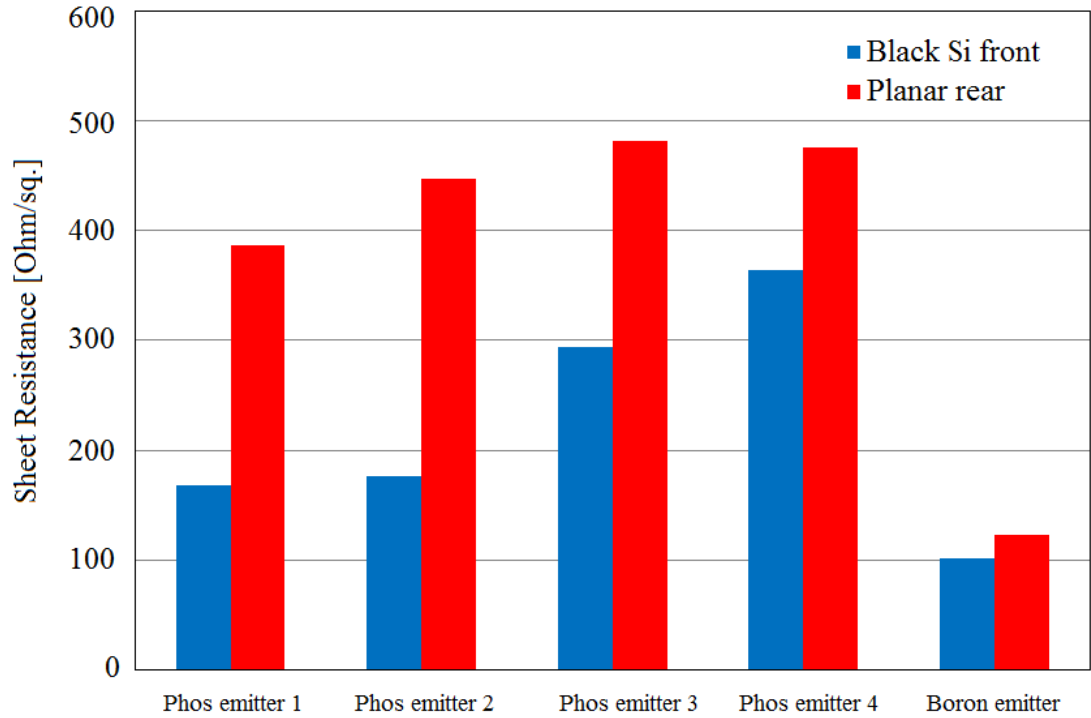
FIGURE 6.10: Micro-four-point probe measurement of the sheet resistance on the nanostructured front and planar rear, respectively, of 4 phosphorus doped p-type and 1 boron doped n-type black Si wafers. All wafers were processed at 770 °C for 30 minutes followed by a 30 minute drive-in at 850 °C. The O_2 gas flow of the drive-in was varied between 250 and 400 sccm.

The result in Figure 6.10 shows that sheet resistance in all cases is significantly lower on the nanostructured front compared to the planar rear. For phosphorus emitters the relative difference between front and rear becomes smaller when the sheet resistance is

higher. For sheet resistances suitable for solar cell fabrication (100-200 Ω/sq. selective emitters) the difference between the nanostructured front and planar rear is more than 100%. For the boron doped emitter the difference is 25%, but obviously based on a data set which is statistically too small to generalize conclusions.

The sheet resistance was furthermore measured at different lateral positions on the wafer in order to investigate the uniformity across an entire wafer and the effect of the surface on the uniformity. The result is shown for the nanostructured front and planar rear, respectively, of 3 different black Si wafers in Figure 6.11.
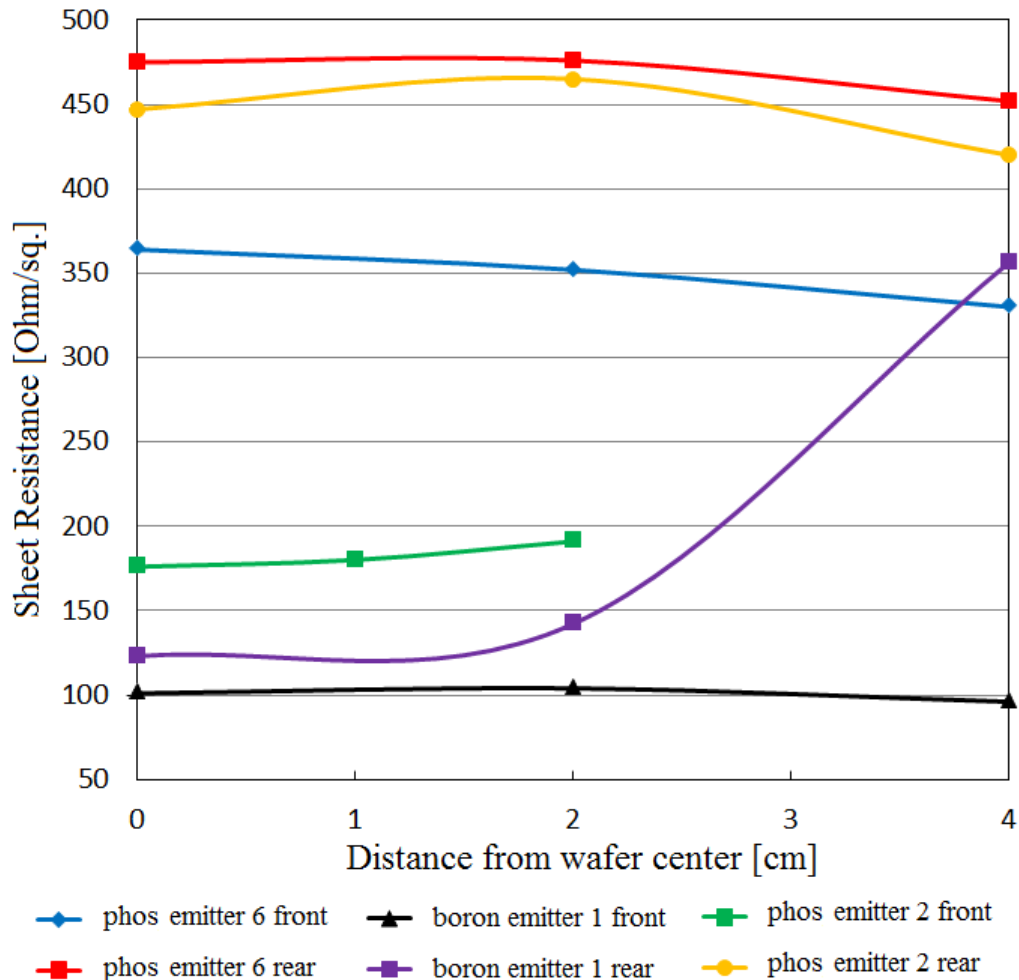
FIGURE 6.11: Micro-four-point probe measurement of the sheet resistance at different positions on the nanostructured front and planar rear, respectively, of 2 phosphorus doped p-type and 1 boron doped n-type black Si 4" wafers.

The result in Figure 6.11 shows that the uniformity is comparable for phosphorus-doped nanostructured and planar surfaces, respectively. For boron doped surfaces, it seems that the nanostructured surface is more uniformly doped compared to the planar surface. It should be stated that the deviation from center to edge of the planar boron doped surface is so significant that it is probably due to non-ideal processing conditions, which would not be the case in an actual cell production. However, the result may

indicate that uniform emitter doping across entire wafers is more easily obtained on nanostructured surfaces. This needs to be more thoroughly investigated.

In order to obtain a more detailed picture of the doped profiles on nanostructured and planar Si, respectively, Hall measurements were performed according to the method described in [125]. The output parameters of the Hall measurements are Hall mobility, μ_{H}, Hall coefficient, R_{H}, and sheet carrier density, N_{S}, defined as [125]

$$\mu_{\mathrm{H}} = r_{\mathrm{H}}\mu, \tag{6.7}$$

where r_{H} is the Hall scattering factor and μ is the carrier mobility,

$$R_{\mathrm{H}} = \mathbf{E} \cdot \frac{(\mathbf{B} \times \mathbf{J})}{|\mathbf{B} \times \mathbf{J}|^2} \tag{6.8}$$

where $\mathbf{E}$ is the electric field, $\mathbf{B}$ is the magnetic flux density and $\mathbf{J}$ is the current density, and

$$N_{\mathrm{S}} \equiv \int_0^h n \; dz = \bar{r}_{\mathrm{H}} \frac{\left(\int_0^h n\mu \; dz\right)^2}{\int_0^h n\mu\mu_{\mathrm{H}} \; dz} \tag{6.9}$$

where n is the carrier density, h is the sheet thickness and z is the direction, in which the carrier density is inhomogenous.

Besides obtaining the sheet carrier density of the doped profiles, the Hall measurements also serve to confirm the polarity of the doped sheet in order to verify that the measured sheet resistances actually represent the doped emitters and not the wafer resistance itself. The results of sheet carrier density, Hall mobility and Hall coefficient are shown in Figure 6.12.

	Phosphorus 1	Phosphorus 2	Phosphorus 3	Boron 1	Boron 2
■ Front	3.09×10^{14}	3.24×10^{14}	1.74×10^{14}	-1.15×10^{15}	-1.24×10^{15}
■ Rear	1.19×10^{14}	5.23×10^{13}	8.46×10^{13}	5.19×10^{13}	-2.84×10^{14}

	Phosphorus 1	Phosphorus 2	Phosphorus 3	Boron 1	Boron 2
■ Front	119	125	121	-54	-54
■ Rear	131	254	151	1191	-191

	Phosphorus 1	Phosphorus 2	Phosphorus 3	Boron 1	Boron 2
■ Front	1.2118	1.1553	2.1521	-0.3261	-0.3014
■ Rear	3.1518	7.1608	4.4257	7.2186	-1.3203

FIGURE 6.12: Hall measurements of the sheet carrier density (top), Hall mobility (middle) and Hall coefficient (bottom) on the nanostructured front and planar rear, respectively, of 3 phosphorus doped p-type and 2 boron doped n-type black Si wafers. The yellow bars refer to measurements that gave a bad van der Pauw fit, probably resulting in wrong values.

Neglecting the single inaccurate measurement point (yellow bar) in each graph in Figure 6.12, the conclusions are clear:

- Sheet carrier density is higher on the nanostructured front than the planar rear.

- Hall mobility is lower on the nanostructured front than the planar rear.

- The Hall coefficient is lower on the nanostructured front than the planar rear.

- The sign of the Hall coefficient is positive for the phosphorus doped and negative for the boron doped emitters, meaning the measured resistances are actually reflecting the doped emitters and not the wafer itself, which has opposite polarity. Since the magnetic field applied in the measurements was negative ($\sim$ -630 T), the sign of the Hall coefficient is opposite to the sign of the dominant charge carrier in the layer according to equation 6.8.

The higher sheet carrier density for the nanostructured front corresponds well with the sheet resistance measured with the micro-four-point probe seen in Figure 6.10, since higher sheet carrier density should give rise to lower sheet resistance. Similarly the Hall coefficient, which is inversely proportional with the sheet carrier density, should be lower on the nanostructured front, as observed. The lower Hall mobility also corresponds well with a higher sheet carrier density, since higher carrier density decreases the carrier mobility. However, the Hall mobility does not scale with Hall coefficient, as expected, in all cases. This is not fully understood yet, but may be due to a non-linear doping profile on the nanostructured front, which is not completely represented by the averaged sheet carrier density.

6.3.2   Comparison with KOH-textured Si

The results in Figures 6.11 and 6.12were based on planar Si compared to black Si. However, from an industrial perspective it is more realistic to compare with conventionally textured Si, typically KOH-textured in case of mono-crystalline Si. In order to make a direct comparison, p-type Cz Si wafers were textured by 2% KOH and 7% IPA at 80 °C for 50 minutes. The KOH-textured wafers were processed by four different POCl$_3$ diffusions in parallel with double-side RIE-textured Cz p-type Si. Table 6.6 shows the four different diffusion processes. Figure 6.13 shows the result of the four different diffu-

Temperature [°C]	Predep Time [min]	Drive-in time [min]
900	15	20
900	20	20
850	20	20
850	30	20

TABLE 6.6: List of POCl$_3$ diffusion processes used for the comparison between KOH- and RIE-textured Si. The temperature was kept constant during predep and drive-in in all cases. The drive-in was performed in O$_2$ atmosphere.

sion processes from Table 6.6 performed on double-side KOH- and RIE-textured Si for comparison.
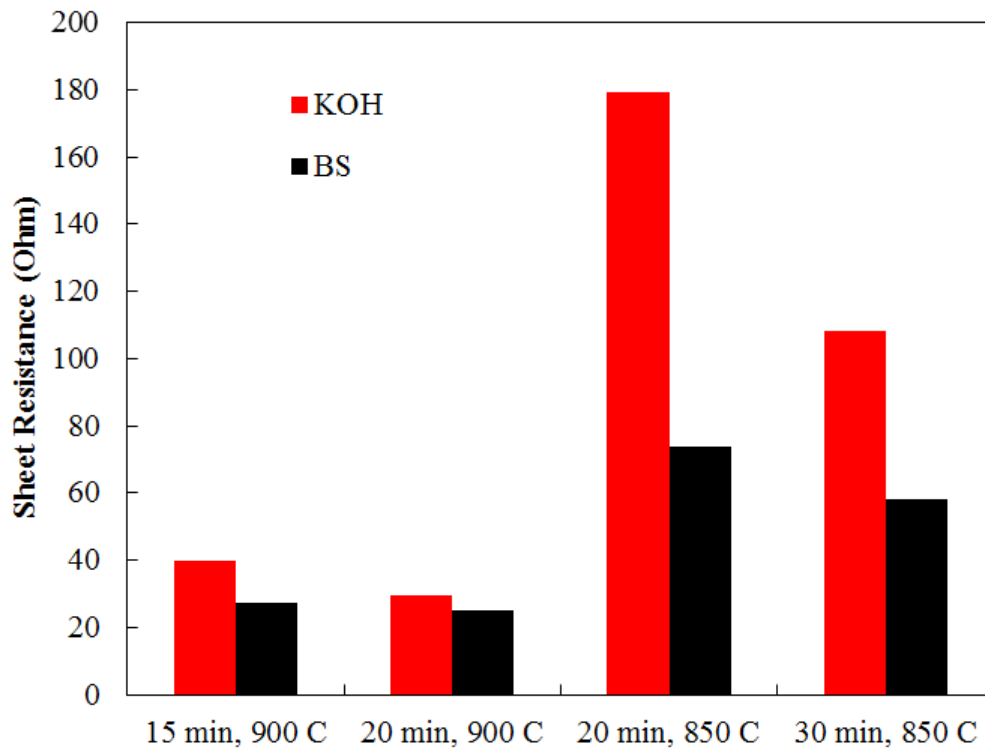
FIGURE 6.13: Sheet resistance of double-side KOH- and RIE-textured Si after four different POCl₃ diffusion processes. The sheet resistance was measured with a four-point probe.

The result in Figure 6.13 shows that the sheet resistance of black Si is lower than similarly processed KOH-textured Si in all cases. If a certain sheet resistance is desired, a lower thermal budget is required for black Si compared to KOH-textured Si. This may be depicted by plotting the same sheet resistances as function of temperature for the two different time groups, 20 and 30 min, as shown in Figure 6.14.
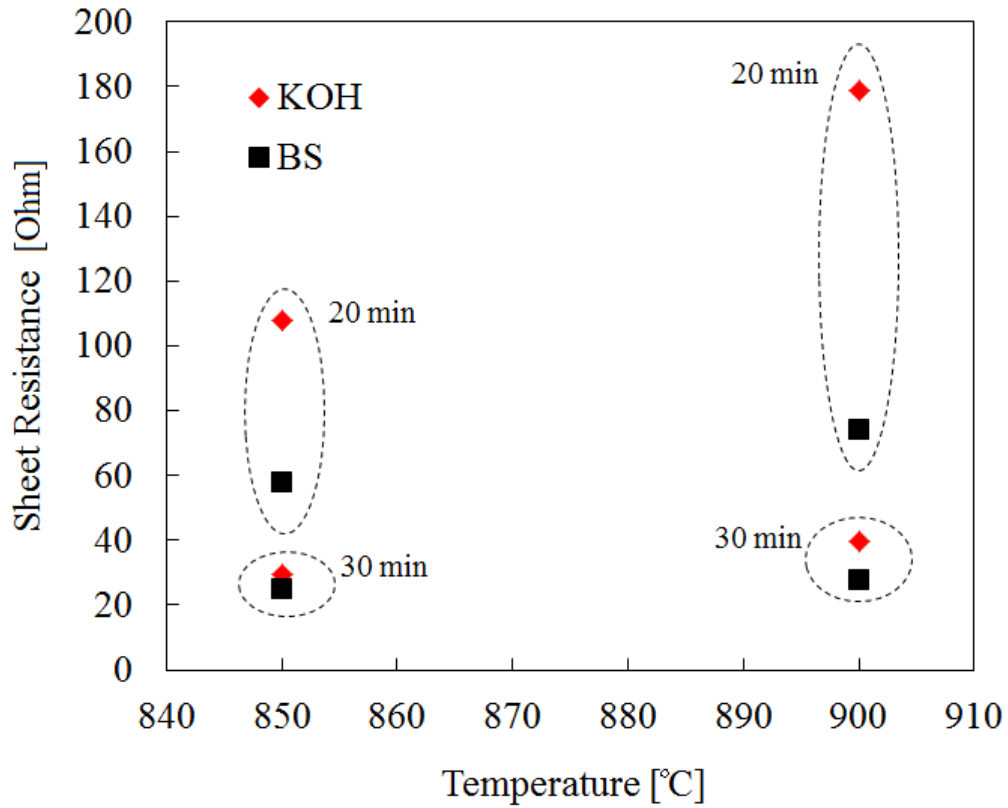
FIGURE 6.14: Sheet resistance of KOH- and RIE-textured Si as function of thermal budget, given as time plus temperature, after four different POCl$_3$ diffusion processes. The sheet resistance was measured with a four-point probe.

The result in Figure 6.14 shows that a given sheet resistance may be obtained on black Si at a lower thermal budget compared to KOH-textured Si. This may be valuable for industrial solar cell production. In order to investigate the effect of the different diffusion processes on carrier lifetime for the differently textured Si wafers, minority carrier lifetime was was on the same wafers using μ-PCD. Figure 6.15 shows the measured lifetimes, each value averaged over the entire 4" wafer.
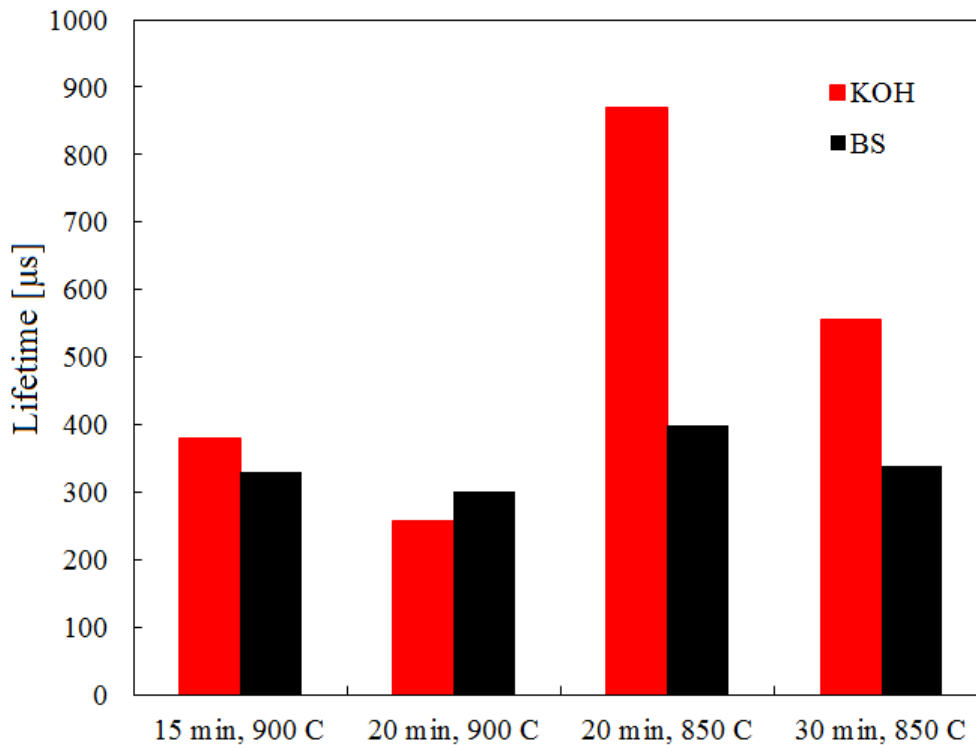
FIGURE 6.15: Minority carrier lifetime of double-side KOH- and RIE-textured Si after four different POCl$_3$ diffusion processes. The lifetime was measured with μ-PCD. The values are the average lifetimes over the entire 4" wafer.

The resulting lifetimes in Figure 6.15 may be a result of Auger recombination in the different emitters or the differently textured surfaces. Auger recombination most likely dominates in this case, since the emitters are relatively highly doped. Thus, the lower lifetime of black Si compared to KOH-textured Si may in this case be at least partly due to higher Auger recombination in the more highly doped emitters.

6.3.3 Simulation Results

In order to verify the results and investigate whether the observed differences may be explained solely by differences in surface area and topology, simulations were carried out using the Athena Silvaco software. The simulation was based on a simple phosphorus diffusion model, in which the dopant concentration was assumed constant and equal to the solid solubility at the Si surface. The script used in Athena is seen in J. Defect induced diffusion was not taken into account in the simplified model. Diffusion temperature and surface concentration was varied and the different diffusion processes simulated are summarized in Table 6.7. The diffusion and annealing time was 30 and 20 minutes, respectively, in all cases. In order to simulate diffusion through a nanostructured Si surface, the topology of the black Si nanostructures was approximated in Athena by defining a non-planar Si surface with dimensions representing the known topology of the black Si used in this work. Structures with 400 nm height, 400 nm pitch between structures and a non-linear graded refractive index was assumed. A sketch of the resulting modelled surface is shown in Figure 6.16.

Process	Process Temp. (Anneal) [°C]	Surface Conc. [cm^{-3}]
1	1000 (1000)	5×10^{20}
2	985 (1000)	2×10^{20}
3	980 (1000)	2×10^{20}
4	975 (900)	8×10^{19}
4	975 (900)	7×10^{19}
6	975 (800)	6×10^{19}
7	975 (800)	5×10^{19}
8	950 (800)	5×10^{19}

TABLE 6.7: List of phosphorus diffusion processes simulated with Athena software from Silvaco.
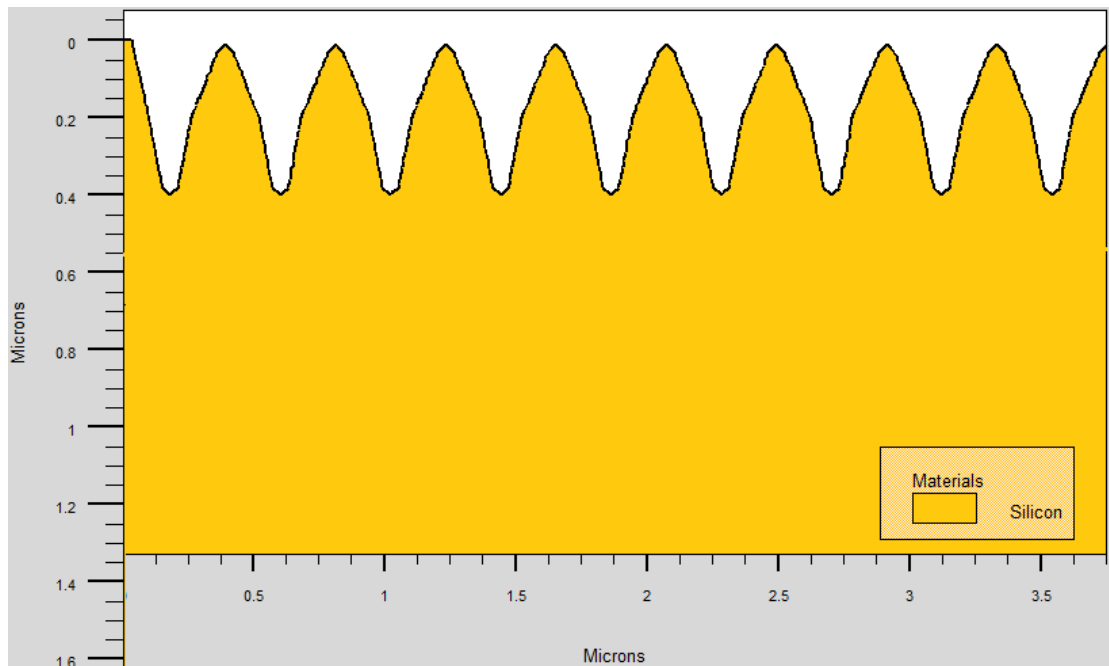
FIGURE 6.16: Sketch of the modelled nanostructured surface used in Athena simulations.

The 8 different diffusion processes listed in Table 6.7 were simulated for nanostructured and planar Si, respectively, and the sheet resistance and junction depth was extracted at four different lateral points within a repeated unit (a single nanostructure) in order to cover differences within the individual nanostructure. Figure 6.17 shows the calculated average sheet resistance for the 8 different diffusion processes listed in Table 6.7 simulated for nanostructured and planar Si, respectively.
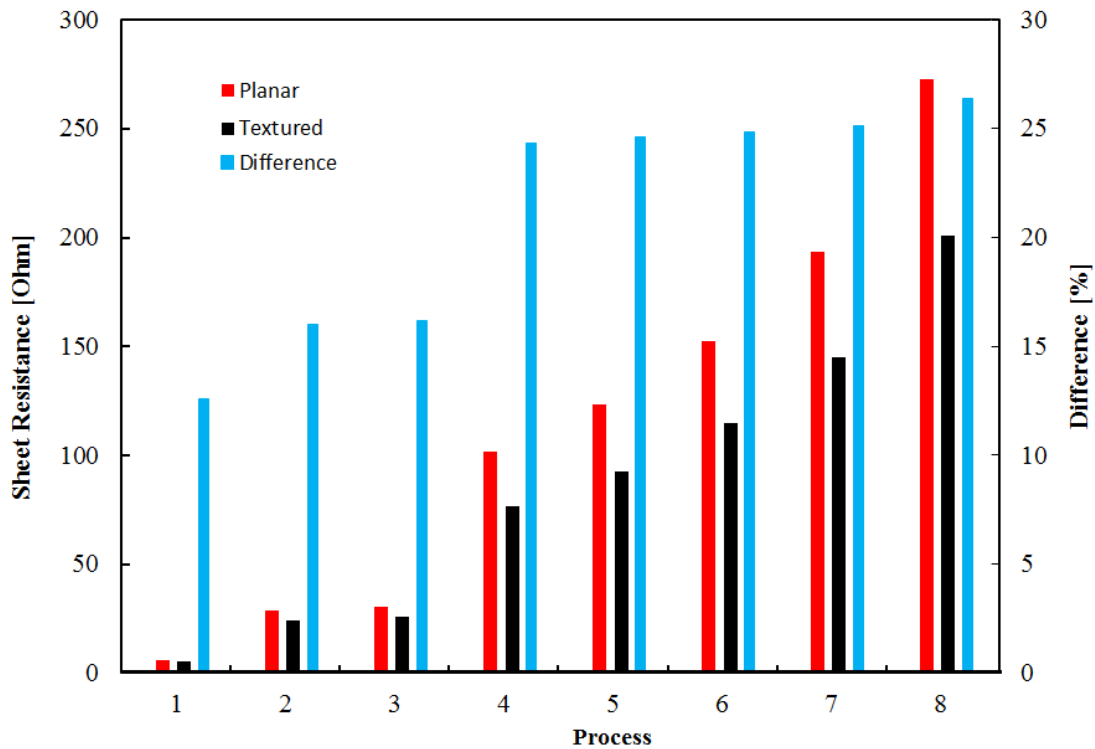
FIGURE 6.17: Simulated sheet resistance for different diffusion processes on nanostructured and planar Si, respectively. The process numbers refer to the diffusion processes listed in Table 6.7.

The result in Figure 6.17 confirms the experimentally measured tendency that sheet resistance is significantly lower on nanostructured compared to planar Si, undergoing the same diffusion process. The relative difference in resistance between nanostructured and planar varies between 12 and 26% for the 8 diffusion processes simulated here. In general the difference is smaller than the difference observed experimentally. This may indicate that the diffusion through nanostructured surfaces is not only enhanced due to a larger surface area but also due to other effects, such as different effective dopant fluxes through different parts of such nanostructured surface or defect induced diffusion, which was unfortunately not included in the simplified simulation model, but may play a role in actual diffusion on black Si.

Besides sheet resistance the resulting junction depth was also extracted. Figure 6.18 shows the calculated average junction depth for the 8 different diffusion processes listed in Table 6.7 simulated for nanostructured and planar Si, respectively.
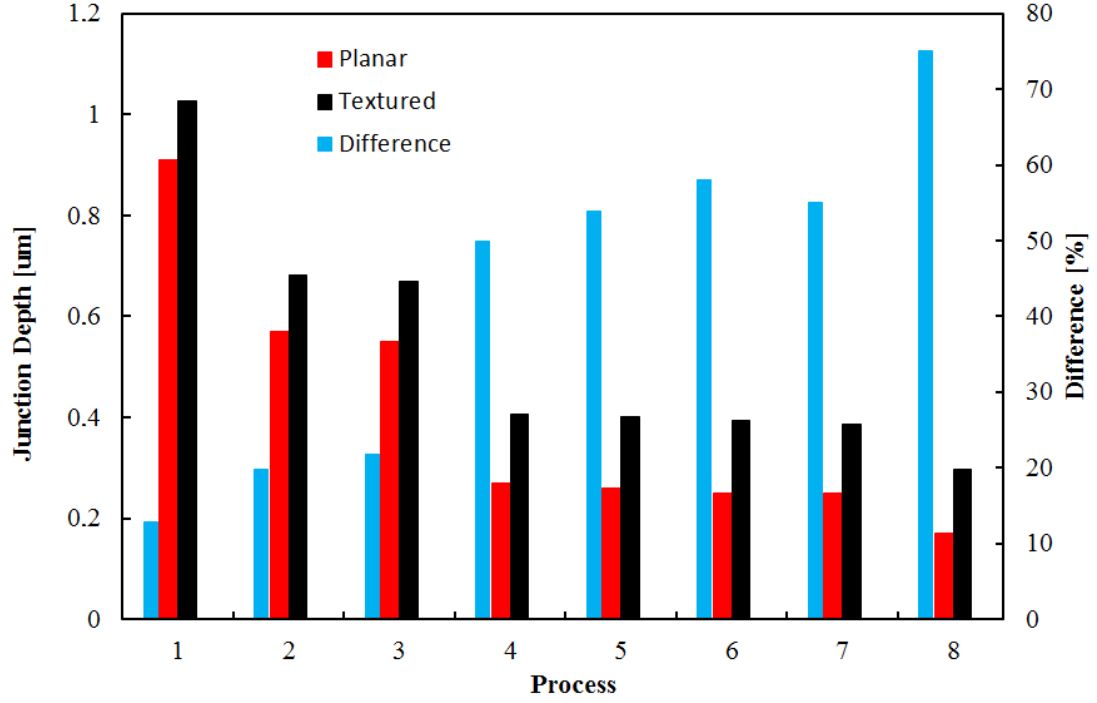
FIGURE 6.18: Simulated junction depth for different diffusion processes on nanostructured and planar Si, respectively. The process numbers refer to the diffusion processes listed in Table 6.7.

The result in Figure 6.18 shows that the junction in all cases is deeper for black Si compared to planar Si. This shows that the lower sheet resistance is not only due to higher carrier density in the sheet but also a deeper junction. This may be important in practice in order to achieve faster diffusion at lower thermal budget without increasing the Auger recombination of the emitter and the surface recombination.

As mentioned the sheet resistance and junction depth was extracted at four equidistant points spanning one repeated unit in order to cover lateral variations within one single nanostructure. Here we define the sheet resistance of any slice in the z-direction, perpendicular to the surface, as

$$\frac{1}{R_{\mathrm{S}}} = \int \sigma \, dz \tag{6.10}$$

, where σ is the conductivity.

Figure 6.19 shows the variation in sheet resistance and junction depth within each nanostructure.
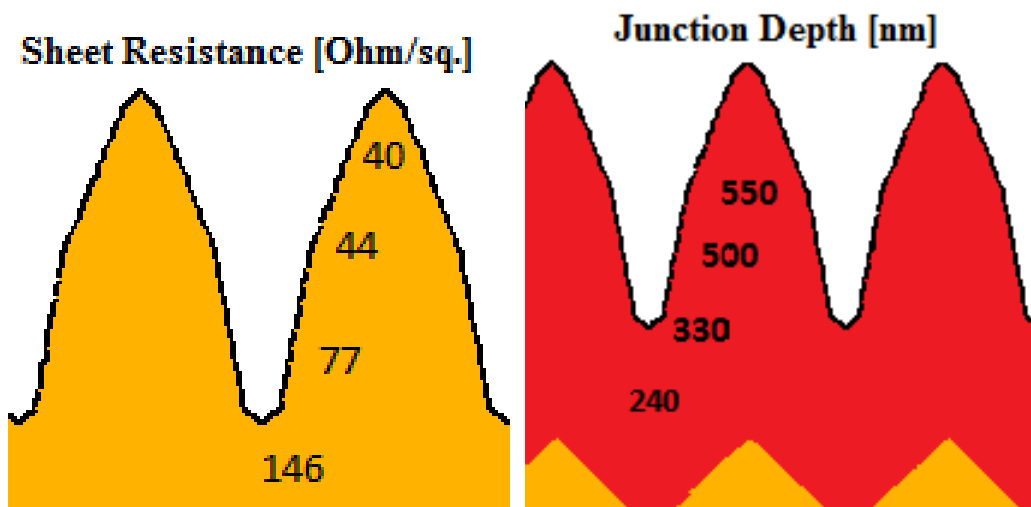
FIGURE 6.19: Example of the simulated junction depth and sheet resistance at different lateral positions within a single nanostructure repeating unit for diffusion process 5.

The result in Figure 6.19 shows how sheet resistance and junction depth varies within each nanostructure repeating unit. The values given in Figure 6.19 are for diffusion process 5, but the variation is representative for most of the modelled processes. The sheet resistance varies more than 200% and the junction depth more than 100% across the individual nanostructure according to the simulation. For process 1, which has the smallest relative variation, the sheet resistance and junction depth still varies 40% and 45%, respectively.

Generally, we can conclude that a nanostructured Si surface will be more highly doped with lower sheet resistance and higher carrier density, when undergoing the same diffusion process as a planar Si surface for comparison. This has been confirmed experimentally by several different measurement techniques and explained partly by the increased surface area and different topology in a simulation. This result first and foremost presents a challenge, since the nanostructured solar cells in this work tend to be too highly doped, unintentionally. This causes increased Auger recombination in the emitter and has probably degraded the efficiency of the fabricated cells in this work. On the other hand, knowing the actual sheet resistance of doped nanostructured surfaces may improve the efficiency of black Si solar cells, simply by controlling the sheet resistance and adjusting for the differences observed in order to e.g. minimize Auger recombination.

From an industrial application perspective this result also presents a promising opportunity to decrease the overall thermal budget of large-scale, industrial thermal diffusion processes, required and used for all emitter formations in the vast majority of the solar industry: If RIE-texturing is applied to industrial Si solar cells, conventional emitters (with sheet resistance of 60-80 Ω/sq.) and selective emitters (with sheet resistance of 100-120 Ω/sq.) may be formed at a lower thermal budget due to the lower sheet resistance on nanostructured Si for a given diffusion process, as described in this work. The thermal budget may be decreased by reduced time, temperature or a combination of the two.

Chapter 7

Outlook

7.1 New Cell Concepts with Black Si

This part of the outlook presents several new black Si solar cell concepts that have all been initially tested, but not completed, in this work. Future work will focus on actual cell fabrication using these novel concepts.

7.1.1 LDSE cell with ALD passivation

Based on the successful combination of black Si texturing and a laser-doped selective emitter (LDSE) cell design presented in Chapter 5 and the excellent surface passivation obtained by ALD Al_2O_3 presented in Chapter 6 a combination of the two concepts seems promising: Since Al is a p-type dopant to Si, and the Al_2O_3 passivation layer is deposited on the nanostructured front of the cell, laser doping a selective emitter is enabled without the need for additional spin-on dopant (such as phosphoric acid), which is otherwise required for 'standard' LDSE cells. Laser doping with Al through Al_2O_3 layers has been thoroughly investigated and reported [118, 119], but has mostly been used on the rear of PER_x-type cells [120, 121]. To our knowledge the combination of front ALD Al_2O_3 passivation and laser doping on black Si has not yet been reported. The cell structure suggested here consists of an n-type substrate with a lightly boron-doped p-type emitter on the front, diffused n-type back-surface field, ALD Al_2O_3 passivation on the RIE-textured front and laser-doped front contacts metallized by subsequent Ni/Cu-plating. The structure is schematically shown in Figure 7.1. This cell type possesses all the features of a high-efficiency cell, without employing any costly or non-scalable process steps such as photolithography: Popularly phrased the excellent absorptance of black Si enables high short-circuit current, the excellent passivation by ALD enables high open-circuit voltage and the laser-doped, Ni/Cu-plated contacts enable high fill factor. The cell sketch in Figure 7.1 includes rear passivation with local openings. This is not necessarily a required feature, but a passivated rear should improve V_{OC} of the device and if laser doping or simply local laser opening is used, a PER_x-type cell could be realized without any use of photolithography.

This cell type was initially fabricated as a proof-of-concept. Unfortunately, the available laser for this test was a pulsed laser with nano- or pico-second laser pulse

Al
SiO$_2$
Al$_2$O$_3$

SiN:x
Cu
Ni
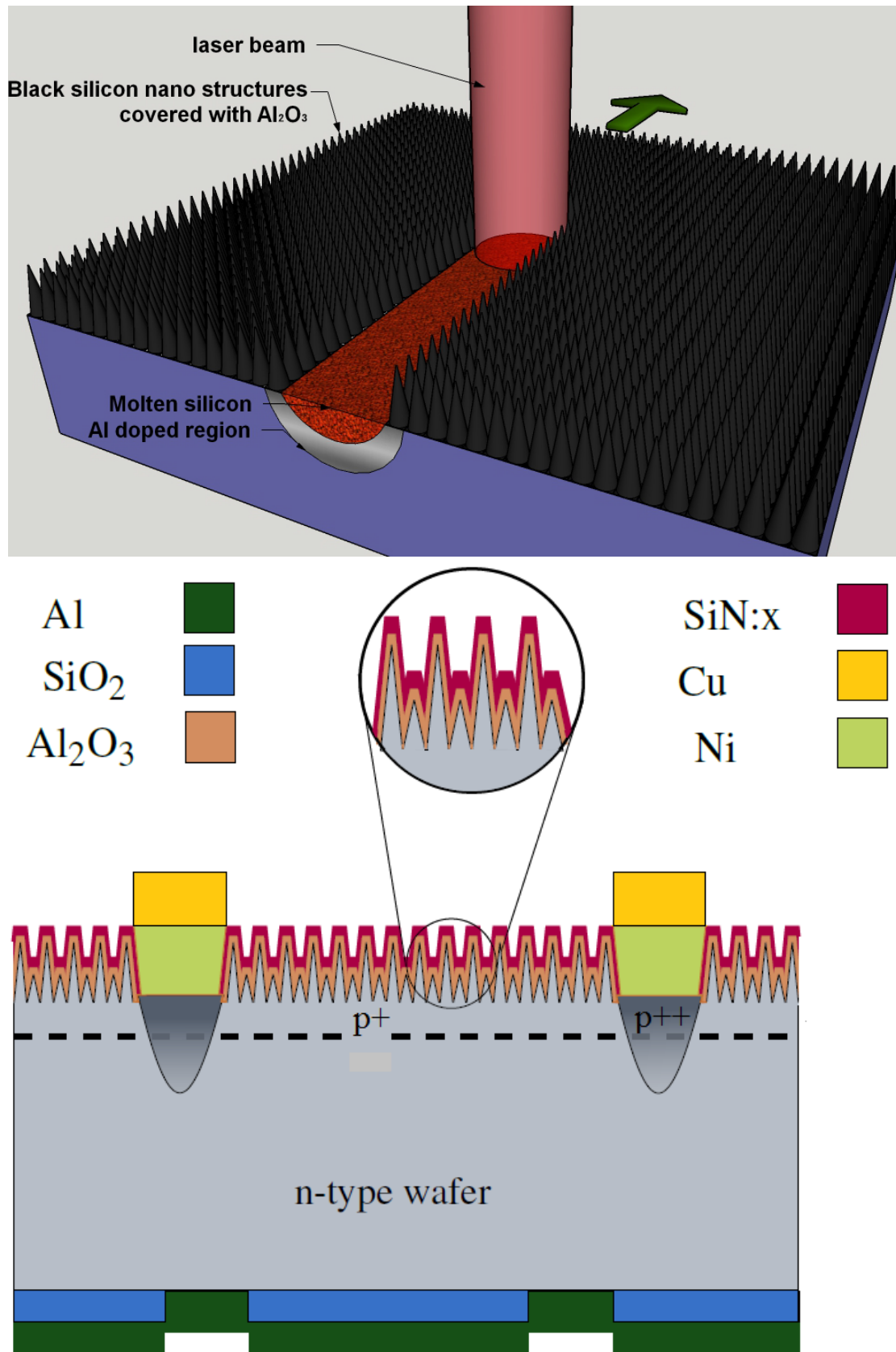
FIGURE 7.1: Illustration of laser doping on ALD Al$_2$O$_3$ passivated black Si (top) and sketch of the ALD Al$_2$O$_3$ passivated, LDSE black Si cell (bottom). Courtesy of Johannes N. Hansen and Patrick L. Mouritzen.
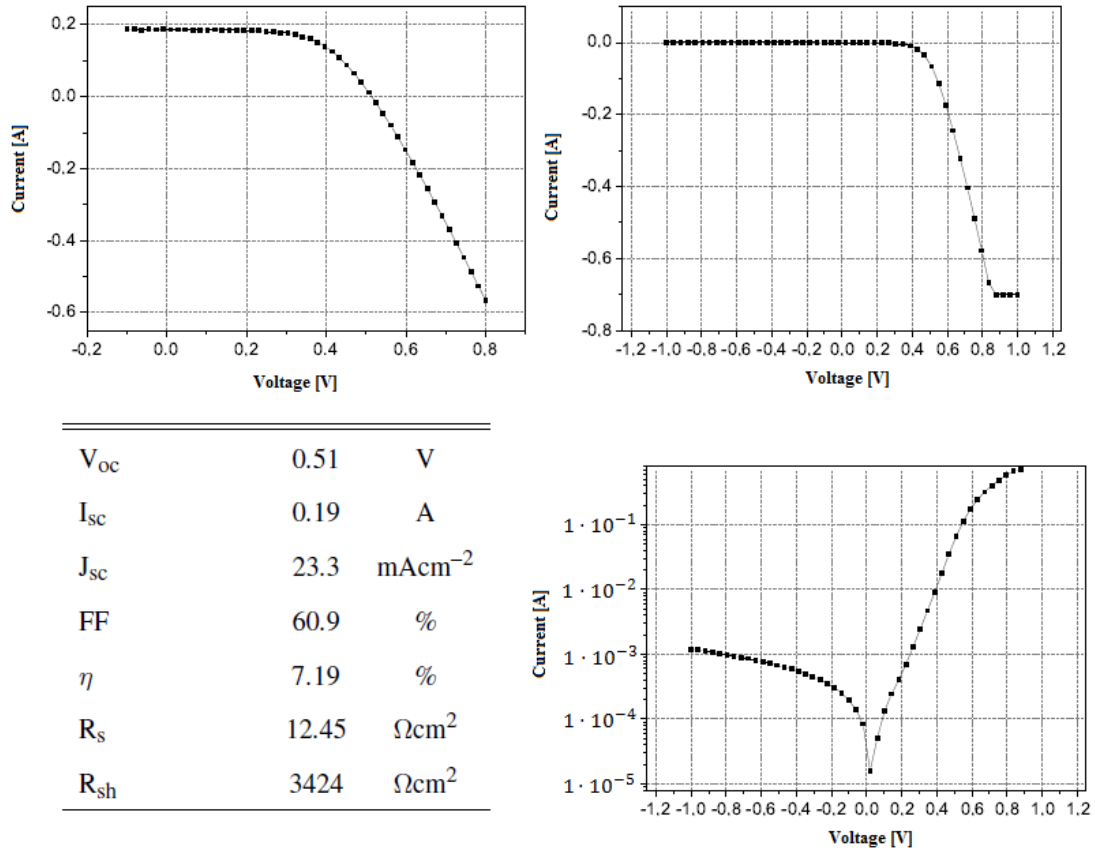
FIGURE 7.2: Initial IV-results of the ALD-passivated, LDSE black Si cell. The figure consists of light IV-curve (top,left), dark IV-curve (top,right), dark IV-curve on semi-log plot (bottom, right) and table with the IV-data (bottom, left).

length, which is not as suitable for laser doping as a continuous wave laser, which was used for the cell described in Chapter 5. The initial cell results are shown in Figure 7.2. The result in Figure 7.2 shows that both current and voltage of the first Al laser-doped black Si cell is too low. This is most probably due to a non-ideal diode, which the dark-IV curve on semi-log plot also reveals. The inverse slope of the linear part of the dark IV-curve on semi-log plot was calculated to 147.43 mV/decade, which corresponds to an ideality factor above 2. This indicates that the selective emitter formed by boron diffusion and subsequent local Al laser doping was not successful. Two main reasons for this were identified:

- Due to a processing error in the boron diffusion the emitter was initially too highly doped, which was solved by a dry etch-back. This may imply a too thin, too lightly doped and non-uniform emitter.

- The Al laser doping resulted in extremely high concentrations of Al, which most probably exceeded the desired range for local laser doping. An Al-Si eutectic might have been formed, which alone could explain the non-ideal diode behaviour.

Figure 7.3 shows the EQE measurement of the cell. The measurement reveals a significant drop in EQE at a wavelength of ~ 450 nm, indicating significant carrier loss in the emitter region, since the absorption length of 450 nm wavelength photons is ~ 240 nm,
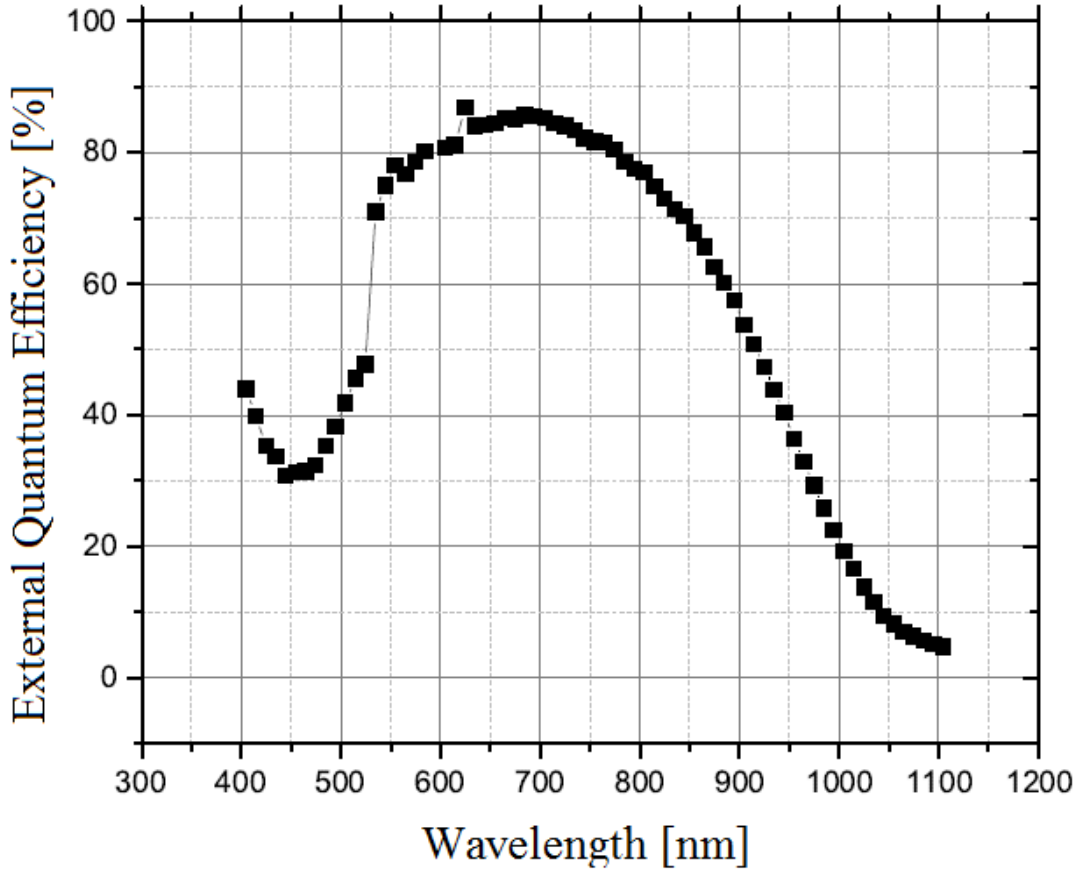
FIGURE 7.3: External Quantum Efficiency (EQE) measurement of the
ALD-passivated, LDSE black Si cell.

which is the top part of the emitter, where the Al concentration resulting from laser
doping is presumably too high. Furthermore, the long wavelength response is too low
probably due to a non-optimized rear, which was patterned with the same pulsed laser
as the front. The fact that the laser doping resulted in too high concentrations of Al was
concluded by SIMS-analysis and calculation of the incorporated dose of Al. The result
of the SIMS-measurement is shown in Figure 7.4. The SIMS-measurement in Figure 7.4
shows a very high Al concentration in the green regions of the ion image, where Al was
diffused into Si by laser doping. Based on the SIMS-data the incorporated dose of Al
was calculated to 1×10^{18} cm^{-2}, whereas the dose of Al in 30 nm Al_2O_3 is 1.4×10^{17}
cm^{-2} according to equation 7.1

$$ C(\text{Al}) = 2\frac{\rho_\text{b}}{M_\text{W}}N_\text{A}t = 2\frac{4 \text{ g/cm}^3}{101.96 \text{ g/mol}}6.022 \times 10^{23} \text{ mol}^{-1} \cdot 30 \text{ nm} = 1.4 \cdot 10^{17} \text{ cm}^{-2} \quad (7.1) $$

where ρ_b is the density of Al_2O_3, M_W is the molar mass of Al_2O_3, N_A is Avogadro's
constant and t is the thickness of the Al_2O_3 layer. The factor of 2 is due to the two
Al atoms in Al_2O_3. Obviously the incorporated dose of Al cannot exceed the available
dose in the passivation layer, so the SIMS-measurement must be slightly inaccurate,
probably due to very high Al concentrations close to the surface. However, this does
not change the fact that the observed Al concentration is very high, which could explain
the non-ideal diode behaviour.
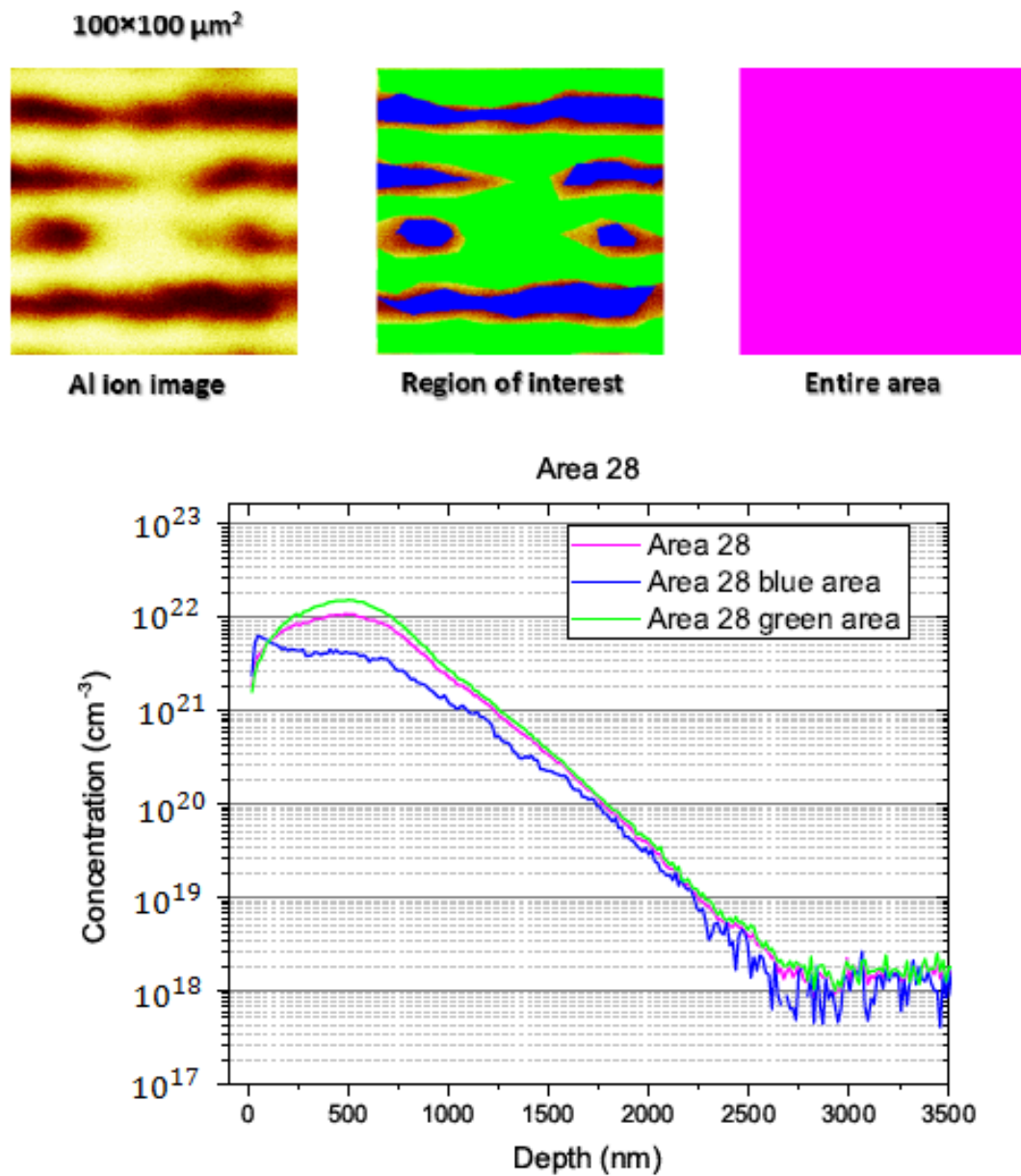
FIGURE 7.4: SIMS-measurement of laser-doped Al region of the ALD-passivated, LDSE black Si cell. The figure consists of Al ion images (top) showing the Al laser-doped regions of interest (green) and the SIMS-measurement (bottom) of the three different regions of the sample.

In order to obtain a much more controlled diffusion of Al by laser doping a continuous wave laser should be used. If an ideality factor close to 1 can be realized and the unintentional etch-back of the boron emitter can be avoided, this cell type should be able to achieve higher power conversion efficiency than the black Si LDSE solar cells presented in Chapter 5 based on the superior passivation quality of ALD Al_2O_3 passivation compared to PECVD SiN_x:H on black Si.

7.1.2 Heterojunction Cell

Based on the excellent lifetime results for black Si passivated with a tunnel-oxide and doped poly-Si presented in Chapter 6, a novel cell structure based on this combination of plasma texturing and a doped poly-Si hetero-junction seems like a promising candidate for a high-efficiency cell structure. The record-efficiency HIT-cells presented by Panasonic [42] and Glunz *et al.* [126], respectively, possess almost ideal electrical properties, but still rely on conventional, alkaline front surface texturing. This means a direct optical loss of at least 2% due to front reflectance. If black Si can be successfully incorporated in a front or rear contacted HIT-cell without compromising the optical properties of black Si or the passivation quality of the hetero-junction, it should be possible to realize a very high power conversion efficiency. Furthermore, the single-side nature of plasma texturing enables advanced rear cell designs, such as local, passivated contacts. Based on these considerations, we suggest three different HIT-type cell structures with black Si texturing:

- n-type cell with diffused boron emitter on the front, ALD Al_2O_3 front passivation and tunnel-oxide/n-type doped poly-Si as rear passivation, which also generates the n^+ back-surface field

- p-type cell with tunnel-oxide/n-type doped poly-Si on the front, acting as front passivation and front pn-(hetero)junction. The rear may be Al screen-printed, with a resulting conventional Al back-surface field, or passivated by tunnel-oxide/p-type doped poly-Si.

- n-type interdigitated-back-contact (IBC) cell with tunnel-oxide/n-type doped poly-Si on the front, acting as front passivation and n^+ front surface field. The rear may be a 'standard' IBC structure with diffused local n^+ and p^+ regions, but may also consist of local heterojunctions made by the tunnel-oxide/doped poly-Si approach. At least the n-type doped poly-Si is obvious to use on the rear as well, since it is automatically deposited on both sides of the wafer in the LPCVD process suggested here.

Figure 7.5 shows schematic drawings of the three suggested HIT-type cell structures to be combined with black Si.

7.1.3 Thin Black Si Cells

Since the Si wafer itself accounts for about 80% of the total cost of manufacturing a conventional Si solar cell, there is a strong commercial and technological interest in realizing thinner Si solar cells. Currently conventional crystalline Si cells are made from
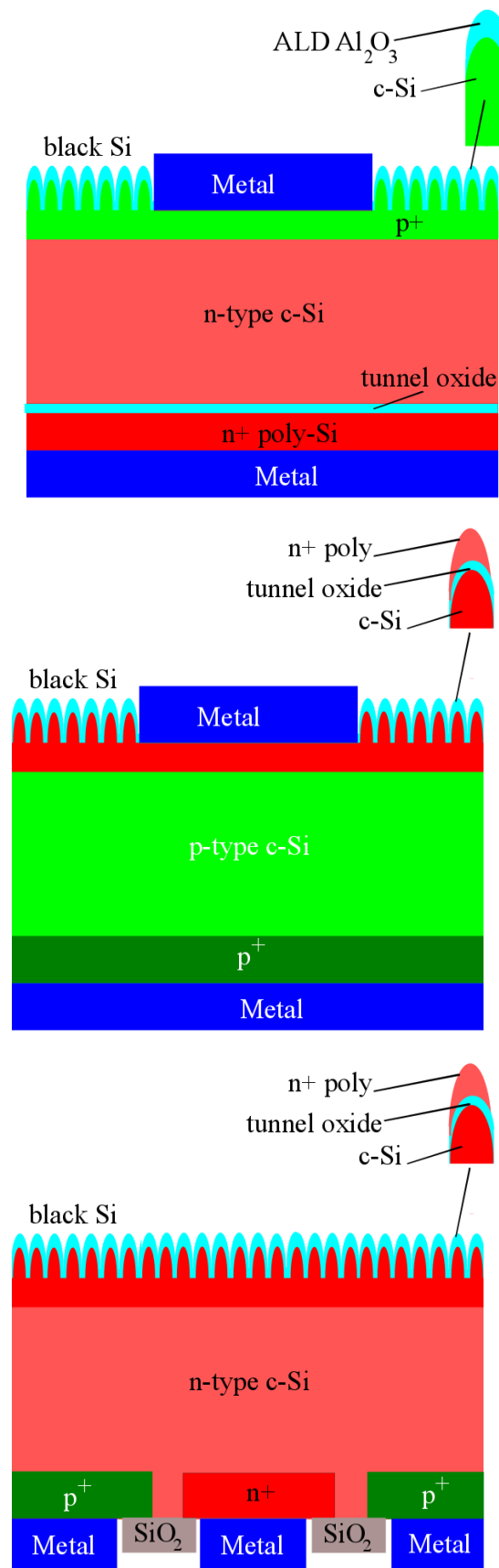
FIGURE 7.5: Schematic drawing of three different proposed HIT-type black Si cells. (top) n-type cell with diffused boron emitter on the front, ALD Al_2O_3 front passivation and tunnel-oxide/n-type doped poly-Si as rear passivation, (middle) p-type cell with tunnel-oxide/n-type doped poly-Si on the front and (bottom) n-type interdigitated-back-contact (IBC) cell with tunnel-oxide/n-type doped poly-Si on the front.
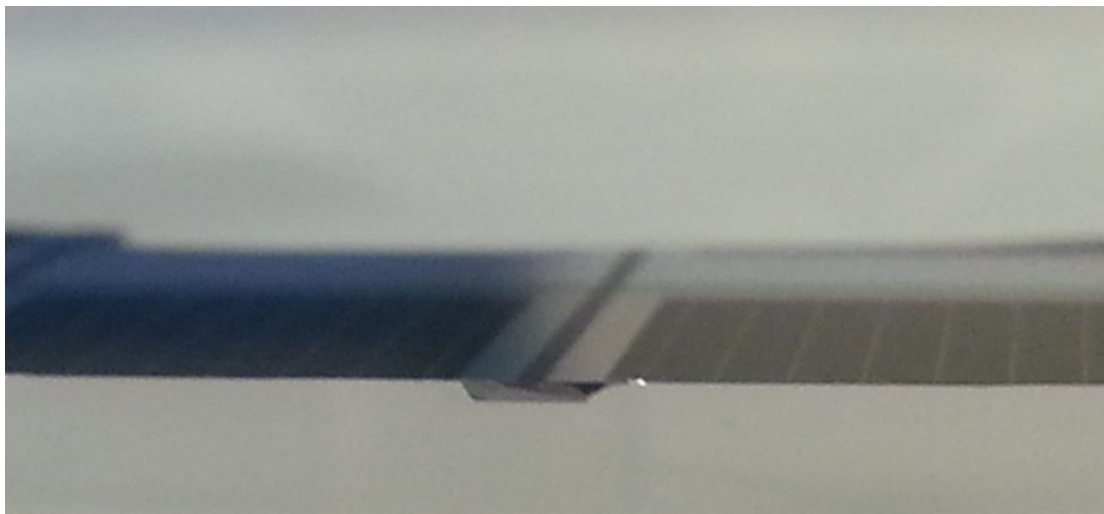
FIGURE 7.6: Photograph of 20 μm thin black Si solar cells shown in profile. The thick region in the middle of the image is the 350 μm backbone between two adjacent 20 μm thin membranes that were processed into complete black Si solar cells. Courtesy of Jeppe Ormstrup and Martin L. Ommen.

160-180 μm Czochralski grown Si substrates, but in theory the optimum efficiency may be achieved with much thinner wafers [127–129, 131]. However, the wafer thickness is currently limited by the kerf-loss when sawing wafer from ingots. Kerf-loss means the amount of Si material, which is removed by the saw and therefore lost from an economic perspective. Solutions to this problem could either be novel techniques for wafering, such as laser or diamond-wire sawing, or novel ways of producing Si wafers, such as epitaxial growth, exfoliation and zone-melting of Si. Several research groups [132–136] and companies such as Solexel, 1366 Technologies, NexWafe and Sharp [137–140] have published results on Si solar cells with thicknesses ranging from 20 to 150 μm. A discussion about the feasibility and potential of these wafer technologies is out of the scope of this work.

However, the increased attention towards much thinner Si wafers introduces a challenge in terms of front texturing, which maskless RIE as suggested here, may solve: When the wafer thickness is reduced below 50 μm, conventional alkaline texturing (such as KOH or NaOH etching) is no longer feasible, simply because such etching process removes 10-15 μm of Si from each side of the wafer, leaving a wafer too thin to handle, if any wafer at all. In other words, such thin wafers need a novel texturing method, which removes significantly less Si while ensuring sufficient light absorption in order to achieve high photo-current and efficiency. This is exactly the properties of black Si produced by maskless RIE, as presented in this work.

Due to this potential, different batches of thin black Si solar cells have been produced during this work. Unfortunately, the efficiency of these cells was too low, primarily due to unoptimized process flows. However, the ability to texture Si wafers with thicknesses down to 20 μm and produce functioning solar cells, indicates that maskless RIE is a promising texturing method for thin Si solar cells in the future. Figure 7.6 shows a photograph of a 20 μm thin black Si cell. The thick region is the 350 μm backbone between two adjacent 20 μm thin membranes, etched down in a 350 μm thick CZ Si wafer and processed into complete black Si solar cells.

7.2 Maskless RIE for rear local contact openings

This section contains results and discussion from the publication entitled "Maskless Nanostructure Definition of Submicron Rear Contact Areas for Advanced Solar Cell Designs" [130] seen in Appendix I.

Besides applying maskless RIE as front texturing for Si solar cells, it was also briefly investigated to apply a slightly adjusted RIE-process in order to masklessly define the local contact areas of advanced cell concept, in which a passivated rear with local contact openings is a main feature and reason for the high efficiencies obtained.

Mask-less reactive ion etching (RIE) has been used for several different applications such as front surface texturing of solar cells [11, 20, 63, 89] and surface-enhanced raman spectroscopy [141]. The primary advantage of mask-less RIE is the ability to define nano-structured topologies with very specific pitch and size in a controlled manner without the use of photolithography. This ability allows for scalable fabrication of nano-scale topologies that would otherwise be impossible or at least require extensive, costly photolithography processing. An example of the need for precise definition of micro- and nano-scale features in a semiconductor device, which normally requires photolithography, is the locally diffused and contacted backside of advanced silicon solar cells such as the passivated emitter rear locally diffused (PERL) world record solar cell [46]. The PERL solar cell and similar advanced cell concepts achieve higher power conversion efficiencies than conventional Si solar cells due to their passivated backside, which reduces rear surface effective recombination velocity (SRV), while allowing for backside Si-metal contacts in locally defined highly doped areas only.

The optimal design of the rear surface of a solar cell must strike a compromise between minimized series resistance and minimized surface recombination, since minimization of the series resistance requires some metallization which increases the effective SRV. Here we consider a backside topology with metallized point contacts – assumed disc shaped with radius a – arranged on a square grid of pitch p on a silicon wafer of thickness W and resistivity ϱ_{b}. As a result only a fraction $f = \pi a^2/p^2$ of the surface is contacted. The metallized contacts have an effective surface recombination velocity S_{cont} as referred the bulk, which may be significantly lower than that at the metal-semiconductor interface ($S_{\mathrm{met}} \leq 10^7$ cm/s) due to the doping profile that may be present below the contact. The remaining part of the surface is assumed to be well passivated with the surface recombination velocity S_{pass}.

The spreading resistance of the individual point contacts may be calculated from the approximate expression due to Cox and Strack [**?**], and if the contacts are non-interacting the total resistance can be obtained simply from a parallel connection of such point contacts. The contacts are, however, interacting and thus heuristic corrections must be made in order to obtain closed form expressions for the specific series resistance. The specific series resistance $R_{\mathrm{s,rear}}$ must ultimately be larger than that of the substrate material $\varrho_{\mathrm{b}}W$. In the literature quite accurate expressions for the specific series resistance exists [143–145], and thus we have

$$R_{\mathrm{s,rear}} = \varrho_{\mathrm{b}}W \left[\frac{p}{2W\sqrt{\pi f}} \arctan\left(\frac{2W}{p} \sqrt{\frac{\pi}{f}} \right) - \exp\left(-\frac{W}{p} \right) \right] + \varrho_{\mathrm{b}}W, \qquad (7.2)$$

Parameter	Description	Value	Unit
D_p	Hole diffusion constant	11.6	cm^2/s
W	Wafer thickness	200	μm
ϱ_b	Wafer resistivity	1	Ω cm
S_cont	Contact recombination velocity	55	cm/s
S_pass	Passivated recombination velocity	5	cm/s

TABLE 7.1: Parameters used in calculations of specific series resistance and effective rear surface recombination velocity, respectively.

where the first term is reminiscent of the Cox and Strack expression, the last term is the bulk substrate specific resistance and the second term a heuristic correction [143] related to the contact interaction, i.e. it assures that the expression is correct also in the large pitch limit. In the case of small contacts and low pitch compared to the wafer thickness $R_\text{s,rear} \simeq \varrho_\text{b} W + \pi \varrho_\text{b} p/(4\sqrt{\pi f})$ to a good approximation. Note, in Eq. 7.2 the specific contact resistance of the metal-semiconductor junction is ignored, since well behaved contacts have specific contact resistances on the order 10^{-6} Ω cm^2.

As discussed by Fischer [143] the effective surface recombination velocity of the heterogeneous point contacted surface is also related to the Cox and Strack expression as is evident from this expression for the effective SRV, $S_\text{rear,eff}$, of a point-contacted, passivated rear surface [142, 143]

$$S_\text{rear,eff} = \frac{D_\text{p}}{W} \left[\frac{p}{2W\sqrt{\pi f}} \arctan\left(\frac{2W}{p} \sqrt{\frac{\pi}{f}} \right) - \exp\left(-\frac{W}{p} \right) + \frac{D_\text{p}}{fWS_\text{cont}} \right]^{-1} + \frac{S_\text{pass}}{1-f},$$
(7.3)

where D_p is the hole diffusivity. The first two terms are recognized from the series resistance expression, the third term is a correction for finite SRV at the contacts, while the last term corrects for the SRV at the passivated surface. The passivation correction deserves a comment: the form shown is the so-called "large scale" correction, but in the present work the "small scale" correction $(1-f)S_\text{pass}$ may be more appropriate as discussed by Fisher [143]. Nevertheless, with parameters used here (see Table 7.1) the third term in the bracket of Eq. 7.3 is dominant, and then the intuitive and simple expression $S_\text{rear,eff} \simeq fS_\text{cont} + (1-f)S_\text{pass}$ is valid to a very good approximation.

Figure 7.7 shows values of SRV and specific series resistance calculated from Eqs. 7.2 and 7.3 as function of metal coverage and contact pitch, respectively. In the calculations the parameters in Table 7.1 are used.

Figure 7.7(a) shows that the effective rear SRV does not change significantly with the contact pitch, when the metal coverage is fixed in perfect agreement with the discussion above, where the SRV was shown to depend almost entirely on the metallized fraction f and the two SRV's of the heterogeneous surface, and is thus almost independent on the pitch.

The specific series resistance decreases with decreasing contact pitch, due to higher contact density. For pitches in the range $0-0.03$ cm the specific series resistance remains below 0.5 Ω cm^2, which is the upper limit of the specific series resistance required to

FIGURE 7.7: Calculation of rear surface recombination velocity and series resistance, respectively, of a silicon solar cell (a) as a function of the pitch between contact openings on the passivated rear with a fixed metal coverage of 1% and (b) as a function of the metal coverage on the rear for a fixed pitch of 1 and 250 μm, respectively.

obtain high fill factors [145, 147]. Figure 7.7(b) shows that the metal coverage should be minimized in order to minimize rear SRV, as expected from the discussion above. The specific series resistance does not change significantly with metal coverage, when the pitch is small, e.g. fixed at 1 μm. When the pitch is sufficiently small, the spreading resistance contribution becomes small, even at very small metal coverages. For a fixed pitch of 250 μm, which is approximately the design of the PERL solar cell [46, 145], the spreading resistance contribution becomes important and thus the specific series resistance increases dramatically for metal coverages below $\sim 1\%$. This is in agreement with the actual design of the PERL solar cell, which has a metal coverage of $\sim 1\%$ [46, 145]. Based on the combined results in Figure 7.7, it appears that the contact pitch should be minimized, while the metal coverage is kept in the range $1-5\%$, in order to optimize the solar cell performance. At a fixed contact pitch of 1μm a 1% metal coverage corresponds to contact windows with ~ 100 nm diameter.

The calculation of SRV was also done for the case of local contacts without any diffusion, such as in a Passivated Emitter and Rear Cell (PERC) [59]. In this case it is assumed that the contact SRV is $S_{\mathrm{cont}} = 10^7$ cm/s. Figure 7.8 shows the result of this calculation. When the contact SRV is sufficiently high, the first two terms in equation 7.3 are comparable to the third term, and then the pitch influences the effective SRV. Furthermore, the metal coverage must be low enough to mitigate the large SRV of the metallized areas. The result in Figure 7.8 shows shows that for non-diffused local contacts ($S_{\mathrm{cont}} = 10^7$ cm/s) the contact pitch must be at least 30 μm and the metal coverage less than 0.05% in order to obtain sufficiently low effective SRV, i.e. below $\sim$ 1000 cm/s. These two requirements yield a maximum contact diameter below 1 μm.

We present a completely mask-less process allowing for controlled definition of local contact areas on a passivated Si surface. The process results in submicron feature size and controllable pitch between contact openings without use of lithography. Figure 7.9 shows a sketch of the process flow used in this novel technique.

The technique consists of a mask-less RIE process, which defines $\sim$ 500 nm tall nano-pillars with $\sim$ 100 nm diameter on the Si surface. The entire surface is then passivated using 30 nm SiO$_2$ deposited by plasma-enhanced chemical vapor deposition (PECVD). Then 200 nm Al is deposited on the surface by e-beam evaporation. Due to the nano-pillar topology and the poor step coverage of the evaporation process, the sidewalls of the nano-pillars are not covered with Al. This enables selective removal of the nano-pillars using buffered hydrofluoric acid (bHF) to etch SiO$_2$ and isotropic RIE masked by Al to etch Si. The isotropic etch leaves local openings whose pitch and size are defined by the initial nano-pillar topology of the otherwise passivated and metallized surface. Figure 7.10 shows SEM images of the surface before and after the isotropic RIE, respectively.

The topology in Figure 7.10 shows local contact areas of $\sim$ 100 nm in diameter, allowing for a much lower pitch than photolithographically defined patterns, while maintaining the targeted metal coverage of $1-5\%$. Although techniques such as electron-beam and advanced optical lithography allow for definition of even smaller pattern dimensions, the cost of such processes is much higher and the scalability much lower than that of the technique presented in this work.

The pillar density of the topology in Figure 7.10 is ~ 3 μm^{-2} [141], which corresponds to a potential metal coverage of 2.4% assuming cylindrical pillars with diameters of 100 nm. Such metal coverage is exactly within the range $1-5\%$ that simultaneously
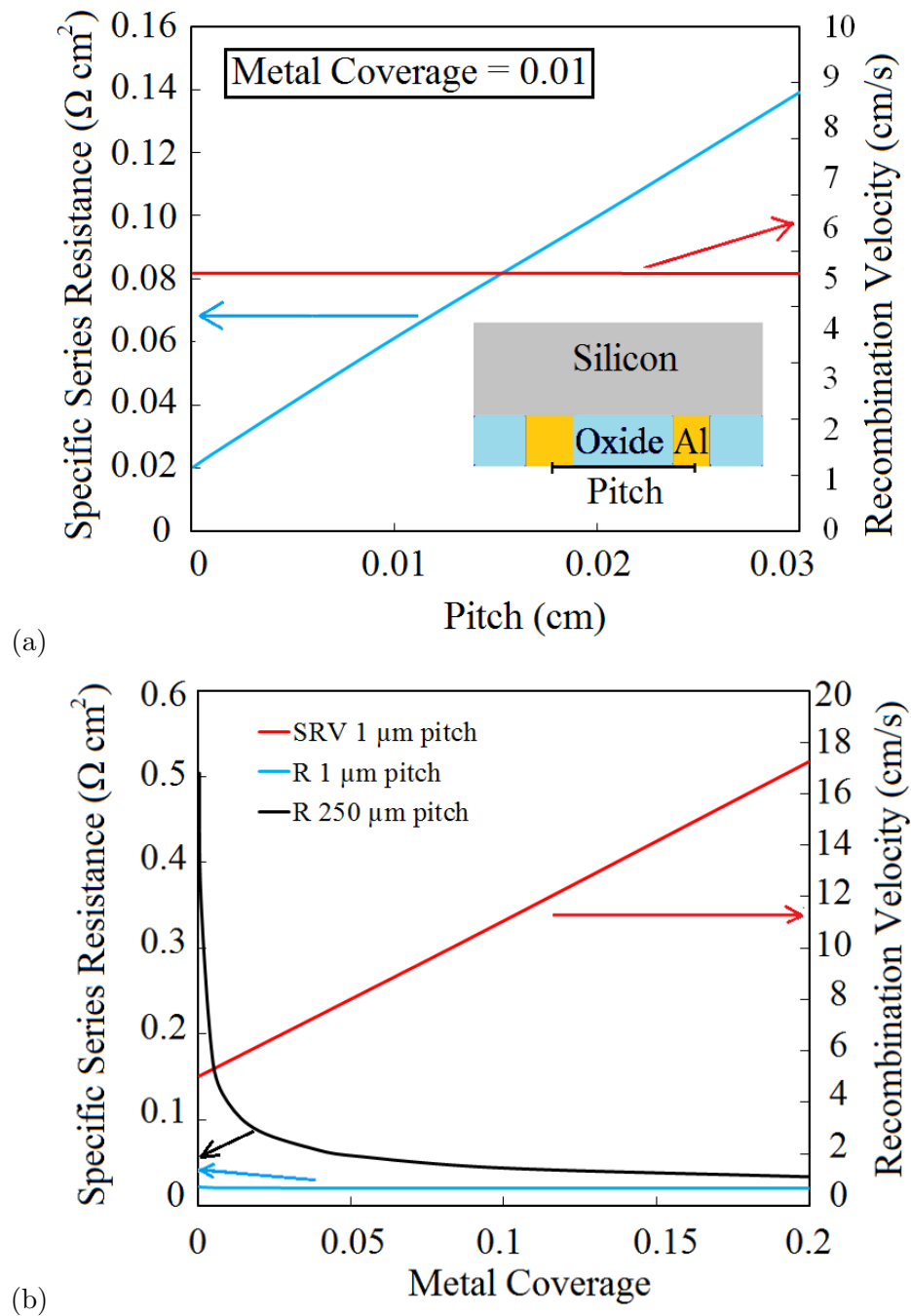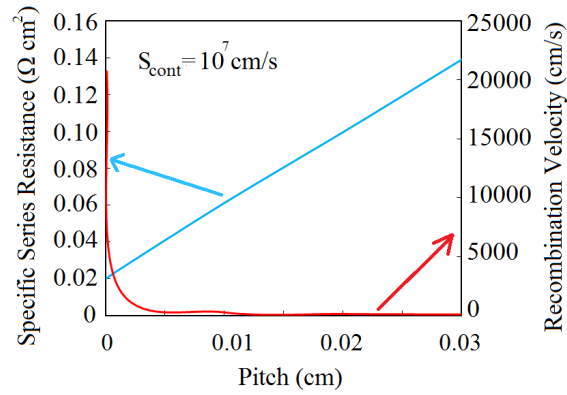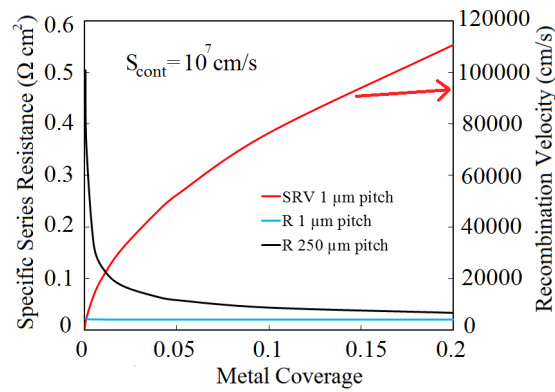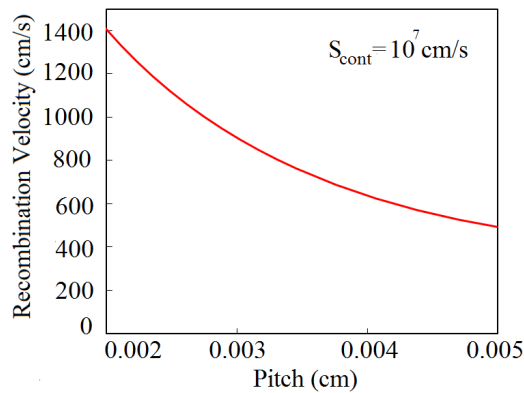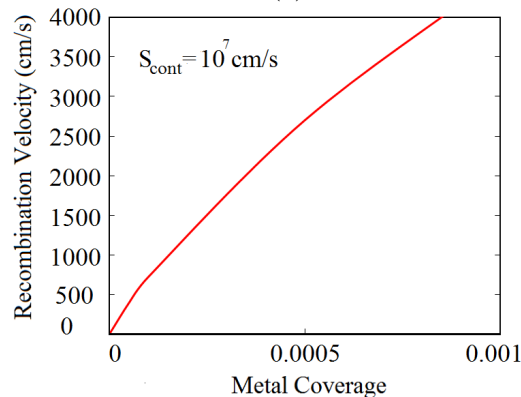
FIGURE 7.8: Calculation of rear surface recombination velocity and specific series resistance, respectively, of a silicon solar cell as a function of the pitch (a) between contact openings on the passivated rear with a fixed metal coverage of 1% and (b) as a function of the metal coverage on the rear for a fixed pitch of 1 and 250 μm, respectively. The contact SRV was changed to $S_{cont} = 10^7$ cm/s. (c)-(d) shows the same result for smaller pitch and metal coverage for clarity.
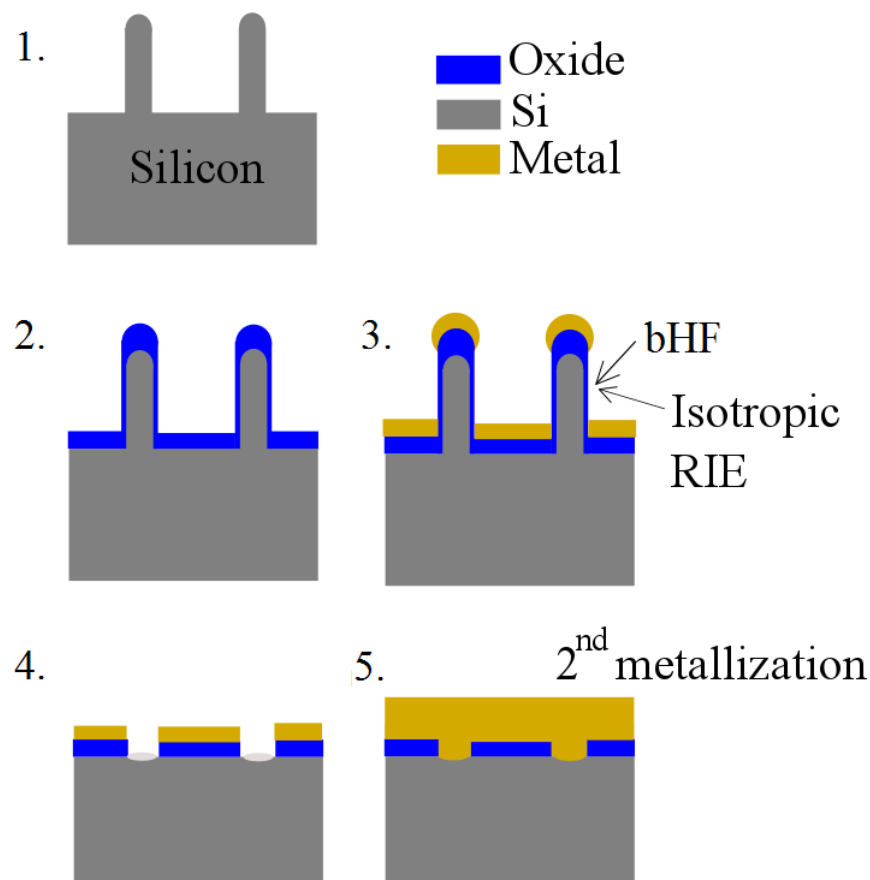
FIGURE 7.9: Sketch of the process flow consisting of 1) maskless nanopillar etch, 2) SiO$_2$ passivation by PECVD, 3) Al evaporation, 4) buffer HF (bHF) and isotropic RIE of pillar sidewalls and 5) second metallization plus optional doping.

minimizes SRV and keeps the rear specific series resistance below $\sim 0.5\ \Omega$ cm^2, required for high fill factors [145, 147], and as shown in Figure 7.7. Minimized pitch at a constant metal coverage in the range $1 - 5\%$, directly implies minimized contact diameter. The initial results of this work show contact openings of ~ 100 nm in diameter, which is significantly smaller than rear contact openings considered elsewhere [147–149].

For the case of non-diffused local contacts with much higher S_{cont}, such as the PERC cell, the requirement is a very small metal coverage, in this case below 0.05%, combined with a sufficiently large pitch, in this case at least 30 μm. This requires very small contact openings, in this case with contact diameter smaller than 1 μm. Such rear design would also be enabled with the type of topology seen in Figure 7.10, as long as the contact pitch can be tuned. This should be possible, since the pitch of nanopillars fabricated by maskless RIE may be tuned in numerous ways, e.g. by varying the chamber pressure, as demonstrated in [141].

Photolithographically defined contacts typically used in PERL solar cells [46, 142] and the more industrially feasible laser-patterned contacts [150–152] are both limited to contact windows well above 1 μm in diameter. Therefore the feature size of ~ 100 nm combined with 2.4% metal coverage demonstrated in this work shows the potential for further optimization of locally defined rear contacts for high-efficiency solar cells, such as the PERL cell, by using the mask-less RIE technique presented in this work.
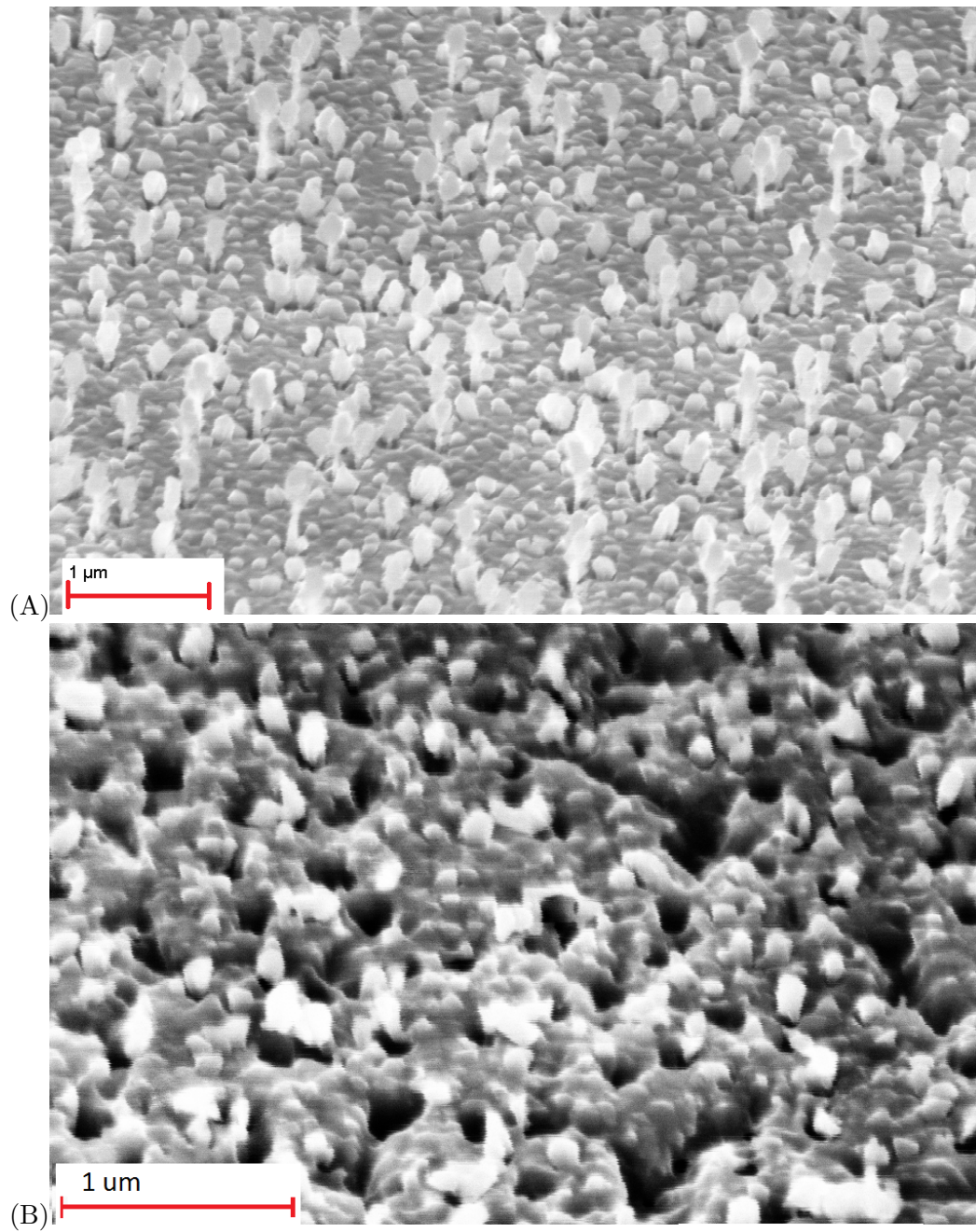
FIGURE 7.10: SEM-image of the nanopillar surface covered with Al before (A) and after (B) isotropic RIE, respectively. The pillar density is $\sim 3~\mu\mathrm{m}^{-2}$, which corresponds to a potential metal coverage of 2.4%. The etching process has removed most of the nanopillars and created holes in the passivated Si surface covered with metal.

7.3 Industrial Application

An important part of this outlook is the potential for industrial implementation of the maskless RIE-texturing, presented in this thesis. As mentioned in the introduction, the fundamental requirements for introducing new cell technology to the solar industry are (a) a reduction of the $/W_p$ production cost and (b) scalability to the solar industry throughput of $\sim$ 3000 wafers/hour. Both of these requirements may only be verified by actually testing the new technology, in this case RIE-texturing, at industry scale and measure the $/W_p$ production cost and throughput, respectively. Such test was outside the scope of this work, but the following points indicate that implementation of maskless RIE-texturing may be possible:

- This work has confirmed higher power conversion efficiency of RIE-textured cells (18.1%) compared to standard, industrial Si cells ($\sim$ 17-18%). Furthermore, improved passivation schemes and optimized emitter properties are expected to increase the efficiency of black Si cells further in the near future.

- The $/W_p$ depends on the efficiency and production cost of the cells. The production cost of RIE-texturing is not fully known and may only be quantified at industrial scale due to economies of scale. However, a RIE tool is very similar to a PECVD tool, since they both consist of vacuum chambers with gas inlets and a plasma generator. Thus, the cost of a large-scale RIE for texturing may be similar to the cost of a PECVD. Since PECVD is the standard tool for AR-coatings in the solar industry, its tool cost must be acceptable for the industry. This assumption was also described and used in [153], which concluded a possible cost saving of 3-6% by replacing conventional texturing with maskless RIE-texturing in the solar industry.

- Large-scale, even in-line, RIE equipment dedicated for texturing is actually being developed by Meyer Burger (former Roth & Rau) [74, 75]. The tool is called MaiaTex. This indicates that there are no physical constraints in terms of scaling RIE equipment to the scale and throughput of the solar industry. It also indicates commercial interest from the solar industry and its equipment suppliers, such as Meyer Burger, in developing and implementing RIE-texturing.

Furthermore, RIE-texturing presents certain advantages compared to conventional texturing:

- The single-sided nature of RIE enables and may simplify the fabrication of advanced cell designs.

- Since RIE only removes a few μm from the front of the wafer, RIE-texturing is possible on very thin Si wafers.

- RIE texturing is suitable for texturing novel wafer types, such as kerfless, diamond-wire sawn, laser-cut and quasi-mono crystalline Si wafers, that are otherwise not textured effectively by conventional methods.

- Dry texturing reduces water consumption and may have process and handling advantages compared to wet texturing.

- Dry texturing reduces the CO_2 emission from the solar cell production itself [154] depending on the effectiveness of the abatement system of the RIE system.

These points are all speculative in nature and do only partly represent the complex task of implementing maskless RIE-texturing in the solar industry. Several disadvantages, such as higher cost, lower throughput and limitations on power conversion efficiency due to the recombination issues described in this work, may turn out to be problematic. However, the objective of this industrial outlook is to present the potential of RIE-texturing from a commercial perspective. These considerations have led to intentional process restrictions throughout this work: For instance, the developed RIE-texturing method has been restricted to a maskless, 1-step process, even though multiple steps and/or photolithography could have yielded even higher efficiency in the end. Similarly, Si wafers were restricted to large-area CZ substrates in order to make the developed technology as relevant for the industrial application as possible.

Chapter 8

Conclusion

This thesis has presented results from the PhD project entitled 'Nanostructuring of Solar Cell Surfaces'. The main objective of this PhD project was to develop nanostructured Si solar cells with higher power conversion efficiency using only scalable and cost-efficient production methods. The nanostructures, known as 'black silicon', were fabricated by single-step, maskless reactive ion etching and used as front texturing of different types of Si solar cells. Since the developed RIE-texturing method is a scalable, 1-step process it has the potential of industrial application in the solar industry. For this reason the work has been restricted to industrially feasible materials and processes. This means that no scarce or expensive materials nor processes such as photolithography has been used in the cell fabrication.

In Chapter 2 the theory behind solar cell operation was presented. This included a derivation of the Shockley diode equation. Chapter 2 also described the presented nanostructure topology theoretically as a graded refractive index in a mean-field approximation between air and Si. Furthermore the formation of black Si was explained.

Chapter 3 presented the experimental and simulated results on optical properties of the developed black Si surfaces. Total AM1.5G-weighted average reflectance well below 1%, in some cases below 0.3%, was measured for different crystalline grades of Si and it was shown that the reflectance of RIE-textured Si remains below that of KOH-textured Si at all incident angles below 70°. Furthermore, the integrated average absorptance was measured to 99.2% in the wavelength range 300-900 nm. This gave rise to a calculated pathlength enhancement for black Si of 20 at a wavelength of $\sim$ 1160 nm, which is comparable to the pathlength enhancement for upright and inverted pyramid texturing with AR-coating.

Chapter 4 presented the fabrication and characterization of RIE- and conventionally textured, screen-printed Si solar cells on 'industrial, large-area' 156x156 mm^2 CZ Si wafers. A power conversion efficiency of 16.5% was obtained for the batch of large-area RIE-textured Si solar cells. The efficiency of the KOH-textured reference cell was 17.8%. Quantum Efficiency measurements and carrier loss analysis showed that the lower efficiency of the RIE-textured cells was primarily due to increased emitter and surface recombination. The large-area screen-printed solar cells were furthermore characterized at varying incident angles. The angle between the cell and the light source was varied in two axes in combination and the current-voltage characteristic was measured for each angle combination. The angle-dependent analysis showed that RIE-textured cells have a higher normalized power output averaged over the range of incident angles between 0 and 90°. This result indicates the potential of improved cell performance and higher

output power at diffuse light conditions and during daily and yearly operation.

Chapter 5 presented the fabrication and characterization of the second batch of RIE-textured solar cells with laser-doped selective emitters (LDSE). A power conversion efficiency of 18.1% and a fill factor of 80.1% was obtained by laser doping and subsequent light-induced plating of a Ni/Cu stack in combination with RIE-texturing. The obtained fill factor of 80.1% is to our knowledge the highest fill factor reported for black Si. The obtained efficiency of 18.1% is the highest efficiency obtained for the black Si solar cells in this work and is comparable with the best cell results reported in literature for front-contacted black Si solar cells. The efficiency is especially encouraging considering the significant observed spurious plating, which accounts for $\sim 4\%$ additional reflection loss. Furthermore the front surface passivation and emitter sheet resistance were not optimized for the best black Si LDSE cell. Thus, the first black Si LDSE solar cell presented in this thesis is considered a proof-of-concept and shows the potential for improved efficiency of RIE-textured solar cells, especially when laser doping on black Si is combined with improved surface passivation schemes such as atomic layer deposition (ALD) of Al_2O_3. In Chapter 6 the passivation quality of ALD Al_2O_3 on black Si was investigated, yielding surface recombination velocity (SRV) below 80 cm/s and implied open-circuit voltage (iV_{OC}) of 680 mV. Combining such electrical properties with the excellent optical properties of black Si presented in Chapter 3, could significantly increase the power conversion efficiency of black Si solar cells in the future. The combination of ALD Al_2O_3 and laser doping on a RIE-textured black Si surface was initially tested, although the obtained efficiencies were very low, probably due to a too high Al concentration resulting from a non-optimized laser doping. This cell type will be further investigated in future studies.

Chapter 6 furthermore presented an even more promising passivation scheme for black Si, consisting of a 1.2 nm tunnel oxide and doped poly-Si stack. Such passivation layer yielded SRV of 20 cm/s and iV_{OC} of 695 mV for black Si. PC1D calculations showed that such passivation qualities combined with the optical properties of black Si could result in 0.4% absolute efficiency improvement over conventionally textured cells and up to 22% power conversion efficiency for black Si cells, without applying any advanced cell designs. In Chapter 6 the emitter formation on nanostructured Si was also investigated. Based on ECV, micro four-point probe and Hall measurements it was shown that the same dopant diffusion process yields lower sheet resistance, deeper pn-junction and higher sheet carrier density on nanostructured Si compared to planar. This information is crucial when fabricating black Si solar cells in the future. Furthermore the result shows the potential of reduced thermal budget in the solar industry, if RIE-texturing replaces conventional texturing, which would require the diffusion process to be adjusted accordingly.

Chapter 7 presented the outlook of the thesis, focusing on novel solar cell concepts based on nanostructured Si. Firstly, the combination of laser-doping and ALD Al_2O_3 passivation on black Si was presented. Secondly, the concept of hetero-junction cells on black Si employing the promising passivation quality of tunnel-oxide and doped poly-Si in combination was presented. Such passivation schemes could completely solve the issue of increased surface recombination of RIE-textured Si. Both front-contacted and interdigitated-back-contacted cell concepts were introduced. Chapter 7 also presented the potential of using maskless RIE to texture thinner Si solar cells. For wafer thicknesses below ~ 50 μm, conventional texturing methods, such as KOH-texturing, are no longer feasible, while maskless RIE only removes a few μm of the substrate, enabling texturing of very thin Si solar cells. This is potentially a promising application in the solar industry, which increasingly focuses on thinner Si substrates in order to reduce

cost by reducing Si consumption per cell. In addition, Chapter 7 presented a novel concept describing the use of maskless RIE to locally define contact openings on the rear of high-efficiency cells such as the PERL-cell. Definition of contact openings of ~ 100 nm in diameter with a potential metal coverage of 2.4% was presented. Such values are to our knowledge only possible to obtain with much more expensive and non-scalable methods, such as e-beam or advanced optical lithography. This makes the presented technique promising for the fabrication of rear point-contact cells, such as the PERL-cell, since the theoretically ideal rear design has minimized contact diameters combined with a metal coverage in the range of 1-5%. Finally, a few remarks on the potential industrial application of maskless RIE-texturing were given in the last part of this thesis. Since the developed maskless RIE-texturing method is a dry, maskless, 1-step and potentially scalable process, the technique meets the requirements for directly replacing conventional texturing in the solar industry. RIE-texturing may be cost-competitive, since the only required tool, a reactive ion etcher, is comparable in fixed and running cost to a PECVD, which is already implemented in the solar industry. Such tools are already being developed by equipment manufacturers. Furthermore, the excellent optical properties of black Si presented in this work show the potential for increased power conversion efficiency of black Si solar cells. The initial cell results showing efficiencies up to 18.1% and fill factors above 80% are encouraging, since the presented cell was not optimized in terms of passivation, emitter and spurious plating. When these are optimized and when RIE-texturing is combined with the presented passivation techniques, the nanoscale texturing method presented in this work may improve not only power conversion efficiency but the cost-efficiency of silicon solar cells in general.

Bibliography

[1] Herbert, B., "Change, Intergovernmental Panel On Climate, Climate Change 2007: The physical science basis." Agenda 6.07 (2007): 333

[2] Root, T.L., Price, J.T., Hall, K.R., Schneider, S.H., Rosenzweig, C., Pounds, J.A., "Fingerprints of global warming on wild animals and plants" Nature **421**, 57-60 (2003), doi:10.1038/nature01333

[3] Jenkinson, D.S., Adams, D.E., Wild, A., "Model estimates of CO2 emissions from soil in response to global warming" Nature **351**, (1991) 304-306, doi:10.1038/351304a0

[4] Cohen, J.E., "Human Population: The Next Half Century", Science **302** 5648 (2003), 1172-1175, doi:10.1126/science.1088665

[5] Hand, M.M., Baldwin, S.; DeMeo, E.; Reilly, J.M.; Mai, T.; Arent, D.; Porro, G.; Meshek, M.; Sandor, D., "Renewable Electricity Futures Study" National Renewable Energy Laboratory, eds. 4 vols. (2012) NREL/TP-6A20-52409.

[6] Tester, J. W., "Sustainable energy: choosing among options", MIT press, 2005.

[7] Crabtree, G. W., Lewis, N. S., "Solar energy conversion", Physics Today, **60** 3 (2007) pp. 37-42.

[8] International Energy Agency (IEA), "2014 Key World Energy Statistics", 2012, pp. 6, 24, 28

[9] Kost, C., Mayer, J. N., Thomsen, J., Hartmann, N., Senkpiel, C., Philipps, S., Nold, S., Lude, S., Saad, N., Schlegl, T., "Levelized cost of electricity renewable energy technologies" (2013), Fraunhofer Institute for Solar Energy Systems - ISE.

[10] Priolo, F., Gregorkiewicz, T., Galli, M., Krauss, T.F., "Silicon nanostructures for photonics and photovoltaics", Nature Nanotechnology **9** 19-32 (2014) DOI: 10.1038/NNANO.2013.271.

[11] Davidsen, R.S., Nordseth, Ø., Boisen, A., Schmidt, M.S., Hansen, O., "Plasma texturing on large-area industrial grade CZ silicon solar cells", 28th EU PVSEC Conference Proceedings (2013).

[12] Zhu, J., Yu, Z., Fan, S., Cui, Y., "Nanostructured photon management for high performance solar cells", Materials Science and Engineering R **70** 330–340 (2010)

[13] Nguyen, K.N., Abi-Saab, D., Basset, P., Richalot, E., Marty, F., Angelescu, D., Leprince-Wang, Y., Bourouina, T., "Black silicon with sub-percent reflectivity: Influence of the 3D texturization geometry", Solid-State Sensors, Actuators and Microsystems Conference (Transducers), 16th International Transducers **11** 354-357 (2011).

[14] Kelzenberg, M.D., Boettcher, S.W., Petykiewicz, J.A., Turner-Evans, D.B., Putnam, M.C., Warren, E.L., Spurgeon, J.M., Briggs, R.M., Lewis, N.S., Atwater, H.A., "Enhanced absorption and carrier collection in Si wire arrays for photovoltaic applications", Nature Materials **9** 239–244 (2010), DOI: 10.1038/NMAT2635.

[15] Huang, Y-F., Chattopadhyay, S., Jen, Y-J., Peng, C-Y., Liu, T-A., Hsu, Y-K., Pan, C-L., Lo, H-C., Hsu, C-H., Chang, Y-H., Lee, C-S., Chen, K-H., Chen, L-C., "Improved broadband and quasiomnidirectional anti-reflection properties with biomimetic silicon nanostructures", Nature Nanotechnology **2** 770 - 774 (2007).

[16] Parretta, A., Sarno, A., Tortora, P., Yakubu, H., Maddalena, P., Zhao, J., Wang, A., "Angle-dependent reflectance measurements on photovoltaic materials and solar cells", Optics Communications **172** 139-151 (1999).

[17] Zhao, L., Zuo, Y.H., Zhou, C.L., Li, H.L., Diao, H.W., Wang, W.J., "Theoretical investigation on the absorption enhancement of the crystalline silicon solar cells by pyramid texture coated with SiNx:H layer", Solar Energy **85** 530-537 (2011).

[18] Macdonald, D., Cuevas, A., Kerr, M., Samundsett, C., Ruby, D., Winderbaum, S., Leo, A., "Texturing Industrial Multicrystalline Silicon Solar Cells", Solar Energy **76** No.1 277-283 (2004)

[19] Rahman, A., Ashraf,A., Xin, H., Tong, X., Sutter, P., Eisaman, M.D., Black, C.T., "Sub-50-nm self-assembled nanotextures for enhanced broadband antireflection in silicon solar cells", Nature Communications **6**, 5963 (2015), DOI: 10.1038/ncomms6963

[20] Liu, X., Coxon, P.R., Peters, M., Hoex, B., Cole, J.M., Fray, D.J., "Black Silicon: Fabrication methods, properties, and solar energy applications", Review Article, Energy & Environmental Science, Royal Society of Chemistry **7** 3223-3263 (2014) DOI: 10.1039/c4ee01152j.

[21] Allen, T., Bullock, J., Cuevas, A., Baker-Finch, S., Karouta, F. "Reactive ion etched black silicon texturing: A comparative study", In Photovoltaic Specialist Conference (PVSC), IEEE **40th**, pp. 0562-0566, IEEE (2014), doi:10.1109/PVSC.2014.6924983

[22] Otto, M., Algasinger, M., Branz, H., Gesemann, B., Gimpel, T., Füchsel, K., Käsebier, T., Kontermann, S., Koynov, S., Li, X., Naumann, V., Oh, J., Sprafke, A.N., Ziegler, J., Zilk, M., Wehrspohn, R.B., "Black Silicon Photovoltaics", Advanced Optical Materials, **3** 2, 147-164 (2015), doi: 10.1002/adom.201400395

[23] Hsu, C. H., Wu, J. R., Lu, Y. T., Flood, D. J., Barron, A. R., Chen, L. C., "Fabrication and characteristics of black silicon for solar cell applications: An overview", Materials Science in Semiconductor Processing, **25**, 2-17 (2014).

[24] Glunz., S.,"High Efficiency Silicon Solar Cells - Research and Production", Proceedings for the European PV Solar Energy Conference 2012 (Keynote), (2012).

[25] The American Society for Testing and Materials, "Standard tables for reference solar spectral inrradiances", G-0173-03e (2006).

[26] Kopp, G., and J. L. Lean, "A new, lower value of total solar irradiance: Evidence and climate significance", Geophys. Res. Lett. **38** L01706 (2011), doi:10.1029/2010GL045777

[27] Becquerel, A-E., "Mémoire sur les effets électriques produits sous l'influence des rayons solaires.", Comptes Rendus 9.567 (1839).

[28] Adams, W. G., Day, R. E., "The action of light on selenium", Philosophical Transactions of the Royal Society of London, 313-349 (1877).

[29] Fritts, C. E., "On a new form of selenium cell, and some electrical discoveries made by its use", American Journal of Science, **156**, 465-472 (1883).

[30] Grondahl, L. O., "Theories of a new solid junction rectifier", Science, **64** 1656, 306-308 (1926).

[31] Ohl, R. S. "Light-sensitive electric device including silicon" USA patent, 2443542 (1941).

[32] Chapin, D. M., Fuller, C. S., Pearson, G. L., "A new silicon p-n junction photocell for converting solar radiation into electrical power", Journal of Applied Physics, **25**, 676-677 (1954).

[33] Green, M. A., Emery, K., Hishikawa, Y., Warta, W., Dunlop, E. D., "Solar cell efficiency tables (Version 45)", Progress in photovoltaics: research and applications, **23** 1, 1-9 (2015), doi: 10.1002/pip.2573

[34] Connolly, J. P., Mencaraglia, D., "III–V Solar Cells", Materials Challenges: Inorganic Photovoltaic Solar Energy, **12**, 209 (2014).

[35] Krogstrup, P., Jørgensen, H. I., Heiss, M., Demichel, O., Holm, J. V., Aagesen, M., Nygard, J., i Morral, A. F., "Single-nanowire solar cells beyond the Shockley-Queisser limit", Nature Photonics, **7** 4, 306-310 (2013), doi:10.1038/nphoton.2013.32

[36] Kayes, B. M., Nie, H., Twist, R., Spruytte, S. G., Reinhardt, F., Kizilyalli, I. C., Higashi, G. S., "27.6% Conversion efficiency, a new record for single-junction solar cells under 1 sun illumination", In Photovoltaic Specialists Conference (PVSC), 2011 37th IEEE, pp. 4-8, IEEE (2011).

[37] Keavney, C., Haven, V., Vernon, S., "Emitter structures in MOCVD InP solar cells", In Photovoltaic Specialists Conference, 1990, Conference Record of the Twenty First IEEE, pp. 141-144, IEEE (1990).

[38] Chopra, K. L., Paulson, P. D., Dutta, V., "Thin-film solar cells: an overview", Progress in Photovoltaics, **12** 2-3, 69-92 (2004), doi: 10.1002/pip.541

[39] Donolato, C., "A reciprocity theorem for charge collection", Applied Physics Letters, **46** 3, 270-272 (1985), doi:10.1063/1.95654

[40] Green, M.A., "Silicon Solar Cells: Advanced Principles & Practice", Textbook, University of New South Wales, (1995).

[41] Philipps, S., Warmuth, W., "Photovoltaics Report", Fraunhofer ISE (2015), https://www.ise.fraunhofer.de/en/downloads-englisch/pdf-files-englisch/photovoltaics-report-slides.pdf

[42] Masuko, K., Shigematsu, M., Hashiguchi, T., Fujishima, D., Kai, M., Yoshimura, N., Yamaguchi, T., Ichihashi, Y., Mishima, T., Matsubara, N., Yamanishi, T., Takahama, T., Taguchi, M., Maruyama, E., Okamoto, S., "Achievement of More Than 25% Conversion Efficiency With Crystalline Silicon Heterojunction Solar Cell", Photovoltaics, IEEE Journal of, **4** 6, pp.1433-1435, (2014) doi: 10.1109/JPHO-TOV.2014.2352151

[43] Shockley, W., Queisser, H. J., "Detailed balance limit of efficiency of p-n junction solar cells", Journal of applied physics, **32** 3, 510-519 (1961).

[44] Tiedje, T., Yablonovitch, E., Cody, G. D., Brooks, B. G., "Limiting efficiency of silicon solar cells", Electron Devices, IEEE Transactions on, **31** 5, 711-716 (1984).

[45] Gu, X., Yu, X., Guo, K., Chen, L., Wang, D., Yang, D. "Seed-assisted cast quasi-single crystalline silicon for photovoltaic application: towards high efficiency and low cost silicon solar cells", Solar Energy Materials and Solar Cells, **101**, 95-101 ISO 690 (2012).

[46] Green, M.A., "Silicon solar cells: State-of-the-art", Phil. Trans. R. Soc. A **371** (2013), DOI: dx.doi.org/10.1098/rsta.2011.0413

[47] Rounsaville, B., Cooper, I. B., Tate, K., Kadish, M., Das, A., Rohatgi, A., "Analysis of cast mono-crystalline ingot characteristics with applications to solar cells" In Photovoltaic Specialists Conference (PVSC), 2012 38th IEEE (pp. 3009-3014) IEEE, ISO 690 (2012)

[48] Yin, W., Wang, X., Zhang, F., Zhang, L.,"19.6% cast mono-MWT solar cells and 268 W modules", In Photovoltaic Specialists Conference (PVSC), Volume 2, 2012 IEEE 38th (pp. 1-5). IEEE, ISO 690 (2012).

[49] Neuhaus, D. H., Münzer, A., "Industrial silicon wafer solar cells", Advances in OptoElectronics, 24521, 1-15 (2007), doi:10.1155/2007/24521

[50] Birmann, K., Zimmer, M., Rentsch, J. "Controlling the surface tension of alkaline etching solutions", Proceedings of the 24th European Photovoltaic Solar Energy Conference (2009).

[51] King, D. L., Buck, M. E., "Experimental optimization of an anisotropic etching process for random texturization of silicon solar cells", Photovoltaic Specialists Conference, Conference Record of the Twenty Second IEEE, p. 303-308, (1991), doi:10.1109/PVSC.1991.169228

[52] Wefringhaus, E., Helfricht, A., "KOH/surfactant as an alternative to KOH/IPA for texturisation of monocrystalline silicon", Proceedings 24th EU PVSEC, Hamburg, Germany, 1860-2 (2009).

[53] Einhaus, R., Vazsonyi, E., Szlufcik, J., Nijs, J., Mertens, R., "Isotropic texturing of multicrystalline silicon wafers with acidic texturing solutions [solar cell manufacture]" Photovoltaic Specialists Conference, Conference Record of the Twenty-Sixth IEEE, p. 167-170 (1997), doi:10.1109/PVSC.1997.654055

[54] Schultz, O., Emanuel, G., Glunz, S. W., Willeke, G. P., "Texturing of multicrystalline silicon with acidic wet chemical etching and plasma etching", Photovoltaic Energy Conversion, Proceedings of 3rd World Conference on **2**, p. 1360-1363 (2003).

[55] Hezel, R., Schörner, R., "Plasma Si nitride—A promising dielectric to achieve high-quality silicon MIS/IL solar cells", Journal of Applied Physics, **52** 4, p.3076-3079 (1981).

[56] Aberle, A. G., "Overview on SiN surface passivation of crystalline silicon solar cells", Solar Energy Materials and Solar Cells, **65** 1, 239-248 (2001), doi:10.1016/S0927-0248(00)00099-4

[57] Duerinckx, F., Szlufcik, J., "Defect passivation of industrial multicrystalline solar cells based on PECVD silicon nitride", Solar Energy Materials and Solar Cells, **72** 1, 231-246 (2002), doi:10.1016/S0927-0248(01)00170-2

[58] Huster, F., "Aluminum-back surface field: bow investigation and elimination", 20th European Photovoltaic Solar Energy Conference and Exhibition, Barcelona, p.635-638 (2005)

[59] Blakers, A. W., Wang, A., Milne, A. M., Zhao, J., Green, M. A., "22.8% efficient silicon solar cell. Applied Physics Letters, **55** 13, 1363-1365 (1989), doi:10.1063/1.101596

[60] Zhao, J., Wang, A., Green, M.A., "24.5% Efficiency silicon PERT cells on MCZ substrates and 24.7% efficiency PERL cells on FZ substrates." Prog. Photovoltaics: Research & Applications **7** 6, p.471-474 (1999)

[61] Wenham, S. R., Green, M. A., "Self aligning method for forming a selective emitter and metallization in a solar cell", U.S. Patent No. **6,429,037** Washington, DC: U.S. Patent and Trademark Office (2002)

[62] Fairfield, J. M., Schwuttke, G. H., "Silicon diodes made by laser irradiation", Solid-State Electronics, **11** 12, 1175-IN6 (1968).

[63] Oh, J., Yuan, H.C., Branz, H., "An 18.2 %-efficient black-silicon solar cell achieved through control of carrier recombination in nanostructures", Nature Nanotechnology **7** 743-748 (2012).

[64] Lederhandler, S., Giacoletto, L. J., "Measurement of minority carrier lifetime and surface effects in junction devices" Proceedings of the IRE, **43** 4, 477-483 (1955).

[65] Sinton, R. A., Cuevas, A., "Contactless determination of current–voltage characteristics and minority-carrier lifetimes in semiconductors from quasi-steady-state photoconductance data", Applied Physics Letters, **69** 17, 2510-2512 (1996).

[66] Brattain, W. H., Bardeen, J., "Surface properties of germanium" Bell System Technical Journal, **32** 1, 1-41 (1953).

[67] Stevenson, D. T., Keyes, R. J., "Measurements of the recombination velocity at germanium surfaces" Physica, **20** 7, 1041-1046 (1954).

[68] Yablonovitch, E., Allara, D. L., Chang, C. C., Gmitter, T., Bright, T. B., "Unusually low surface-recombination velocity on silicon and germanium surfaces" Physical review letters, **57** 2, 249 (1986).

[69] Planck, M., "On the law of distribution of energy in the normal spectrum", Annalen der Physik, **4** 553, 1., (1901).

[70] Rau, U. "Reciprocity relation between photovoltaic quantum efficiency and electroluminescent emission of solar cells", Physical Review B, **76** 8, 085303 (2007).

[71] Green, M. A., "Radiative efficiency of state-of-the-art photovoltaic cells", Progress in Photovoltaics: Research and Applications, **20** 4, 472-476 (2012), doi: 10.1002/pip.1147

[72] Van Roosbroeck, W., Shockley, W., "Photon-radiative recombination of electrons and holes in germanium", Physical Review, **94** 6, 1558 (1954).

[73] Cuevas, A., "The Recombination Parameter J0", Energy Procedia, 55, 53-62 (2014).

[74] Chan, B. T., Kunnen, E., Uhlig, M., de Marneffe, J. F., Xu, K., Boullart, W., Poortmans, J., "Study of SF6/N2O Microwave Plasma for Surface Texturing of Multicrystalline (150 μm) Solar Substrates", Japanese Journal of Applied Physics, **51** 10S, 10NA01 (2012), doi: 10.1143/JJAP.51.10NA01

[75] Sontag, D., Schlemm, H., Köhler, G., Uhlig, M., Sperlich, H.-P., Kehr, M., Vetter, E., "Highly flexible coating system for the PV industry", Article PV Production Annual 2014, Meyer Burger Group (2014)

[76] Gaudig, M., Hirsch, J., Schneider, T., Sprafke, A. N., Ziegler, J., Bernhard, N., Wehrspohn, R. B., "Properties of black silicon obtained at room-temperature by different plasma modes" Journal of Vacuum Science & Technology A, 33(5), 05E132 (2015), doi:10.1116/1.4929540

[77] d'Agostino, R., Flamm, D. L., "Plasma etching of Si and SiO2 in SF6–O2 mixtures", Journal of Applied Physics, **52** 1, 162-167 (1981), doi:10.1063/1.328468

[78] Syau, T., Baliga, B. J., Hamaker, R. W., "Reactive ion etching of silicon trenches using SF 6/O 2 gas mixtures", Journal of The Electrochemical Society, **138** 10, 3076-3081 (1991), doi: 10.1149/1.2085371

[79] Kovacs, G. T., Maluf, N. I., Petersen, K. E., "Bulk micromachining of silicon", Proceedings of the IEEE, **86** 8, 1536-1551, ISO 690 (1998), doi:10.1109/5.704259

[80] Quirk, M., Serda, J., "Semiconductor manufacturing technology (Vol. 1)" Upper Saddle River, NJ: Prentice Hall, (2001)

[81] Plummer, J. D., "Silicon VLSI technology: fundamentals, practice, and modeling", Pearson Education India (2000)

[82] Her, T.H., Finlay, R.J., Wu, C., Deliwala, S., Mazur, E., "Microstructuring of silicon with femtosecond laser pulses", Appl. Phys. Lett. **73** 1673-1675 (1998).

[83] Jansen, H., Deboer, M., Legtenberg, R., Elwenspoek, M., "The Black Silicon Method - a Universal Method for Determining the Parameter Setting of a Fluorine-Based Reactive Ion Etcher in Deep Silicon Trench Etching with Profile Control", Journal of Micromechanics and Microengineering **5** 115-120 (1995).

[84] Chen, G., Kashkoush, I., "Effect of pre-cleaning on texturization of c-Si wafers in a KOH/IPA mixture", ECS Transactions, 25(15), 3-10 (2010).

[85] Green, M. A., Keevers, M. J. "Optical properties of intrinsic silicon at 300 K", Progress in Photovoltaics: Research and Applications, **3** 3, 189-192 (1995).

[86] Davidsen, R. S., Ormstrup, J., Ommen, M. L., Larsen, P. E., Schmidt, M. S., Boisen, A., Nordseth, Ø., Hansen, O., "Angle resolved characterization of nanostructured and conventionally textured silicon solar cells", Solar Energy Materials and Solar Cells **140**, 134-140 (2015), doi:10.1016/j.solmat.2015.04.001

[87] Stephens, R.B., Cody, G.D., "Optical Reflectance and Transmission of a Textured Surface", Thin Solid Films **45** 19-29 (1977)

[88] Davidsen, Rasmus Schmidt; Wu, Kaiyu; Schmidt, Michael Stenbæk; Boisen, Anja; Hansen, Ole, "Simulation and Measurement of Angle Resolved Reflectance from Black Si Surfaces", Proceedings of the 31st European Photovoltaic Solar Energy Conference and Exhibition

[89] Repo, P., Benick, J., Vähänissi, V., Schön, J., von Gastrow, G., Steinhauser, B., Schubert, M.C., Hermle, M., Savin, H., "N-type black silicon solar cells", SiliconPV, Energy Procedia **38** 866-871 (2013).

[90] Yoo, J., "Reactive ion etching (RIE) technique for application in crystalline silicon solar cells", Solar Energy **84** 730-734 (2010).

[91] Wang, W-C., Lin, C-W., Chen, H-J., Chang, C-W., Huang, J-J., Yang, M-J., Tjahjono, B., Huang, J-J., Hsu, W-C., Chen, M-J., "Surface Passivation of Efficient Nanotextured Black Silicon Solar Cells Using Thermal Atomic Layer Deposition", ACS Appl. Mater. Interfaces **5** 9752 - 9759 (2013), doi: dx.doi.org/10.1021/am402889k

[92] Savin, H., Repo, P., von Gastrow, G., Ortega, P., Calle, E., Garín, M., Alcubilla, R., "Black silicon solar cells with interdigitated back-contacts achieve 22.1% efficiency", Nature nanotechnology **10** 624–628 (2015), doi: 10.1038/NNANO.2015.89

[93] Davidsen, R. S., Li, H., To, A., Wang, X., Han, A., An, J., Colwell, J., Chan, C., Wenham, A., Schmidt, M.S., Boisen, A., Hansen, O., Wenham, S., Barnett, A., "Black silicon laser-doped selective emitter solar cell with 18.1% efficiency" Solar Energy Materials and Solar Cells **144**, 740-747 (2016), doi:10.1016/j.solmat.2015.10.018

[94] Kyeong, D., Cho, S-H., Lim, J-K., Lee, K., Hwang, M-I., Lee, W-J., Cho, E.C., "Approaching 20%-efficient selective-emitter solar cells with copper front contacts on industrial 156 mm CZ Si wafers", Proceedings, 27th European Photovoltaic Solar Energy Conference and Exhibition (2012)

[95] Hallam, B., Urueña, A., Russell, R., Aleman, M., Abbott, M., Dang, C., Wenham, S., Tous, L., Poortmans, J., "Efficiency enhancement of i-PERC solar cells by implementation of a laser doped selective emitter", Solar Energy Materials & Solar Cells **134** 89-98 (2015)

[96] Tousa, L., Russella, R., Dasa, J., Labiea, R., Ngamoc, M., Horzela, J., Philipsena, H., Sniekersb, J., Vandermissena, K., van den Brekeld, L., Janssensa, T., Alemana, M., van Dorpa, D.H., Poortmansa, J., Mertens, R., "Large area copper plated silicon solar cell exceeding 19.5% efficiency", 3rd Workshop on Metallization for Crystalline Silicon Solar cells (2011)

[97] Hallam, B., Wenham, S., Sugianto, A., Mai, L., Chong, C., Edwards, M., Jordan, D., Fath, P., "Record Large-Area p-Type CZ Production Cell Efficiency of 19.3% Based on LDSE Technology", IEEE Journal of Photovoltaics **1** No. 1 43-48 (2011)

[98] Wang, X., Allen, V., Vais, V., Zhao, Y., Tjahjono, B., Yao, Y., Wenham, S., Lennon, A., "Laser-doped metal-plated bifacial silicon solar cells", Solar Energy Materials & Solar Cells **131** 37-45 (2014)

[99] Flynn, S., Lennon, A., "Copper penetration in laser-doped selective-emitter silicon solar cells with plated nickel barrier layers", Solar Energy Materials & Solar Cells **130** 309–316 (2014)

[100] Rehman, A.u., Lee, S.H., "Review of the Potential of the Ni/Cu Plating Technique for Crystalline Silicon Solar Cells", Materials **7** 1318-1341 (2014), DOI:10.3390/ma7021318

[101] Geisler, C., Hördt, W., Kluska, S., Mondon, A., Hopman, S., Glatthaar, M., "Overcoming electrical and mechanical challenges of continuous wave laser processing for Ni–Cu plated solar cells", Solar Energy Materials & Solar Cells **133** 48–55 (2015)

[102] Su Zhou, Chunlan Zhou, Wenjing Wang, Junjie Zhu, Yehua Tang, Jingwei Chen, Yan Zhao, "Comprehensive study of light induced plating of nickel and its effect on large area laser doped crystalline solar cells" Solar Energy Materials & Solar Cells **125** 33–38 (2014)

[103] Tjahjono, B. S., "Laser doped selective emitter solar cells", Doctoral dissertation, University of New South Wales, ISO 690 (2010).

[104] Liao, B., Stangl, R., Ma, F., Hameiri, Z., Mueller, T., Chi, D., Aberle, A.G., Bhatia, C.S., Hoex, B., "Deposition temperature independent excellent passivation of highly boron doped silicon emitters by thermal atomic layer deposited Al2O3", Journal of Applied Physics **114** 094505 (2013), doi: 10.1063/1.4819970

[105] Dingemans, G., van de Sanden, M. C. M., Kessels, W. M. M., "Influence of the Deposition Temperature on the c-Si Surface Passivation by Al2O3 Films Synthesized by ALD and PECVD", Electrochemical and Solid-State Letters **13** 3 H76-H79 (2010), doi: 10.1149/1.3276040

[106] Dingemans, G., Seguin, R., Engelhart, P., van de Sanden, M. C. M., Kessels, W. M. M., "Silicon surface passivation by ultrathin Al2O3 films synthesized by thermal and plasma atomic layer deposition", Phys. Status Solidi RRL **4** 1–2 p.10–12 (2010), doi: 10.1002/pssr.200903334

[107] Agostinelli, G., Delabie, A., Vitanov, P., Alexieva, Z., Dekkers, H. F. W., De Wolf, S., Beaucarne, G., "Very low surface recombination velocities on p-type silicon wafers passivated with a dielectric with fixed negative charge", Solar Energy Materials and Solar Cells **90** 18 3438-3443 (2006).

[108] Schmidt, J., Merkle, A., Brendel, R., Hoex, B., Van de Sanden, M. C. M., Kessels, W. M. M., "Surface passivation of high-efficiency silicon solar cells by atomic-layer-deposited Al2O3", Progress in photovoltaics: research and applications, **16** 6 461-466 (2008).

[109] Otto, M., Kroll, M., Käsebier, T., Salzer, R., Tünnermann, A., "Extremely low surface recombination velocities in black silicon passivated by atomic layer deposition", Appl. Phys. Lett. **100** 191603 (2012), doi: 10.1063/1.4714546

[110] Repo, P., Haarahiltunen, A., Sainiemi, L., Yli-Koski, M., Talvitie, H., Schubert, M. C., Savin, H., "Effective passivation of black silicon surfaces by atomic layer deposition", Photovoltaics, IEEE Journal of, **3** 1, 90-94 (2013).

[111] von Gastrow, G., Alcubilla, R., Ortega, P., Yli-Koski, M., Conesa-Boj, S., i Morral, A. F., Savin, H., "Analysis of the Atomic Layer Deposited Al2O3 field-effect passivation in black silicon", Solar Energy Materials and Solar Cells **142**, 29-33 (2015), doi:10.1016/j.solmat.2015.05.027

[112] Benick, J., Hoex, B., Van de Sanden, M. C. M., Kessels, W. M. M., Schultz, O., Glunz, S. W. "High efficiency n-type Si solar cells on Al 2 O 3-passivated boron emitters. Appl. Phys. Lett, **92** 25, 253504-1 (2008).

[113] Sinton, R. A., A. Cuevas, "A quasi-steady-state open-circuit voltage method for solar cell characterization" 16th European Photovoltaic Solar Energy Conference **25** 1152-1155 (2000).

[114] Trupke, T., Bardos, R. A., Abbott, M. D., Cotter, J. E., "Suns-photoluminescence: Contactless determination of current-voltage characteristics of silicon wafers" Applied Physics Letters, **87** 9, 093503 (2005)

[115] Wurfel, P. "The chemical potential of radiation", Journal of Physics C: Solid State Physics, **15** 18, 3967 (1982).

[116] Trupke, T., Bardos, R. A., Schubert, M. C., Warta, W. "Photoluminescence imaging of silicon wafers", Applied Physics Letters, **89** 4, 044107 (2006)

[117] Heiss, M., "Investigation of atomic layer deposition of dielectric layers on black silicon surfaces", B.Sc.-thesis, DTU / TU München (2014).

[118] Lin, D., Abbott, M., Lu, P.H., Xiao, B., Hallam, B., Tjahjono, B., Wenham, S., "Incorporation of deep laser doping to form the rear localized back surface field in high efficiency solar cells", Solar Energy Materials & Solar Cells **130** (2014) 83–90

[119] Harder, N.-P., Larionova, Y., Brendel, R., "Al$^+$-doping of Si by laser ablation of Al2O3/SiN passivation", Phys. Status Solidi A **210** 9 1871–1873 (2013), doi:10.1002/pssa.201329058

[120] E. Cornagliotti, E., Tous, L., Uruena, A., Rothschild, A., Russell, R., Lu, V., Radosavljevic, S., John, J., Toman, J., Aleman, M., Duerinckx, F., Poortmans, J., Szlufcik, J., Dielissen, B., Souren, F., Gay, X, Görtzen, R., Hallam, B., "Integration of spatial ALD aluminum oxide for rear side passivation of p-type PERC/PERL solar cells", 28th EU PVSEC Proceedings (2013), p. 976-981

[121] Saint-Cast, P., Benick, J., Kania, D., Weiss, L., Hofmann, M., Rentsch, J., Glunz, S. W., "High-efficiency c-Si solar cells passivated with ALD and PECVD aluminum oxide" Electron Device Letters, IEEE, 31(7), 695-697 (2010).

[122] Wang, X., Juhl, M., Abbott, M., Hameiri, Z., Yao, Y., Lennon, A. "Use of QSSPC and QSSPL to monitor recombination processes in p-type silicon solar cells", Energy Procedia, **55**, 169-178 (2014), doi: 10.1016/j.egypro.2014.08.110

[123] Cuevas, A., Stocks, M., Macdonald, D., Sinton, R. "Applications of the quasi-steady-state photoconductance technique", Proceedings for the 2nd World PVSEC, Vienna (1998)

[124] Komatsu, Y., Harata, D., Schuring, E. W., Vlooswijk, A. H., Katori, S., Fujita, S., Venema, P.R., Cesar, I., "Calibration of electrochemical capacitance-voltage method on pyramid texture surface using scanning electron microscopy", Energy Procedia **38**, 94-100 (2013), doi:10.1016/j.egypro.2013.07.254

[125] Petersen, D. H., Hansen, O., Lin, R., Nielsen, P. F., "Micro-four-point probe Hall effect measurement method", Journal of Applied Physics, **104** 1, 013710 (2008), doi: 10.1063/1.2949401

[126] S.W. Glunz, F. Feldmann, A. Richter, M. Bivour, C. Reichel, H. Steinkemper, J. Benick, M. Hermle, "The Irresistible Charm of a Simple Current Flow Pattern – Approaching 25% with a Solar Cell Featuring a Full-Area Back Contact", Proceedings, 31st EUPVSEC (2015)

[127] Petti, C., Newman, B., Brainard, R., Li, J., "Optimal thickness for crystalline silicon solar cells", Twin Creek Technologies, Inc., http://howcanihelpsandiego.com/wpcontent/uploads/2012/02/Silicon-Solar-Cell-Optimal-Thickness.

[128] Burgers, A. R., Manshanden, P., Weeber, A. W., Van Straaten, B. H. M., "Influence of wafer thickness on the performance of multicrystalline Si solar cells: an experimental study", Energy Research Centre of the Netherlands ECN (2001).

[129] Sah, C. T., Yamakawa, K. A., Lutwack, R., "Effect of thickness on silicon solar cell efficiency", Electron Devices, IEEE Transactions on, **29** 5, 903-908 (1981).

[130] Davidsen, R.S., Schmidt, M.S., Boisen, A., Hansen, O., "Maskless Nanostructure Definition of Submicron Rear Contact Areas for Advanced Solar Cell Designs" Microelectronic Engineering, Special Issue on Micro/Nano Fabrication (2015)

[131] Brendel, R., Queisser, H. J., "On the thickness dependence of open circuit voltages of pn junction solar cells", Solar energy materials and solar cells **29** 4, 397-401 (1993).

[132] S. Reber, , A. Hurrle, A. Eyer, G. Willeke, "Crystalline silicon thin-film solar cells—recent results at Fraunhofer ISE", Solar Energy **77** 6, p.865–875 (2004).

[133] Radhakrishnan, H.S., Martini, R., Depauw, V., Van Nieuwenhuysen, K., Debucquoy, M., Govaerts, J., Gordon, I., Mertens, R., Poortmans, J., "Improving the Quality of Epitaxial Foils Produced Using a Porous Silicon-based Layer Transfer Process for High-Efficiency Thin-Film Crystalline Silicon Solar Cells," Photovoltaics, IEEE Journal of, **4** 1, pp.70-77 (2014), doi: 10.1109/JPHO-TOV.2013.2282740

[134] Wang, Q., "Thin Crystalline Si PV: Growth, Cell Process and Module Integration", Presentation, PVMC c-S Feedstock/Wafering Workshop, San Francisco, CA, (2012).

[135] Jeong, S., McGehee, M. D., Cui, Y., "All-back-contact ultra-thin silicon nanocone solar cells with 13.7% power conversion efficiency", Nature communications **4** (2013), doi: 10.1038/ncomms3950

[136] Haase, F., Kajari-Schröder, S. and Brendel, R., "High efficiency back-contact back-junction thin-film monocrystalline silicon solar cells from the porous silicon process", Journal of Applied Physics **114**, 194505 (2013), doi:http://dx.doi.org/10.1063/1.4832775

[137] Tomita, T., "C-Si solar cell modules", Progress in Photovoltaics: Research and Applications, **13** 6, p.471-479 (2005), doi: 10.1002/pip.640

[138] Moslehi, M. M., Kapur, P., Kramer, J., Rana, V., Seutter, S., Deshpande, A., Brown, R., "World-record 20%+ efficiency 156 mm x 156 mm full square solar cells using low-cost kerfless ultrathin epitaxial silicon and porous silicon lift-off technology for industry-leading high performance smart PV modules", PV Asia Pacific Conference (APVIA/PVAP) **24** (2012)

[139] Fatemi, H. "Productization and Manufacturing Scaling of High-Efficiency Solar Cell and Module Products Based on a Disruptive Low-Cost, Mono-Crystalline Technology", Contract (NREL) **303**, 275-3000 (2012)

[140] Lorenz, A. "1366 Direct Wafer: Demolishing the Cost Barrier for Silicon Photovoltaics" (No. DOE-1366-04738), 1366 Technologies (2013)

[141] Schmidt, M.S., Boisen, A., Hübner, J., "Large Area Fabrication of Leaning Silicon Nanopillars for Surface Enhanced Raman Spectroscopy", Advanced Materials **24** 10, p.11-18 (2012)

[142] Benick, J., Hoex, B., van de Sanden, M.C.M., Kessels, W.M.M., Schultz, O., Glunz, S.W., "High efficiency n -type Si solar cells on Al2O3-passivated boron emitters" Appl. Phys. Letters **92**, 253504 (2008).

[143] Fischer, B., "Loss Analysis of Crystalline Silicon Solar Cells using Photoconductance and Quantum Efficiency Measurements" (Thesis), in Fachbereich Physik, pp.198, University of Konstanz (2003).

[144] Wolf, A., Biro, D., Nekarda, J., Stumpp, S., Kimmerle, A., Mack, S., Preu, R., "Comprehensive analytical model for locally contacted rear surface passivated solar cells", Journal of Applied Physics, **108** 12, 124510 (2012).

[145] Zhao, J., Wang, A., Green, M. A., "Series resistance caused by the localized rear contact in high efficiency silicon solar cells", Solar Energy Materials and Solar Cells, **32** 1, 89-94 (1994).

[146] Lenio, M. A., Howard, J., Lu, D. P. H., Jentschke, F., Augarten, Y., Lennon, A., Wenham, S. R., "Series Resistance Analysis of Passivated Emitter Rear Contact Cells Patterned Using Inkjet Printing", Advances in Materials Science and Engineering **965418** (2012), doi:10.1155/2012/965418

[147] Altermatt, P. P., Heiser, G., Aberle, A. G., Wang, A., Zhao, J., Robinson, S. J., Green, M. A., "Spatially resolved analysis and minimization of resistive losses in high-efficiency Si solar cells", Progress in photovoltaics: research and applications, **4** 6, 399-414 (1996).

[148] Gatz, S., Dullweber, T., Brendel, R., "Evaluation of series resistance losses in screen-printed solar cells with local rear contacts", Photovoltaics, IEEE Journal of, **1** 1, 37-42 (2011).

[149] Gerenton, F., Mandorlo, F., Brette, J. B., Lemiti, M., "Pattern of Partial Rear Contacts for Silicon Solar Cells", Energy Procedia **77**, 677-686 (2015).

[150] Schneiderlöchner, E., Preu, R., Lüdemann, R., Glunz, S. W., "Laser-fired rear contacts for crystalline silicon solar cells", Progress in Photovoltaics: Research and Applications, **10** 1, 29-34 (2002), doi:10.1002/pip.422

[151] Lin, D., Abbott, M., Lu, P. H., Xiao, B., Hallam, B., Tjahjono, B., Wenham, S., "Incorporation of deep laser doping to form the rear localized back surface field in high efficiency solar cells", Solar Energy Materials and Solar Cells **130**, 83-90 (2014), doi:10.1016/j.solmat.2014.06.037

[152] Nekarda, J., Stumpp, S., Gautero, L., Hörteis, M., Grohe, A., Biro, D., Preu, R., "LFC on screen printed aluminium rear side metallization", In Proceedings of the 24th European Photovoltaic Solar Energy Conference, pp. 1411-1415, WIP Renewable Energies Hamburg, Germany (2009).

[153] Nilsonne, H., "Identification and Commercialization of Highly Valuable Manufacturing Innovations", ISO 690 (2012).

[154] Agostinelli, G., Dekkers, H. F. W., De Wolf, S., Beaucarne, G., "Dry etching and texturing processes for crystalline silicon solar cells: sustainability for mass production", 19th European Photovoltaic Solar Energy Conference, EUPVSEC, Paris (2004).

Appendix A

Publications

A.1   Papers

Appendix B:
"Black Silicon Laser-Doped Selective Emitter Solar Cell with 18.1% Efficiency", **Davidsen, Rasmus Schmidt**; Li, Hongzhao; To, Alexander; Wang, Xi; Han, Alex; An, Jack; Colwell, Jack; Chan, Catherine; Wenham, Alison; Schmidt, Michael Stenbæk; Boisen, Anja; Hansen, Ole; Wenham, Stuart; Barnett, Allen.
Published in: Solar Energy Materials & Solar Cells **144** 740–747, 2016.

Appendix C:
"Simulation and Measurement of Angle Resolved Reflectance from Black Si Surfaces"
Davidsen, Rasmus Schmidt; Wu, Kaiyu; Schmidt, Michael Stenbæk; Boisen, Anja; Hansen, Ole.
Published in: Proceedings for 30th European PV Solar Energy Conference and Exhibition (EU PVSEC), 2015.

Appendix D:
"Angle resolved characterization of nanostructured and conventionally textured silicon solar cells", **Davidsen, Rasmus Schmidt**; Ormstrup, Jeppe; Ommen, Martin Lind; Larsen, Peter Emil; Schmidt, Michael Stenbæk; Boisen, Anja; Nordseth, Ørnulf; Hansen, Ole.
Published In: Solar Energy Materials & Solar Cells, Vol. 140, 2015, p. 134-140.

Appendix E:
"Inkjet Patterned ALD Aluminium Oxide for Rear PERC Metal Contacts", To, Alexander; **Davidsen, Rasmus Schmidt**; An, Xinrui ; Lennon, Alison ; Barnett, Allen.
Published In: Proceedings of the 42nd IEEE Photovoltaic Specialists Conference. IEEE, 2015.

Appendix F:
"Improvement of Infrared Detectors for Tissue Oximetry using Black Silicon Nanostructures", Petersen, Søren Dahl; **Davidsen, Rasmus Schmidt**; Alcala, Lucia R.; Schmidt, Michael Stenbæk; Boisen, Anja; Hansen, Ole; Thomsen, Erik Vilain.

Published In: Procedia Engineering, Vol. 87, 2014, p. 652-655.

Appendix G:
"Plasma etching on large-area mono-, multi- and quasi-mono crystalline silicon", **Davidsen, Rasmus Schmidt**; Schmidt, Michael Stenbæk; Boisen, Anja; Hansen, Ole.
Published In: Proceedings of the 39th International Conference on Micro and Nano Engineering, 2013.

Appendix H:
"Plasma texturing on large-area industrial grade CZ silicon solar cells", **Davidsen, Rasmus Schmidt**; Nordseth, Ørnulf ; Boisen, Anja; Schmidt, Michael Stenbæk; Hansen, Ole.
Published In: Proceedings for 28th European PV Solar Energy Conference and Exhibition (EU PVSEC), 2013.

Appendix I:
"Maskless Nanostructure Definition of Submicron Rear Contact Areas for Advanced Solar Cell Designs", **Davidsen, Rasmus Schmidt**; Schmidt, Michael Stenbæk; Boisen, Anja; Hansen, Ole.
Submitted to: Micro-Electronics Engineering, Micro/Nanofabrication 2015, October 2015.

A.2   Posters

"Maskless Nanostructure Definition of Submicron Rear Contact Areas for Advanced Solar Cell Designs" **Davidsen, Rasmus Schmidt**; Schmidt, Michael Stenbæk; Boisen, Anja; Hansen, Ole.
Poster session presented at 41th International Conference on Micro and Nano Engineering (MNE), 2015, Haag, The Netherlands.

"Simulation and Measurement of Angle Resolved Reflectance from Black Si Surfaces" **Davidsen, Rasmus Schmidt**; Wu, Kaiyu; Schmidt, Michael Stenbæk; Boisen, Anja; Hansen, Ole.
Poster session presented at 30th European PV Solar Energy Conference and Exhibition (EU PVSEC), 2015, Hamburg, Germany.

"Plasma etching on large-area mono-, multi- and quasi-mono crystalline silicon", **Davidsen, Rasmus Schmidt**; Schmidt, Michael Stenbæk; Boisen, Anja; Hansen, Ole.
Poster session presented at 39th International Conference on Micro and Nano Engineering (MNE), 2013, London, United Kingdom.

"Plasma texturing on large-area industrial grade CZ silicon solar cells", **Davidsen, Rasmus Schmidt**; Nordseth, Ørnulf; Schmidt, Michael Stenbæk; Boisen, Anja;

Hansen, Ole.
Poster session presented at 28th European PV Solar Energy Conference and Exhibition
(EU PVSEC), 2013, Paris, France.

A.3 Patents

"Plasma texturing method for silicon solar cells"
Patent Nr. PCT/DK2014/050305
Filing / Priority Date: 27-9-2013

"A photodetector for use in spatially resolved spectroscopy applications"
Patent Nr. 14188236.5-1504 / EP14188236
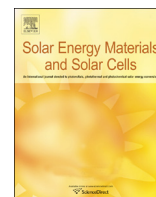Filing / Priority Date: 5-9-2014

Appendix B

Black Silicon Laser-Doped Selective Emitter Solar Cell with 18.1% Efficiency

Authors:
Rasmus Schmidt Davidsen, Hongzhao Li, Alexander To, Xi Wang, Alex Han, Jack An, Jack Colwell, Catherine Chan, Alison Wenham, Michael Stenbæk Schmidt, Anja Boisen, Ole Hansen, Stuart Wenham, Allen Barnett

Black silicon laser-doped selective emitter solar cell with 18.1% efficiency

Rasmus Schmidt Davidsen [a,*], Hongzhao Li [c], Alexander To [c], Xi Wang [c], Alex Han [c], Jack An [c], Jack Colwell [c], Catherine Chan [c], Alison Wenham [c], Michael Stenbæk Schmidt [a], Anja Boisen [a], Ole Hansen [a,b], Stuart Wenham [c], Allen Barnett [c]

[a] Department of Micro- and Nanotechnology, Technical University of Denmark (DTU), Denmark
[b] Danish National Research Foundation's Center for Individual Nanoparticle Functionality (CINF), Technical University of Denmark, DK-2800 Kgs.Lyngby, Denmark
[c] School of Photovoltaic and Renewable Energy Engineering, UNSW Australia, Sydney 2052, NSW, Australia

ARTICLE INFO

ABSTRACT

We report fabrication of nanostructured, laser-doped selective emitter (LDSE) silicon solar cells with power conversion efficiency of 18.1% and a fill factor (FF) of 80.1%. The nanostructured solar cells were realized through a single step, mask-less, scalable reactive ion etch (RIE) texturing of the surface. The selective emitter was formed by means of laser doping using a continuous wave (CW) laser and subsequent contact formation using light-induced plating of Ni and Cu. The combination of RIE-texturing and a LDSE cell design has to our knowledge not been demonstrated previously. The resulting efficiency indicates a promising potential, especially considering that the cell reported in this work is the first proof-of-concept and that the fabricated cell is not fully optimized in terms of plating, emitter sheet resistance and surface passivation. Due to the scalable nature and simplicity of RIE-texturing as well as the LDSE process, we consider this specific combination a promising candidate for a cost-efficient process for future Si solar cells.

1. Introduction

Nanoscale texturing of silicon (Si) surfaces has been shown [1–7] to reduce the total weighted average optical reflectance to well below 1% over a broad range of wavelengths and incident angles. Compared to the typical front surface reflectance of ~ 2 and $\sim 8\%$, from conventionally textured mono- [8] and multi-crystalline [9] Si solar cells, respectively, nanoscale texturing such as described in [10–12] offers a potential of improved power conversion efficiency for Si solar cells due to reduced reflectance loss.

We use black silicon [13,14,11] nanostructuring to achieve low reflectance, which can be modelled in a mean-field approximation as a graded refractive index at the Si-air interface [15]. von Gastrow et al. [16] reported excellent passivation of black Si surfaces using atomic layer deposition (ALD) of Al_2O_3. Repo et al. [17] achieved a power conversion efficiency of 18.7% on 400 µm thick float-zone Si using cryogenic deep reactive ion etching (RIE) as

texturing and plasma assisted atomic layer deposition (ALD) of Al_2O_3 for a passivated emitter rear locally diffused (PERL) cell and 22.1% on an interdigitated back contact (IBC) cell with similar ALD-passivation [18]. Oh et al. [19] achieved a power conversion efficiency of 18.2% on 300 µm thick float-zone Si by combining a metal-assisted wet etching black silicon process for texturing, tetramethylammonium hydroxide (TMAH) damage removal etch and thermal SiO_2 passivation. Yoo [20] used industry grade Czochralski (Cz) Si and RIE texturing and achieved a power conversion efficiency of 16.7%. Wang et al. [21] applied black Si by metal-assisted wet etching and ALD of Al_2O_3 on industry grade Cz Si and achieved 18.2% efficiency.

The primary reason for the relatively low efficiencies reported for black Si solar cells so far is the significant emitter and surface recombination [19,2] resulting from increased surface area, defects from the texturing process and increased emitter doping through the nanostructured surface yielding increased Auger recombination. These effects usually lead to reduced short-circuit current and open-circuit voltage. Thus, a selective emitter design could improve the efficiency of black Si solar cells. In order to achieve a selective emitter without the use of multiple high-temperature process steps and photolithography, laser doping and subsequent self-aligned Ni/Cu-plating has been suggested by several groups [22–24]. The laser-doped

---

selective emitter (LDSE) process offers excellent sheet resistance control, self-alignment of front metal contacts to the local highly doped areas and a fast, low-temperature process scalable to industrial throughput. Hallam et al. achieved 19.3% efficiency for a LDSE solar cell on large-area Cz Si substrates using an industrial turnkey production line with the addition of laser-doping and plating [25]. The LDSE process has also been successfully applied to bifacial silicon solar cells [26]. An important feature of the LDSE cell process is the replacement of screen-printed Ag front contacts with plated Ni/Cu-contacts. Due to the economic benefits of replacing Ag by Cu in the solar industry [27] and the extensive studies of Ni/Cu-plating applied for Si solar cells [28–31] the self-aligned, high-performing Ni/Cu-plated front contacts is an important and promising feature of LDSE solar cells.

This work presents LDSE black Si solar cells fabricated on p-type Cz Si substrates textured by a single step, maskless RIE process. To our knowledge this combination has not been previously reported and the resulting cell is thus considered a first proof-of-concept. The emitter diffusion and surface passivation were not fully optimized, since the main goal of this study was the combination of LDSE and RIE-texturing. The primary objective of this work is to investigate how laser doping and plating processes are affected by the RIE-textured surface and vice versa. It is not obvious how a differently textured surface affects e.g. electrical properties of the laser doped regions and subsequent plating. The surface topology may alter the interaction between the laser beam and the material. Thus a different emitter profile may change the defect generation and risk of Schottky contact formation. Besides laser doping and plating, several process steps could be affected by changing from conventional to RIE-texturing: emitter diffusion could change with effective surface area and deposition of anti-reflective coating may not yield the expected layer thickness and uniformity due to the nanostructured front surface. Such effects could then further affect the subsequent laser doping and plating processes. An example hereof is spurious plating on the surface in case of pinholes in the dielectric coating resulting from a different surface topology.

For these reasons there is a need for an investigation of such RIE-textured LDSE solar cells.

2. Approach

The maskless RIE process presented in this work is applied as the texturing step in the following solar cell fabrication process:

- Saw damage removal by etching in 30% KOH at 75 °C for 2 min and subsequent cleaning in 20% HCl at room temperature for 5 min and rinsing in deionized water.
- Texturing using maskless RIE at room temperature in a O_2 and SF_6 plasma with a gas flow ratio of O_2:SF_6=1:1, chamber pressure of 24 mTorr, 13.56 MHz radio-frequency platen power of 100 W using a SPTS RIE system.
- Emitter formation using a tube furnace from Tempress Systems with liquid $POCl_3$ as dopant source at a temperature of 840 °C and atmospheric pressure for 50 min in O_2 and N_2 ambient, followed by removal of phosphor-silicate glass (PSG) in 5% hydrofluoric acid (HF).
- Plasma enhanced chemical vapour deposition (PECVD) of 75 nm hydrogenated amorphous silicon nitride (SiN_x:H) anti-reflective coating at 400 °C using a Roth & Rau MAiA tool.
- Screen-printing of Al rear contact with standard Al paste, which was fired using a Sierra Therm infra-red fast-firing furnace, with a peak temperature set point of 835 °C and a belt speed of 4500 mm/min.
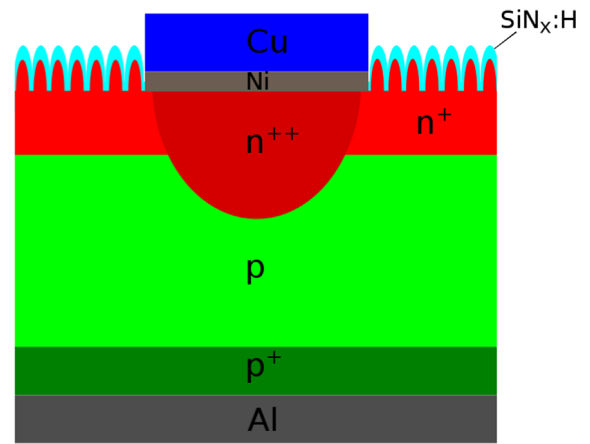

Fig. 1. Sketch of the black Si LDSE solar cell structure. The cells are textured in a single-step, maskless RIE process. The highly doped regions of the selective emitter is formed by means of local laser doping using phosphoric acid dopant and a continuous wave laser. The rear contact is screen-printed and fired Al and the front contacts are plated Ni/Cu. The dimensions of the different layers are not to scale.

- Laser doping of the front surface using spin-on of 85% phosphoric acid as doping source followed by laser doping using a continuous wave laser at a wavelength of 532 nm, 20 W laser power and 2–4 m/s laser scan speed.
- Light-induced plating of Ni acting as seed and barrier layer for the subsequent Cu plating.
- Ni sintering using rapid thermal processing (RTP) in N_2 ambient at 350 °C for 2 min.
- Light-induced plating of Cu onto the Ni seed layer.
- Edge isolation by laser ablation using a 20 W Nd:YAG Lee laser tool.

The starting substrates were 25×25 mm^2 p-type, CZ mono-crystalline Si with a thickness of 200 μm and a resistivity of 1–3 Ω cm.

Fig. 1 shows a schematic cross-section of the fabricated solar cell.

3. Characterization

J–V curves and photovoltaic performance including short-circuit current density, J_{SC}, open-circuit voltage, V_{OC}, fill factor, FF, and power conversion efficiency were measured on complete cells under 1 sun illumination (1000 W/m^2, AM1.5G) using a ELH halogen light source, Advantest TR6143 DC Source Measurement Unit and Labview software for data collection. The illumination was calibrated using the known short-circuit current of a reference mono-crystalline Si screen-printed solar cell.

A LEO 1550 Scanning Electron Microscope (SEM) was used to characterize the nanostructured surface topology.

Suns-V_{OC} [32,33] measurements were performed using a Sinton WCT-120 Lifetime tester. The J_{SC} value from the IV-measurement was used.

Reflectance was measured using a Perkin Elmer integrating sphere and spectrometer. The absorptance was measured using a center mount sample holder inside the integrating sphere.

External Quantum Efficiency (EQE) was measured without bias light using a PV Measurement QE system and Internal Quantum Efficiency (IQE) was calculated based on the EQE and reflectance measurements.

Photoluminescence (PL) [34] was measured at open-circuit conditions using a BTi luminescence imaging tool. Cross-sectional Focused Ion Beam (FIB)/SEM images of the plated Ni/Cu
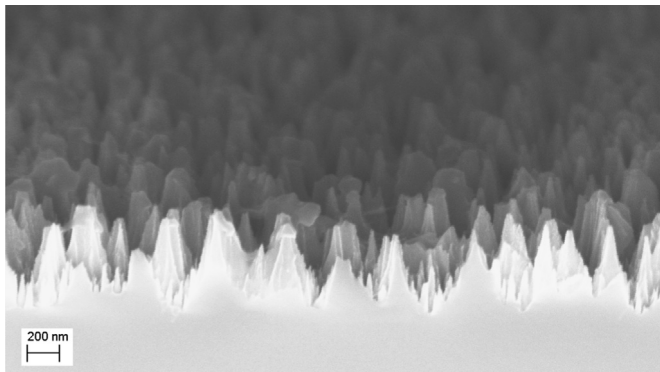
Fig. 2. SEM-image at 40° tilt of the RIE-textured Si surface before any further processing. The nanostructures have a height of ~300–500 nm and a distance between the structures of ~300–500 nm. The nanostructures are conical-like hillocks randomly distributed across the entire solar cell surface.

front contacts were taken using a Helios Nanolab 600 tool from FEI.

4. Results

Fig. 2 shows a SEM image of the RIE-textured Si surface at 40° tilt before any further processing. The nanostructures have a height of ~300–500 nm and a distance between the structures of ~300–500 nm. The nanostructures are conical-like hillocks randomly distributed across the entire solar cell surface.

Fig. 3 shows the total light absorptance of the RIE-textured Si wafer before any further processing as function of wavelength. The absorptance was measured using a centre-mount sample holder placed inside the integrating sphere. The incident angle of the light source deviated 8° from normal incidence due to the geometry of the measurement setup. The absorptance is ~99% in most of the solar spectrum up to a wavelength of ~1000 nm, at which the light starts to transmit through the 200 μm thick Si wafer. The integrated average absorptance is 99.2% in the wavelength range 300–900 nm and decreases to 91.7% from 900 to 1000 nm. The calculated absorptance of a 200 μm Si wafer without any texturing but with an assumed reflectance of 0% is plotted for comparison. Also, the simulated absorptance of a 200 μm Si wafer textured with upright random pyramids with 75 nm SiN_x:H AR-coating is shown for comparison. It is seen that RIE-texturing results in increased absorptance of wavelengths above 1000 nm compared to non-textured Si and similar absorptance of wavelengths above 1000 nm compared to conventionally textured mono-crystalline Si solar cells. This indicates some path-length enhancement of longer wavelengths within the RIE-textured wafer. Based on the absorption coefficient of Si the path-length enhancement of RIE-textured Si is estimated to 20 times at a wavelength of 1100 nm.

The fabricated RIE-textured LDSE solar cells were characterized under 1 sun illumination (1000 W/m², AM1.5G). Fig. 4 shows the measured J–V curve of the best black Si LDSE cell at 1 sun. The short-circuit current density, J_{SC}, is 36.3 mA/cm² and open-circuit voltage, V_{OC}, is 624 mV. The power conversion efficiency is 18.1% and the fill factor, FF, is 80.1%. The pseudo light J–V curve and Suns-V_{OC} measurement seen in Fig. 5 shows that the best black Si LDSE cell has a pseudo fill factor, pFF, of 82.3% and a pseudo power conversion efficiency, pEff, of 18.7% without the effect of series resistance. The high pFF indicates that shunting is low and the pseudo efficiency indicates that series resistance accounts for ~0.6% point efficiency loss compared to the actual power conversion efficiency. The linearly increasing relationship between the
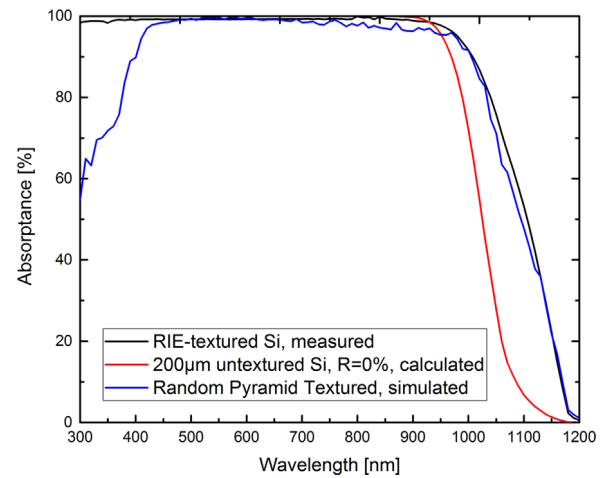

Fig. 3. Light absorptance of the black Si surface before cell processing as function of the wavelength. The absorptance was measured with a center-mount inside an integrating sphere. The incident angle of the light source deviated 8° from normal incidence due to the geometry of the measurement setup.
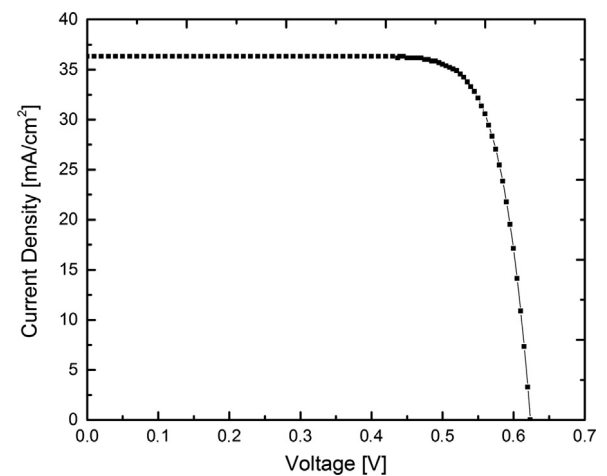
Fig. 4. Current density-voltage characteristic of the best black Si LDSE solar cell under 1 sun illumination (1000 W/m², AM1.5G). The short-circuit current density, J_{SC}, is 36.3 mA/cm² and open-circuit voltage, V_{OC}, is 624 mV. The power conversion efficiency is 18.1% and the fill factor, FF, is 80.1%.

illumination and V_{OC} seen in the bottom part of Fig. 5 indicates that neither shunting nor Schottky contacts are significant for the best black Si LDSE cell. This result is encouraging, because it indicates that RIE-texturing does not lead to increased laser damage or defects at the edges of the laser-doped lines. This does not seem to be the case from the Suns-V_{OC} measurement. The increase in V_{OC} for intensities of 6–7 suns compared to the double diode model may be due to saturation of the surface recombination, which dominates the cell performance at 1 sun.

Table 1 shows measured J_{SC}, V_{OC}, power conversion efficiency and FF for three different RIE-textured LDSE solar cells processed at three different laser speeds. The results in Table 1 show that the three RIE-textured LDSE solar cells have efficiencies in the range 17.5–18.1%. The differences are primarily due to differences in FF. The different fill factors may be explained by the different laser speeds according to the result in Fig. 6, which shows Suns-V_{OC} at low injection for the three RIE-textured LDSE cells with different laser speeds. Fig. 6 shows that a laser speed of 3 m/s leads to the highest open circuit voltage at low injection and an almost linear relationship between V_{OC} and illumination intensity. The cell processed at a laser speed of 2 m/s has significantly lower V_{OC} at low

Fig. 5. Result of the Pseudo Light *J*–*V* (top) and (middle) Suns-V_{OC} measurement of the best black Si LDSE cell processed at a laser speed of 3 m/s. The measurement shows a pseudo fill factor, pFF, of 82.3% and a pseudo efficiency, pEff, of 18.7% without the effect of series resistance.

Table 1

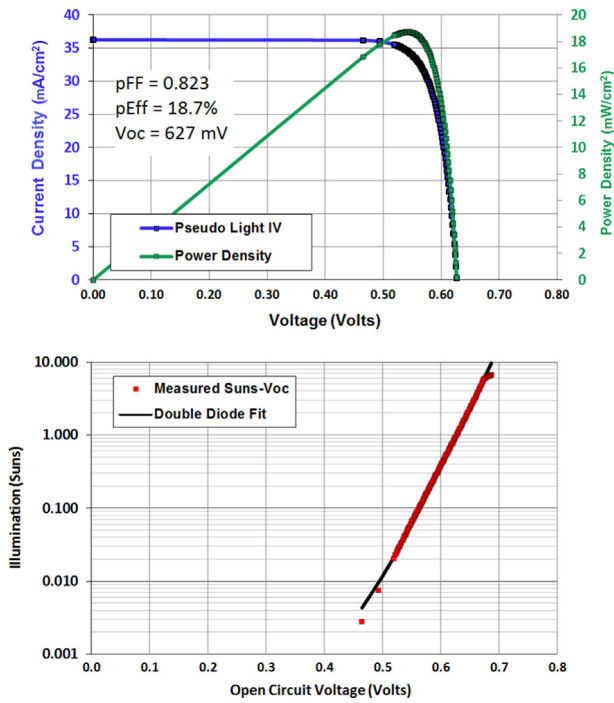Power conversion efficiency, short-circuit current density, open-circuit voltage and fill factor at 1 sun illumination (1000 W/m², AM1.5G) of conventionally and RIE-textured LDSE Si cells with laser speeds of 2, 3 and 4 m/s, respectively. Furthermore, the pseudo fill factor, pFF, determined by Suns-V_{OC} measurements is given.

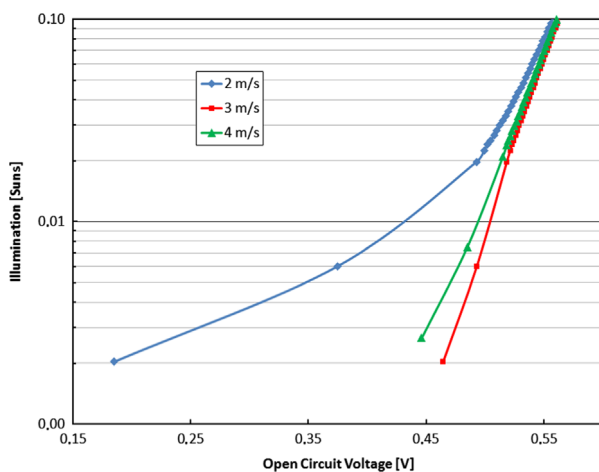| Laser speed (m/s)	Efficiency (%)	J_{SC} (mA/cm²)	V_{OC} (V)	FF (%)	pFF (%)
2	17.5	36.0	0.624	77.9	81.0
3	18.1	36.3	0.624	80.1	82.3
4	17.5	35.8	0.624	78.4	82.0

Fig. 6. Suns-V_{OC} measurement at low injection of three black Si LDSE cells processed at laser speeds of 2, 3 and 4 m/s, respectively.

injection and a less linear relationship between V_{OC} and intensity. This is also reflected in the lower pFF of this particular sample.

After Ni/Cu-plating it was clear that significant spurious plating had occurred and that the surface had local scratches and pinholes through the dielectric, in which Ni and Cu has plated unintentionally.

The top part of Fig. 7 shows photographs of the finished cells where the plating defects are visible. The bottom part of Fig. 7 shows a SEM-image of the RIE-textured surface of the final cells, where an example of the spuriously plated Ni/Cu is also visible. In order to investigate the lines defined by the laser, optical microscope images were taken. The top image in Fig. 8 shows an optical microscope image of laser-doped lines on the RIE-textured Si surface. The image was taken at the point where a metal finger intersects the busbar. The laser-scribed lines are approximately 20 µm wide with ~5 µm) laser damage on each side of the lines. Note that each busbar consists of 10 separate lines about 20 µm wide, spaced ~80 µm apart and metallized in the same light-induced plating process as the fingers. The middle image of Fig. 8 shows an optical microscope image of the Ni/Cu-plated metal lines in this case from the busbar lines. It is seen that the plated contacts are between 18 and 28 µm wide. The total contact fraction is ~2.5% of the total cell area assuming 23 µm wide fingers. The bottom image in Fig. 8 shows a top-view SEM-image of a Ni/Cu-plated line. In the SEM-image an example of spurious metal plating is also seen.

Fig. 9 shows a SEM-image of the cross-section of a laser-doped line plated with Ni/Cu. The cross-section was defined by a Focused Ion Beam (FIB). The plated metal line is ~30 µm wide and ~10 µm in height. The layer on top of the Ni/Cu-line is Pt used solely for sample protection during FIB cutting. Note that the black silicon nanostructures can be seen on the sides of the laser-doped line. The nanostructures are not seen in the laser-doped region in the center of the plated Si region, since the Si in this region has been melted and re-solidified during the laser doping process.

Fig. 10 shows EQE and IQE of the complete 18.1% cell and total reflectance of the RIE-textured Si with ~75 nm SiN$_x$:H anti-reflective (AR) coating, before any further processing. The IQE is calculated from the measured EQE and reflectance. The IQE plotted in Fig. 10 might be underestimated, since the reflectance was measured on textured Si with AR-coating but without any metal, while the EQE was measured on the complete cell. The beam spot of the light source of the EQE-measurement was placed between two metal fingers, but any metal present within the beam spot of the EQE-measurement will increase reflectance and thus decrease EQE and thereby the calculated IQE, since the reflectance in Fig. 10 is measured without any metal on the surface. The low IQE for short wavelengths may be due to a too highly doped emitter resulting in increased Auger recombination and may also be due to increased surface recombination at the nanostructured Si surface.

The measured short-circuit current density can be compared to the expected value calculated from the EQE and the solar spectrum to verify consistency in the measurements. Let $E_\lambda(\lambda)$ be the solar spectral irradiance as a function of wavelength λ according to AM1.5G and $Q_{ext}(\lambda)$ the measured EQE. Then the spectral current density is $J_\lambda(\lambda) = e\lambda E_\lambda(\lambda)Q_{ext}(\lambda)/(hc)$ since hc/λ is the photon energy and e the unit charge, while h is Planck's constant and c the vacuum speed of light. It follows that the expected short-circuit current density is

$$J_{SC} = \int_{\lambda_{min}}^{\lambda_{max}} \frac{e\lambda}{hc} E_\lambda(\lambda)Q_{ext}(\lambda)\, d\lambda. \tag{1}$$

A numerical integration using $\lambda_{min} = 300$ nm and $\lambda_{max} = 1200$ nm results in the expected short-circuit current density 36.5 mA/cm² which is in almost perfect agreement with the 36.3 mA/cm² that was measured.

Fig. 11 shows the total reflectance of the RIE-textured surface with AR-coating before and after Ni/Cu-plating, respectively, as function of wavelength. It is clear that after metal plating the reflectance of the complete cell increases significantly. However, the increase is presumably partly due to the spurious plating seen in Fig. 7. The beam spot size of the light source was ~2 cm in
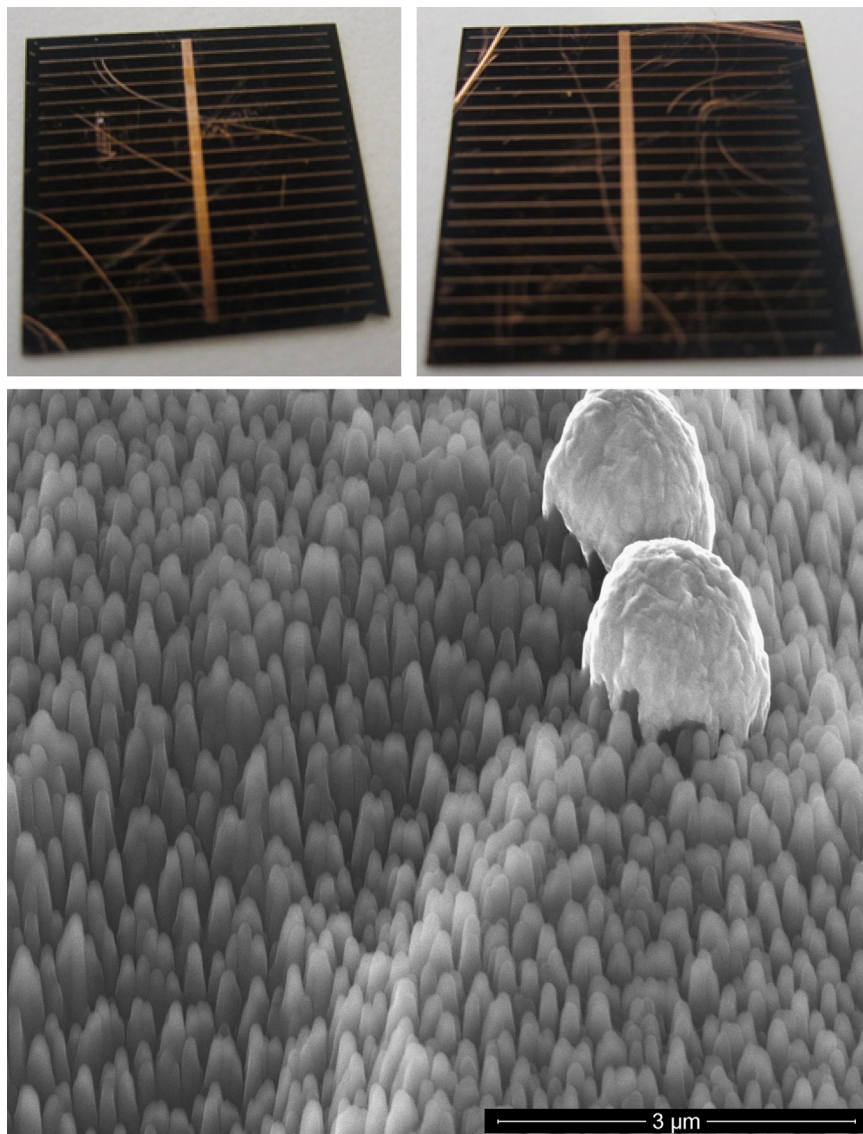
Fig. 7. (Top) Photographs of 2 of the final black Si LDSE solar cells. The images show significant spurious plating of Ni/Cu and scratches in the front surface. (Bottom) SEM-image at 52° tilt of the RIE-textured surface of the final black Si LDSE solar cell surface. The SEM-image also shows examples of spuriously plated Ni/Cu.

diameter and covered the majority of the cell area including the busbar and metal fingers.

Fig. 12 shows an open-circuit photoluminescence (PL) image of the 18.1% cell after Ni plating and sintering. The PL-image shows increased recombination at the laser-doped, Ni-plated busbar and fingers, which is expected for Si-metal interfaces. Furthermore, circular points or agglomerations of lower PL-signal intensity can be seen all over the surface. This indicates that the firing temperature used after rear Al screen-printing was slightly too high for the particular samples, leading to a non-uniform back-surface field.

5. Discussion

The power conversion efficiency of 18.1% of the black Si LDSE cell fabricated in this work is comparable to the best efficiencies reported for front-contacted black Si solar cells [17,19,21]. Table 2 shows selected cell results reported for black Si solar cells [11]. From Table 2 it appears that the cell in this work has superior fill factor compared to existing black silicon cells, while J_{SC} and V_{OC} are on par or slightly reduced compared to [17]. The lack of

improvement to J_{SC} and V_{OC} may be explained by the unintentionally too heavily doped emitter, inadequate surface passivation and the unintentional spurious plating; optimized processing is thus expected to improve both key parameters significantly. The very high fill factor on the other hand is due to a near optimum laser power and scan speed used during laser doping of the best device, resulting in very low contact resistance. We note that the optimum laser doping conditions are different from those on planar silicon probably due to stronger coupling of the laser power into the structure.

In general, this result is encouraging considering that industrial grade Cz Si wafers were used and that the complete cells in this work were not fully optimized.

First of all the cells had significant spurious plating as shown in Fig. 7. This induces a direct loss of current, since the reflectance of the complete cells is significantly higher than a similar cell without spurious plating. The reflectance difference is shown in Fig. 11 and the additional integrated average reflectance in the range 300–1000 nm attributed only to spurious plating can be estimated by the following considerations. The integrated average reflectance in the range 300–1000 nm is 1.20% before plating and 6.38% after plating. The front contact grid only covers ~2.5% of the cell
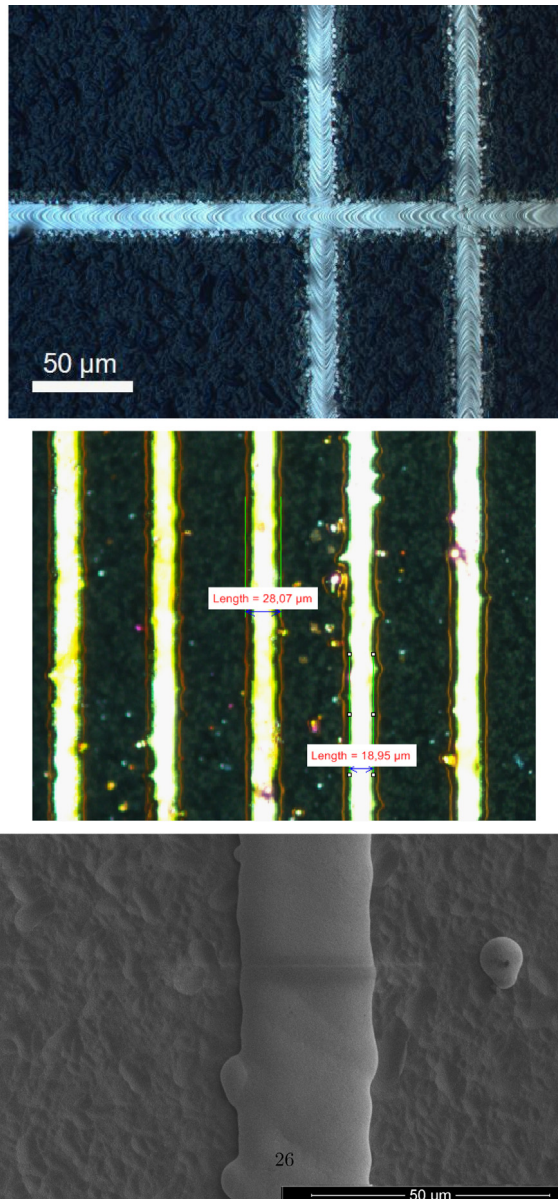
Fig. 9. SEM-image at 52° tilt showing the cross-section of a Ni/Cu-plated metal line. The cross-section was defined by a Focused Ion Beam (FIB). The plated metal line is ∼30 µm wide and ∼10 µm in height. The layer seen on top of the Ni/Cu-line is Pt used solely for sample protection during FIB cutting. Note that the black silicon nanostructures are visible at the edges of the plated Ni/Cu line.

Fig. 10. External and Internal Quantum Efficiency and total reflectance as function of wavelength of the 18.1% black Si LDSE solar cell. The reflectance data are for RIE-textured Si with AR-coating before any further processing. The IQE is calculated based on the measured EQE and reflectance of the surface measured before laser and plating processes. EQE was measured without any bias light.

Fig. 8. (Top) Optical microscope image of the laser-doped lines on the black Si front surface before Ni/Cu-plating. (Middle) Optical microscope image showing the width of the Ni/Cu-plated metal lines in this case from the busbar. (Bottom) Top-view SEM-image of a Ni/Cu-plated metal line.

area assuming 23 µm wide fingers. Based on the metal grid coverage the grid itself only accounts for additional reflectance of ∼1.23% assuming 50% reflectance of Cu in the wavelength range 300–1000 nm. The spurious plating must account for the difference between the additional reflectance after plating and reflectance from the grid. Thus the spurious plating accounts for ∼3.95%. This is a direct reflection loss, which can be at least partly avoided by minimizing spurious plating. Furthermore, spurious plating in scratches such as seen in Fig. 7 is likely to cause increased surface recombination, since the plated metal contacts directly to a lightly doped emitter, which shields minority carriers less than a heavily doped emitter, thus causing enhanced recombination at the metal-Si interface. It is however encouraging that the Suns-V_{OC} measurement in Fig. 5 does not indicate any increased defect generation or Schottky contact formation.

The Suns-V_{OC} result in Fig. 6 indicates the relationship between laser speed and pseudo FF. From the result in Fig. 6 it seems that 3 m/s leads to the most ideal performance, ultimately leading to a

Fig. 11. Total reflectance of the RIE-textured Si surface with AR-coating before and after laser doping and Ni/Cu-plating, respectively, as function of wavelength. The beam spot size of the light source was ∼2 cm in diameter and covered the majority of the cell area including the busbar and metal fingers.

higher FF and power conversion efficiency than the cells processed at 2 and 4 m/s, respectively. The lower V_{OC} at low injection for the cell processed at 2 m/s may be due to increased laser damage at the slower scan speed leading to increased Shockley-Read-Hall recombination in the laser doped regions. The pseudo FF of the cell processed at 4 m/s is almost as high as for 3 m/s. However, the FF is still significantly lower, which indicates that the problem for this cell is rather series resistance. This may be due to a lighter doping caused by the faster scan speed. Thus, it seems that a laser speed of 3 m/s is close to the optimal compromise between minimized laser damage and minimized series resistance for RIE-textured laser-doped solar cells.

Assuming that the spurious plating is due to pinholes and other non-uniformities in the dielectric AR-coating, the problem could be minimized by increasing the thickness of the SiN_x:H layer. The layer may be even thinner than expected, because the deposition rate in the PECVD process may not be the same for RIE-textured Si compared to conventionally textured Si. Even a non-uniform layer would not induce spurious plating as long as the dielectric layer is completely covering the Si surface with sufficient thickness to completely isolate the surface from the plating electrolyte. It is assumed that the pretreatment using hydrofluoric acid (HF) immediately prior to Ni plating further increases the risk of pinholes, since the SiN_x:H coating is etched by HF to some degree. A negative effect of increasing the SiN_x:H thickness could be increased reflectance and absorption in the AR-coating. However, the AR-properties of the SiN_x:H coating are less critical on RIE-

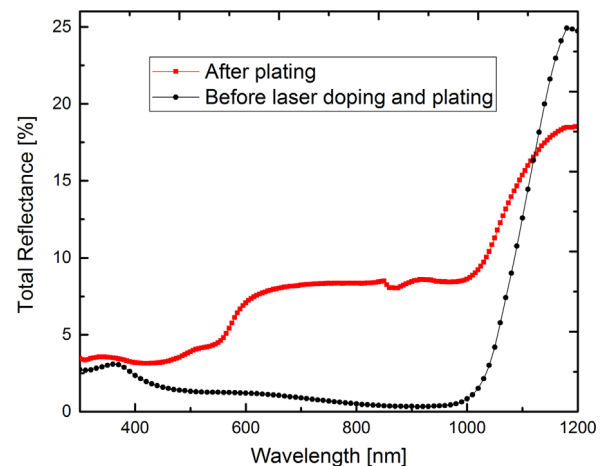textured Si, due to the very low reflectance from the black Si surface itself. The increased absorption in the AR-coating could be minimized by adjusting the layer thickness and the HF process in order to minimize pinholes, while maintaining an acceptably low absorption in the AR-coating.

The phosphorus emitter was too heavily doped resulting in a sheet resistance of 40 Ω measured with a 4-point probe after phosphorus diffusion. This was unintentional, since the full area sheet resistance of such selective emitter should ideally be on the order of 100 Ω, which was also measured on planar Si reference wafers from the same diffusion process. This suggests that the decreased sheet resistance is due to faster diffusion of dopant atoms through the nanostructured Si surface. By decreasing time and temperature of the diffusion process, we expect to improve the emitter in future studies. From the QE measurement seen in Fig. 10 a significant decrease in EQE and IQE is seen for wavelengths below 600 nm. This indicates significant emitter and surface recombination, which is expected from black Si, if the surface is not well passivated. Since a standard SiN_x:H AR-coating was used as the only passivation layer on these cells, it is expected that the short wavelength response can be significantly improved in future studies by optimizing the SiN_x:H coating or by applying different dielectric coatings.

From the PL-image in Fig. 12 small circular structures with slightly lower PL-signal can be seen. We suggest that this is due to a too high firing temperature used for rear Al screen-printing on these particular samples. We expect this to be improved in future studies.

By combining the potential improvements mentioned above significantly higher power conversion efficiency of this new kind of cell structure is expected. This will be investigated in future studies.

6. Conclusion

Ni/Cu-plated black Si LDSE solar cells have been fabricated on industrial grade Cz Si substrates textured in a single step, maskless RIE-process. The best cell has a power conversion efficiency of 18.1% with a fill factor of 80.1%. Since the cell was not optimized in terms of spurious plating, emitter sheet resistance and surface passivation, it is expected that the efficiency of black Si LDSE cells will be significantly higher in the near future. To our knowledge this is the first RIE-textured LDSE cell reported and we therefore consider this a proof-of-concept.
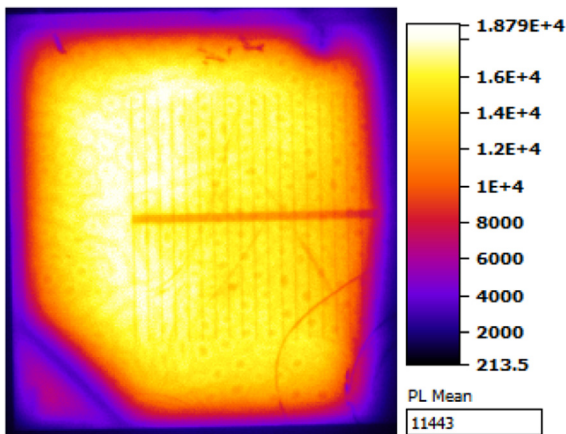
Fig. 12. Open-circuit Photoluminescence (PL) image of the cell after Ni plating and sintering, but before Cu plating and edge isolation. The feature in the bottom left corner of the image is due to the shape of the screen-printed Al on the rear.

Table 2
Selected black silicon solar cell results reported in the literature. The table shows power conversion efficiency, J_{SC}, V_{OC}, fill factor and type of solar cell and Si substrate. For further details about the cell type we refer to the references. (MACE, Metal-Assisted Chemical Etching.)

Author	Texturing	Eff. (%)	J_{SC} (mA/cm^2)	V_{OC} (V)	FF (%)	Cell type Passivation, Cell area
This work	RIE	18.1	36.3	0.624	80.1	CZ LDSE SiN_x, 6.25 cm^2
Repo et al. [17]	RIE	18.7	39.2	0.632	75.8	FZ PERL ALD Al$_2$O$_3$, 4 cm^2
Yoo [20]	RIE	16.7	36.8	0.617	76.0	CZ Screen-printed SiN_x, 156.25 cm^2
Oh et al. [19]	MACE	18.2	36.5	0.628	79.6	FZ, evaporated contacts Thermal SiO$_2$, 0.8081 cm^2
Wang et al. [21]	MACE	18.2	41.3	0.598	75.1	CZ, evaporated contacts ALD Al$_2$O$_3$, 0.92 cm^2
Savin et al. [18]	RIE	22.1	42.2	0.665	78.7	FZ, IBC ALD Al$_2$O$_3$, 78.5 cm^2 (4 in)

Acknowledgements

References

[1] F. Priolo, T. Gregorkiewicz, M. Galli, T.F. Krauss, Silicon nanostructures for photonics and photovoltaics, Nat. Nanotechnol. 9 (2014) 19–32, http://dx.doi.org/10.1038/NNANO.2013.271.

[2] R.S. Davidsen, Ø. Nordseth, A. Boisen, M.S. Schmidt, O. Hansen, Plasma texturing on large-area industrial grade CZ silicon solar cells, in: 28th EU PVSEC Conference Proceedings, 2013.

[3] J. Zhu, Z. Yu, S. Fan, Y. Cui, Nanostructured photon management for high performance solar cells, Mater. Sci. Eng. R 70 (2010) 330–340.

[4] K.N. Nguyen, D. Abi-Saab, P. Basset, E. Richalot, F. Marty, D. Angelescu, Y. Leprince-Wang, T. Bourouina, Black silicon with sub-percent reflectivity: influence of the 3D texturization geometry, in: 16th International Transducers Solid-State Sensors, Actuators and Microsystems Conference (Transducers), vol. 11, 2011, pp. 354–357.

[5] M.D. Kelzenberg, S.W. Boettcher, J.A. Petykiewicz, D.B. Turner-Evans, M.C. Putnam, E.L. Warren, J.M. Spurgeon, R.M. Briggs, N.S. Lewis, H.A. Atwater, Enhanced absorption and carrier collection in Si wire arrays for photovoltaic applications, Nat. Mater. 9 (2010) 239–244, http://dx.doi.org/10.1038/NMAT2635.

[6] Y.-F. Huang, S. Chattopadhyay, Y.-J. Jen, C.-Y. Peng, T.-A. Liu, Y.-K. Hsu, C.-L. Pan, H.-C. Lo, C.-H. Hsu, Y.-H. Chang, C.-S. Lee, K.-H. Chen, L.-C. Chen, Improved broadband and quasi-omnidirectional anti-reflection properties with biomimetic silicon nanostructures, Nat. Nanotechnol. 2 (2007) 770–774.

[7] A. Parretta, A. Sarno, P. Tortora, H. Yakubu, P. Maddalena, J. Zhao, A. Wang, Angle-dependent reflectance measurements on photovoltaic materials and solar cells, Opt. Commun. 172 (1999) 139–151.

[8] L. Zhao, Y.H. Zuo, C.L. Zhou, H.L. Li, H.W. Diao, W.J. Wang, Theoretical investigation on the absorption enhancement of the crystalline silicon solar cells by pyramid texture coated with SiNx:H layer, Solar Energy 85 (2011) 530–537.

[9] D. Macdonald, A. Cuevas, M. Kerr, C. Samundsett, D. Ruby, S. Winderbaum, A. Leo, Texturing industrial multicrystalline silicon solar cells, Sol. Energy 76 (1) (2004) 277–283.

[10] A. Rahman, A. Ashraf, H. Xin, X. Tong, P. Sutter, M.D. Eisaman, C.T. Black, Sub-50-nm self-assembled nanotextures for enhanced broadband antireflection in silicon solar cells, Nat. Commun. 6 (2015) 5963, http://dx.doi.org/10.1038/ncomms6963.

[11] X. Liu, P.R. Coxon, M. Peters, B. Hoex, J.M. Cole, D.J. Fray, Black silicon: fabrication methods, properties, and solar energy applications, Rev. Artic. Energy Environ. Sci. R. Soc. Chem. 7 (2014) 3223–3263, http://dx.doi.org/10.1039/c4ee01152j.

[12] T. Allen, J. Bullock, A. Cuevas, S. Baker-Finch, F. Karouta, Reactive ion etched black silicon texturing: a comparative study, in: IEEE 40th Photovoltaic Specialist Conference (PVSC), IEEE, Denver, Colorado, USA, 2014, pp. 0562–0566. http://dx.doi.org/10.1109/PVSC.2014.6924983.

[13] T.H. Her, R.J. Finlay, C. Wu, S. Deliwala, E. Mazur, Microstructuring of silicon with femtosecond laser pulses, Appl. Phys. Lett. 73 (1998) 1673–1675.

[14] H. Jansen, M. Deboer, R. Legtenberg, M. Elwenspoek, The black silicon method – a universal method for determining the parameter setting of a fluorine-based reactive ion etcher in deep silicon trench etching with profile control, J. Micromech. Microeng. 5 (1995) 115–120.

[15] R.B. Stephens, G.D. Cody, Optical reflectance and transmission of a textured surface, Thin Solid Films 45 (1977) 19–29.

[16] G. von Gastrow, R. Alcubilla, P. Ortega, M. Yli-Koski, S. Conesa-Boj, A.F. i Morral, H. Savin, Analysis of the atomic layer deposited Al2O3 field-effect passivation in black silicon, Sol. Energy Mater. Sol. Cells 142 (2015) 29–33, http://dx.doi.org/10.1016/j.solmat.2015.05.027.

[17] P. Repo, J. Benick, V. Vähänissi, J. Schön, G. von Gastrow, B. Steinhauser, M.C. Schubert, M. Hermle, H. Savin, N-type black silicon solar cells, in: SiliconPV, Energy Procedia, vol. 38, 2013, pp. 866–871.

[18] H. Savin, P. Repo, G. von Gastrow, P. Ortega, E. Calle, M. Garn, R. Alcubilla, Black silicon solar cells with interdigitated back-contacts achieve 22.1% efficiency, Nat. Nanotechnol. 10 (2015) 624–628, http://dx.doi.org/10.1038/NNANO.2015.89.

[19] J. Oh, H.C. Yuan, H. Branz, An 18.2%-efficient black-silicon solar cell achieved through control of carrier recombination in nanostructures, Nat. Nanotechnol. 7 (2012) 743–748.

[20] J. Yoo, Reactive ion etching (RIE) technique for application in crystalline silicon solar cells, Sol. Energy 84 (2010) 730–734.

[21] W.-C. Wang, C.-W. Lin, H.-J. Chen, C.-W. Chang, J.-J. Huang, M.-J. Yang, B. Tjahjono, J.-J. Huang, W.-C. Hsu, M.-J. Chen, Surface passivation of efficient nanotextured black silicon solar cells using thermal atomic layer deposition, ACS Appl. Mater. Interfaces 5 (2013) 9752–9759, http://dx.doi.org/10.1021/am402889k.

[22] D. Kyeong, S.-H. Cho, J-K. Lim, K. Lee, M-I. Hwang, W-J. Lee, E.C. Cho, Approaching 20%-efficient selective-emitter solar cells with copper front contacts on industrial 156 mm CZ Si wafers, in: Proceedings of 27th European Photovoltaic Solar Energy Conference and Exhibition, 2012.

[23] B. Hallam, A. Uruea, R. Russell, M. Aleman, M. Abbott, C. Dang, S. Wenham, L. Tous, J. Poortmans, Efficiency enhancement of i-PERC solar cells by implementation of a laser doped selective emitter, Sol. Energy Mater. Sol. Cells 134 (2015) 89–98.

[24] L. Tousa, R. Russella, J. Dasa, R. Labiea, M. Ngamoc, J. Horzela, H. Philipsena, J. Sniekersb, K. Vandermissena, L. van den Brekeld, T. Janssensa, M. Alemana, D.H. van Dorpa, J. Poortmansa, R. Mertens, Large area copper plated silicon solar cell exceeding 19.5% efficiency, in: 3rd Workshop on Metallization for Crystalline Silicon Solar Cells, 2011.

[25] B. Hallam, S. Wenham, A. Sugianto, L. Mai, C. Chong, M. Edwards, D. Jordan, P. Fath, Record large-area p-type cz production cell efficiency of 19.3% based on LDSE technology, IEEE J. Photovolt. 1 (1) (2011) 43–48.

[26] X. Wang, V. Allen, V. Vais, Y. Zhao, B. Tjahjono, Y. Yao, S. Wenham, A. Lennon, Laser-doped metal-plated bifacial silicon solar cells, Sol. Energy Mater. Sol. Cells 131 (2014) 37–45.

[27] M.A. Green, Silicon solar cells: state-of-the-art, Philos. Trans. R. Soc. A (2013), http://dx.doi.org/10.1098/rsta.2011.0413.

[28] S. Flynn, A. Lennon, Copper penetration in laser-doped selective-emitter silicon solar cells with plated nickel barrier layers, Sol. Energy Mater. Sol. Cells 130 (2014) 309–316.

[29] A.u. Rehman, S.H. Lee, Review of the potential of the Ni/Cu plating technique for crystalline silicon solar cells, Materials 7 (2014) 1318–1341, http://dx.doi.org/10.3390/ma7021318.

[30] C. Geisler, W. Hördt, S. Kluska, A. Mondon, S. Hopman, M. Glatthaar, Overcoming electrical and mechanical challenges of continuous wave laser processing for Ni–Cu plated solar cells, Sol. Energy Mater. Sol. Cells 133 (2015) 48–55.

[31] Su Zhou, Chunlan Zhou, Wenjing Wang, Junjie Zhu, Yehua Tang, Jingwei Chen, Yan Zhao, Comprehensive study of light induced plating of nickel and its effect on large area laser doped crystalline solar cells, Sol. Energy Mater. Sol. Cells 125 (2014) 33–38.

[32] R.A. Sinton, A. Cuevas, A quasi-steady-state open-circuit voltage method for solar cell characterization, in: 16th European Photovoltaic Solar Energy Conference, vol. 25, 2000, pp. 1152–1155.

[33] T. Trupke, R.A. Bardos, M.D. Abbott, J.E. Cotter, Suns-photoluminescence: contactless determination of current–voltage characteristics of silicon wafers, Appl. Phys. Lett. 87 (9) (2005) 093503.

[34] T. Trupke, R.A. Bardos, M.C. Schubert, W. Warta, Photoluminescence imaging of silicon wafers, Appl. Phys. Lett. 89 (4) (2006) 044107.

Appendix C

Simulation and Measurement of Angle Resolved Reflectance from Black Si Surfaces

Authors:
Rasmus Schmidt Davidsen, Kaiyu Wu, Michael Stenbæk Schmidt, Anja Boisen, Ole Hansen

Simulation and Measurement of Angle Resolved Reflectance from Black Si Surfaces

Rasmus Schmidt Davidsen,* Kaiyu Wu, Michael Stenbæk Schmidt, Anja Boisen, Ole Hansen[†]

Department of Micro- and Nanotechnology, Technical University of Denmark

EUPVSEC Topic 2.3: Silicon Solar Cell Characterisation and Modelling

Introduction Nanostructures etched in silicon surfaces such as reactive ion etch (RIE) textured black Si have shown to be potentially useful in photovoltaic applications [1] [2] [3] [4]. In particular, the reduced reflectance over a broad range of incident angles [5] compared to that of bare silicon and silicon with a simple anti-reflex coating. Nguyen et al. [6] simulated the reflectance of nanostructures with peak heights of 900 nm as a function of incident angle. The investigation of angle-resolved optical behavior of nanostructured Si is particularly important considering the reported angle-dependence of power output [7] [8] of commercial Si solar cells.

This work differs from previous studies such as [6] by focusing on smaller nanostructures. The risk of increased surface recombination due to the etched nanostructures implies a compromise between optical performance and surface recombination. Thus, smaller nanostructures resulting in minimal surface recombination yet minimal reflectance are ideal. For this reason this work focuses on nanostructured surfaces with peak heights of 300 nm and two different graded refractive index schemes resembling experimentally fabricated surfaces relevant for photovoltaics.

In this work we have simulated and experimentally measured the reflectance from nanostructured silicon surfaces realized by mask-less RIE texturing. The reflectance was evaluated as a function of the incident angle of the light.

Simulation model To simplify modelling of the reflectance of the black silicon microstructure a mean field approach was used; here the refractive index n was varied gradually – either linearly or non-linearly – from that of silicon n_{si} to that of air n_{air} across a distance equal to the height h of the nanostructures according to

$$n(z) = \begin{cases} n_{\mathrm{Si}} & \text{, for } z \leq 0 \\ n_{\mathrm{air}} & \text{, for } z \geq h \\ n_{\mathrm{air}} f(z,h,\Lambda) + n_{\mathrm{Si}} \left[1 - f(z,h,\Lambda)\right] & \text{, for } 0 < z < h \end{cases} \tag{1}$$

where Λ is a nonlinearity parameter. The index shape function was defined as $f(z,h,\Lambda) = \ln\left(1 + z/\Lambda\right)/\ln\left(1 + h/\Lambda\right)$ in case of a non-linear index profile and $f(z,h,\Lambda) = z/h$ in case of a linear index profile; here the parameters $\Lambda = 10$ nm and $h = 300$ nm were used. With this index profile the time-harmonic Maxwell equations were solved in the form of the Helmholtz equations (e.g. $\nabla^2 \mathbf{E} = -k^2 \mathbf{E}$, where k is the wave number) for the electric and magnetic fields $\mathbf{E}$ and $\mathbf{H}$, respectively. The calculation was done for the case of a plane optical wave of wavelength $\lambda = 550$ nm incident at an angle θ to the surface normal. From the fields Poynting's vector $\mathbf{S} = \mathbf{E} \times \mathbf{H}$ and its time average z-components $\langle \mathbf{S} \rangle \cdot \mathbf{e}_z$ were calculated at the source and the detector, from which the reflectance R was calculated.

---

*e-mail: rasda@nanotech.dtu.dk, phone: +45 45255848, Department of Micro- and Nanotechnology, Technical University of Denmark (DTU), Ørsteds Plads building 345East, 2800 Lyngby, Denmark

[†]ole.hansen@nanotech.dtu.dk;   anja.boisen@nanotech.dtu.dk;   michael.schmidt@nanotech.dtu.dk; kaiwu@nanotech.dtu.dk

Simulation Results   The results of the simulations are shown in the reflectance graphs in Fig. 1 where reflectances for TE and TM waves are shown along with the mean reflectance of a 50/50 mixture of TE and TM waves as a function of the incident angle, the calculated reflectances in Fig. 1(a) are for a linearly graded index, while the reflectances for the nonlinear graded index are shown in Fig. 1(b). As expected, the reflectance is higher for TE than for TM waves. In all cases the reflectance is very low (less than 1% for non-linear graded index and less than 5% for linearly graded index) for incident angles below $45°$. At larger incident angles the reflectance increases rather steeply. We observe that the reflectance resulting from the non-linear graded index is generally lower than the linear graded index and stays below 1% until the incident angle is increased above $45°$. In addition the difference in reflectance between TE and TM waves is less pronounced.
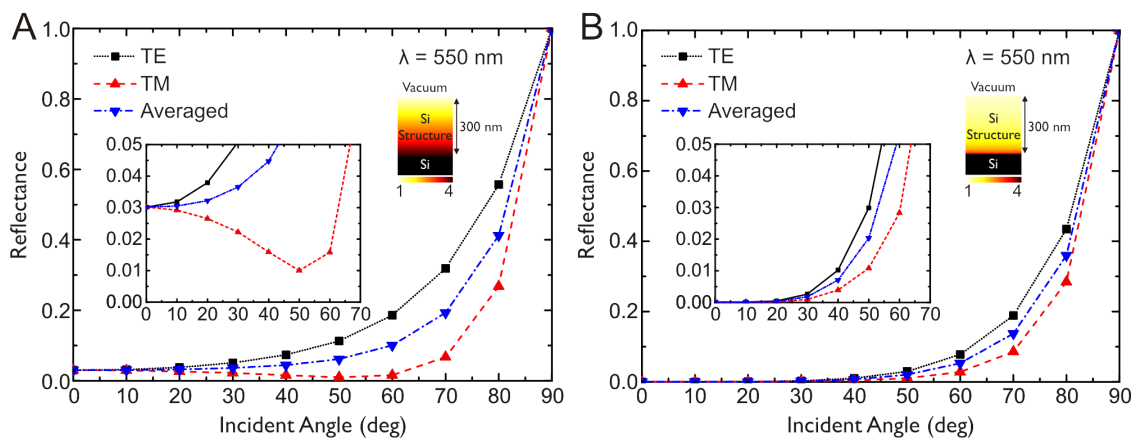
Figure 1: *Simulated reflectance as function of incident angle at a wavelength of 550 nm for surfaces with nanostructures of 300 nm in height in case of (a) linearly graded refractive index, (b) non-linearly graded refractive index. The insets in (a) and (b) show the simulated reflectance at incident angles from $0 − 70°$*

Experimental Method and Results   Black Si was realized by means of maskless RIE at room temperature in an O_2 and SF_6 plasma. The texturing process was carried out at a gas flow ratio of $O_2:SF_6 \simeq 1:1$, a pressure of 10-30 mTorr, a platen power of 30-100 W at 13.56 MHz in a STS RIE system. The resulting surface morphology was characterized using scanning electron microscopy (SEM), and SEM images of the structures are shown in Fig. 2. The different morphologies shown in Fig. 2 indicate that the graded refractive index profile may be approximately linear in some cases and non-linear to some extent in other cases.

2
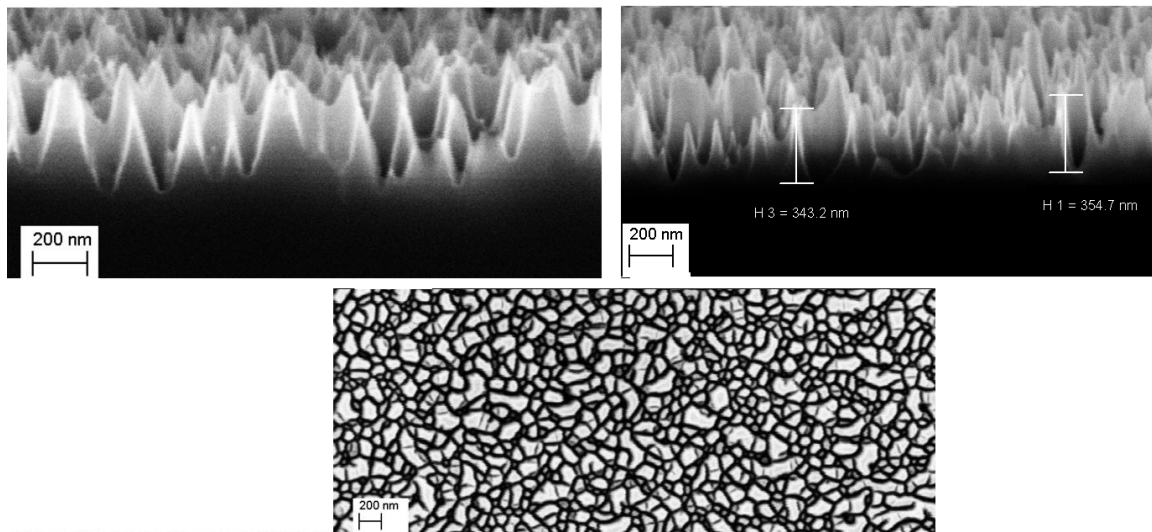
Figure 2: *SEM-images at 45° (top) and 0° (bottom) tilt of RIE-textured Si surfaces with 300 nm nanostructure height. The nanostructures represent approximately linear (top,left) and non-linear (top,right) graded refractive index profiles.*

The specular angular-dependent optical reflectance of the nanostructured silicon surface was measured for wavelengths in the range 300-1000 nm using a Woollam VASE ellipsometer.
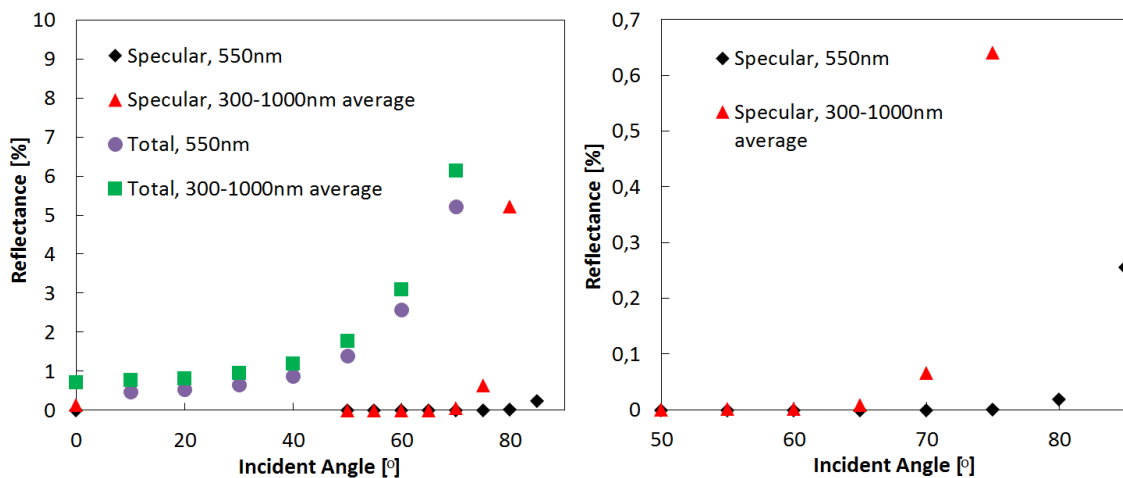
Figure 3: *Experimental specular and total reflectance as a function of incident angle. The average reflectance in the wavelength range 300-1000 nm and the value at a wavelength of 550 nm (directly comparable to the simulation) are shown (left). The specular reflectance at incident angles from 50 − 85° is shown to the right.*

Fig. 3 shows the measured specular and total reflectance as a function of the incident angle. Both the average reflectance in the wavelength range 300-1000 nm and the reflectance at 550 nm are shown.

The reflectance is seen to be dominated by non-specular reflectance. In agreement with the simulation the specular reflectance is seen to be very low, but the experimental specular reflectance stays low even at very high incident angles (i.e. below 0.1% at angles below 65°). The measured total reflectance is more comparable in magnitude to and agrees quite well with the calculated reflectance. The reason is that due to the surface topology a major part of the reflected waves are reflected in a direction different from that of the detector in a specular reflection measurement set-up and escape detection.

We note, that the simple simulation model – by construction – is unable to model real diffuse reflection; this can be accomplished using a much more detailed model of the nanostructured surface, which is part of future work.

Conclusion   Angle-resolved reflectance from nanostructured Si surfaces realized by maskless RIE texturing has been simulated and measured. The simulation and experimental measurement data show the same trend. Experimentally a total reflectance below 1% for incident angles below 30° and specular reflectance below 0.1% at incident angles below 70° is seen. In both simulation and experiment the specular reflectance is below 10% at incident angles below 65° and below 1% at incident angles below 45° in the case of non-linear graded refractive index. From the simulation results the non-linear graded refractive index yields lower reflectance than the linearly graded refractive index. Modelling of the diffuse reflectance is part of future work.

References

[1] Davidsen, R.S., Nordseth, Ø., Boisen, A., Schmidt, M.S., Hansen, O., "Plasma texturing on large-area industrial grade CZ silicon solar cells", 28th EU PVSEC Conference Proceedings (2013).

[2] Liu, X., Coxon, P.R., Peters, M., Hoex, B., Cole, J.M., Fray, D.J., "Black Silicon: Fabrication methods, properties, and solar energy applications", Review Article, Energy & Environmental Science, Royal Society of Chemistry (2014), DOI: 10.1039/c4ee01152j.

[3] Repo, P., Benick, J., Vähänissi, V., Schön, J., von Gastrow, G., Steinhauser, B., Schubert, M.C., Hermle, M., Savin, H., "N-type black silicon solar cells", SiliconPV, Energy Procedia 38 (2013) 866-871.

[4] Oh, J., Yuan, H.C., Branz, H., "An 18.2 %-efficient black-silicon solar cell achieved through control of carrier recombination in nanostructures", Nature Nanotechnology vol.7 (2012) 743-748.

[5] Kelzenberg, M.D., Boettcher, S.W., Petykiewicz, J.A., Turner-Evans, D.B., Putnam, M.C., Warren, E.L., Spurgeon, J.M., Briggs, R.M., Lewis, N.S., Atwater, H.A., "Enhanced absorption and carrier collection in Si wire arrays for photovoltaic applications", Nature Materials Vol 9 (2010), DOI: 10.1038/NMAT2635.

[6] Nguyen, K.N., Abi-Saab, D., Basset, P., Richalot, E., Marty, F., Angelescu, D., Leprince-Wang, Y., Bourouina, T., "Black silicon with sub-percent reflectivity: Influence of the 3D texturization geometry", Transducers 11 (2011)

[7] King, D.L., Kratochvil, J.A., Boyson, W.E., "Measuring Solar Spectral and Angle-of-Incidence Effects on Photovoltaic Modules and Solar Irradiance Sensors", 26th IEEE Photovoltaic Specialists Conference (1997).

[8] Anderson, M.C., "Stand Structure and Light Penetration II. A Theoretical Analysis", Journal of Applied Ecology Vol. 3 No. 1 (1966) 41-54.

Appendix D

Angle resolved characterization of nanostructured and conventionally textured silicon solar cells

Authors:
Rasmus Schmidt Davidsen, Jeppe Ormstrup, Martin Lind Ommen, Peter Emil Larsen, Michael Stenbæk Schmidt, Anja Boisen, Ørnulf Nordseth, Ole Hansen
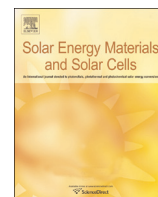
Angle resolved characterization of nanostructured and conventionally textured silicon solar cells

Rasmus Schmidt Davidsen [a,*], Jeppe Ormstrup [a], Martin Lind Ommen [a], Peter Emil Larsen [a],
Michael Stenbæk Schmidt [a], Anja Boisen [a], Ørnulf Nordseth [c], Ole Hansen [a,b]

[a] Department of Micro- and Nanotechnology, Technical University of Denmark (DTU), Denmark
[b] Danish National Research Foundation's Center for Individual Nanoparticle Functionality (CINF), Technical University of Denmark, DK-2800 Kgs. Lyngby, Denmark
[c] IFE, Institute for Energy Technology, Norway

ARTICLE INFO

ABSTRACT

We report angle resolved characterization of nanostructured and conventionally textured silicon solar cells. The nanostructured solar cells are realized through a single step, mask-less, scalable reactive ion etching (RIE) texturing of the surface. Photovoltaic properties including short circuit current, open circuit voltage, fill factor (FF) and power conversion efficiency are each measured as function of the relative incident angle between the solar cell and the light source. The relative incident angle is varied from 0° to 90° in steps of 10° in orthogonal axes, such that each solar cell is characterized at 100 different angle combinations. The angle resolved photovoltaic properties are summarized in terms of the average, angle-dependent electrical power output normalized to the power output at normal incidence and differently textured cells on different silicon substrates are compared in terms of angle resolved performance. The results show a 3% point improvement in average electrical power output normalized with respect to normal incidence power output of RIE textured, multicrystalline Si cells compared to conventional multicrystalline Si cells and above 1% point improvement of RIE textured monocrystalline Si cells compared to conventional monocrystalline Si cells.

1. Introduction

Solar cells are generally characterized at standard test conditions i.e. at light intensity of 1000 W/m^2, AM1.5G[1] illumination, temperature of 25 °C and light at normal incidence, which means that the incident simulated sunlight beam is directed at an angle of 90° relative to the solar cell plane. However these conditions only represent a very limited fraction of actual, realistic operating conditions for solar cells and panels. The temperature of the cell and the intensity and incidence angle of the sunlight indeed vary between different geographical locations and throughout the duration of a day and a year. Furthermore solar cells are subject to diffuse light whenever clouds, dust or any obstacles in the air scatter the sunlight before it reaches the solar cell surface. For this reason there is a need for a more detailed characterization scheme for solar cells, which takes these variations into account. In particular when considering alternative solar cell types employing

features such as nanoscale texturing of the solar cell surface, the angle-resolved and low light performance becomes more important, since nanoscale texturing has been shown [1–3] to yield superior reflectance properties over a broad range of incident angles compared to conventionally textured solar cells.

We use black silicon (BS) [4,5] nanostructuring to achieve low reflectance due to the resulting graded refractive index at the Si–air interface. Low broadband reflectance at different incident angles has been reported for moth-eye surfaces [6,7] and different types of black silicon [8] are fabricated by means of various methods. This work focuses on black Si fabricated by maskless reactive ion etching (RIE). Repo et al. [9] achieved a power conversion efficiency of 18.7% on 400 μm thick float-zone Si using cryogenic deep RIE as texturing and plasma assisted atomic layer deposition (ALD) of Al$_2$O$_3$ for a passivated emitter rear locally diffused (PERL) cell. Oh et al. [3] achieved a power conversion efficiency of 18.2% on 300 μm thick float-zone Si by combining a metal-assisted wet etching black silicon process for texturing, TMAH damage removal etch and double-sided thermal SiO$_2$ passivation. Yoo [10] used industry grade Czochralski Si and RIE texturing and achieved a power conversion efficiency of 16.7%. Several groups have reported improved light absorption over a broad range of incident angles of nanostructured [11–14] and

---

differently textured Si including the PERL-cell [15,16]. Considering these reported improved angle-dependent optical properties of nanostructured Si and the correlation between overcast sky (diffuse light) conditions and relative incident angle of the sunlight [17–20], the relationship between nanostructured Si solar cells and angle-dependent photovoltaic performance is of utmost interest with respect to optimization of solar cell performance under realistic operating conditions such as diffuse light. Lee et al. [21] show improved average power conversion efficiency as function of incident angle of nanostructured thin film Si solar cells in comparison with "conventional" thin film Si cells with single and double anti-reflective (AR) coatings. However, a detailed study of the angle-dependent photovoltaic performance of nanostructured, large-area Si solar cells based on industrial type Si substrates in direct comparison with conventionally textured Si solar cells, has not yet been reported.

This work presents an angle-resolved characterization approach of solar cells in general and measured angle-resolved photovoltaic properties of nanostructured Si solar cells in comparison with conventionally textured Si solar cells.

2. Approach

The maskless RIE process presented in this work is applied as the texturing step in the following solar cell fabrication process:

- Saw damage removal by etching in 30% KOH at 75 °C for 2 min and subsequent cleaning in 20% HCl at room temperature for 5 min and rinsing in deionized water.
- Texturing using maskless RIE at room temperature in a O_2 and SF_6 plasma with a gas flow ratio of O_2: $SF_6 \approx 1$: 1, chamber pressure of 28 mTorr, 13.56 MHz radio-frequency platen power of 30 W using a STS RIE system.
- Emitter formation using a tube furnace from Tempress Systems with liquid $POCl_3$ as dopant source and N_2 as carrier gas at a temperature of 840 °C and atmospheric pressure for 50 min in O_2 ambient, followed by removal of phosphor-silicate glass (PSG) in 5% hydrofluoric acid (HF).
- Plasma enhanced chemical vapour deposition (PECVD) of 60 nm hydrogenated amorphous silicon nitride (SiN_x:H) anti-reflective coating at 400 °C using a PlasmaLab System133 from Oxford Instruments.
- Screen-printing of Ag front and Al rear contacts with standard Ag and Al pastes using an Ekra X5-STS screen printer, followed by co-firing of the front and rear contacts at 800 °C using an RTC Model LA-309 belt furnace.
- Edge isolation by laser ablation using a J-1030-515-343 FS System from Oxford Lasers Ltd.

The starting substrates were 156×156 mm^2 p-type, CZ mono-, multi- and quasi-mono-crystalline Si wafers with a thickness of 200 μm and a resistivity of 1–3 Ω cm.

3. Characterization

Normal incidence reflectance measurements of the RIE-textured mono-, multi and quasi-mono Si surfaces were performed using a broadband lightsource (Mikropack DH-2000), an integrating sphere (Mikropack ISP-30-6-R), and a spectrometer (Ocean Optics QE65000, 280–1000 nm). The reference solar spectral irradiance for AM1.5 was used to calculate the weighted average reflectance in the wavelength range from 280 to 1000 nm. The angle-dependent optical reflectance was measured with monochromatic light from 350 nm to 1200 nm using an APEX monochromator illuminator with an Oriel Cornerstone

260 1/4 m monochromator. A quartz crystal achromatic depolarizer from Thorlabs was used in the beam path to randomize the partly polarized light from the monochromator. The sample was inserted inside a 150 mm integrating sphere with a centre mount configuration and rotated to any desired angle of incidence.

$I–V$ curves and photovoltaic properties including short-circuit current, I_{SC}, open-circuit voltage, V_{OC}, fill factor, FF, and electrical output power, P_{el}, were measured on complete cells under 1 sun illumination (1000 W/m^2, AM1.5G) using a Newport Oriel 92190 large-area Xe light source and a Keithley 2651A high-power source meter.

In order to characterize the solar cell performance at varying incident angles, $I–V$ curves were measured on differently textured Si solar cells mounted and contacted on a stage, which prior to each $I–V$ curve measurement was tilted to a position given by two angles, θ and ϕ, around two orthogonal axes: θ is the tilt of the cell plane with respect to the original, horizontal x-axis and ϕ is the tilt of the cell plane with respect to the tilted y-axis. The light source was fixed during all measurements. The measurement setup including the two angles θ and ϕ is sketched in Fig. 4. The incidence angle was varied using two JVL QuickStep stepping motors connected to the solar cell stage. Each angle was randomly varied in steps of 10° in the range 0–90° unless otherwise specified. At each angle combination, (θ, ϕ), the $I–V$ curve was measured under 1 sun and the result collected using LabView, such that a total of 100 $I–V$ curves were measured for each cell. The measured $I–V$ curves were then analysed in order to determine I_{SC}, V_{OC}, FF and P_{el} at each angle combination, (θ, ϕ), using SciLab. Finally the angle-resolved photovoltaic properties were plotted and the average electrical power output normalized to the normal incidence power output was calculated in order to compare the angle-dependency of different cells. A LEO 1550 Scanning Electron Microscope (SEM) was used to characterize the nanostructured surface topology.

4. Results

An example of the nanostructured surfaces realized by maskless RIE in this work is seen in Fig. 1.

The nanostructures seen in Fig. 1 are conical-like hillocks randomly distributed across the entire solar cell surface. The nanostructures are on average 300–400 nm tall with an area density of ~ 100 μm^{-2}. The topology is shown with and without ~ 60 nm PECVD SiN_x:H in Fig. 1. It is seen from Fig. 1(a) that the SiN_x:H AR-coating does not change the RIE-textured topology significantly, but makes the nanostructure edges slightly more round and smooth.

Fig. 2 shows total weighted average reflectance of RIE-textured Si below 1.1% for all three crystalline grades of Si, which is a clear improvement compared to KOH- and acidic-textured Si used in standard industrial Si solar cells. With anti-reflective coating KOH-textured Si has reflectance of 2% [22], while acidic-textured multi-crystalline Si has reflectance of 8% [23]. It is seen that the average reflectance is unaffected by the ~ 60 nm PECVD SiN_x:H AR-coating. The results furthermore show negligible increase in reflectance after emitter diffusion. The RIE-textured Si shows $\sim 0.1\%$ minimum reflectance independent of crystalline grade. The power conversion efficiencies at normal incidence of the fabricated solar cells are summarized in Table 1. Table 1 shows that the RIE-textured cells have lower power conversion efficiency than the conventionally textured cells primarily due to lower short-circuit current, but also reduced open-circuit voltage. Based on IQE-measurements and LASSIE[2] analysis, the current and voltage losses were explained by increased emitter and surface

---

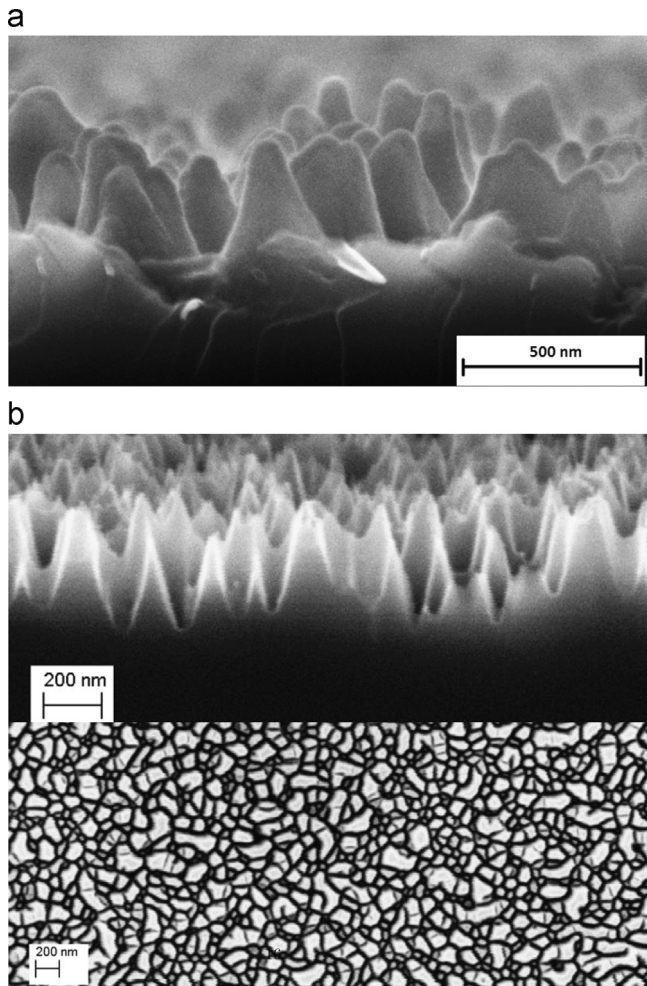[2] Loss analysis of silicon solar cells by IQE evaluation.

a

b

Fig. 1. SEM-image at 45° (a, b, top) and 0° (b, bottom) tilt of the RIE-textured Si surface with (a) and without (b) ~60 nm PECVD SiN_x:H AR-coating, respectively.
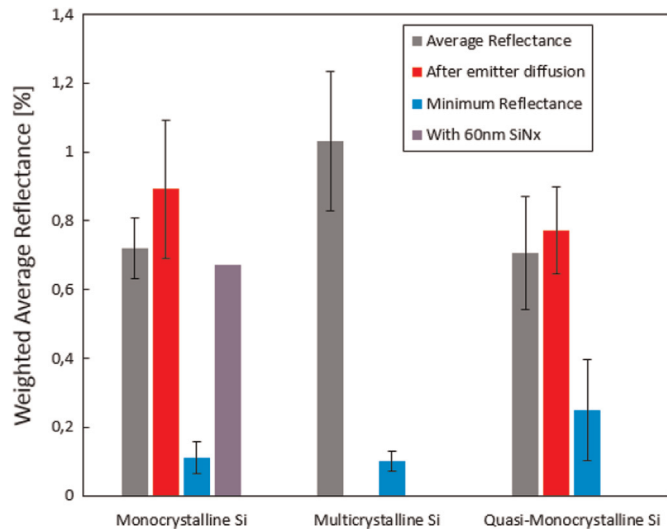

Fig. 2. Total weighted (AM1.5) average reflectance before and after emitter diffusion as well as the minimum reflectance of mono-, multi- and quasi-mono Si surfaces, respectively. The average reflectance of RIE-textured mono-crystalline Si with ~60 nm PECVD SiN_x:H AR-coating is also shown.

recombination [24]. For the cells fabricated in this work, the texturing and thus reflectance was not fully optimized. Since the RIE-texturing has been further optimized after these cells were

Table 1
Power conversion efficiency, short-circuit current, open-circuit voltage and fill factor at normal incidence of conventionally and RIE-textured mono-, multi- and quasi-mono-crystalline Si cells, respectively.

Cell	Efficiency (%)	J_{SC} (mA/cm^2)	V_{OC} (mV)	FF
Normal incidence				
Conventional mono	17.8	36.8	619	0.78
Conventional multi	16.5	34.4	619	0.77
RIE mono	16.5	35.2	609	0.78
RIE multi	14.5	31.7	592	0.77
RIE quasi-mono	13.0	30.0	575	0.75
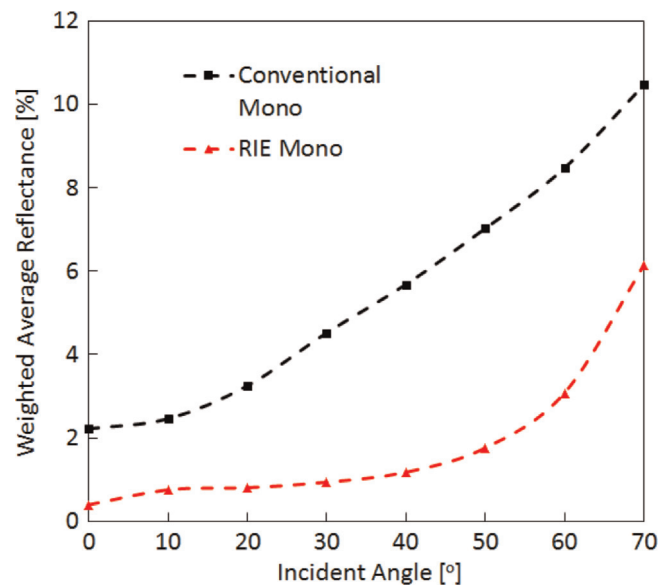
Fig. 3. Incident angle dependent total weighted average reflectance of KOH-textured (squares) and RIE-textured (triangles) mono-crystalline Si substrates.

fabricated, with a resulting weighted average reflectance below 1%, it is expected that the power conversion efficiency will be increased in future studies. In addition, optimized post-RIE processing may reduce emitter recombination.

Fig. 3 shows the total weighted (AM1.5) average reflectance as function of incident angle for standard, KOH-textured (squares) and RIE-textured (triangles) mono-crystalline Si substrates. The reflectance was measured using an integrating sphere with one axis angle variation of the incident optical fiber relative to the Si substrate. The results in Fig. 3 show that the reflectance of RIE-textured Si is significantly below that of KOH-textured Si at all incident angles below 70°. Furthermore the reflectance of KOH-textured Si increases more with incident angle up to 50° than the reflectance of RIE-textured Si. For angles above 50° the reflectance of RIE-textured Si increases more with incident angle than that of KOH-textured Si. This result shows the potential for improved solar cell performance using RIE-texturing at non-ideal incident angles.

There are two reasons for measuring parameters such as I_{SC}, V_{OC}, FF and power output as function of two different incident angles and plotting the result in a 2-D plot such as in Fig. 4: First of all, the intention of this work is to demonstrate a new and different method for characterization of solar cells in general. By measuring I–V-data as function of two orthogonal incident angles in combination, realistic angle-resolved scenarios such as diffuse light conditions can be investigated in more detail. Secondly, this method allows for a quantification of any asymmetric features of the solar cell with respect to incident angle of the light, whether on the surface or inside the cell. Examples of this are isotropic compared to anisotropic texturing methods and light trapping properties. We
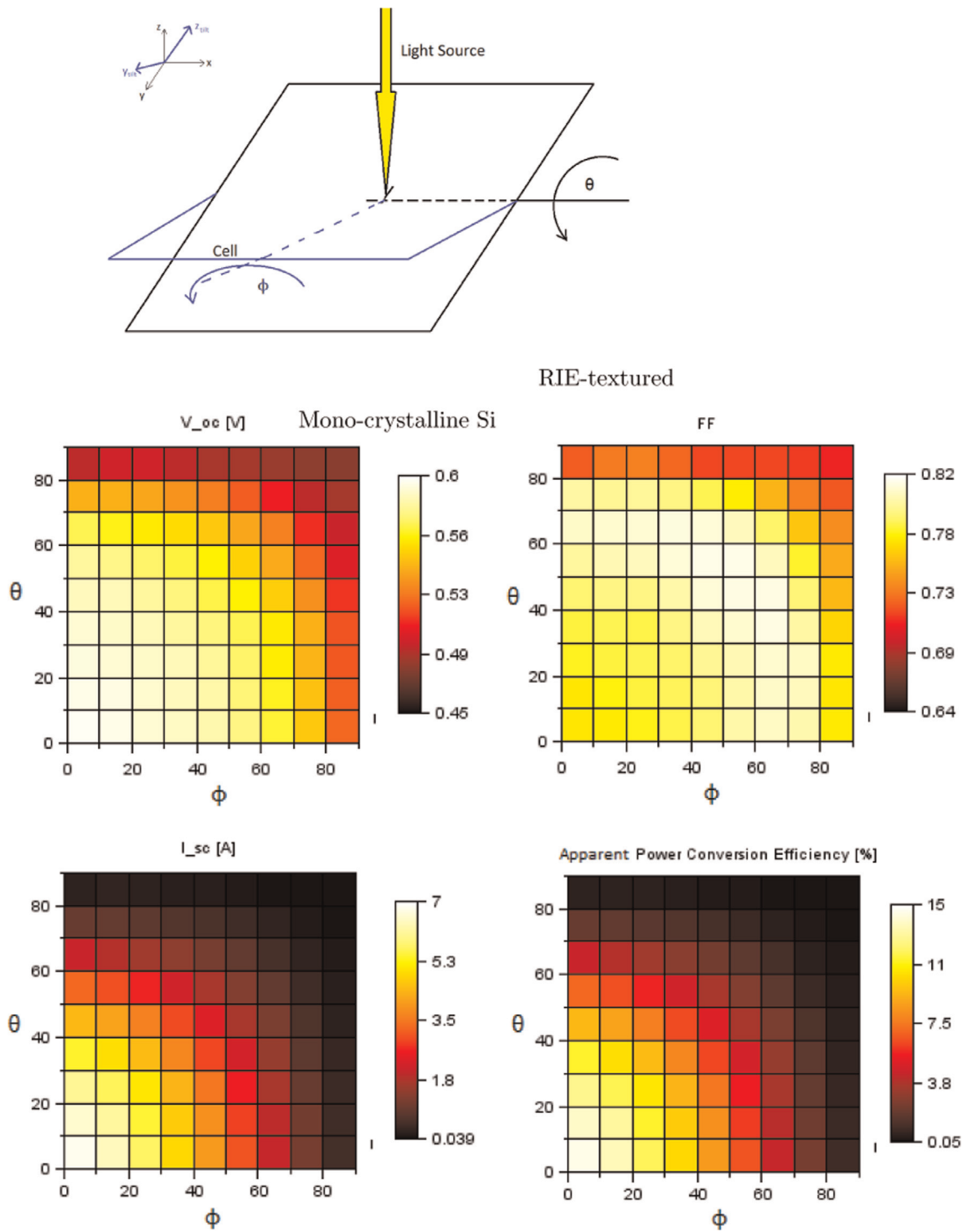
Fig. 4. Angle-resolved measurement including short-circuit current, open-circuit voltage, fill factor and power conversion efficiency. The result is for a RIE-textured mono-crystalline Si solar cell. A sketch of the measurement and coordinate system is seen in the top of the figure. The angles, θ and ϕ are indicated.

acknowledge that the asymmetric behaviour seen in Fig. 4 is not significant considering the uncertainties of the measurement. Thus, the choice of a 2-D plot in this case is a demonstration of the method and its capabilities, rather than a thorough analysis of asymmetric angle-resolved behaviour.

Fig. 4 shows that V_{OC} and FF do not change significantly for angles below 80°. I_{SC} and consequently P_{el} decrease with increasing incident angle. This is expected since the optical input power, P, on the solar cell decreases with cosine to the incident angle,

since the effective illuminated area decreases with cosine to the angle according to Eq. (1). In the experimental setup the optical power incident on the cell for angle variation θ is given by

$$P = P(\theta) = \Phi_0 W^2 \cos(\theta) = P_0 \cos(\theta) \qquad (1)$$

under ideal conditions. Here W is the edge length of the cell, Φ_0 is the optical intensity and P_0 is the optical power incident on the cell at normal incidence. The efficiency of the cell, which may be angle dependent, is

$$\eta(\theta) = \frac{P_{el}(\theta)}{P(\theta)} \qquad (2)$$

where P_{el} is the electrical output power at optimal load conditions. Part of any angular dependence in the efficiency is due to angular dependence of the reflection coefficient, $r(\theta)$, and this dependency is made explicit, if an internal efficiency η_{int} is defined such that

$$\eta(\theta) = \eta_{int}(\theta)[1 - r(\theta)] \qquad (3)$$

The internal efficiency, $\eta_{int}(\theta)$, could be angle dependent due to increased photon path length within the silicon for increasing θ and consequently increasing collection probability. Investigation of this effect is beyond the scope of this work.

These efficiencies are the physically relevant parameters for the cell. For convenient presentation of the raw measurement data, an artificial apparent efficiency η_{app} may be defined as

$$\eta_{app}(\theta) = \frac{P_{el}(\theta)}{P_0} = \eta(\theta)\cos(\theta) \qquad (4)$$

and from the rightmost expression in Eq. (4), it is seen that if the cell has an efficiency without angular dependency, then the apparent efficiency has a cosine angular dependency. The measured apparent efficiency for the RIE-textured mono-crystalline Si cell is plotted in Fig. 5; in the plot the expected apparent efficiency given in Eq. (4) assuming a constant η is also shown for comparison. For simplicity the results are only shown with angle variation in one axis.

Fig. 5 shows that the experimentally measured apparent efficiency is higher than expected for incident angles below 60°. This may in part be explained by divergence of the light source, which changes the actual optical input power according to the following equation:

$$P(\theta) = \Phi_0 W^2 \frac{\cos(\theta)}{1 - \left(\frac{W}{2L}\sin(\theta)\right)^2} \qquad (5)$$

where L is a characteristic length parameter of the divergence. Note that the term $1 - ((W/2L)\sin(\theta))^2$ is a possible correction term related purely to the measurement setup. Eq. (5) shows that divergence of the light source accounts for measured apparent efficiency values higher than expected. However, efficiency values lower than expected, as seen for incident angles higher than 60° in Fig. 5, cannot be explained by divergence of the light source and are most probably a result of increased reflectance at higher incident
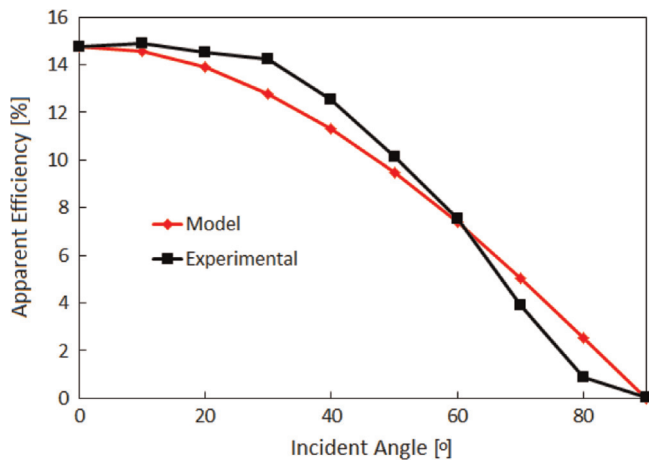
Fig. 5. Angle-resolved apparent efficiency measurement as function of the incident angle in one axis in comparison with the expected apparent efficiency decreasing with cosine to the angle. Experimental data for the RIE-textured mono-crystalline Si solar cell are shown.
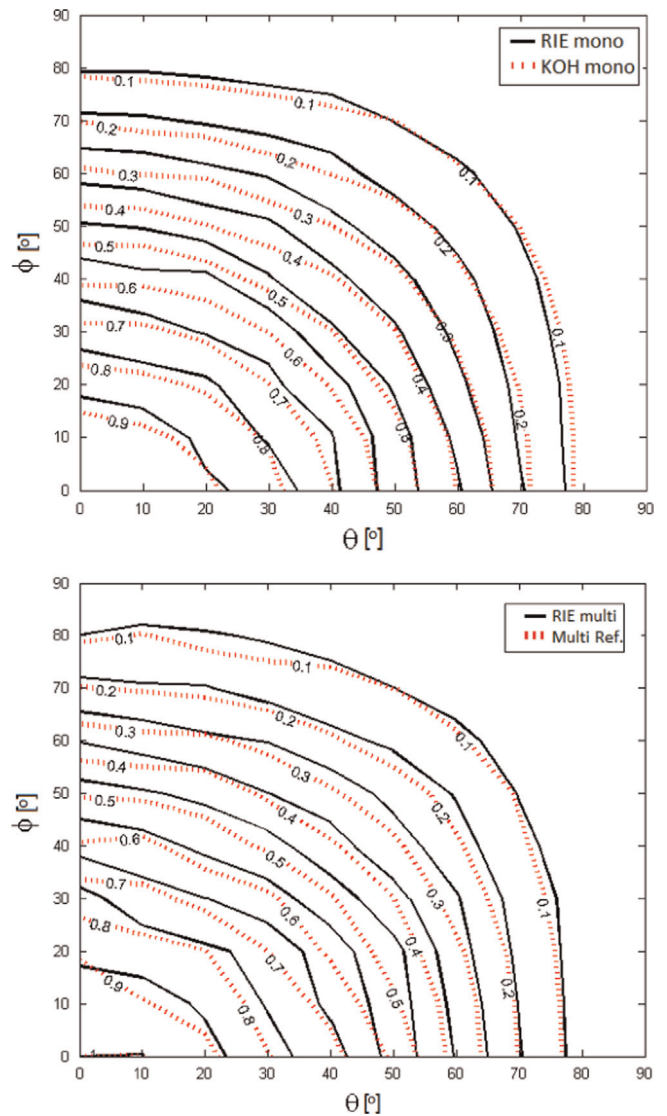
Fig. 6. Angle-resolved electrical power output normalized to the power output at (0,0) for the RIE-textured and conventionally textured mono- (top) and multi-crystalline (bottom) Si cell, respectively.

angles. P_{el} decreases according to Eq. (3) when the reflected part of the optical input power, $r(\theta)$, increases with the incident angle as shown in Fig. 3.

In order to evaluate the actual angle dependency of the differently textured solar cells, the measured electrical power output was normalized to the electrical power output at normal incidence, (0,0). Fig. 6 shows the angle-dependent normalized power output for the RIE- and conventionally textured mono- and multi-crystalline Si cell, respectively, for comparison. Fig. 6 shows that the RIE-textured mono- and multi-crystalline cells in general have slightly higher angle-resolved efficiency normalized to the efficiency at normal incidence compared to the conventionally textured cells. For certain incidence angles above 60° the conventionally textured mono-crystalline cell shows slightly higher normalized efficiency compared to the RIE-textured. Fig. 6 also shows an asymmetric behaviour with respect to the two angles, θ and ϕ. The asymmetry occurs for both RIE- and conventionally textured cells, which indicates that the asymmetric behaviour is partly due to imperfections in the measurement setup. However, it is seen that the asymmetry is slightly larger for the conventional cells for most angles. This might be explained by the different rotational symmetries for the differently textured topologies: The

black silicon cell – due to the random nature of the surface nanostructures – should only be affected by the polar angle of the incident light, whereas the azimuthal angle should not matter. The same may not be true for KOH textured cells, where the pyramids may be of random size, but they all share a fourfold symmetry in the azimuthal angle; it follows that some degree of variation with the azimuthal angle may be present for KOH cells.

The asymmetric behaviour may also be due to the front metallization, which reduces the symmetry to twofold or lower.

Yet, the observed asymmetry is too small compared to the uncertainties of this measurement to conclude whether the asymmetry is actually due to topology differences or measurement inaccuracy.

Angle-resolved properties similar to the results in Fig. 4 were measured for nanostructured mono-, multi- and quasi-mono-crystalline Si cells and conventionally textured mono- and multi-crystalline Si cells for comparison. Since texturing of quasi-mono-crystalline Si cells is not yet fully established or standardized, no such cell was produced. Based on the measured angle-resolved electrical power output, the average normalized electrical power output, Ψ_{av}, relative to the power output at normal incidence can be compared for each of the differently textured cells. Ψ_{av} is given by the expression in Eq. (6) and the resulting values of average relative power output are shown in Table 2 and Fig. 7:

$$\Psi_{av} = \frac{1}{N} \sum_{\theta=0}^{90} \sum_{\phi=0}^{90} \frac{P_{el}(\theta, \phi)}{P_{el}(0, 0)} \tag{6}$$

In Eq. (6) N denotes the total number of efficiency values which is being averaged over. In the case of averaging over incident angles in the range of 0–90° in steps of 10° in both axes, $N=100$. P_{el} denotes the measured electrical power output of the cell.

The results in Fig. 7 and Table 2 show that the average normalized power output is also higher for the RIE-textured cells compared to the reference cells in the incident angle range of 0–40°. Furthermore the difference between the RIE-textured and the reference cells is even more significant in this smaller range of angles closer to normal incidence. This angular range is arguably more interesting than 0–90° due to e.g. higher sunlight intensity close to normal incidence and the effective restriction of incident angles of light reaching the solar cells due to refraction and reflection of light from the protective glass covering solar cells in practice. In order to account for these differences, it is needed to do a complete weighing of the different incident angles and angle ranges. Such analysis is out of the scope of this work, but the results indicate the need for a more detailed analysis.

5. Discussion

The results in Table 1 show that the RIE-textured cells have lower power conversion efficiency at normal incidence due to increased surface recombination of the RIE-textured cells [24].

Table 2
Average normalized electrical power output relative to the power output at normal incidence, averaged over a range of incident angles from 0° to 90° and 0° to 40°, respectively, in two orthogonal axis for conventional and RIE-textured mono-, multi- and quasi-mono-crystalline Si solar cells, respectively.

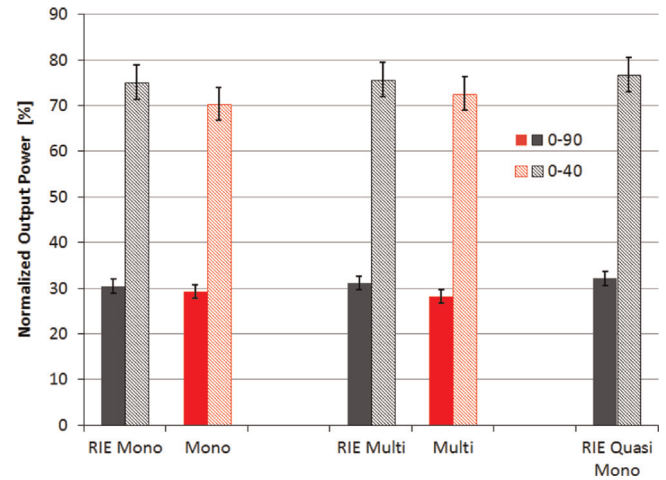| Ψ_{av} (%), [θ; ϕ]	[0–90°; 0–90°]	[0–40°; 0–40°]
RIE mono	30.44	75.15
RIE multi	31.13	75.69
RIE quasi-mono	32.16	76.81
Conventional mono	29.22	70.39
Conventional multi	28.18	72.62

Fig. 7. Average normalized electrical power output in the range 0–90° and 0–40°, respectively, relative to the power output at normal incidence for conventionally and RIE-textured mono, multi and quasi-mono-crystalline Si cells, respectively.

However, the average electrical power output normalized to the power output at normal incidence shown in Fig. 7 is higher for the RIE-textured cells compared to the conventionally textured cells; both for mono- and multi-crystalline Si. This indicates a less angle-dependent power output of such nanostructured Si solar cells compared with conventionally textured Si solar cells in general. Less angle-dependent power output implies potentially higher power output over a broad range of incident angles representing e.g. angle variation during daily and yearly operation of solar cells and panels. Furthermore, and perhaps more importantly, such less angle-dependent behaviour as seen in Fig. 7 represents improved performance under diffuse light conditions for nanostructured solar cells compared with conventionally textured solar cells. Since diffuse light is a realistic and important operating condition, which affects the performance of commercial solar cells and panels significantly, this result shows the potential of nanoscale texturing, such as maskless RIE-texturing, as a way of improving the overall performance of Si solar cells by enhancing the diffuse and low light performance and thus create a more stable and angle-independent solar cell performance. This behavior may change when measuring solar modules, in which the solar cells are covered by encapsulants that may affect the optical performance. Such analysis is beyond the scope of this work, but will be examined in future studies.

6. Conclusion

A method for angle-resolved characterization of solar cells in general and measured angle-dependent photovoltaic properties of nanostructured and conventionally textured mono-, multi- and quasi-mono crystalline Si solar cells, respectively, have been presented. Compared with conventionally textured cells the nanostructured solar cells have lower power production over a broad range of incident angles due to lower power conversion efficiency in general. However, the RIE-textured multi-crystalline Si cells show a 3% point improvement in average normalized angle resolved power output compared to conventionally textured and the RIE-textured mono-crystalline Si cells show above 1% point improvement compared to conventionally textured.

Acknowledgements

References

[1] X. Liu, P.R. Coxon, M. Peters, B. Hoex, J.M. Cole, D.J. Fray, Black silicon: fabrication methods, properties, and solar energy applications, Energy Environ. Sci., R. Soc. Chem. 7 (2014) 3223–3263. http://dx.doi.org/10.1039/c4ee01152j (Review article).

[2] A. Rahman, A. Ashraf, H. Xin, X. Tong, P. Sutter, M.D. Eisaman, C.T. Black, Sub-50-nm self-assembled nanotextures for enhanced broadband antireflection in silicon solar cells, Nat. Commun. 6 (2015) 5963. http://dx.doi.org/10.1038/ncomms6963.

[3] J. Oh, H.C. Yuan, H. Branz, An 18.2%-efficient black-silicon solar cell achieved through control of carrier recombination in nanostructures, Nat. Nanotechnol. 7 (2012) 743–748.

[4] T.H. Her, R.J. Finlay, C. Wu, S. Deliwala, E. Mazur, Microstructuring of silicon with femtosecond laser pulses, Appl. Phys. Lett. 73 (1998) 1673–1675.

[5] H. Jansen, M. Deboer, R. Legtenberg, M. Elwenspoek, The black silicon method—a universal method for determining the parameter setting of a fluorine-based reactive ion etcher in deep silicon trench etching with profile control, J. Micromech. Microeng. 5 (1995) 115–120.

[6] S.A. Boden, D.M. Bagnall, Optimization of moth-eye antireflection schemes for silicon solar cells, Prog. Photovolt.: Res. Appl. 18 (2010) 195–203. http://dx.doi.org/10.1002/pip.951.

[7] S.J. Wilson, M.C. Hutley, The optical properties of 'moth eye' antireflection surfaces, Opt. Acta: Int. J. Opt. 29 (7) (1982) 993–1009. http://dx.doi.org/10.1080/713820946.

[8] F. Priolo, T. Gregorkiewicz, M. Galli, T.F. Krauss, Silicon nanostructures for photonics and photovoltaics, Nat. Nanotechnol. 9 (2014) 19–32. http://dx.doi.org/10.1038/NNANO.2013.271.

[9] P. Repo, J. Benick, V. Vähänissi, J. Schön, G. von Gastrow, B. Steinhauser, M.C. Schubert, M. Hermle, H. Savin, N-type black silicon solar cells, SiliconPV, Energy Procedia 38 (2013) 866–871.

[10] J. Yoo, Reactive ion etching (RIE) technique for application in crystalline silicon solar cells, Sol. Energy 84 (2010) 730–734.

[11] J. Zhu, Z. Yu, S. Fan, Y. Cui, Nanostructured photon management for high performance solar cells, Mater. Sci. Eng. R 70 (2010) 330–340.

[12] K.N. Nguyen, D. Abi-Saab, P. Basset, E. Richalot, F. Marty, D. Angelescu, Y. Leprince-Wang, T. Bourouina, Black silicon with sub-percent reflectivity: influence of the 3D texturization geometry, in: 16th International Conference on Solid-State Sensors, Actuators and Microsystems (Transducers 11), 2011, pp. 354–357.

[13] M.D. Kelzenberg, S.W. Boettcher, J.A. Petykiewicz, D.B. Turner-Evans, M.C. Putnam, E.L. Warren, J.M. Spurgeon, R.M. Briggs, N.S. Lewis, H.A. Atwater, Enhanced absorption and carrier collection in Si wire arrays for photovoltaic applications, Nat. Mater. 9 (2010) 239–244. http://dx.doi.org/10.1038/NMAT2635.

[14] Y.-F. Huang, S. Chattopadhyay, Y.-J. Jen, C.-Y. Peng, T.-A. Liu, Y.-K. Hsu, C.-L. Pan, H.-C. Lo, C.-H. Hsu, Y.-H. Chang, C.-S. Lee, K.-H. Chen, L.-C. Chen, Improved broadband and quasiomnidirectional anti-reflection properties with biomimetic silicon nanostructures, Nat. Nanotechnol. 2 (2007) 770–774.

[15] A. Parretta, A. Sarno, P. Tortora, H. Yakubu, P. Maddalena, J. Zhao, A. Wang, Angle-dependent reflectance measurements on photovoltaic materials and solar cells, Opt. Commun. 172 (1999) 139–151.

[16] J. Zhao, A. Wang, M.A. Green, 24.5% efficiency silicon PERT cells on MCZ substrates and 24.7% efficiency PERL cells on FZ substrates, Prog. Photovolt.: Res. Appl. 7 (1999) 471–474.

[17] D.L. King, J.A. Kratochvil, W.E. Boyson, Measuring solar spectral and angle-of-incidence effects on photovoltaic modules and solar irradiance sensors, in: 26th IEEE Photovoltaic Specialists Conference, 1997, pp. 1113–1116.

[18] M.C. Anderson, Stand structure and light penetration. II. A theoretical analysis, J. Appl. Ecol. 3 (1) (1966) 41–54.

[19] R. Perez, P. Ineichen, R. Seals, J. Michalsky, R. Stewart, Modeling daylight availability and irradiance components from direct and global irradiance, Sol. Energy 44 (5) (1990) 271–289.

[20] P. Mialhe, The solar cell output power dependence on the angle of incident radiation, Renew. Energy 1 (3/4) (1991) 519–521.

[21] Y.M. Song, J.S. Yu, Y.T. Lee, Antireflective submicrometer gratings on thin-film silicon solar cells for light-absorption enhancement, Opt. Lett. 35 (3) (2010) 276–278.

[22] L. Zhao, Y.H. Zuo, C.L. Zhou, H.L. Li, H.W. Diao, W.J. Wang, Theoretical investigation on the absorption enhancement of the crystalline silicon solar cells by pyramid texture coated with SiNx:H layer, Sol. Energy 85 (2011) 530–537.

[23] D. Macdonald, A. Cuevas, M. Kerr, C. Samundsett, D. Ruby, S. Winderbaum, A. Leo, Texturing industrial multicrystalline silicon solar cells, Sol. Energy 76 (1) (2004) 277–283.

[24] R.S. Davidsen, Ø. Nordseth, A. Boisen, M.S. Schmidt, O. Hansen, Plasma texturing on large-area industrial grade CZ silicon solar cells, in: 28th EU PVSEC Conference Proceedings, 2013.

Appendix E

Inkjet Patterned ALD Aluminium Oxide for Rear PERC Metal Contacts

Authors:
Alex To, **Rasmus Schmidt Davidsen**, Xinrui An, Alison Lennon, Allen Barnett

Inkjet Patterned ALD Aluminium Oxide for Rear PERC Metal Contacts

Alexander To[1], Rasmus Schmidt Davidsen[2], Xinrui An[1], Alison Lennon[1] and Allen Barnett[1]

[1]University of New South Wales, Kensington, NSW, 2031 Australia

[2]Department of Micro- and Nanotechnology, Technical University of Denmark (DTU)

Abstract — **A method of patterning atomic layer deposition (ALD) deposited aluminium oxide dielectrics (Al_2O_3) using an inkjet printer is outlined. This method has applications in creating PERC cell type rear contacts. It is simpler, and uses fewer chemicals than immersive etching techniques such as those involved in photolithography, and the patterning does not cause damage to the silicon evident in laser ablation techniques. Holes with varying diameter between 61-159 μm were etched onto a 50 nm thick ALD Al_2O_3 passivating dielectric at numerous print settings. The relationship between the printing parameters and the feature size of the holes is discussed.**

Index Terms —**Aluminium Oxide, Inkjet, PERC, Silicon, Solar Cells.**

I. INTRODUCTION

With renewed commercial and research interest in Passivated Emitter Rear Contact (PERC) solar cells, there has been increasing focus on methods which create localised point openings in rear passivating dielectrics [1-3]. With excellent surface passivation properties on p-type silicon [4-8], aluminium oxide (Al_2O_3) deposited by atomic layer deposition or plasma enhanced chemical vapour deposition (PECVD) is commonly used to passivate the p-type rear surface of industrial PERC style cells. Current methods employ pulsed laser ablation of a dielectric stack to remove localised regions [9,10]. However a major drawback of this method is the possibility of creating laser-induced damage though micro-crack formation, point defects, surface melting, etc., which can reduce cell performance [9-13].

We investigate the application of direct etching methods to create small point-like openings directly onto thin ALD Al_2O_3 dielectrics in a single application. Our group has previously demonstrated a method for patterning anodised aluminium oxide (AAO) with inkjet printing techniques and phosphoric acid (H_3PO_4) to form rear contact openings [15], and Liu et al. have used a technique developed by Lennon et al. to etch Al_2O_3/SiN_x stacks, which involves spin coating a thin layer of polyacrylic acid on to the sample and printing ammonium fluoride [16-18]. In this submission we demonstrate the direct etching of ALD Al_2O_3 which does not require any spin-coating steps. This method has the advantage of simplicity and uses less material. Unlike laser ablation, it does not subject the surface of the wafer to high localised heating, removing the risk of laser-induced damage on the silicon surface.

Etching of Al_2O_3 dielectrics approximately 50 nm thick is demonstrated using droplets of H_3PO_4 deposited using an inkjet printer. We examine the relationship between the dimensions of the etched features and the amount of etchant deposited and characterise the features using an optical microscope.

II. ETCHING METHOD

The point contact patterns were prepared on 200 μm thick, 1.6 Ω cm boron doped p-type CZ <100> wafers. To create a textured rear surface, the wafers underwent a five minute saw damage etch in 25% (w/v) NaOH at 80 ± 2 ^{0}C. Prior to ALD deposition, all the wafers underwent a full Radio Corporation of America (RCA) clean and a short dip in 5% (w/v) hydrofluoric acid (HF) to remove the native oxide on the surface.
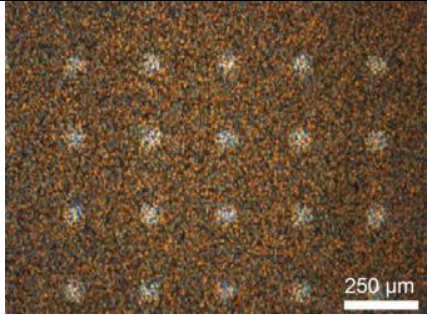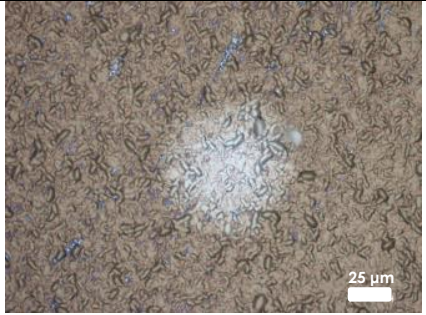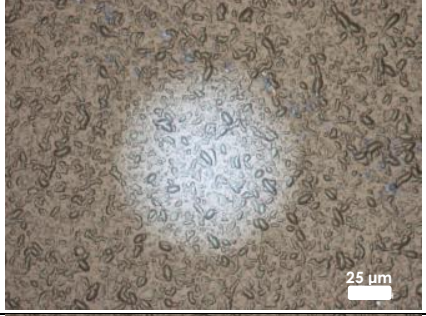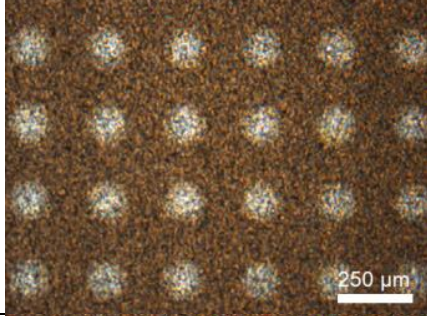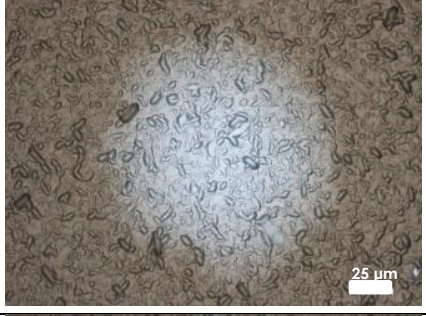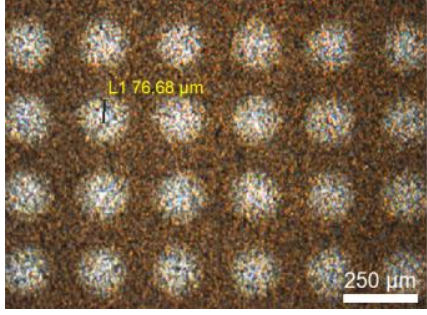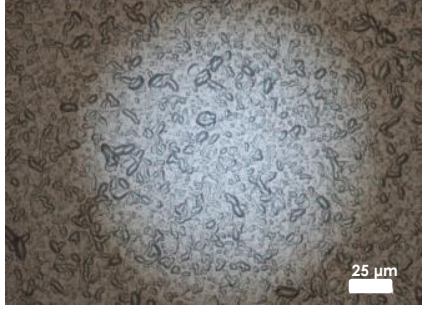
An ALD Al_2O_3 passivating dielectric was grown on the rear using a thermal ALD system (Cambridge Nanotech Savannah S100). 500 deposition cycles at a deposition temperature of 200 ^{0}C were used to grow a thin passivating Al_2O_3 dielectric of approximately 50 nm in thickness (growth rate of 1.08 Å/cycle). All samples were then annealed in a nitrogen ambient environment for 10 minutes at 425 ^{0}C.

A solution of 50% (w/v) H_3PO_4 was inkjet-printed onto the Al_2O_3 surface using a FUJIFLM Dimatix Materials Printer (DMP-2831), which utilised a piezoelectric ink cartridge with sixteen nozzles, each having a nominal drop volume of 10 pL. In order to maintain a droplet velocity of 10 m/s, printing was performed at 5 kHz and a nozzle voltage range of 10.8-12.6 V. A single nozzle was used in each printing run to increase printing accuracy. The platen temperature was maintained at 60^{0}C in order to accelerate the etch reaction whilst the ink temperature was kept at a constant 30 ^{0}C in order to maintain consistency of the fluid viscosity and print process.

A test pattern consisting of a sequence of dots spaced 250 μm apart within an array 20 mm wide and 2 mm in length was used to ascertain the amount of etching on the substrate. Varying levels of etchant were deposited by reprinting over the same location in numerous passes of the nozzle to add more layers of etchant to the original print site.

After printing, wafers were left on the heated platen for varying durations to allow the etch reaction to occur. The wafers were then rinsed in deionised (DI) water and the

	20x Magnification		50x Magnification
Array 1 1 layer Average diameter = 61 µm			
Array 2 2 layers Average diameter = 90 µm			
Array 3 4 layers Average diameter = 119 µm			
Array 4 8 layers Average diameter = 159 µm			

resulting etched patterns were characterised by optical microscope imaging. The diameters of 16 random features was measured and aggregated to give the average feature diameter.

III. RESULTS

Table I shows the etched features as a result of printing. The change in the surface colour in the images reveals the underlying silicon which is now exposed due to the Al_2O_3 layer being etched.

The results indicate that full etching of the 50 nm dielectric can be achieved with a single layer of etchant. The amount of etchant applied increases proportionally with the amount of layers deposited, and increasing the amount of etchant deposited increased the size of the etched features. This trend is evident in Fig. 1, which graphs the diameter of the etched features as a function of the number of layers printed. This increase in diameter is a result of the etchant spreading over the surface and etching a larger area of the underlying dielectric.

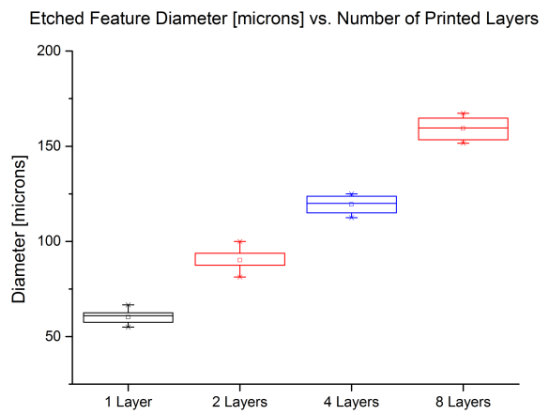Fig.1. Box plot of etched hole diameter as a function of the number of layers printed onto the substrate.

This shows that different sized features can be created by depositing various amounts of etchant. The settings can also be tuned to print any spacing of dots which can be used to tune the percentage of area exposed to metal to optimize contact resistance and contact recombination.

IV. CONCLUSION

We have described a technique to create localised point-like openings on an ALD deposited Al_2O_3 which can be used to create PERC solar cells. A single layer of H_3PO_4 was shown to be an effective etchant of ALD deposited Al_2O_3, and this technique can be used to create openings which are on average 61 μm in diameter for ALD thicknesses up to 50 nm. Furthermore, the process flexibility of inkjet printing allows for the etched area to be customised by varying the number of layers printed and the pattern design, which in turn affects the amount of underlying silicon exposed to metal, which is useful when optimizing rear point contact schemes for PERC cells.

REFERENCES

[1] P. Saint-Cast, J. Benick, D. Kania, L.Weiss, M. Hofmann, J. Rentsch, R. Preu, S.W. Glunz, "High-Efficiency c-Si Solar Cells Passivated With ALD and PECVD Aluminum Oxide", *Electron Device Letters, IEEE* , vol.31, no.7, pp.695,697, 2010.

[2] R. Ferré, F. Schwarz, B. Beier, T. Dullweber, C. Jahn, S. Gatz, "20.5% Industrial PERC cells with PECVD Al_2O_3/SiN_x rear-passivation and flat-top nanosecond laser contact opening", *29th European Photovoltaic Solar Energy Conference and Exhibition*, 2014.

[3] E. Urrejola, R. Petres, J. Glatz-Reichenbach, K. Peter, E. Wefringhaus, H. Plagwitz, G. Schubert, "High efficiency industrial PERC solar cells with all PECVD-based rear surface passivation", *26th European Photovoltaic Solar Energy Conference and Exhibition,* pp. 2233 – 2235, 2011

[4] G. Agostinelli, A. Delabie, P. Vitanov, Z. Alexieva, H.F.W. Dekkers, S. De Wolf, G. Beaucarne, "Very low surface recombination velocities on p-type silicon wafers passivated with a dielectric with fixed negative charge", *Solar Energy Materials and Solar Cells*, Vol. 90, no. 18–19, pp. 3438-3443, 2006.

[5] B. Hoex, J.J. Gielis, M.C.M. van de Sanden, W.M. Kessels, "On the c-Si surface passivation mechanism by the negative-charge-dielectric Al2O3", *Journal of Applied Physics*, Vol. 104, Issues 11, 113703, 2008.

[6] J. Schmidt, B. Veith, R. Brendel, "Effective surface passivation of crystalline silicon using ultrathin Al2O3 films and Al2O3/SiNx stacks", *Physica Status Solidi (RRL) – Rapid Research Letter,* Vol. 3, Issue 9, 2009.

[7] J. Schmidt, F. Werner, B. Veith, D. Zielke, S. Steingrube, P.P. Altermatt, S. Gatz, T. Dullweber, R. Brendel, "Advances in the Surface Passivation of Silicon Solar Cells", *Energy Procedia*, Vol. 15, pp. 30-39, 2012.

[8] Dingemans, G. and Kessels, W. M. M., "Status and prospects of Al2O3-based surface passivation schemes for silicon solar cell", *Journal of Vacuum Science & Technology*, Vol. 30, 2012.

[9] J. Kim, Y. Hwang, J. Kim, J. Lim, E. Lee, "Investigation of Rear Side Selective Laser Ablation and Damage Etching Process for Industrial PERC Solar Cells", *Energy Procedia*, Vol. 55, pp. 791-796, 2014

[10] M. Kim, S. Park, D. Kim, "Highly efficient PERC cells fabricated using the low cost laser ablation process", *Solar Energy Materials Solar Cells*, Vol. 117, pp. 126-131, 2013.

[11] P. Engelhart, S. Hermann, T. Neubert, H. Plagwitz, R. Grischke, R. Meyer, U. Klug, A. Schoonderbeek, U. Stute, R. Brendel, G. Dingemans, W. M. M. Kessels, "Laser ablation of SiO2 for locally contacted Si solar cells with ultra-short pulses", *Progress in Photovoltaics: Research and Applications*, Vol. 15, no. 6, pp. 521-527, 2007.

[12] E. Schneiderlöchner, R. Preu, R. Lüdemann, S.W. Glunz, "Laser-fired rear contacts for crystalline silicon solar cells", *Progress in Photovoltaics: Research and Applications*, Vol. 10, no. 1, pp. 29-34, 2002.

[13] Z. Du, N. Palina, J.Chen, M. Hong, B. Hoex, "Rear-Side Contact Opening by Laser Ablation for Industrial Screen-Printed Aluminium Local Back Surface Field Silicon Wafer Solar Cells", *Energy Procedia*, Vol. 25, pp. 19-27, 2012.

[14] T. Schutz-Kuchly, A. Slaoui1, J. Zelgowski, A. Bahouka, M. Pawlik, J.-P. Vilcot, E. Delbos, M. Bouttemy, R. Cabal, "UV and IR laser induced ablation of Al2O3/SiN:H and a-Si:H/SiN:H," *EPJ Photovoltaics*, Vol. 5, 2014

[15] J. Cui, A. To, Z. Li, J. Rodriguez, A.J. Lennon, "Inkjet Patterned Anodic Aluminum Oxide for Rear Metal Contacts of Silicon Solar Cells", *Energy Procedia*, vol. 38, pp. 691-700, 2013.

[16] A.J. Lennon, R.Y. Utama, M.A.T. Lenio, A.W.Y. Ho-Baillie, N.B. Kuepper, S.R. Wenham, "Forming openings to semiconductor layers of silicon solar cells by inkjet printing", *Solar Energy Materials and Solar Cells*, vol. 92, no. 11, pp. 1410 - 1415, 2008,

[17] Lennon AJ; Ho-Baillie AWY; Wenham SR, 2009, "Direct patterned etching of silicon dioxide and silicon nitride dielectric layers by inkjet printing", *Solar Energy Materials and Solar Cells*, vol. 93, no. 10, pp. 1865 - 1874,

[18] L. Licheng, D. Zheren, L. Fen, B. Hoex, A.G. Aberle, "Aluminum local back surface field solar cells with inkjet-opened rear dielectric films," *38th IEEE* , *Photovoltaic Specialists Conference (PVSC)*, pp. 2204-2207, 2012

Appendix F

Improvement of Infrared Detectors for Tissue Oximetry using Black Silicon Nanostructures

Authors:
Søren Dahl Petersen, **Rasmus Schmidt Davidsen**, Lucia R. Alcala, Michael Stenbæk Schmidt, Anja Boisen, Ole Hansen, Erik Vilain Thomsen

EUROSENSORS 2014, the XXVIII edition of the conference series

Improvement of Infrared Detectors for Tissue Oximetry using Black Silicon Nanostructures

S. D. Petersen[a]*, R. S. Davidsen[a], L. R. Alcalá[a], M. S. Schmidt[a], A. Boisen[a], O. Hansen[a], E.V. Thomsen[a]

[a]DTU Nanotech, Technical University of Denmark, Kongens Lyngby, DK-2800, Denmark

Abstract

We present a nanostructured surface, made of dry etched black silicon, which lowers the reflectance for light incident at all angles. This surface is fabricated on infrared detectors used for tissue oximetry, where the detection of weak diffuse light signals is important. Monte Carlo simulations performed on a model of a neonatal head shows that approximately 60% of the injected light will be diffuse reflected. However, the change in diffuse reflected light due to the change in cerebral oxygenation is very low and the light will be completely isotropic scattered. The reflectance of the black silicon surface was measured for different angels of incident and was fund to be below 10% for angles of incident up to 70°. The quantum efficiency of detectors with the black silicon nanostructures was measured and compared to detectors with a simple anti-reflection coating. The result was an improvement in quantum efficiency for both normal incident light and light incident at 38°.

Keywords: Tissue oximetry; infrared detectors; black silicon; quantum efficiency; diffuse reflected light

1. Introduction

Near infrared tissue oximetry, as a medical diagnostic method, is next in line to continue in the successful footsteps of pulse oximetry, which today is widely used at hospitals. Tissue oximetry is of special interest within

* Corresponding author. Tel.: +45-45255692; fax: +45-45887762.
  E-mail address: sdpet@nanotech.dtu.dk

neonatology where it is used to non-invasively monitor the oxygenation of brain tissue on prematurely born infants [1]. The most widely used measurement method is spatially resolved spectroscopy (SRS) where light of different wavelengths is injected into the tissue and the diffuse reflected light is measured as a function of distance to the light source, generally done using distances of several centimeters, see Fig. 1a. We have previously presented a device for SRS measurements on neonates, consisting of nine individual detectors, made from silicon polyimide and PDMS and optimized for detection of light with a wavelength of 700-1000 nm, which can be seen in Fig. 1b [2].

Although a majority of the light is diffuse reflected from most tissue types the changes in signal due to changes in cerebral oxygenation are typically small. In order to maximize the detected signal the reflectance from the surface of the detectors should be as low as possible. A typical solution is to apply anti-reflection (AR) coatings to the detector surface, but such coatings are very dependent on the incident angle of light and the diffuse reflected light will be incident on the detectors at all angles (0-90°). We present a solution to this problem by using black silicon nanostructures, which are dry etched into the silicon surface of the detectors. Black silicon has already proven to be a very effective anti-reflection surface for solar cells because it offers low reflectance for a wide range of wavelengths as well as for a wide range of incident angles [3].
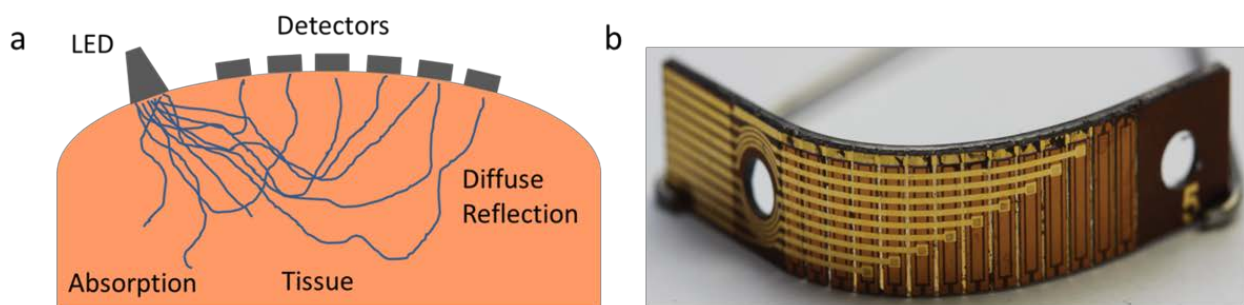
Fig. 1. (a) The principle behind spatially resolved spectroscopy. (b) A flexible array of infrared detectors used for tissue oximetry.

2. Results and discussion

2.1. Monte Carlo simulations

In order to investigate how the diffuse reflected light will behave as a function of cerebral oxygenation for a neonate we have used Monte Carlo simulation on a model of a neonatal head [4]. The model consists of four different layers corresponding to the skin, the skull, the cerebrospinal fluid and the cerebral tissue into which a pencil beam of light is injected. When the cerebral oxygenation changes it will lead to a change in the ratio between oxygenated hemoglobin and deoxygenated hemoglobin. This will in turn change the absorption coefficient of the cerebral tissue. Using data of the absorption coefficient for the two different types of hemoglobin the change in diffuse reflected light can be simulated as function of the cerebral oxygenation (StO2) for different wavelengths [5]. The results can be seen in Fig. 2a, which shows the diffuse reflected light as function of cerebral oxygenation for three different wavelengths. It can be seen that approximately 60% of the injected light will be diffuse reflected. However, the change in diffuse reflected light due to the change in cerebral oxygenation is very small, which indicates that the infrared detectors need to be of very high quality. Furthermore, the distance which the light has to travel before being completely isotropic scattered can be described as being greater than the inverse of the reduced scattering coefficient, which for the tissues in a neonatal head will be approximately 20 cm^{-1}. This means that the light will be isotropic scattered after travelling >0.5 mm into the tissue. The diffuse reflected light will therefore be both very weakly changing as function of cerebral oxygenation and arrive at the detectors from all angles between 0-90°.
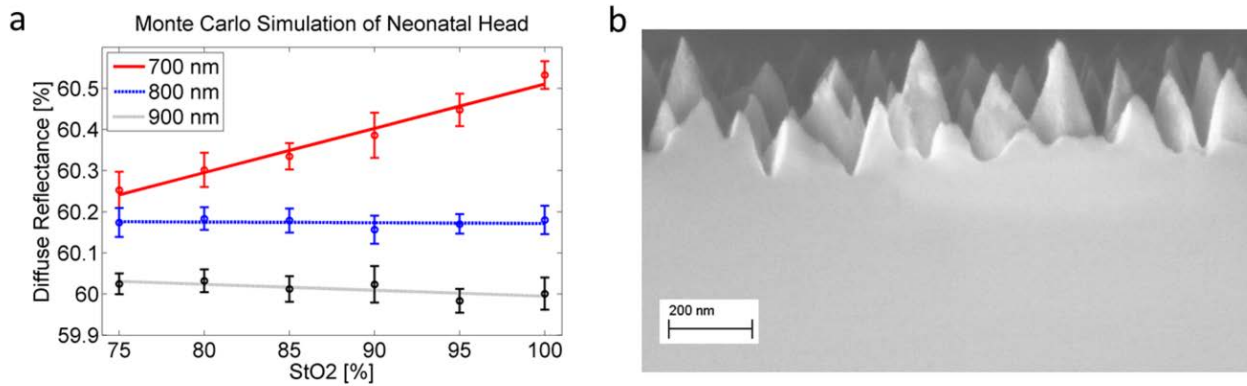
Fig. 2. (a) Results from Monte Carlo simulations. (b) SEM image of the black silicon nanostructures.

2.2. Device fabrication

The infrared detectors are fabricated on high quality (001) p-type silicon wafers with a resistivity of 10,000 Ω/cm. The detectors are fabricated as back side pn-junction diodes, using boron and phosphorous diffusions, where the junction is located on the opposite side of the light incident surface. This ensures that the electrical interconnects will not obscure for the incident light. A p-type front side field doping is also made by diffusion, in order to ensure that the generated minority carrier electrons will not diffuse towards the front side surface where the recombination velocity will be very high. The back side electrical interconnects are made by aluminum metallization and finally the black silicon nanostructures are etched into the front side using RIE with an SF_6/O_2 plasma. The black silicon nanostructures have a random topology and a height of 100-300 nm, as can be seen from Fig. 2b. Other devices where fabricated with a 50 nm SiO_2 / 50 nm SiN anti-reflection coating instead of the black silicon nanostructured surface. This ensured that the performance of the black silicon surface could be compared to a more standard AR coating.

The dry etching process for making the black silicon nanostructures has the advantage that it is compatible with polymers and metals that are on the silicon wafers when the etching process is performed. This is essential for many medical devices made from a silicon wafer platform, where a wet etch used for fabrication of the black silicon is not possible [6].

2.3. Reflectance and quantum efficiency measurements

The reflectance of the black silicon and the SiO_2/SiN AR coating were measured for light with a wavelength of 700-1000 nm using an integrating sphere and an ellipsometer, respectively. The result can be seen in Fig. 3a. For all the measured angles the black silicon can be seen to have a lower reflectance when compared to the AR coating. The quantum efficiency where measured, as a function of wavelength, for finished devices with both the black silicon nanostructures and the AR coating. The measurements were performed using a monochromator with 10 nm steps and a calibration photodiode with a known responsively and were done for normal incident light and light incident at 38° (the largest possible angle for our setup). The results can be seen in Fig. 3b. The devices with the black silicon nanostructures can be seen to have larger quantum efficiency for almost the entire wavelength span. For the entire spectrum (700-1000 nm) the devices with the black silicon nanostructures have an average quantum efficiency of 83.7% and 79.1% for light incident at 0° and 38° respectively. Whereas the devices with the AR coating have an average quantum efficiency of 74.1% and 61.6% for light incident at 0° and 38° respectively.

The anti-reflection properties of the black silicon nanostructures are seen to outperform the SiO_2/SiN AR coating both in terms of dependence on wavelength and angle. The quantum efficiency is higher for the devices with the black silicon nanostructures in the entire spectrum (700-1000nm). Furthermore, the quantum efficiency is only decreasing with 5.4% for the devices with the black silicon nanostructures when the incident angle is increased to 38°. For the devices with the AR coating the decrease is 16.9%. For many commercial infrared detectors for medical

use an IR transparent plastic coating is used, which acts as a cut-off filter for wavelengths below 700 nm. These commercial devices exhibit the same high quantum efficiency as the black silicon devices presented in this paper, but they still suffer from a strong angular dependence for the reflectance. For a typical commercial IR photodiode, coated with such a filter, a quantum efficiency reduction of approximately 25% at a light incident angle of 40° is normal [7].
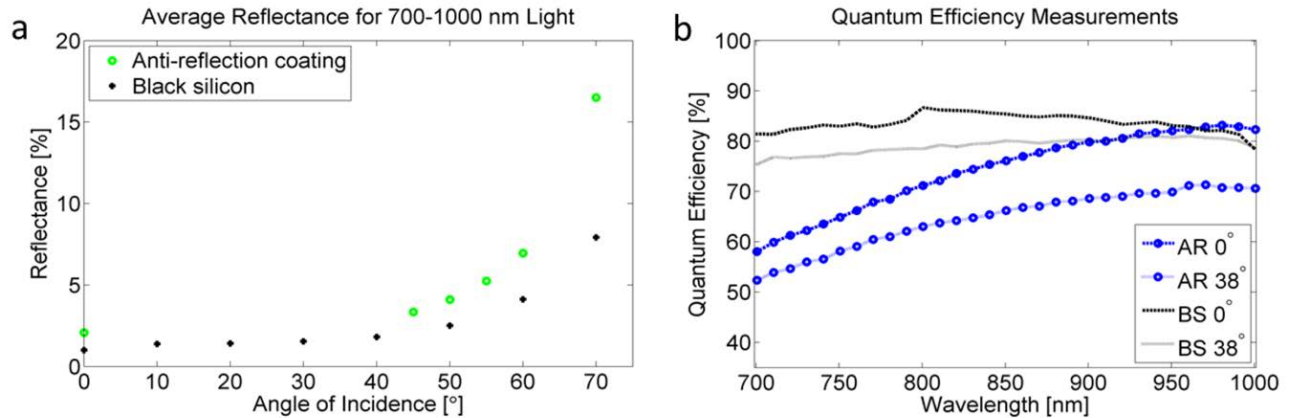
Fig. 3. (a) Reflectance measurements of AR coating and black silicon nanostructures. (b) Quantum efficiency measurements.

3. Conclusion

We have presented a black silicon nanostructured surface, which have been used to improve the anti-reflection capabilities for infrared detectors for tissue oximetry. The importance of the detector improvement has been proven by Monte Carlo simulations that showed how the diffuse reflected light would only be weakly dependent on the cerebral oxygenation and be completely isotropic scattered. The black silicon nanostructures are fabricated using a dry etch RIE process, which is compatible with wafers containing polymers and metals making it useful for various applications. Investigations of the black silicon nanostructured surfaces showed a decrease in reflectance for angles from 0-70° when comparing with a standard AR coating. Furthermore, the anti-reflection effect of the black silicon nanostructures was tested on infrared detectors. This showed higher quantum efficiencies for devices with the black silicon nanostructures at two angles when comparing them to devices with an anti-reflection coating and thus an improvement for the devices ability to detect weak diffuse scattered light.

References

[1] G. Greisen, T. Leung and M. Wolf, Has the time come to use near-infrared spectroscopy as a routine clinical tool in preterm infants undergoing intensive care, Phil. Trans. R Soc. A, 369 (2011) 4440–4451.
[2] S. D. Petersen, A. Thyssen, M. Engholm and E. V. Thomsen, A Flexible Infrared Sensor for Tissue Oximetry, Microelectronic Engineering, 111 (2013) 130-136.
[3] R. S. Davidsen, M. S. Schmidt, A. Boisen and O. Hansen, Plasma Etching on Large-area Mono-, Multi- and Quasi-mono Crystalline Silicon, Proceedings of the 39th International Conference on Micro and Nano Engineering, 2013.
[4] L. Wang, S. L. Jacques and L. Zheng, MCML - Monte Carlo Modeling of Light Transport in Multi-layered Tissue, Computer Methods and Programs in Biomedicine, 47 (1995) 131-146.
[5] B. L. Horecker, The Absorption Spectra of Hemoglobin and its Derivatives in the Visible and Near Infra-red Regions, J. Biol. Chem., 148 (1943) 173-183.
[6] Y. Su, S. Li, G. Zhao, Z. Wu, Y. Yang, W. Li and Y. Jiang, Optical Properties of Black Silicon Prepared by Wet Etching, J. Mat. Sci: Mater Electron, 23 (2012) 1558-1561.
[7] http://docs-europe.electrocomponents.com/webdocs/0655/0900766b806557c0.pdf

Appendix G

Plasma etching on large-area mono-, multi- and quasi-mono crystalline silicon

Authors:
Rasmus Schmidt Davidsen[*], Anja Boisen, Michael Stenbæk Schmidt, Ole Hansen

Plasma etching on large-area mono-, multi- and quasi-mono crystalline silicon

Rasmus Schmidt Davidsen*[1], **Michael Stenbæk Schmidt**[1], **Anja Boisen**[1], **Ole Hansen**[1]

[1] Department of Micro- and Nanotechnology, Technical University of Denmark (DTU), 2800-Lyngby,
Denmark
* rasda@nanotech.dtu.dk, Ørsteds Plads building 345East, 2800 Lyngby, Denmark

Keywords: plasma etching, nanostructures, black silicon, solar cells

We use plasma etched Black Si (BS)[1][2] nanostructures to achieve low reflectance due to the resulting graded refractive index at the Si-air interface. The goal of this investigation is to develop a suitable texturing method for Si solar cells. Branz et al. [3]report below 3% average reflectance for their 16.8% efficient black Si cell using a metal-assisted, chemical etching method on FZ mono-crystalline Si substrates. Yoo et al. [4] use RIE similar to this work on large-area, multi-crystalline Si cells and achieve a 16.1% efficiency despite a relatively high reflectance of 13.3%. Despite several advantages such as; (i) excellent light trapping, (ii) dry, single-sided and scalable process method and (iii) etch independence on crystallinity of Si, RIE-texturing has so far not been proven superior to standard wet texturing, primarily as a result of lower power conversion efficiency due to increased surface recombination. This work shows promising potential of future improvements in power conversion efficiency, since excellent light absorption has been shown for large-area, industry grade CZ Si wafers with several identified areas of improvement. We show that the RIE nanostructures lead to superior light absorption independent of crystalline grade and incident angle.

A texturing method which is applicable to all industrially relevant grades of Si and which yields improved performance at non-ideal incident angles has a major scientific and commercial relevance.

The nanostructures were fabricated using maskless RIE in a O_2 and SF_6 plasma, and the surface topology was optimized for solar cell applications by varying gas flows, pressure, power and process time. The starting substrates were 156x156 mm p-type, CZ mono-, multi- and quasi-mono crystalline Si wafers, respectively, with a thickness of 200 μm.

Reflectance measurements of the RIE-textured mono-, multi and quasi-mono Si surfaces were performed using a broadband lightsource (Mikropack DH-2000), an integrating sphere (Mikropack ISP-30-6-R), and a spectrometer (Ocean Optics QE65000, 280-1000 nm). The reference solar spectral irradiance for AM 1.5 was used to calculate the weighted average reflectance in the wavelength range from 280-1000 nm.

Our mask-less, scalable RIE nanostructuring of the Si surface is shown to reduce the AM1.5-weighted average reflectance to a level below 1 % in a fully optimized RIE texturing, and thus holds a significant potential for improvement of solar cell performance compared to current industrial standards. The reflectance is shown to remain below that of conventional textured cells also at high angle of incidence. The process is shown to be equally applicable to mono-, multi- and quasi-mono-crystalline Si.
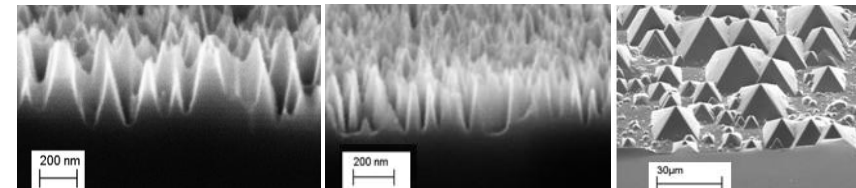
Figure 1: (left, middle) SEM-image at 45° tilt of two different types of black silicon surface after RIE-texturing. The nanostructures are h ≈ 3-400 nm tall and the area density is D ≈ 100μm^{-2}.
(right) KOH-etched pyramid structures used for conventional solar cell texturing.
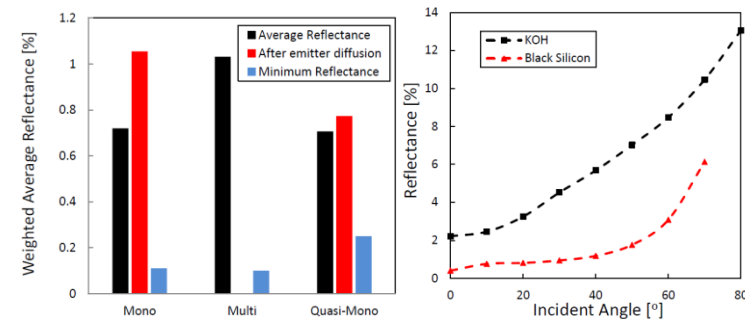
Figure 2: (Left) Weighted average reflectance of mono-, multi- and quasi-mono Si surfaces, respectively. (Right) Weighted average reflectance as function of incident angle for a KOH-textured (squares) and RIE-textured (triangles) mono-c Si substrates.
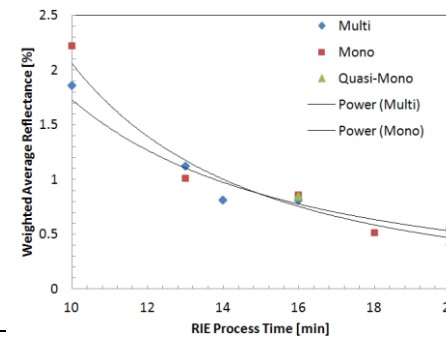
Figure 3: Weighted average reflectance as function of RIE process time for mono-, multi- and quasi-mono crystalline Si, respectively. All other parameters were fixed. The general trend suggests that the reflectance decreases with t^{-2}.

[1] Department of Micro- and Nanotechnology, Technical University of Denmark (DTU)
ole.hansen@nanotech.dtu.dk, anja.boisen@nanotech.dtu.dk, michael.schmidt@nanotech.dtu.dk
* rasda@nanotech.dtu.dk, Ørsteds Plads building 345East, 2800 Lyngby, Denmark

[1] T.H. Her, R.J. Finlay, C. Wu, S. Deliwala, E. Mazur, "Microstructuring of silicon with femtosecond laser pulses", Appl. Phys. Lett. 73 (1998)
[2]H. Jansen, M. Deboer, R. Legtenberg, M. Elwenspoek, "The Black Silicon Method - a Universal Method for Determining the Parameter Setting of a Fluorine-Based Reactive Ion Etcher in Deep Silicon Trench Etching with Profile Control", J Micromech Microengineering. 5 (1995)
[3]Oh, J., Yuan, H.C., Branz, H., "An 18.2%-efficient black-silicon solar cellachieved through control of carrier recombination in nanostructures", Nature Nanotechnology, September 2012
[4]Yoo, J., "Reactive ion etching (RIE) technique for application in crystalline silicon solar cells", Solar Energy 84 (2010)

Appendix H

Plasma texturing on large-area industrial grade CZ silicon solar cells

Authors:
Rasmus Schmidt Davidsen[*], Ørnulf Nordseth, Anja Boisen, Michael Stenbæk Schmidt, Ole Hansen

Plasma texturing on large-area industrial grade CZ silicon solar cells

Rasmus Schmidt Davidsen[*,1], Ørnulf Nordseth[2], Anja Boisen[1], Michael Stenbæk Schmidt[1], Ole Hansen[1]
[1]Department of Micro- and Nanotechnology, Technical University of Denmark (DTU)
[2]Institute for Energy Technology, Norway, ornulf.nordseth@ife.no
ole.hansen@nanotech.dtu.dk, anja.boisen@nanotech.dtu.dk, michael.schmidt@nanotech.dtu.dk
* rasda@nanotech.dtu.dk, Ørsteds Plads building 345East, 2800 Lyngby, Denmark

ABSTRACT: We report on an experimental study of nanostructuring of silicon solar cells using reactive ion etching (RIE). A simple mask-less, scalable RIE nanostructuring of the solar cell surface is shown to reduce the AM1.5-weighted average reflectance to a level below 1 % in a fully optimized RIE texturing, and thus holds a significant potential for improvement of the cell performance compared to current industrial standards. The reflectance is shown to remain below that of conventional textured cells also at high angle of incidence. The process is shown to be equally applicable to mono-, multi- and quasi-mono-crystalline Si. The process was successfully integrated in fabrication of solar cells using only industry standard processes on a Czochralski (CZ) silicon starting material. The resulting cell performance was compared to cells with conventional texturing. For cells, where the nanostructuring was not fully optimized (reflectance larger than 2 %), an efficiency of 16.5 % at 1 sun was demonstrated.
Keywords: anti-reflective coating, c-Si, Czochralski, multicrystalline, silicon, solar cell efficiency, texturisation

1 INTRODUCTION

We use Black Silicon (BS)[1][2] nanostructuring to achieve low reflectance due to the resulting graded refractive index at the Si-air interface. Oh et al. achieved power conversion efficiency of 18.2 % [3] on 300 μm thick float-zone Si by combining a metal-assisted wet etching black silicon process for texturing, TMAH damage removal etch and double-sided thermal SiO_2 passivation. In a more industrially relevant cell using only standard processes, industry grade CZ Si and RIE-texturing was used by Yoo et al. [4] a power conversion efficiency of 16.7 % was achieved. However, despite several advantages such as excellent light trapping, a dry, single-sided and scalable process method and etch independence on crystallinity of Si, RIE-texturing has so far not been proven superior to standard wet texturing, primarily as a result of lower power conversion efficiency due to increased surface recombination. This work does not fully solve this problem, but the results show promising potential of future improvements in power conversion efficiency, since excellent light absorption and decent power conversion efficiency has been shown for large-area, industry grade CZ Si wafers with several identified areas of improvement. We show that the RIE nanostructures lead to superior light absorption independent of crystalline grade and incident angle.
A texturing method which is applicable to all industrially relevant grades of Si and yielding improved performance at non-ideal incident angles has a major scientific and commercial relevance.

2 APPROACH

The nanostructures are fabricated as the texturing step in the following solar cell process: 1) Saw damage removal, 2) Texturing using maskless RIE in a O_2 and SF_6 plasma 3) Emitter formation using a $POCl_3$ doping process, followed by PSG-removal in 5 % buffered HF, 4) Deposition of SiN_X:H anti-reflective coating using PECVD with SiH_4, NH_3 and N_2, 5) Screen-printing of front and rear, 6) Edge isolation using laser ablation.

The starting substrates were 156x156 mm p-type, CZ mono-c Si wafers with a thickness of 200 μm and a resistivity of 1-20 Ω cm.

3 CHARACTERIZATION

Reflectance measurements of the RIE-textured mono-, multi and quasi-mono Si surfaces were performed using a broadband lightsource (Mikropack DH-2000), an integrating sphere (Mikropack ISP-30-6-R), and a spectrometer (Ocean Optics QE65000, 280-1000 nm). The reference solar spectral irradiance for AM 1.5 was used to calculate the weighted average reflectance in the wavelength range from 280-1000 nm. I-V curves on complete cells were measured under 1 Sun illumination (1000 W/m^2) using a xenon light bulb, while the IQE measurements were carried out in a LOANA setup from PV-tools.

4 RESULTS

Figure 1: SEM-image at 45° tilt of the black silicon surface after RIE-texturing. The nanostructures are h ≈ 3-400 nm tall and the area density is D ≈ 100μm^{-2}.

Figure 2: Weighted (AM1.5) average reflectance before and after emitter diffusion as well as the minimum reflectance of mono-, multi- and quasi-mono Si surfaces, respectively.
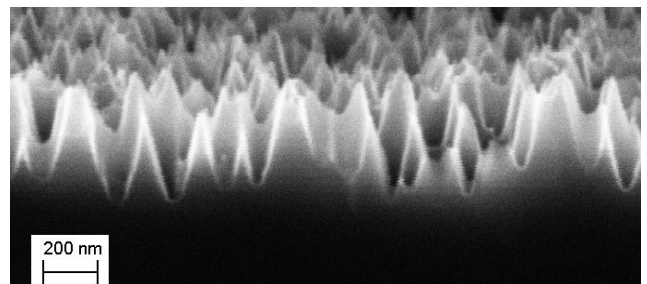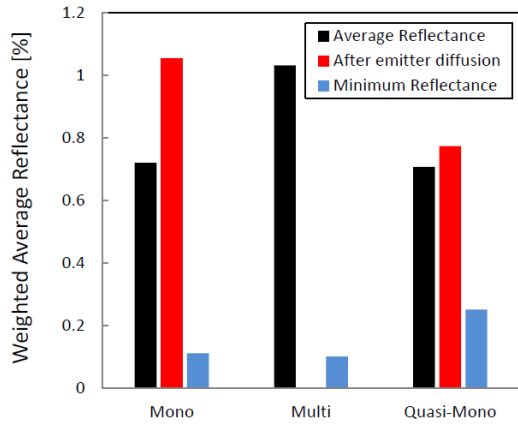
Figure 2 shows average reflectance of RIE-textured Si below 1% for all three crystalline grades of Si, which is a clear improvement compared to KOH- and acidic-textured Si used in standard industrial Si solar cells. The results furthermore show negligible increase in reflectance after emitter diffusion. The RIE-textured Si show near-zero minimum reflectance independent of crystalline grade.
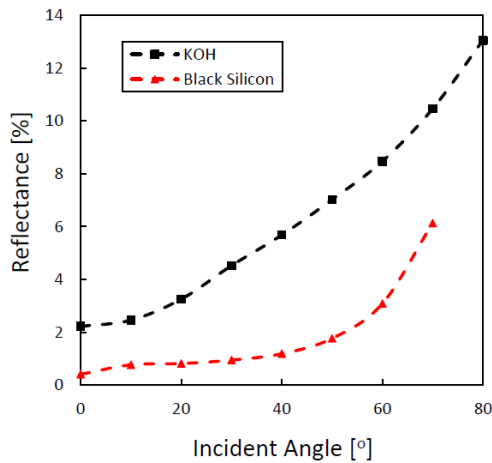
Figure 3: Total weighted (AM1.5) average reflectance as function of incident angle for a standard, KOH-textured (squares) and RIE-textured (triangles) mono-c Si substrates. The reflectance was measured using an integrating sphere with one axis angle variation of the incident optical fiber relative to the Si substrate.

Figure 3 shows that the reflectance of KOH-textured Si increases more with incident angle up to 50° than the reflectance of RIE-textured Si. For angles above 50° the reflectance of RIE-textured Si increases more with incident angle than KOH-textured Si. The reflectance of RIE-textured Si is significantly lower than KOH-textured Si for incident angles of 0-80°. This result shows the potential of improved solar cell performance using RIE-texturing at non-ideal incident angles. This will be investigated in detail in future studies.
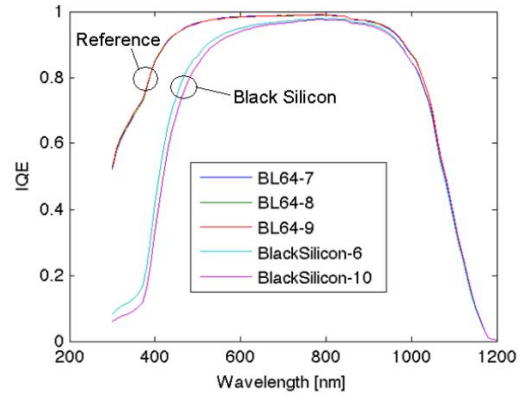
Figure 4: Internal Quantum Efficiency of two different black Si cells and three KOH-textured reference cells.

Figure 4 shows that the IQE of the RIE-textured solar cells is lower than the IQE of the KOH-textured, reference cells – especially at wavelengths below 600nm. It is assumed that the decreased IQE of the black Si cells compared to the KOH-cells at wavelengths below 600nm indicates increased surface recombination, since light with shorter wavelength is absorbed closer to the surface. In order to confirm this, a LASSIE[1] tool was used to evaluate the loss of current density of the differently textured solar cells. The result of this analysis is seen in Table I.

	Total Carrier Loss	Emitter recombination
KOH	1.385 mA/cm^2	0.761 mA/cm^2
RIE	4.163 mA/cm^2	3.322 mA/cm^2

Table I: Calculated total carrier loss and carrier loss due to emitter, bulk and rear surface recombination for the KOH- and RIE-textured cell.

The assumption that emitter recombination is the primary explanation behind the lower IQE for the RIE-textured cells compared to the KOH-textured is confirmed by the calculated carrier losses in Table I, since the emitter recombination is the dominant carrier loss mechanism of the RIE-textured cells.

	PCE [%]	J_{SC} [mA/cm^2]	V_{OC} [V]	FF	R_{av} [%]
KOH	17.6	36.8	0.62	77.8	2-3
RIE, type 1	15.7	35.3	0.61	72.8	2.85
RIE, type 2	16.5	35.2	0.61	77.7	2.20

Table II: PV performance results including power conversion efficiency, PCE, short-circuit current, J_{SC}, open-circuit voltage, V_{OC}, fill factor, FF and weighted average reflectance after emitter diffusion, R_{av}, of the RIE- and KOH-textured cells.

Table 2 shows that the RIE-textured cells have lower PCE than the KOH-cell due to lower J_{SC}. The current loss is explained by the increased emitter recombination shown in Table 1. Since the RIE-texturing has been further optimized after these cells were fabricated, with a resulting reflectance below 1%, it is expected that the

---

[1] Loss Analysis of Silicon Solar cells by IQE Evaluation

PCE will be increased in future studies.

5 CONCLUSION

The effect of a one-step, maskless, single-sided and scalable RIE texturing process applied on large-area Si solar cells has been documented resulting in 16.5% power conversion efficiency using only standard processes and industrial grade Cz wafers. The obtained efficiency is lower than the 17.6% efficiency of the KOH-textured reference cell. This is explained by non-optimal texturing and increased emitter recombination. Based on the excellent light absorption properties independent of Si grade and less dependent on incident angle compared to KOH-texturing, the efficiency is expected to be improved in future studies.

REFERENCES

[1] T.H. Her, R.J. Finlay, C. Wu, S. Deliwala, E. Mazur, "Microstructuring of silicon with femtosecond laser pulses", Appl. Phys. Lett. 73 (1998) 1673-1675.

[2] H. Jansen, M. Deboer, R. Legtenberg, M. Elwenspoek, "The Black Silicon Method - a Universal Method for Determining the Parameter Setting of a Fluorine-Based Reactive Ion Etcher in Deep Silicon Trench Etching with Profile Control", J Micromech Microengineering. 5 (1995) 115-120.

[3] Oh, J., Yuan, H.C., Branz, H., "An 18.2%-efficient black-silicon solar cellachieved through control of carrier recombination in nanostructures", Nature Nanotechnology, September 2012

[4] Yoo, J., "Reactive ion etching (RIE) technique for application in crystalline silicon solar cells", Solar Energy 84, (2010), 730–734

Appendix I

Maskless Nanostructure Definition of Submicron Rear Contact Areas for Advanced Solar Cell Designs

Authors:
Rasmus Schmidt Davidsen, Michael Stenbæk Schmidt, Anja Boisen, Ole Hansen
Submitted to:
MicroElectronic Engineering, Micro- and Nanofabrication (2015)

Maskless Nanostructure Definition of Submicron Rear Contact Areas for Advanced Solar Cell Designs

Rasmus Schmidt Davidsen[a],[*] Michael Stenbæk Schmidt[a], Anja Boisen[a], Ole Hansen[a]

[a]Department of Micro- and Nanotechnology, Technical University of Denmark,

Ørsteds Plads building 345East, DK-2800 Lyngby, Denmark

e-mail: rasda@nanotech.dtu.dk; michael.schmidt@nanotech.dtu.dk; anja.boisen@nanotech.dtu.dk; ole.hansen@nanotech.dtu.dk;

Abstract

We present a completely mask-less process allowing for controlled definition of local contact areas on a passivated Si surface. Without use of lithography, contact windows with sub-micron feature size and controllable pitch are obtained. A contact to passivated Si fraction of 2.4% and a contact diameter of ~ 100 nm were realized by Al evaporation on nano-pillars fabricated by mask-less reactive ion etching (RIE), followed by plasma enhanced chemical vapor deposition (PECVD) SiO_2 passivation with subsequent removal of the nano-pillars by isotropic RIE. The resulting contact diameter and metal coverage may enable optimal specific series resistance and surface recombination velocity on the backside of point-contacted solar cells. Calculations of the specific series resistance and effective surface recombination velocity as function of contact pitch and metal coverage show optimal photovoltaic performance at minimized pitch, minimized contact diameter and a metal coverage in the range of $1 - 5\%$. The technique has the potential for realizing advanced high-efficiency solar cell concepts, such as PERL solar cells, without the use of photolithography.

I. Introduction

Mask-less reactive ion etching (RIE) has been used for several different applications such as front surface texturing of solar cells [1, 2, 3, 4] and surface-enhanced raman spectroscopy [5]. The primary advantage of mask-less RIE is the ability to define nano-structured topologies with very specific pitch and size in a controlled manner without the use of photolithography. This ability allows for scalable fabrication of nano-scale topologies that would otherwise be impossible or at least require extensive, costly photolithography processing. An example of the need for precise definition of micro- and nano-scale features in a semiconductor device, which normally requires photolithography, is the locally diffused and contacted backside of advanced silicon solar cells such as the passivated emitter rear locally diffused (PERL) world record solar cell [6]. The PERL solar cell and similar advanced cell concepts achieve higher power conversion efficiencies than conventional Si solar cells due to their passivated backside, which reduces rear surface effective recombination velocity (SRV), while allowing for backside Si-metal contacts in locally defined highly doped areas only.

---

[*]e-mail: rasda@nanotech.dtu.dk, phone: +45 45255848, Department of Micro- and Nanotechnology, Technical University of Denmark (DTU), Ørsteds Plads building 345East, DK-2800 Lyngby, Denmark

1

II. Theory

The optimal design of the rear surface of a solar cell must strike a compromise between minimized series resistance and minimized surface recombination, since minimization of the series resistance requires some metallization which increases the effective SRV. Here we consider a backside topology with metallized point contacts – assumed disc shaped with radius a – arranged on a square grid of pitch p on a silicon wafer of thickness W and resistivity ϱ_b. As a result only a fraction $f = \pi a^2 / p^2$ of the surface is contacted. The metallized contacts have an effective surface recombination velocity S_{cont} as referred the bulk, which may be significantly lower than that at the metal-semiconductor interface ($S_{\text{met}} \leq 10^7$ cm/s) due to the doping profile that may be present below the contact. The remaining part of the surface is assumed to be well passivated with the surface recombination velocity S_{pass}.

The spreading resistance of the individual point contacts may be calculated from the approximate expression due to Cox and Strack [7], and if the contacts are non-interacting the total resistance can be obtained simply from a parallel connection of such point contacts. The contacts are, however, interacting and thus heuristic corrections must be made in order to obtain closed form expressions for the specific series resistance. The specific series resistance $R_{\text{s,rear}}$ must ultimately be larger than that of the substrate material $\varrho_b W$. In the literature quite accurate expressions for the specific series resistance exists [8, 9, 10], and thus we have

$$R_{\text{s,rear}} = \varrho_b W \left[\frac{p}{2W\sqrt{\pi f}} \arctan \left(\frac{2W}{p} \sqrt{\frac{\pi}{f}} \right) - \exp \left(-\frac{W}{p} \right) \right] + \varrho_b W, \tag{1}$$

where the first term is reminiscent of the Cox and Strack expression, the last term is the bulk substrate specific resistance and the second term a heuristic correction [8] related to the contact interaction, i.e. it assures that the expression is correct also in the large pitch limit. In the case of small contacts and low pitch compared to the wafer thickness $R_{\text{s,rear}} \simeq \varrho_b W + \pi \varrho_b p / (4\sqrt{\pi f})$ to a good approximation. Note, in Eq. 1 the specific contact resistance of the metal-semiconductor junction is ignored, since well behaved contacts have specific contact resistances on the order 10^{-6} Ω cm^2.

As discussed by Fischer [8] the effective surface recombination velocity of the heterogeneous point contacted surface is also related to the Cox and Strack expression as is evident from this expression for the effective SRV, $S_{\text{rear,eff}}$, of a point-contacted, passivated rear surface [11, 8]

$$S_{\text{rear,eff}} = \frac{D_p}{W} \left[\frac{p}{2W\sqrt{\pi f}} \arctan \left(\frac{2W}{p} \sqrt{\frac{\pi}{f}} \right) - \exp \left(-\frac{W}{p} \right) + \frac{D_p}{fWS_{\text{cont}}} \right]^{-1} + \frac{S_{\text{pass}}}{1-f}, \tag{2}$$

where D_p is the hole diffusivity. The first two terms are recognized from the series resistance expression, the third term is a correction for finite SRV at the contacts, while the last term corrects for the SRV at the passivated surface. The passivation correction deserves a comment: the form shown is the so-called "large scale" correction, but in the present work the "small scale" correction $(1-f) S_{\text{pass}}$ may be more appropriate as discussed by Fisher [8]. Nevertheless, with parameters used here (see Table 1) the third term in the bracket of Eq. 2 is dominant, and then the intuitive and simple expression $S_{\text{rear,eff}} \simeq fS_{\text{cont}} + (1-f) S_{\text{pass}}$ is valid to a very good approximation.

Figure 1 shows values of SRV and specific series resistance calculated from Eqs. 1 and 2 as function of metal coverage and contact pitch, respectively. In the calculations the parameters in Table 1 are used.

2

Parameter	Description	Value	Unit
D_p	Hole diffusion constant	11.6	cm^2/s
W	Wafer thickness	200	μm
ϱ_b	Wafer resistivity	1	Ω cm
S_{cont}	Contact recombination velocity	55	cm/s
S_{pass}	Passivated recombination velocity	5	cm/s

Table 1: Parameters used in calculations of specific series resistance and effective rear surface recombination velocity, respectively.
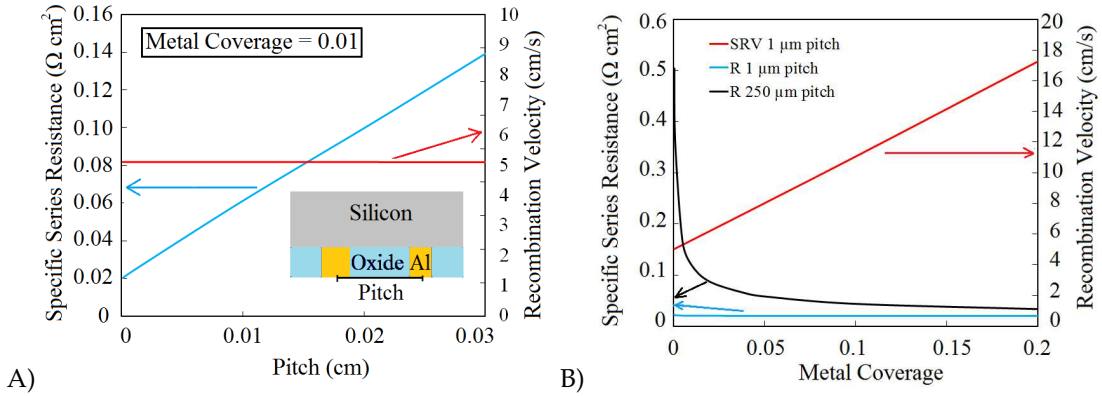
Figure 1: Calculation of rear surface recombination velocity and series resistance, respectively, of a silicon solar cell (A) as a function of the pitch between contact openings on the passivated rear with a fixed metal coverage of 1% and (B) as a function of the metal coverage on the rear for a fixed pitch of 1 and 250 μm, respectively.

Figure 1A shows that the effective rear SRV does not change significantly with the contact pitch, when the metal coverage is fixed in perfect agreement with the discussion above, where the SRV was shown to depend almost entirely on the metallized fraction f and the two SRV's of the heterogeneous surface, and is thus almost independent on the pitch.

The specific series resistance decreases with decreasing contact pitch, due to higher contact density. For pitches in the range $0 - 0.03$ cm the specific series resistance remains below 0.5 Ω cm^2, which is the upper limit of the specific series resistance required to obtain high fill factors [9, 12]. Figure 1B shows that the metal coverage should be minimized in order to minimize rear SRV, as expected from the discussion above. The specific series resistance does not change significantly with metal coverage, when the pitch is small, e.g. fixed at 1 μm. When the pitch is sufficiently small, the spreading resistance contribution becomes small, even at very small metal coverages. For a fixed pitch of 250 μm, which is approximately the design of the PERL solar cell [6, 9], the spreading resistance contribution becomes important and thus the specific series resistance increases dramatically for metal coverages below $\sim 1\%$. This is in agreement with the actual design of the PERL solar cell, which has a metal coverage of $\sim 1\%$ [6, 9]. Based on the combined results in Figure 1, it appears that the contact pitch should be minimized, while the metal coverage is kept in the range $1 - 5\%$, in order to optimize the solar cell performance. At a fixed contact pitch of 1μm a 1% metal coverage corresponds to contact windows with ~ 100 nm diameter.

The calculation of SRV was also done for the case of local contacts without any diffusion, such as in a Passivated Emitter and Rear Cell (PERC) [13]. In this case it is assumed that the contact SRV is $S_{\text{cont}} = 10^7$ cm/s. When the contact SRV is sufficiently high, the first two terms in equation 2 are comparable to the third term, and then the pitch influences the effective SRV. Furthermore, the metal coverage must be low enough to mitigate the large SRV of the metallized areas. A calculation shows that for non-diffused local contacts ($S_{\text{cont}} = 10^7$ cm/s) the contact pitch must be at least 30 μm and the metal coverage less than 0.05% in order to obtain sufficiently low effective SRV, i.e. below $\sim$ 1000 cm/s. These two requirements yield a maximum contact diameter below 1 μm.

III. Experimental Method and Results

We present a completely mask-less process allowing for controlled definition of local contact areas on a passivated Si surface. The process results in submicron feature size and controllable pitch between contact openings without use of lithography. Figure 2 shows a sketch of the process flow used in this novel technique.
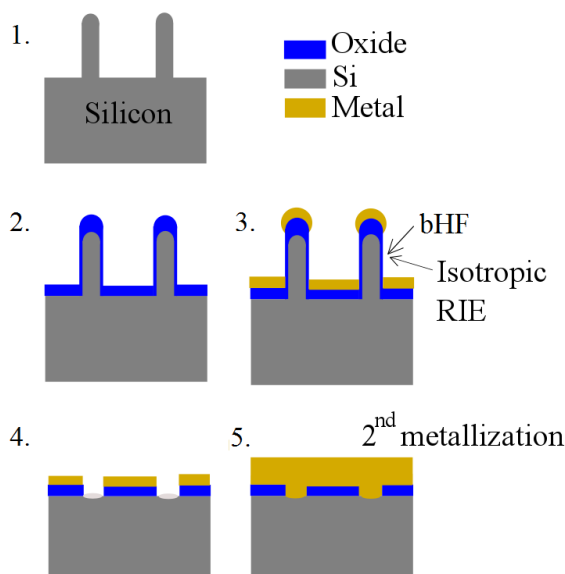
Figure 2: Sketch of the process flow consisting of 1) maskless nanopillar etch, 2) SiO$_2$ passivation by PECVD, 3) Al evaporation, 4) buffer HF (bHF) and isotropic RIE of pillar sidewalls and 5) second metallization plus optional doping.

The technique consists of a mask-less RIE process, which defines $\sim$ 500 nm tall nano-pillars with $\sim$ 100 nm diameter on the Si surface. The entire surface is then passivated using 30 nm SiO$_2$ deposited by plasma-enhanced chemical vapor deposition (PECVD). Then 200 nm Al is deposited on the surface by e-beam evaporation. Due to the nano-pillar topology and the poor step coverage of the evaporation process, the sidewalls of the nano-pillars are not covered with Al. This enables selective removal of the nano-pillars using buffered hydrofluoric acid (bHF) to etch SiO$_2$ and isotropic RIE masked by Al to etch Si. The isotropic etch leaves local openings whose pitch and size are defined by the initial nano-pillar topology of the otherwise passivated and metallized surface. Figure 3 shows SEM images of the surface before and after the isotropic RIE, respectively.
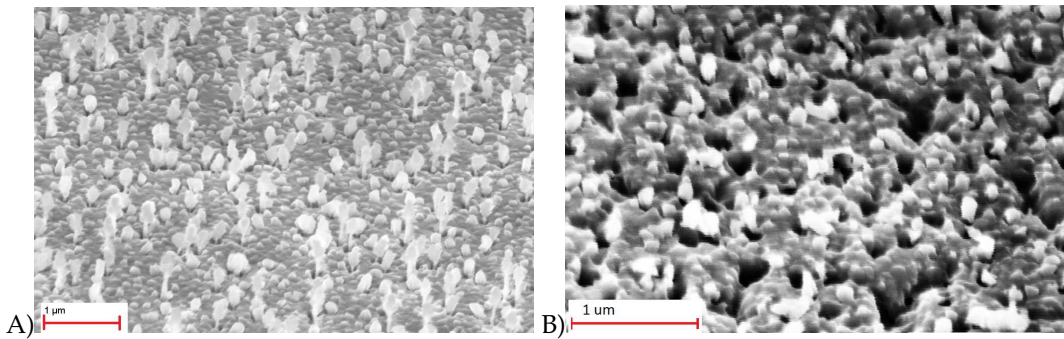
Figure 3: SEM-image of the nanopillar surface covered with Al before (A) and after (B) isotropic RIE, respectively. The pillar density is $\sim 3~\mu m^{-2}$, which corresponds to a potential metal coverage of 2.4%. The etching process has removed most of the nanopillars and created holes in the passivated Si surface covered with metal.

IV. Discussion

The topology in Figure 3 shows local contact areas of ~ 100 nm in diameter, allowing for a much lower pitch than photolithographically defined patterns, while maintaining the targeted metal coverage of $1 - 5\%$. Although techniques such as electron-beam and advanced optical lithography allow for definition of even smaller pattern dimensions, the cost of such processes is much higher and the scalability much lower than that of the technique presented in this work.

The pillar density of the topology in Figure 3 is $\sim 3~\mu m^{-2}$ [5], which corresponds to a potential metal coverage of 2.4% assuming cylindrical pillars with diameters of 100 nm. Such metal coverage is exactly within the range $1 - 5\%$ that simultaneously minimizes SRV and keeps the rear specific series resistance below $\sim 0.5~\Omega~cm^2$, required for high fill factors [9, 12], and as shown in Figure 1. Minimized pitch at a constant metal coverage in the range $1 - 5\%$, directly implies minimized contact diameter. The initial results of this work show contact openings of ~ 100 nm in diameter, which is significantly smaller than rear contact openings considered elsewhere [14, 12, 15].

For the case of non-diffused local contacts with much higher S_{cont}, such as the PERC cell, the requirement is a very small metal coverage, in this case below 0.05%, combined with a sufficiently large pitch, in this case at least 30 μm. This requires very small contact openings, in this case with contact diameter smaller than 1 μm. Such rear design would also be enabled with the type of topology seen in Figure 3, as long as the contact pitch can be tuned. This should be possible, since the pitch of nanopillars fabricated by maskless RIE may be tuned in numerous ways, e.g. by varying the chamber pressure, as demonstrated in [5].

Photolithographically defined contacts typically used in PERL solar cells [6, 11] and the more industrially feasible laser-patterned contacts [16, 17, 18] are both limited to contact windows well above 1 μm in diameter. Therefore the feature size of ~ 100 nm combined with 2.4% metal coverage demonstrated in this work shows the potential for further optimization of locally defined rear contacts for high-efficiency solar cells, such as the PERL cell, by using the mask-less RIE technique presented in this work.

V. Conclusion

We have presented a completely mask-less process allowing for controlled definition of local contact areas on a passivated Si surface without any use of lithography. The process results in

submicron feature size and controllable pitch between contact windows. A metal coverage of 2.4% and contact diameter of ~ 100 nm was realized by Al evaporation on nano-pillars fabricated by mask-less RIE, PECVD SiO_2 passivation and subsequent removal of nano-pillars by isotropic RIE. The technique has the potential for cost effective realization of advanced high-efficiency solar cell concepts, such as PERL solar cells, without the use of photolithography.

REFERENCES

[1] J. Oh, H.C. Yuan, H. Branz, An 18.2 %-efficient black-silicon solar cell achieved through control of carrier recombination in nanostructures, Nature Nanotechnology **7**, (2012) 743-748.

[2] R.S. Davidsen, J. Ormstrup, M.L. Ommen, P.E. Larsen, M.S. Schmidt, A. Boisen, O. Hansen, Angle resolved characterization of nanostructured and conventionally textured silicon solar cells, Solar Energy Materials and Solar Cells **140**, (2015) 134-140.

[3] X. Liu, P.R. Coxon, M. Peters, B. Hoex, J.M. Cole, D.J. Fray, Black Silicon: Fabrication methods, properties, and solar energy applications, Review Article, Energy & Environmental Science, Royal Society of Chemistry (2014).

[4] P. Repo, J. Benick, V. Vähänissi, J. Schön, G. von Gastrow, B. Steinhauser, M.C. Schubert, M. Hermle, H. Savin, N-type black silicon solar cells, SiliconPV, Energy Procedia **38**, (2013) 866-871.

[5] M.S. Schmidt, A. Boisen, J. Hübner, Large Area Fabrication of Leaning Silicon Nanopillars for Surface Enhanced Raman Spectroscopy, Advanced Materials **24** 10, (2012) 11-18.

[6] J. Zhao, A. Wang, M.A. Green, 24.5% Efficiency silicon PERT cells on MCZ substrates and 24.7% efficiency PERL cells on FZ substrates, Prog. Photovoltaics: Research & Applications **7** 6, (1999) 471-474.

[7] R.H. Cox, H. Strack, Ohmic contacts for GaAs devices, Solid-State Electronics, **10** 12, (1967) 1213-1218.

[8] B. Fischer, Loss Analysis of Crystalline Silicon Solar Cells using Photoconductance and Quantum Efficiency Measurements (Thesis), in Fachbereich Physik 198, University of Konstanz, (2003).

[9] J. Zhao, A. Wang, M.A. Green, Series resistance caused by the localized rear contact in high efficiency silicon solar cells, Solar Energy Materials and Solar Cells, **32** 1, (1994) 89-94.

[10] A. Wolf, D. Biro, J. Nekarda, S. Stumpp, A. Kimmerle, S. Mack, R. Preu, Comprehensive analytical model for locally contacted rear surface passivated solar cells, Journal of Applied Physics, **108** 12, (2012) 124510.

[11] J. Benick, B. Hoex, M.C.M. van de Sanden, W.M.M. Kessels, O. Schultz, S.W. Glunz, High efficiency n-type Si solar cells on Al2O3-passivated boron emitters, Appl. Phys. Letters **92**, (2008) 253504.

[12] P.P. Altermatt, G. Heiser, A.G. Aberle, A. Wang, J. Zhao, S.J. Robinson, M.A. Green, Spatially resolved analysis and minimization of resistive losses in high efficiency Si solar cells, Progress in photovoltaics: research and applications, **4** 6, (1996) 399-414.

[13] A.W. Blakers, A. Wang, A.M. Milne, J. Zhao, M.A. Green, 22.8% efficient silicon solar cell, Applied Physics Letters, **55** 13, 1363-1365 (1989).

[14] S. Gatz, T. Dullweber, R. Brendel, Evaluation of series resistance losses in screen-printed solar cells with local rear contacts, IEEE Journal of Photovoltaics, **1** 1, (2011) 37-42.

[15] F. Gerenton, F. Mandorlo, J.B. Brette, M., Lemiti, Pattern of Partial Rear Contacts for Silicon Solar Cells, Energy Procedia **77**, (2015) 677-686.

[16] E. Schneiderlöchner, R. Preu, R. Lüdemann, S.W. Glunz, Laser-fired rear contacts for crystalline silicon solar cells, Progress in Photovoltaics: Research and Applications, **10** 1, (2002) 29-34.

[17] D. Lin, M. Abbott, P.H. Lu, B. Xiao, B. Hallam, B. Tjahjono, S. Wenham, Incorporation of deep laser doping to form the rear localized back surface field in high efficiency solar cells, Solar Energy Materials and Solar Cells **130**, (2014) 83-90.

[18] J. Nekarda, S. Stumpp, L. Gautero, M. Hörteis, A. Grohe, D. Biro, R. Preu, LFC on screen printed aluminium rear side metallization, In Proceedings of the 24th European Photovoltaic Solar Energy Conference, WIP Renewable Energies Hamburg, Germany (2009) 1411-1415.

Appendix J

Athena Silvaco script used for diffusion simulations

```
go athena
2
3 # simulation of needed thickness of oxide to withstand fosfor predep
and anneal
4
line x loc = 0.0 spacing=0.01
line x loc = 3.75 spacing=0.01
line y loc = 0 spacing = 0.01
line y loc = 2.00 spacing = 0.01
9
10 #initialize the mesh
init silicon orientation=100 c.boron=1e15

etch silicon start x=0 y=-0.1
etch cont x=.1 y=0.2
etch cont x=.15 y=0.38
etch cont x=.18 y=0.4
etch cont x=.21 y=0.38
etch cont x=.26 y=0.2
etch cont x=.36 y=0.03
etch cont x=.39 y=0.01
etch cont x=.42 y=0.03
etch cont x=.52 y=0.2
etch cont x=.57 y=0.38
etch cont x=.60 y=0.4
etch cont x=.63 y=0.38
etch cont x=.68 y=0.2
etch cont x=.78 y=0.03
etch cont x=.81 y=0.01
etch cont x=.84 y=0.03
etch cont x=.94 y=0.2
etch cont x=.99 y=0.38
etch cont x=1.02 y=0.4
etch cont x=1.05 y=0.38
etch cont x=1.1 y=0.2
etch cont x=1.2 y=0.03
etch cont x=1.23 y=0.01
etch cont x=1.26 y=0.03
etch cont x=1.36 y=0.2
etch cont x=1.41 y=0.38
etch cont x=1.44 y=0.4
etch cont x=1.47 y=0.38
etch cont x=1.52 y=0.2
etch cont x=1.62 y=0.03
etch cont x=1.65 y=0.01
etch cont x=1.68 y=0.03
etch cont x=1.78 y=0.2
etch cont x=1.83 y=0.38
etch cont x=1.86 y=0.4
etch cont x=1.89 y=0.38
etch cont x=1.94 y=0.2
etch cont x=2.04 y=0.03
etch cont x=2.07 y=0.01
etch cont x=2.1 y=0.03
etch cont x=2.2 y=0.2
etch cont x=2.25 y=0.38
```

```
etch cont x=2.28 y=0.4
etch cont x=2.31 y=0.38
etch cont x=2.36 y=0.2
etch cont x=2.46 y=0.03
etch cont x=2.49 y=0.01
etch cont x=2.52 y=0.03
etch cont x=2.62 y=0.2
etch cont x=2.67 y=0.38
etch cont x=2.7 y=0.4
etch cont x=2.73 y=0.38
etch cont x=2.78 y=0.2
etch cont x=2.88 y=0.03
etch cont x=2.91 y=0.01
etch cont x=2.94 y=0.03
etch cont x=3.04 y=0.2
etch cont x=3.09 y=0.38
etch cont x=3.12 y=0.4
etch cont x=3.15 y=0.38
etch cont x=3.2 y=0.2
etch cont x=3.3 y=0.03
etch cont x=3.33 y=0.01
etch cont x=3.36 y=0.03
etch cont x=3.46 y=0.2
etch cont x=3.51 y=0.38
etch cont x=3.54 y=0.4
etch cont x=3.57 y=0.38
etch cont x=3.62 y=0.2
etch cont x=3.72 y=0.03
etch cont x=3.75 y=0.01
etch done x=3.75 y=0.01

struct outf=oxidation.str

tonyplot -st oxidation.str

#Predep process

diff time=0.5 hours temp=975 c.phosphorus=8e19

#Solid soluability at 1000 degrees

#Drive-in process

diff time=20 min temp=800
...
region.occno=1
extract name="xj" xj material="Silicon" mat.occno=1 x.val=2.07
junc.occno=1
extract name="rho" sheet.res material="Silicon" mat.occno=1 x.val=2.07
region.occno=1
extract name="xj" xj material="Silicon" mat.occno=1 x.val=2.15
junc.occno=1
extract name="rho" sheet.res material="Silicon" mat.occno=1 x.val=2.15
region.occno=1
extract name="xj" xj material="Silicon" mat.occno=1 x.val=2.23
junc.occno=1
```

```
extract name="rho" sheet.res material="Silicon" mat.occno=1 x.val=2.23
region.occno=1
extract name="xj" xj material="Silicon" mat.occno=1 x.val=2.28
junc.occno=1
extract name="rho" sheet.res material="Silicon" mat.occno=1 x.val=2.28
region.occno=1

#structure outfile=pdiffusion.str

#tonyplot -overlay pdiffusion.str

quit
```

Appendix K

SciLab script used for angle-resolved measurements

```
clear;

//**********************************************************************
*******
// Specify the solar cell ID; directory, substrate ID, cell ID and measurement
number.
//**********************************************************************
*******
//directory='C:\Documents and
Settings\rasda\Desktop\measurements\PhotoSolar_AngleMeasurements\bs_pseudo_full_
series'
directory='C:\Users\rasda\Dropbox\PhD\PhotoSolar_AngleMeasurements\sunpower
tests\cell4'
substrate_ID='test';
cell_ID='1';
meas_no='1';


//----------------------------------------------------------------------
------------------------
//Makes a 2D-spline of the the data in "my_matrix" and finds the maximum of the
surface.
//Assumes that the vectors
//x_vector=x-coordinate. y_vector=y-coordinate. my_matrix=data series.
n=fineness of interpolation grid.
//----------------------------------------------------------------------
------------------------
function [maximum, az_at_max, ev_at_max]=find_maximum_position(x_vector,
y_vector, my_matrix, n_grid)
    C=splin2d(x_vector', y_vector', my_matrix) //2D-spline.
    n=n_grid //Fineness of interpolation grid.
    xx=[x_vector(1):abs(x_vector(size(x_vector,'r'))-
x_vector(1))/n:x_vector(size(x_vector,'r'))];
    yy=[y_vector(1):abs(y_vector(size(y_vector,'r'))-
y_vector(1))/n:y_vector(size(y_vector,'r'))];
    [XX,YY]=ndgrid(xx,yy); //Make the 2D interpolation grid.
    zz=interp2d(XX,YY,x_vector',y_vector',C) //Make 2D interpolation.
    format(5)
    [maximum,s]=max(zz) //Find mpp_max and matrix indices at max (s).
    az_at_max=xx(s(1)) //az @ max.
    ev_at_max=yy(s(2)) //ev @ max.
endfunction

//**********************************************************************
*****************************
//Function "read_IV_file" reads an IV-file and extracts, azimuth, elevation
angle, short circuit current, open circuit voltage, maximum power point and fill
factor.
//**********************************************************************
*****************************
function [param]=read_IV_file(filename)
  z=mopen(filename, 'r')
  l=[];
  while l~='Azimuth:'
    l=mfscanf(1,z,'%s'); //read header until 'Azimuth:'
  end
  az=mfscanf(1,z, '%e') //Read azimuth angle.

  l=[];
  while l~='Elevation:' //Read header on until 'Elevation:'
```

```
    l=mfscanf(1,z,'%s')
  end
  ev=mfscanf(1,z, '%e') //Read elevation angle.

  l=[];
  while l~='(W/m2)'
    l=mfscanf(1,z,'%s'); //read header until (W/m2)
  end
  [m,V, I, T, P]=mfscanf(-1, z, '%e %e %e %e')
  mclose(z)

  //**********************************
  //Calculate short circuit current, Isc.
  //**********************************
  disp("**********")
  disp(filename)
  disp([V I])
  IV_curve=splin(V,I, "monotone") //Make spline fit.
  Isc=interp(0,V,I,IV_curve); //Given three vectors (x,y,d) defining a spline or
sub-spline function (see splin) with yi=s(xi), di = s'(xi) this function
evaluates s (and s', s'', s''' if needed) at xp(i) interp(xp,x,y,d):

  //**********************************
  //Calculate open circuit voltage, Uo.
  //**********************************
  [iu,k]=gsort(I,'g','i'); //Sorts the I-values.
  vu=V(k);

  //Small subroutine that deletes doublet values - Scilab spline cannot work if
two entries have the same value.
  doublets=[];
  for i=1:length(iu)-1
    if iu(i)==iu(i+1) then
      doublets=cat(1,doublets,i+1)
    end
    i=i+1
  end
  iu([doublets],:)=[];
  vu(doublets,:)=[];

  //Make spline fit.
  VI_curve=splin(iu,vu, "monotone");
  Uo=interp(0, iu,vu, VI_curve);

  //********************************************************************
  //Calculates the maximum power point from the IV spline curve, pmx.
  //********************************************************************
  P=[];
  t=linspace(Uo,0);//Creates 100 equidistant points from 0:Uo.
  for n=1:length(t)
    P(n)=interp(t(n), V,I,IV_curve)*t(n);
  end
  pmx=max(P)

  //****************************
  //Calculates the fill factor, FF.
  //****************************
  //FF=pmx/(Isc*Uo);
```

```
    //sha=strtod(shadow);
    //S=evstr(shadow, 1);
    A=0.015;

    eta=(pmx/(1000*A)*100); // Using 1000 W/m^2, converts to %


    param=struct('az', az, 'ev', ev,'Isc', Isc, 'Uo', Uo, 'pmx', pmx, 'eta', eta,
'A', A, 'shadow', shadow)
    endfunction

  //calculate power conversion efficiency
shadow=mgetl('C:\Documents and
Settings\rasda\Desktop\PhD\Matlab_filer\shadow9090.txt', 100);
  //for q=1:length(shadow);
      //a=(shadow(q)*0.0221); // area of solar cell in m^2
  //end

  function [param2]=read_shadow_file(filename)
   z=mopen(filename,'r');
   l=[];
   [s]=mfscanf(-1, z, '%e') //Read shadow value.
   mclose(z)
   param2=struct('s',s)
endfunction

for q=1:100;
fs(q)=read_shadow_file('C:\Documents and
Settings\rasda\Desktop\PhD\Matlab_filer\shadow9090.txt');
A(q)=fs(q).s;
end

//Makes an array containing all the files in "directory" that contains the
specified substrate_ID, cell_ID and meas_no.
//IV_files=findfiles(directory,
substrate_ID+'_'+cell_ID+'_'+string(meas_no)+'*', "*.txt")
IV_files=findfiles(directory, substrate_ID+'_'+cell_ID+'_'+string(meas_no)+
'*.txt')

//Runs the read_IV_file-function on all the chosen files.
for j=1:length(length(IV_files))
  fs(j)=read_IV_file(directory+'\'+IV_files(j))
  az(j)=fs(j).az;
  ev(j)=fs(j).ev;
  //ev(j)=round(fs(j).ev/10)*10; //NB!NB! 2012-04-18: Inserted for odd-angle
measurements ...
  Isc(j)=fs(j).Isc;
  Uo(j)=fs(j).Uo;
  pmx(j)=fs(j).pmx;
 // FF(j)=fs(j).FF;
  //shadow(j)=shadow(i);
  //A(j)=A-A.shadow;
  eta(j)=fs(j).eta;
end

//shadow=mgetl('C:\Documents and
Settings\rasda\Desktop\PhD\Matlab_filer\shadow9090.txt', 100)
```

```
//Sorts the az vector in increasing values
[az,k]=gsort(az,'g','i');
ev=ev(k); //Shuffle values to get the same order as in the above sorted az
vector.
Isc=Isc(k);
Uo=Uo(k);
pmx=pmx(k);
//FF=FF(k);

//shadow=shadow(k);
eta=eta(k);
//etas= eta(j)/(1-shadow);

Ptotal=sum(pmx(k));
Pave=sum(pmx(k))/1296;
etanorm=sum(pmx(k))/pmx(1);
etaav=sum(eta(k))/1296;
etanorm2=etaav/max(eta(k));

//p1=pmx(1);
//p2=pmx(12);
//p3=pmx(25);
//p4=pmx(60);
//p5=pmx(81);
//s1=shadow(7);

az_x=unique(az);//Returns a vector with the unique values of az vector, i.e.
removes duplicates.
ev_y=unique(ev);//Returns a vector with the unique values of ev vector, i.e.
removes duplicates.

dim_az=length(az_x);//Returns the length of the unique azimuth vector.
dim_ev=length(ev_y);//Returns the length of the unique elevation vector.
//Dimension of the matrices is thus dim_az*dim_ev.

//********************************************************************
//The routine below creates the matrices with the correct dimensions.
//********************************************************************
for l=1:dim_az;
    [ev_sort,k]=gsort(ev((l-1)*dim_ev+1:l*dim_ev),'g','i'); //Sorts a subset of
the ev vector.

    Isc_temp=Isc((l-1)*dim_ev+1:l*dim_ev); //Takes out a subset of Isc vector.
    Uo_temp=Uo((l-1)*dim_ev+1:l*dim_ev); //Takes out a subset of Uo vector.
    pmx_temp=pmx((l-1)*dim_ev+1:l*dim_ev); //Takes out a subset of pmx vector.
    //FF_temp=FF((l-1)*dim_ev+1:l*dim_ev); //Takes out a subset of FF vector.
    eta_temp=eta((l-1)*dim_ev+1:l*dim_ev);//Subset of eta vector
    //etanormal_temp=etanormal((l-1)*dim_ev+1:l*dim_ev);

    Isc_temp=Isc_temp(k); //Shuffle values to get the same order as the above
sorted ev vector.
    Uo_temp=Uo_temp(k);
    pmx_temp=pmx_temp(k);
   // FF_temp=FF_temp(k);
    eta_temp=eta_temp(k);
    //etanormal_temp=etanormal_temp(k);

    Isc_matrix(l,:)=Isc_temp'; //Defines the l'th row in the Isc_matrix.
    Uo_matrix(l,:)=Uo_temp'; //Defines the l'th row in the Uo_matrix.
```

```
        pmx_matrix(l,:)=pmx_temp'; //Defines the l'th row in the pmx_matrix.
        //FF_matrix(l,:)=FF_temp'; //Defines the l'th row in the FF_matrix.
        eta_matrix(l,:)=eta_temp';
        //etanormal_matrix(1,:)=etanormal_temp';
end

//-----------------------------
//Convert A -> mA and V -> mV.
//-----------------------------
Uo_matrix=Uo_matrix //Convert V -> mV (changed to Volt instead)
Isc_matrix=Isc_matrix //Convert A -> mA
pmx_matrix=pmx_matrix*1000; //Convert W -> mW

//*********************************
//Makes 3D-surface plots.
//*********************************
//subplot(351)
//title('Substrate ID='+string(substrate_ID)+', cell ID='+string(cell_ID),
'fontsize', 3)
//---------------
//Plot #01 - Voc.
//---------------
subplot(351)
plot3d1(az_x,ev_y,Uo_matrix);
title('V_oc [V]');
xset("colormap",hotcolormap(150));
ax=gca();
ax.cube_scaling="on";
xlabel('Phi');
ylabel('Theta');
Uo_min=min(Uo_matrix)
Uo_max=max(Uo_matrix)
colorbar(Uo_min, Uo_max)
a = gca();
a.view = '2d';

//-------------------------
//Plot #02 - Voc, contour.
//-------------------------
subplot(352)
contour2d(az_x,ev_y,Uo_matrix,{-0.6,-0.65,-0.7})
title('Voc [V]');
f=gcf();
//f.color_map=jetcolormap(7)
ax=gca();
ax.cube_scaling="on";
xlabel('Phi');
ylabel('Theta');
f=gcf()

//---------------
//Plot #03 - Isc.
//---------------
subplot(353)
plot3d1(az_x,ev_y,Isc_matrix);
title('I_sc [A]');
f=gcf();
//f.color_map=graycolormap(64);
ax=gca();
```

```
ax.cube_scaling="on";
xlabel('Phi');
ylabel('Theta');
//xset("colormap",hotcolormap(100));
Isc_min=min(Isc_matrix)
Isc_max=max(Isc_matrix)
colorbar(Isc_min, Isc_max)
a = gca();
a.view = '2d';

//------------------------
//Plot #04 - Isc, contour.
//------------------------
subplot(354)
contour2d(az_x,ev_y,Isc_matrix,{-1,-2,-3,-4})
title('Isc [A]');
f=gcf();
//f.color_map=jetcolormap(7)
//f.color_map=hotcolormap(100)
ax=gca();
ax.cube_scaling="on";
xlabel('Phi');
ylabel('Theta');
f=gcf()

//--------------
//Plot #05 - FF.
//--------------
//subplot(353)
//xset("colormap",hotcolormap(100));
//FF_min=min(FF_matrix)
//FF_max=max(FF_matrix)
//colorbar(FF_min, FF_max)
//plot3d1(az_x,ev_y,FF_matrix);
//title('FF');
//f=gcf();
//f.color_map=jetcolormap(7);
//ax=gca();
//ax.cube_scaling="on";
//xlabel('Phi');
//ylabel('Theta');
//a = gca();
//a.view = '2d';

//-----------------------
//Plot #06 - FF, contour.
//-----------------------
//subplot(356)
//contour2d(az_x,ev_y,FF_matrix,{0.5,0.8})
//title('FF');
//f=gcf();
//f.color_map=jetcolormap(7);
//f.color_map=hotcolormap(100)
//ax=gca();
//ax.cube_scaling="on";
//xlabel('Azimuth');
//ylabel('Elevation');
//f=gcf()
```

```
//--------------
//Plot #07 - MPP.
//--------------

//subplot(258)
//xset("colormap",hotcolormap(150));
//MPP_min=min(pmx_matrix)
//MPP_max=max(pmx_matrix)
//colorbar(MPP_min, MPP_max)
//plot3d1(az_x,ev_y,pmx_matrix);
//title('MPP [mW]');
//f=gcf();
//ax=gca();
//ax.cube_scaling="on";
//xlabel('Azimuth');
//ylabel('Elevation');
//a = gca();
//a.view = '2d';

//------------------------
//Plot #08 - MPP, contour.
//------------------------
//subplot(259)
//contour2d(az_x,ev_y,pmx_matrix,2)
//title('MPP [mW]');
//f=gcf();
//ax=gca();
//ax.cube_scaling="on";
//xlabel('Azimuth');
//ylabel('Elevation');

//--------------
//Plot #09 - Efficiency.
//--------------
subplot(355)
//xset("colormap",hotcolormap(100));
eta_min=min(eta_matrix)
eta_max=max(eta_matrix)
colorbar(eta_min, eta_max)
plot3d1(az_x,ev_y,eta_matrix);
title('Power Conversion Efficiency [%]');
f=gcf();
//f.color_map=jetcolormap(7);
ax=gca();
ax.cube_scaling="on";
xlabel('Phi');
ylabel('Theta');
a = gca();
a.view = '2d';

//------------------------
//Plot #10 - Efficiency.
//------------------------
subplot(356)
contour2d(az_x,ev_y,eta_matrix,{8,10,12,14,16,18,19})
title('Power Conversion Efficiency [%]');
f=gcf();
//f.color_map=jetcolormap(7)
//f.color_map=hotcolormap(100)
```

```
ax=gca();
ax.cube_scaling="on";
xlabel('Phi');
ylabel('Theta');
f=gcf()

//--------------
//Plot #11 - Normalized Efficiency.
//--------------
subplot(357)
//xset("colormap",hotcolormap(100));
etanormal=eta_matrix/eta(1)
eta_min=min(etanormal)
eta_max=max(etanormal)
contour2d(az_x,ev_y,etanormal,{0.5,0.6,0.7,0.8,0.9})
title('Normalized Efficiency');
f=gcf();
//f.color_map=jetcolormap(7);
ax=gca();
ax.cube_scaling="on";
xlabel('Phi');
ylabel('Theta');
f=gcf();

//--------------
//Plot #11 - Relative Efficiency.
//--------------
//subplot(359)
//xset("colormap",hotcolormap(100));
//etarel=eta_matrix/(cos(az)*cos(ev))
//eta_min=min(etarel)
//eta_max=max(etarel)
//contour2d(az_x,ev_y,etarel,{0.1,0.2,0.3,0.4,0.5,0.6,0.7,0.8,0.9})
//title('Relative Efficiency');
//f=gcf();
//f.color_map=jetcolormap(7);
//ax=gca();
//ax.cube_scaling="on";
//xlabel('Phi');
//ylabel('Theta');
//f=gcf();

disp(Ptotal, etanorm, etaav, max(eta(k)), etanorm2, eta(1));
```